POLITECNICO DI MILANO
DEPARTMENT OF ELECTRONICS, INFORMATION, AND BIOENGINEERING
DOCTORAL PROGRAMME IN INFORMATION ENGINEERING

INCREASING CAPACITY OF WIRELESS NETWORKS THROUGH AERIAL BASE STATIONS

Doctoral Dissertation of:
Navuday Sharma

Supervisor:
Prof. Maurizio Magarini

Tutor:
Prof. Andrea Virgilio Monti Guarnieri

The Chair of the Doctoral Program:
Prof. Andrea Bonarini

2015/2018 – XXXI Cycle

To my beloved parents.

Certificate

This is to certify that the research work presented in this thesis, entitled **"Increasing Capacity of Wireless Networks through Aerial Base Stations"** was conducted by **"Mr. Navuday Sharma (ID. 853701)"** under the supervision and guidance of **Prof. Maurizio Magarini**. No part of this thesis, in full or parts, has been submitted anywhere else for any other degree or diploma. This thesis is submitted to **Telecommunication Engineering of Dipartimento di Elettronica, Informazione e Bioingegneria (DEIB), Politecnico di Milano, ITALY** in fulfillment of the requirements for the degree of **Doctor of Philosophy** for XXXI Cycle (2015-2018).

Maurizio Magarini
Department of Electronics, Information, and Bio-engineering
Politecnico di Milano

Acknowledgment

I would like to extend thanks to the many people, in many countries, who so generously contributed to the work presented in this thesis. Firstly, I would like to express my sincere gratitude to my advisor **Prof. Maurizio Magarini** for the continuous support of my Ph.D study and related research, for his patience, motivation, and immense knowledge. His guidance helped me in all the time of research and writing of this thesis. Apart from this, his polite and understanding attitude, patience, perfection in his work and constant encouragement motivated me throughout my period at Politecnico di Milano. I could not have imagined having a better advisor and mentor for my Ph.D study. Also, I am also hugely appreciative to **Dipartimento di Elettronica, Informazione e Bioingegneria, Politecnico di Milano** for providing me the opportunity to do Ph.D studies.

My sincere thanks also goes to **Prof. Dushantha Nalin Jayakody**, who provided me an opportunity to join their team as a visiting researcher at Infocomm Lab, Tomsk Polytechnic University, Russian Federation for nine months, co-supervised and gave access to the laboratory and research facilities in that duration.

Similar, profound gratitude goes to **Prof. Vishal Sharma** from MobiSec Lab, Soonchunhyang University, South Korea and **Dr. Haris Pervaiz** from 5G Innovation Centre, University of Surrey, UK for providing guidance in my work and contributions in my articles. I would also like to thank my other research collaborators, **Prof. Rahim Tafazolli** from 5G Innovation Centre, University of Surrey, UK, **Prof. Qiang Ni** from Lancaster University, UK, **Prof Luca Reggiani** and **Prof Laura Dossi** from

Consiglio Nazionale delle Ricerche - Istituto di Elettronica e di Ingegneria dell'Informazione e delle Telecomunicazioni (CNR-IEIIT).

I thank my fellow lab-mates in for the stimulating discussions, for the sleepless nights we were working together before deadlines, and for all the fun we have had in the last three years.

Last but not the least, I would like to thank my parents for their unbelievable and unconditional support throughout writing this thesis. They are the most important people in my world and I dedicate this thesis to them.

Abstract

In the past decade, due to immense high speed data and wider connectivity requirements, the cellular technologies have been continuously evolving leading to a major revolution in telecommunication industry. Currently, under IMT 2020, commonly known as 5^{th} Generation of Cellular Technology, the targeted applications have been broadly classified as: enhanced mobile broadband (eMBB), massive machine type communication (mMTC), ultra-reliable and low latency communications (uRLLC), vehicle-to-vehicle (V2V) and vehicle-to-infrastructure (V2X).

In order to address the increasing data requirements, particularly, during flash crowds such as concerts, rallies, festivals, sport events etc, where many people gathered around in an area, use data services such as video streaming, photo sharing, video calls etc, higher densification of terrestrial network architecture is gaining immense importance in the name of Ultra-Dense Networks (UDNs). The data traffic increases manifold due to development of high resolution and big screen smart devices such as phones, tablets, laptops with 4K resolution, which eventually demands for higher data.

Recently, Unmanned Aerial Vehicles (UAVs), generally known as drones were started to be investigated to provide data service to the users in suburban areas. Such projects were initially started by Google and Facebook to develop solar powered drones providing internet services. Later, companies such as Qualcomm, China mobile and Nokia started to investigate on other aspects such as controlling the drones through LTE base stations, cooperative communication among the drone network etc. Successful handovers

were reported by Qualcomm with zero link failure in autonomous drone control through LTE network. Similar project was conducted by Ericsson and China mobile with deployment of prototype in field trial. Also, with techniques such as swarm optimization and collision avoidance algorithms, the drone network could be deployed in the city environment as well, as reported by Nokia.

With such interest from industry and academia, research on UAVs acting as Aerial Base Stations (ABS) attained immediate attention. Therefore, this thesis mainly discusses about several technological aspects pertaining to such a system. Although, there are many research directions to the development of an ABS network, here we address certain directions. The work in this thesis, initially starts with the Air-to-Ground (A2G) Channel Modeling. There are many A2G channel models existing in the literature but since the work done here is to provide cellular network by UAVs, Low Altitude Aerial Platforms (LAPs) were preferred up to the altitude of 2000 m. The existing channel models mostly deal with commercial or military aircrafts, which fly at very high speeds near to subsonic or supersonic ranges. Such high speeds are not preferred for an ABS network to avoid frequent handovers. Also, some researchers have argued about the effect of Doppler shift at higher speeds which would finally lower the performance of the system. However, from the analysis and simulations provided in this thesis, effect of Doppler was not much observed with A2G channel and implementation of 5G waveforms. Due to unavailability of channel parameters for LAPs, measurements were performed using a radio propagation simulator for different environments: Suburban, Urban and Urban High Rise. These environments were generic since they were developed using ITU-R parameters for the simulator. Therefore, results from this simulator could be applied to practical environments with small degree of inaccuracy. Further, the work on cell coverage, capacity and interference analysis was conducted with simulation results obtained from the ray tracing simulator and verification of these results were done by performing analytical analysis and obtaining closed-form expressions. The graphs plotted using these expressions, matched with the graphs obtained from simulations with same simulation parameters. Later, in this thesis a new system was proposed as an optimal replacement to UDNs, to support the flash crowds. This system was termed as Ultra-Dense Cloud Drone Network (UDCDN). This system is advantageous as it offers reduction in Total Cost of Ownership (TCO) as compared to UDNs. Also, UDCDN is on-demand deployment system, $i.e.$ it is deployed by the mobile operator only when required based on the data traffic information obtained from the cloud. Further, in the the-

sis, work has been done on implementing parameters for Ultra-Reliable Low Latency Communication (uRLLC) of 5G Physical Layer (PHY) on the ABS network to provide reliable and faster connectivity for ground users. Symbol Error Rate (SER) improvements were seen when uRLLC was implemented for A2G channel with Generalized Frequency Division Multiplexing (GFDM) modulation. Further, results were also provided by introducing Carrier Frequency Offset (CFO) in the system model.

Following the above work, other aspects were also considered in the thesis. Apart from primarily ABS network, a heterogeneous network (HetNet), consisting of multi-tier drone and terrestrial network, is seen as a more feasible options for the present cellular network. Therefore, further this thesis discusses about three major aspects which optimize the multi-tier ABS network: survivability, coverage and mobility laws to avoid issues related to inter-cell interference, frequent handovers, power deficiency etc. Later, work has also been done on interference alignment (IA) for maximizing the sum rate. However, IA demands for independent channels to provide better efficiency but at LAPs obtaining independent channels seems improbable. Therefore, such study serves better for a High Altitude Aerial Platform (HAP). An optimal receiver separation distance was also defined for the system.

Another set of work has been performed in this thesis, which formed as a minor project apart from the major one reported throughout. The aim of this project was to develop an Internet of Thing (IoT) based Health and Usage Monitoring Systems (HUMS) for a helicopter. HUMS is an integrated recording and monitoring system that includes sensors, data acquisition technology and software algorithms (both on-board and ground-based) that are provided as a unit with the goals of reducing maintenance costs and improving safety and availability. For this system, the goal was to deploy various sensors all throughout the aircraft for monitoring different avionics components health and lifecycle. This data was to be send to a common gateway, known as a Transmission Data Concentrator (TDC) for data aggregations and processing. This processed data was sent to the cloud using cellular network when the aircraft is in the range of terrestrial network, otherwise using the satellite network.

List of Publications

Journal:

- **N. Sharma**, M. Magarini and D.N.K. Jayakody, "Channel Characterization at 2.4 GHz for Low Altitude Aerial Base Stations", IEEE Vehicular Technology Magazine (under review).

- **N. Sharma**, A. Kumar, D.N.K. Jayakody, M. Magarini, H. Pervaiz, R. Tafazolli and Q. Ni, "Tactile Internet-Enabled "LTE-Compatible" Aerial Base Station: Performance and Trade-off", in IEEE Transactions of Vehicular Technology (TVT) (under review).

- **N. Sharma**, M. Magarini, D. N. K. Jayakody, V. Sharma and J. Li, "On-Demand Ultra-Dense Cloud Drone Networks: Opportunities, Challenges and Benefits", in IEEE Communications Magazine, vol. 56, no. 8, pp. 85-91, August 2018.

- V. Sharma and **N. Sharma**, "Control over Skies: Survivability, Coverage and Mobility Laws for Hierarchical Aerial Base Stations", in IEEE Wireless Communications (under review).

- **N. Sharma**, M. Magarini, D.N.K. Jayakody and V. Sharma, "Closed-Form Expressions for Cell Coverage Area by Low Altitude Aerial Base Station", IEEE Networking Letters (under review).

- S.P.G, **N. Sharma**, M. Magarini and P. Muthuchidambaranathan, "Effect of imperfect CSI on interference alignment in multiple-High Altitude Platforms based communication", Physical Communication, Elsevier, 2017, pp. 1-7.

- D. Scazzoli, A. Kumar, **N. Sharma**, M. Magarini, G. Verticale, "Fault Recovery in Time-Synchronized Mission Critical ZigBee-Based Wireless Sensor Networks", International Journal of Wireless Information Networks, Springer, 2017, pp. 268-277.

Conferences:

- **N. Sharma**, M. Magarini, L. Dossi, L. Reggiani and R. Nebuloni, "A study of channel model parameters for aerial base stations at 2.4 GHz in different environments", 2018 15th IEEE Annual Consumer Communications and Networking Conference (CCNC), Las Vegas, NV, 2018, pp. 1-6.

- **N. Sharma**, A. Kumar, M. Magarini, S. Bregni and D.N.K Jayakody, "Impact of CFO on Tactile Internet- Enabled UAV Using "Better than Nyquist" Pulse Shaping in GFDM", IEEE VTC Spring 2019 (under review).

- D.G. Cileo, **N. Sharma** and M. Magarini, "Coverage, capacity and interference analysis for an aerial base station in different environments", 2017 International Symposium on Wireless Communication Systems (ISWCS), Bologna, 2017, pp. 281-286.

- S.P.G, **N. Sharma**, M. Magarini and P. Muthuchidambaranathan, "Interference Alignment in Multiple-High Altitude Platforms based Communication with a Generalized Long Distance Line of Sight Channel Model", International Conference on Communication, Management and Information Technology (ICCMIT), Warsaw, 2017, pp. 1-5.

- D. Scazzoli, A. Kumar, **N. Sharma**, M. Magarini and G. Verticale, "A novel technique for ZigBee coordinator failure recovery and its impact on timing synchronization", 2016 IEEE 27th Annual International Symposium on Personal, Indoor, and Mobile Radio Communications (PIMRC), Valencia, 2016, pp. 1-5.

Contents

List of Figures

List of Tables

List of Acronyms

2CM 2D Channel Model

3CM 3D Channel Model

3GPP 3rd Generation Partnership Project

A2G Air-to-Ground

A-AoA Azimuth-Angle-of-Arrival

ABG Alpha-Beta-Gamma

ABS Aerial Base Station

AI Artificial Intelligence

AoA Angle-of-Arrival

AoD Angle-of-Departure

AP Access Point

ATC Aircraft Traffic Controller

AWGN Additive White Gaussian Noise

BBU Base Band Unit

BER Bit Error Rate

BLER Block Error Rate

List of Tables

BTN Better than Nyquist

CAD Computer Aided Design

CAPEX Capital Expenditure

CCI Co-Channel Interference

CDF Cumulative Distribution Function

CFO Carrier Frequency Offset

CI Close-In

CNPC Control and Non-Payload Communication

CO Central Office

COTS Commercial Off The Shelf

CP Cyclic Prefix

C-RAN Centralized Radio Access Network

CSI Channel State Information

D2D Device to Device

DoF Degrees of Freedom

EASA European Aviation Safety Agency

E-AoA Elevation-Angle-of-Arrival

EM Electromagnetic Radiation

eMBB Enhanced mobile broadband

FAA Federal Aviation Administration

Farcsech Flipped-Inverse Hyperbolic Secant

FBMC Filter Bank Multi-Carrier

FC-RAN Fog-Cloud based Radio Access Network

FFD Full Function Device

F-OFDM Filtered-Orthogonal Frequency Division Multiplexing

F-RAN Fog Radio Access Network

Fsech Flipped-Hyperbolic Secant

FSO Free Space Optical

GFDM Generalized Frequency Division Multiplexing

GS Ground Station

HAP High Altitude Aerial Platform

HetNets Heterogeneous Networks

H-RAN Heterogenous Radio Access Network

IA Interference Alignment

ICAO International Civil Aviation Organization

ICI Inter-Carrier Interference

IID Independent and Identically Distributed

IoD Internet of Drones

IoT Internet of Things

ITU International Telecommunications Union

LAP Low Altitude Aerial Platform

LoRaWAN Long Range Wide Area Network

LoS Line-of-Sight

LPWAN Low Power Wide Area Network

LSP Large Scale Parameter

LTE Long Term Evolution

LTE-MTC LTE-Machine Type Communication

M2M Machine-to-Machine

MBS Macro Base Station

MEC Mobile Edge Computing

MF Matched Filter

MIMO Multiple-In Multiple-Out

mMTC Massive machine type communications

NB-IoT Narrow-Band IoT

NBRL N-Block Recursive Learning

NET Network Layer

NFV Network Function Virtualization

NLoS Non-Line of Sight

NR New Radio

OOB Out-Of-Band

OFDM Orthogonal Frequency Division Multiplexing

OFDMA Orthogonal Frequency Division Multiple Access

OPEX Operational Expenditure

PAN Personal Area Network

PER Packet Error Rate

PHY Physical Layer

PL Path Loss

PLE Path Loss Exponent

PRB Physical Resource Block

QoE Quality-of-Experience

QoS Quality of Service

QPSK Quadrature Phase Shift Keying

RAT Radio Access Technology

RBS Reference Broadcast Synchronization

R-Farcsech Reverse Flipped-Inverse Hyperbolic Secant

RFD Reduced Function Device

RMS Root Mean Sqaure

RRH Radio Remote Head

RSSI Received Signal Strength Indicator

SDN Software Defined Networking

SDR Software Defined Radio

SER Symbol-Error-Rate

SIR Signal-to-Interference Ratio

SINR Signal-to-Interference plus Noise Ratio

SNR Signal-to-Noise Ratio

SPF Single point of Failure

SSP Small Scale Parameter

SVD Singular-Value Decomposition

SWIPT Simultaneous Wireless Information and Power Transfer

TCN Terrestrial Cellular Network

TCO Total Cost of Ownership

TDC Transmission Data Concentrator

TPSN Timing-sync Protocol for Sensor Network

UAV Unmanned Aerial Vehicle

UDCDN Ultra-Dense Cloud Drone Network

UDN Ultra-Dense Network

UE User Equipment

UFMC Universal Filtered Multi-Carrier

uRLLC Ultra-reliable and low latency communications

V2V Vehicle-to-Vehicle

V2X Vehicle-to-Infrastructure

VM Virtual Machine

VNF Virtual Network Function

VSWR Voltage Standing Wave Ratio

WPT Wireless Power Transfer

WSN Wireless Sensor Network

ZF Zero Forcing

CHAPTER 1

Introduction

1.1 Background and Motivation

Wireless Communication technology goes through a revolutionary change in every ten years. Each generation of mobile technology provides capacity enhancements to satisfy the vastly increasing data requirements of the mobile users. This pertains mainly to development of handsets or user equipments (UE) supporting high resolution videos. Following this trend, the fifth generation of cellular technology, IMT 2020, commonly referred to as 5G, demands more data hungry devices and applications. In fact, 5G is not limited to mobile broadband but its usage patterns are also envisaged to support a wide variety of use cases in three broad categories:

- Enhanced mobile broadband (eMBB): eMBB is an extension of 4G broadband service to support high data rates and provide moderate data rates to cell-edge users, while guaranteeing moderate reliability with packet error rate (PER) of the order of 10^{-3}.
- Ultra-reliable and low latency communications (uRLLC): The current 4G wireless cellular network have a latency of 50 ms which can go up to several seconds and target block error rate (BLER) of 10^{-1} before

re-transmission since 4G is mainly targeted for broadband communication unlike 5G. However, this service of 5G put strict constraints on round-trip latency of less than 1 ms along with ultra-high reliability with target BLER of 10^{-9}. This service targets applications with stringent latency and reliability requirements such as tele-surgery, intelligent transportation, industry automation, augmented/virtual reality, etc.

- Massive machine type communications (mMTC): This service is used to connect to large number of internet of things (IoT) devices which are sporadically active and transmit small amounts of data.

In order to accomplish these services, various 5G technologies such as denser multi-radio access technology (RAT), heterogeneous networks (HetNets), massive multi-input-multi-output (MIMO), millimeter (mm) wave signals, direct device to device (D2D) communication, full duplex systems, etc are being researched to enable the high-capacity mission-related data transmissions for rate-demanding applications. Integrating Unmanned Aerial Vehicles (UAVs), commonly known as drones into 5G (and beyond) cellular systems is a promising technology to achieve such goals. Earlier UAVs were used mainly for military applications such as surveillance, reconnaissance and weapon delivery. Later, its commercial use began with film-making, remote sensing and monitoring, goods delivery service, disaster search and rescue etc. Now its potential to be used as an Aerial Base Station (ABS) [1] has been recognized by many companies such as Qualcomm, Ericsson, Nokia, China mobile etc. These companies have been performing field tests for handovers, received signal strengths, cooperative functioning in groups, autonomous control over Long Term Evolution (LTE) network. With interests developed to deploy ABS network, research began intensively towards assisting technologies and algorithms to support such system. Initially, the research directions were to work upon the transceiver design and channel models for ABS. Later, the research oriented more toward multi-tier ABS network to be integrated with terrestrial network.

Motivated with such profound interest of industry and academia, this thesis was developed to work on various aspects addressing ABS network with simulation and analytical results. This thesis has been organized in three parts described as follows:

- Primary Contributions: This work was done with major inputs. Here the major aspects discussed were on Air-to-Ground (A2G) channel

[1] The term UAV, ABS and drones are used interchangeably through out the thesis.

model. The channel model was developed using a deterministic approach or map-based approach rather than a stochastic one. This approach is more feasible as it deals with higher accuracy of the channel modeling parameters. However, only limitation of this approach was the large simulation time. In this ray tracing simulator was implemented on Suburban, Urban and Urban High Rise environments. Further, cell coverage, capacity and interference analysis was performed on the basis of the received power obtained from the ray tracing simulator, with further provision of closed-form expressions for cell coverage. Later, a new system, Ultra-Dense Cloud Drone Network (UDCDN), was proposed as a suitable and cost effective replacement to Ultra-Dense Networks (UDNs). Finally, work on information transmission with low latency has been performed with A2G channel model for ABSs.

- Secondary Contributions: This work deals with the research conducted in collaboration with other researchers with secondary inputs. Here, work was done on obtaining survivability, coverage and mobility laws for the ABS network to avoid issues relating to performance degradation of the system. Further, interference alignment (IA) has been implemented for High Altitude Aerial Platforms (HAPs) to maximize the sum rate.

- Minor project: This project was done to develop an IoT platform based health monitoring system for avionics components installed on the aircraft. The data from the various sensors deployed on the aircraft was sent to a common gateway or the transmission data concentrator (TDC). The information from the TDC was sent to the cloud using cellular or satellite network based on the range of connectivity with the aircraft. A redundant gateway was used to address the failure of primary gateway, by taking over its functionalities. Further, the data from sensors was accessed by the Aircraft Traffic Controller (ATC) operators to monitor the health of aircraft in real time. The data can also be stored in the cloud for later observations. This system is particularly useful for fleet management.

1.2 Contribution and Outline of the Thesis

The thesis is outlined as follows. Chap. 2, **"Modeling of Air-to-Ground Channel"** provides the following contributions.

- A deterministic approach was followed to model the parameters of A2G channel. A ray tracing simulation setup was developed using commercial radio wave propagation software, Wireless InSite. The simulations were performed over generalized environments: Suburban, Urban and Urban High Rise, developed according to ITU-R parameters on a design software. Due to generalized environments, the channel parameters obtained could be implemented in real scenarios with small degree of inaccuracy.

- Different channel modeling campaigns and literature review was provided. Further, three channel modeling approaches were described: deterministic, stochastic and hybrid.

- A 3D channel model was described since A2G channel model includes elevation angle, which makes it 3D.

- The Close-In (CI) reference distance model was described to be used as Path Loss (PL) and shadow fading model. Two fundamental parameters, Path Loss Exponent (PLE) and standard deviation of shadowing were used mainly to define the CI model. Further, the key role of probability of Line-of-Sight (LoS) was mentioned and average PL model was shown.

- Simulation results for PLE, ricean factor and standard deviation were shown with respect to altitude and elevation angle of the ABS from the ground users, for the different considered environments. Also, simulations for shadowing correlation, root mean sqaure (RMS) delay spread and Angle-of-Arrival (AoA) (both azimuth and elevation) were shown with respect to receiver distance from transmitter, at different ABS altitudes and environments. Further, Cumulative Distribution Function (CDF) of RMS delay spread and AoA (both azimuth and elevation) are also provided.

Contributions of Chap. 3, **"Cell Coverage, Capacity and Interference analysis for Low Altitude Aerial Base Station"** are as follows:

- This chapter focuses on obtaining cellular coverage area by an ABS based on the received power by ground users, from the ray tracing simulations performed in Chap. 2. The simulations were performed in different environments and for different thresholds of received power. The variation of cell coverage was observed with two fundamental parameters for ABS, $i.e,$ altitude and transmission power. Similarly,

capacity and interference analysis was performed. Also the literature review regarding considered topics have been provided.

- The closed-form expressions are also provided for cell coverage based on solid angle approach. These expression takes into account certain set of variables such as propagation factors, ABS altitude, elevation angle and rotation angle caused due to wind gusts or drone maneuvers.
- The simulations performed with the analytical expression led to same results with certain margin of inaccuracy, as obtained from the ray tracing data, with same simulation parameters. Thereby, the validity of analytical expressions were proofed.
- The geometric increase in cell coverage area due to rotation angle have been shown in this chapter. However, the trade-off of cellular coverage with the transmission power constraint leading to decrease in coverage area has been a part of future works.

Further in Chap. 4, **"On-Demand Ultra-Dense Cloud Drone Networks"**, the contributions given are:

- In this chapter, a new system architecture is proposed, known as UD-CDN. This architecture serves a timely replacement for UDN. This is because, it reduces manifold the Total Cost of Ownership (TCO) of the mobile operators. UDN consumes too much power to provide high speed data to the mobile users, while UDCDN is an on-demand deployment system which serves the flash crowds for limited time period.
- The proposed system architecture is provided, with literature review of similar proposed architectures is given. Further, the challenges and benefits of UDCDN are described in detail. Later, ABS health monitoring is also discussed as an essential factor in such systems since the ABSs, can hover much near to the flash crowds. Lastly, fronthauling and backhauling issues are described.

Contribution for Chap. 5, **"Low Latency-Enabled "LTE-Compatible" Aerial Base Station: Performance and Trade-off"** are given as follows:

- In this chapter, an optimal altitude of ABS, for minimum Symbol-Error-Rate (SER) and maximum ABS cell coverage, in different environments was obtained. Optimal altitude was obtained from static ABS by performing ray tracing simulations at different heights.

- Here the deterministic or map-based channel modeling approach [Nurmela et al., 2015] was used rather than stochastic and hybrid, to obtain A2G channel parameters. Map-based approach is based on ray tracing using a three dimensional propagation environment which inherently accounts for propagation mechanisms such as reflection, diffraction, scattering etc. This approach provides the most accurate modeling solutions with minor inaccuracies.

- Also, three dimensional propagation environment makes the channel results site-specific but this limitation was eliminated by creating generalized environments described in Sec. 2.2. Therefore, the results can be implemented for any realistic environments.

- Further, Generalized Frequency Division Multiplexing (GFDM) was implemented in the system model for ABS downlink performance analysis, as being considered the suitable and compatible waveform, for LTE, LTE-A and LTE-Pro hybrid systems [Ferreira et al., 2017, Gaspar et al., 2014] due to its backward compatibility with 4G systems. Also, parameters of 5G PHY LTE grid were used as given in Table 5.2 to infer low latency scenario.

- A2G channel parameters for SER calculations were employed in the GFDM model. Also, power delay profiles were provided for A2G channel in different environments at optimal altitude. For obtaining the A2G channel, similar ray tracing simulations were performed with static and moving ABS. Further, distribution of received power for ground receivers in different environments is also given at optimal ABS altitude, which supplements to find the variation of optimal altitude with cell radius.

- The simulations were performed for LAPs to promote the densification of cellular architecture satisfying the high data traffic demands of 5G mobile users created during flash crowds [Yang et al., 2017b] in mass events such as music concerts, public rallies, cultural festivals, sport events etc, as shown in Fig. 5.1. This leads to requirement of on-demand and easily deployable UDCDN [Sharma et al., 2018b] which serves as suitable replacement for UDNs [Kamel et al., 2016] to support huge data traffic demands.

- Later, various "Better than Nyquist" (BTN) pulse shaping filters were implemented in the GFDM transceiver to obtain SER at optimal ABS altitude and show significant performance gains as compared to Nyquist

pulse shaping filters. These simulations were conducted for both static and moving ABS, to analyze the effect of Doppler shift on SER. The relevant characteristics and system description of GFDM are given in [Michailow et al., 2014].

In Chap. 6, **"Impact of Carrier Frequency Offset on Low Latency-Enabled UAV using "Better than Nyquist" Pulse Shaping in GFDM"** the contributions are:

- Carrier Frequency Offset (CFO), was introduced in the same system model as described in Chap. 5.
- Three sets of SER analysis have been shown with variation of CFO, ABS altitude and pulse shaping. Also same A2G channel model was used as shown in Chap. 2.

Contributions of Chap. 7, **"Control over Skies: Survivability, Coverage and Mobility Laws for Hierarchical Aerial Base Stations"**, are provided in the following bullets:

- This chapter provides mainly laws of survivability, mobility and coverage to address the issues related to multi-tier ABS network. A wide literature review is provided with similar aspects to address the problem and solutions related to multi-tier ABS network. Further, hierarchy of the system architecture is described.
- Problems related to ABS network coverage, survivability and mobility are discussed. Later, different optimization issues and constraints are described related to this multi-tier architecture with proposed solutions in terms of coverage control, mobility control and survivability laws.
- An N-Block Recursive Learning Framework is described which helps to provide update policies for coverage, mobility and survivability laws. Further, performance evaluation of the system was shown with discussions on open issues and challenges.

Contributions provided by Chap. 8, entitled **"Effect of Imperfect CSI on Interference Alignment in Multiple-High Altitude Platforms based Communication with a Generalized Long Distance Line of Sight Channel Model"** are as follows:

- This chapter provides IA techniques implemented on HAPs for maximizing sum rate. A literature review is provided in this regard.

- Also, the existing long distance LoS channel model is discussed with possibility of applying IA in X channel. Multiple antennas were used at HAP and ground user receiver. Later, minimum separation between the ground receiver was obtained to achieve independent channels.
- Application of IA in a more generalized channel was proposed taking into account the AoA and angle-of-departure (AoD). The bit error rate (BER) performance was reported for both IA and non-IA based communication.
- In view of actual scenario, effect of imperfect channel state information (CSI) was investigated.

Further, in Chap. 9, **"Fault Recovery in Time-Synchronized Mission Critical ZigBee-based Wireless Sensor Networks"**, the contributions are as follows:

- This chapter provides results on reliability and precise time stamping for mission critical wireless sensor networks (WSNs). A detailed literature review is provided on WSNs, with popular technologies for providing connectivity. Special attention was given to Zigbee standard for energy contained application.
- Single point of Failure (SPF) problem was described and solution was proposed to improve the reliability, by changing Personal Area Network (PAN) Identifier in place of reprogramming the router to become new coordinator in the network.
- Further methods of WSN synchronization, synchronization problems and its recovery solutions are provided. Also, a fast recovery procedure is discussed.
- Later, synchronization management and experimental measurement results are also provided.

Part I

Primary Contributions of the Thesis

CHAPTER 2

Modeling of Air-to-Ground Channel

DUE to the usage of aerial platforms as base stations, especially in densely-packed urban areas, the requirement of obtaining the appropriate channel model and its parameters attained wide importance. This chapter investigates on making an accurate prediction for channel model parameters. Here, the focus is on a simple PL and shadow fading channel model that is commonly used to describe the propagation between an aerial base station and a user on the ground. A commercial 3D ray-tracing simulator is used to extract the main parameters used in the model and the LoS/NLoS probabilities as a function of the transmitter height and elevation angle. Also, three reference scenarios: Suburban, Urban and Urban High Rise generated according to ITU-R specifications are considered. As a novel contribution, the details of different channel characteristics such as spatial correlation and CDFs for small scale parameters (SSPs) - received signal power, delay spread and AoA, are presented for different ABS heights. Various channel modeling approach and framework for 3D channel models were also focused. Also, statistical parameters for delay spread and AoA were provided.

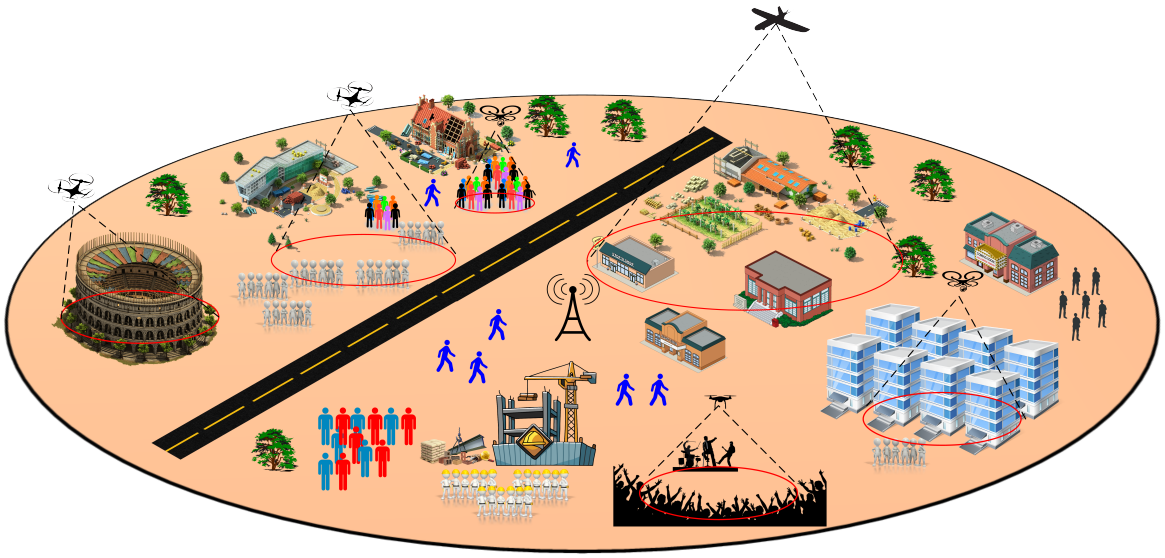

Figure 2.1: *ABS network providing cellular services in different scenarios.*

2.1 Introduction

In the past decade, the growth and development of wireless technology has led to the quick adoption of smart devices such as phones, tablets, watches, and wearables for health monitoring, with machine type communication. For such devices there are different requirements like high data rate, high reliability, and low latency. These requirements will be fulfilled by 5G for which the possible scenarios and the envisioned applications are illustrated in [Osseiran et al., 2014, Andrews et al., 2014]. Recently, several research works have considered the possibility of satisfying these requirements by installing cellular base stations on aerial platforms [Qua, , Nok, a]. However, earlier drones, also known as UAVs, were developed for military purposes such as surveillance and reconnaissance [Lyon, 2004]. Now, drones are being successfully implemented in many civil operations [Hayat et al., 2016] such as remote sensing, weather detection, precision agriculture, wildlife monitoring, film making, 3D mapping, search and rescue, etc.

2.1.1 Literature Overview

The use of UAVs with an on-board base station has been considered in several papers [Bor-Yaliniz and Yanikomeroglu, 2016, Sharma et al., 2016,

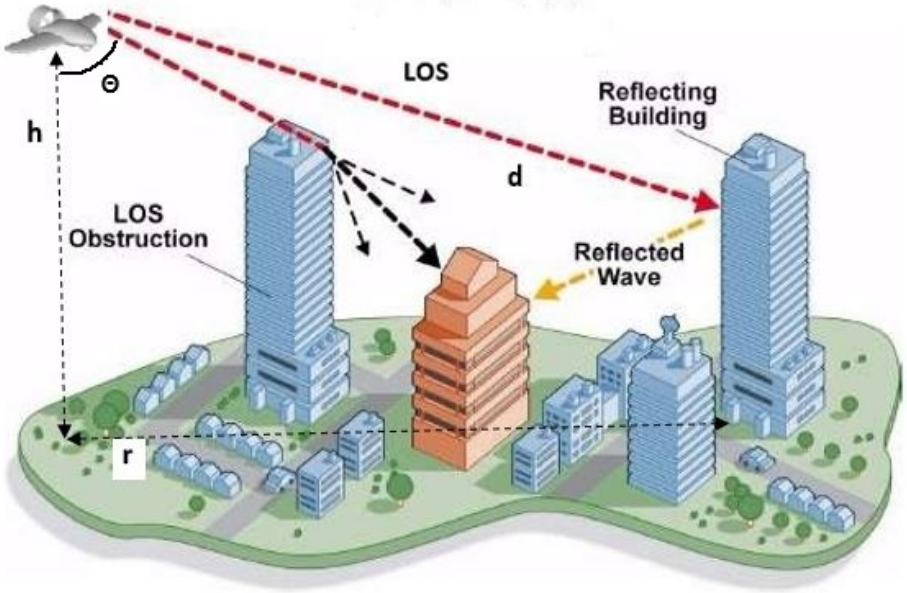

Figure 2.2: *Example of LoS and NLoS links.*

Bor-Yaliniz et al., 2016]. Due to the flexibility of drones with on-demand deployment, they have gained enormous attention in telecommunication industry as ABS to support high speed data demands of flash crowds [Yang et al., 2017b] such as concerts, public rallies, sport events or cultural festivals, where large mass of people are confined in a small area as shown in Fig. 2.1. One of the main advantages of having base station on-board a UAV is that of dynamically changing the coverage area according to traffic intensity. In these situations, UAVs can fly near to the crowd for fulfilling data requirements [Sharma et al., 2016]. However, a safe flying distance for such an operation has not been standardized yet. Moreover, the use of a UAV as flying base stations allows to provide better cellular coverage and boosting the capacity of the mobile user stations at ground [Mozaffari et al., 2016a, Mozaffari et al., 2016c]. Such a system is cost effective and highly efficient.

Both low (LAPs) and high altitude aerial platforms (HAPs) have been considered for proximity applications [Kong et al., 2011]. While either a UAV or an airship can be used to implement an HAP, only a UAV seems to be a promising platform for LAPs. This limitation is due to the large size of the airship, its low payload capacity, low speed, and difficult maneuverability that prevents it to fly at altitudes near to the mobile users on the ground.

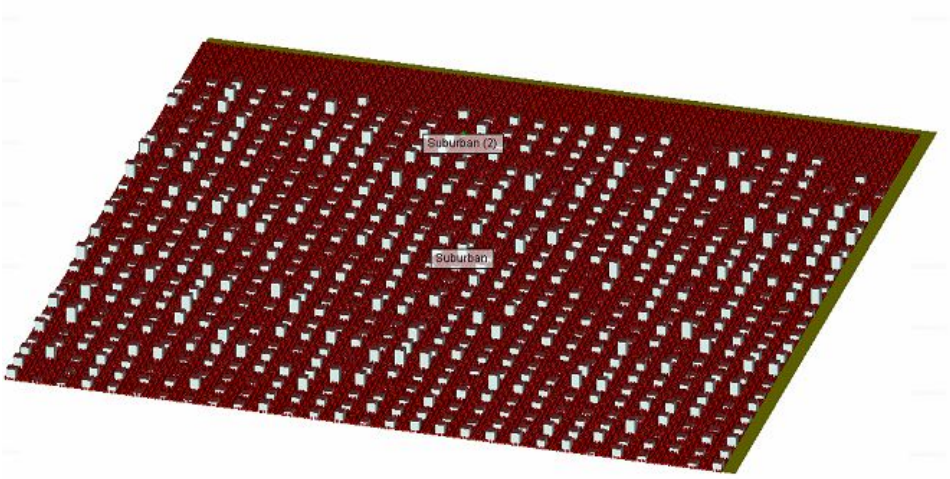

Figure 2.3: *Suburban environment used for ray tracing simulations.*

However, small UAVs such as quadcopters are easier to deploy and can fly close to the ground, thus providing better services to the users with a LoS. Therefore, LAPs/UAVs were chosen for the simulations since they provide better flexibility for small cells.

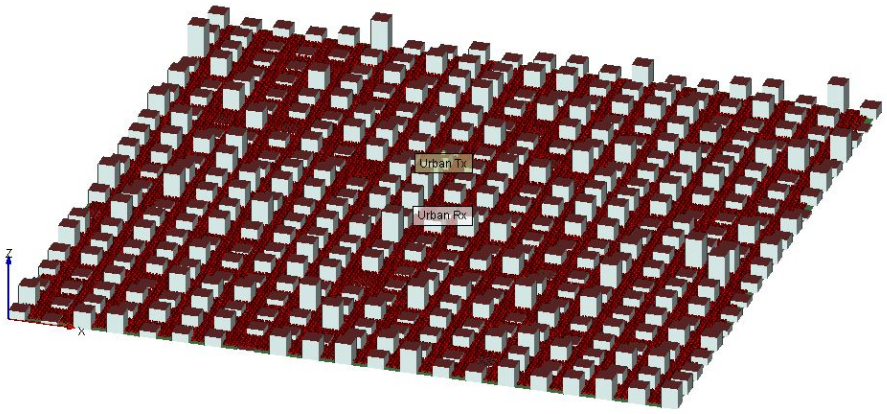

Figure 2.4: *Urban environment used for ray tracing simulations.*

However, due to growing interest for such ABS and for a system level design of mixed analog-digital front-ends for ABS, an appropriate channel model is needed, with full channel characterization. However, since this system development is at its infancy, there is not much literature available

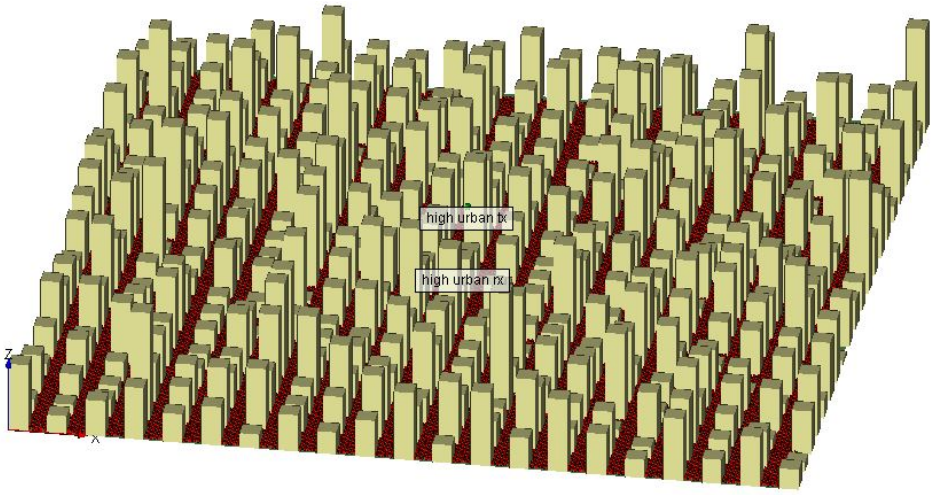

Figure 2.5: *Urban High Rise environment used for ray tracing simulations.*

on the fading channel characterization. A survey on A2G channel modeling for UAVs has been provided in [Khawaja et al., 2018, Altaf Khuwaja et al., 2018]. Most of the literature focuses on the portion of two spectral bands, L-band (960-977 MHz) and C-band (5030-5091 MHz), allocated for reliable control and non-payload communication (CNPC) data links for drones, over near urban, hilly suburban, sea surface, mountains etc, with transmitter and receiver link distance in the range of 1-19 Kms, approximately. Since practical measurement campaigns were conducted using transportable ground station transmitter and receiver antennas mounted aircraft, these measurements were bound to be site specific and may not be similar for other environments. Apart from these, several other measurements have been performed to propose new propagation models for A2G links. In [Afonso et al., 2016], authors perform statistical analysis with multiple sets of measurements to provide received power and quality of service measurements, such as round-trip time and jitter, between a receiver mounted UAV and base station at a building rooftop of height 11 m with link distance ranging up to 3 kms, for different cellular technologies such as EDGE, HSPA+ and LTE. Morever, another statistical analysis of narrowband UAV fading channel in urban area to develop a time-series generator is shown in [Simunek et al., 2013], where a transmitter mounted airship is flown over Prague city at an altitude of 100-170 m under low elevation angles with receiver, ranging from 1-6 deg. In [Yanmaz et al., 2011], authors' model the uplink and downlink channel via field measurements for an open

Table 2.1: *City layout parameters*

Scenario	α_0	β_0	γ_0	Number of Buildings	Building Width (m)	Street Width (m)
Suburban	0.1	750	8	750	11.54	24.97
Urban	0.3	500	15	500	24.49	20.23
Urban High Rise	0.5	300	50	300	40.82	16.91

Table 2.2: *Material properties used in simulation*

Material	Thickness (m)	Roughness (m)	Conductivity	Permittivity
Concrete	0.3	0	0.05	6
Wet earth	0	0	0.02	25

field and campus scenario. They provide PLE, received signal strength and throughput performance for different drone yaw angles and heights. Some studies have also been performed over A2G MIMO channel in [Willink et al., 2016], where authors' propose UAVs as a broadcast node and viable relay for high capacity communications. The measurements were carried out at 915 MHz with drone altitude at 200 m approximately for obtaining time varying channel characteristics, impacted not only by the velocity of the drone but its elevation and roll. Also, measurements have been performed in open fields at ultra-wideband for low altitudes of drones up to 16 m to obtain stochastic PL and multipath channel model [Khawaja et al., 2016]. Reference [Amorim et al., 2017] show the results of PL and shadowing for A2G channel for low altitude ABS. It provides an experimental study with drone flights to maximum heights of 120 m with 800 MHz transmission frequency.

All these major experimental studies have focused on developing appropriate A2G channel models to integrate UAVs into cellular networks. However, most of them are site-specific (mainly suburban or near urban scenarios) with low altitudes of ABS. However, concerning the high data rate demands of flash crowds [Yang et al., 2017b] and on-demand UAV deployment, more investigation is required to come up with channel measurements. This can be applied to generalized environments, thus they can be fit in every scenario with minimal variations. Also, different altitudes of the ABS should be considered to find channel variation with respect to the height of ABS, which contributes to novelty of the system.

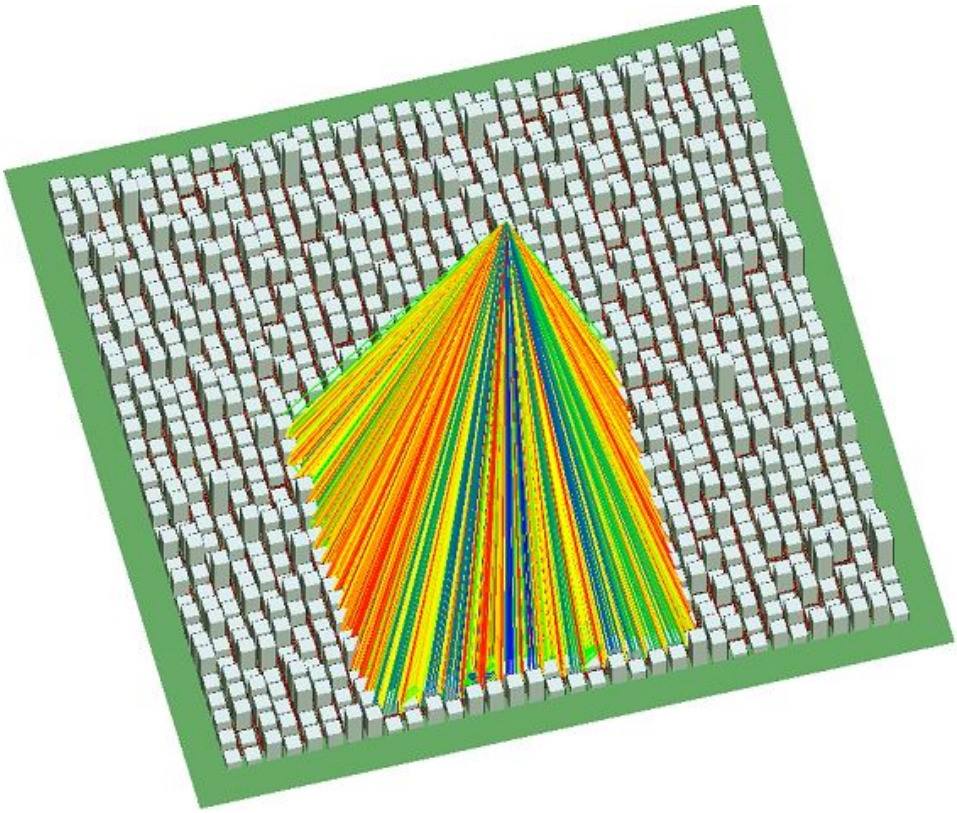

Figure 2.6: *Simulation setup of 2000×2000 m^2, with simulated area of 1000×1000 m^2 of Urban High Rise Scenario with ABS altitude of* 2000*m for ray tracing in Wireless InSite*

2.1.2 State of the Art and Contributions

In this work, the aforementioned limitations addressed were overcame by choosing ABS height and elevation angle with respect to receivers as the fundamental design parameters. Significant quantities such as the average propagation PL and the standard deviation of the shadow fading were predicted for the development of the channel model. Also PLE, standard deviation of shadowing and ricean factor in generalized environments, were calculated. Moreover, LoS and Non-Line of Sight (NLoS) links were distinguished, which are other novel parameters for A2G channel. As seen from the preceding literature survey, the A2G channel for LAPs is different from the well developed terrestrial and satellite communication channels. Models for PL and shadow fading have been proposed in [Al-Hourani et al., 2014a] for LAPs and in [Holis and Pechac, 2008] for HAPs, respectively, as

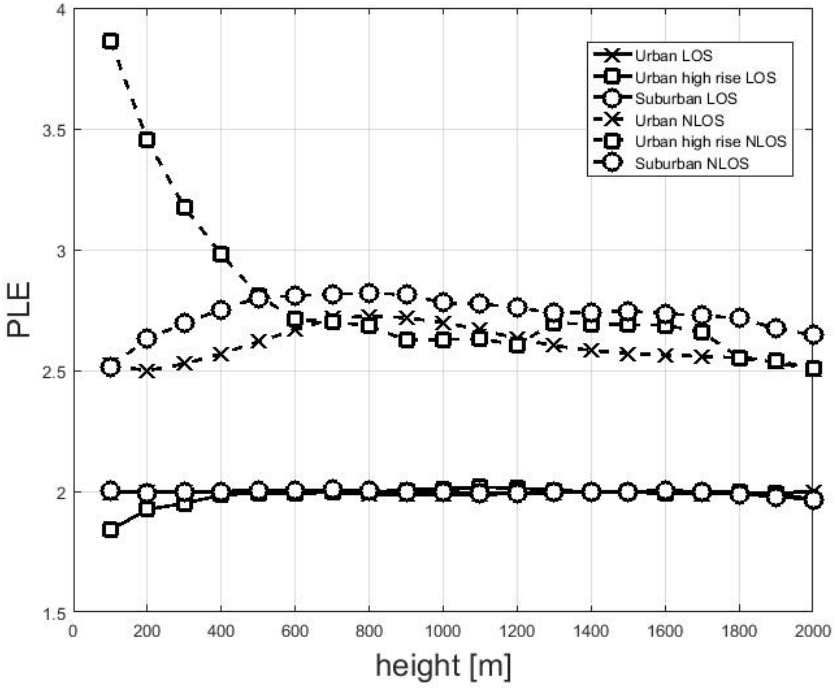

Figure 2.7: *PLE as a function of the transmitter height for LoS (continuous line) and NLoS (dashed line) in different environments.*

a function of the transmitter-to-receiver elevation angle. The elevation angle includes the PL dependence on both the transmitter-to-receiver horizontal distance and the transmitter height. However, this study is constrained to LAPs only and, therefore, a different approach is adopted here. First, the CI propagation model, *i.e.*, a standard approach for path-loss prediction that uses a $d_0 = 1$ m close-in free space reference distance [Sun et al., 2015], is considered. The CI model depends on two parameters that are the PLE and the standard deviation of large scale shadowing σ. Both the two parameters are calculated as a function of the transmitter height and link elevation angle. This procedure highlights the effects of the transmitter height and elevation angle, being the fundamental design parameters. Moreover, LoS and NLoS cases were distinguished according to the presence or absence of the free-space LoS path in the simulated link, whereas in [Al-Hourani et al., 2014a] they are estimated from the shape of the PL histogram across the test area. This allows to calculate the corresponding PLEs together with their associated LoS probabilities as a function of the

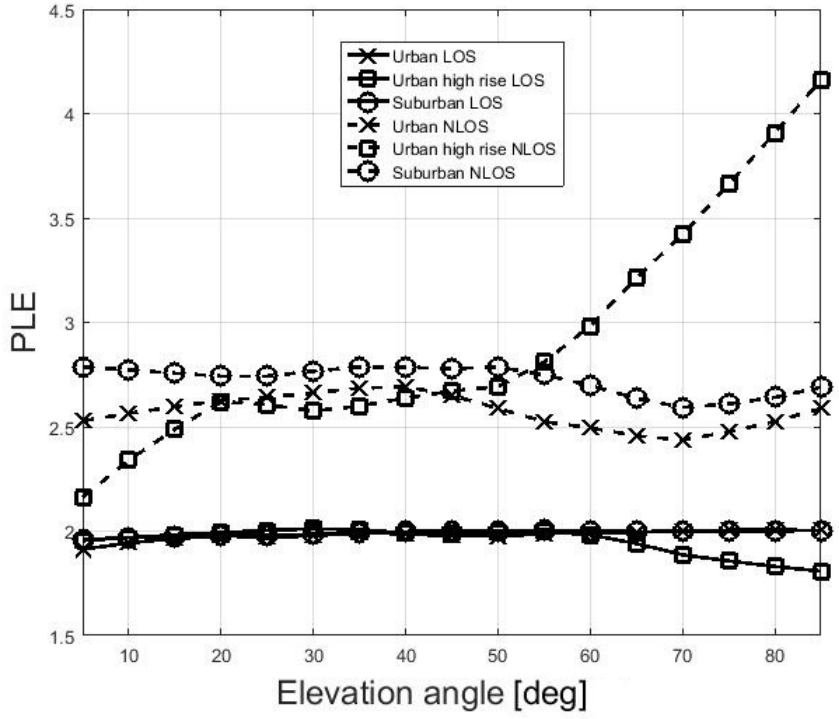

Figure 2.8: *PLE as a function of the link elevation for LoS (continuous line) and NLoS (dashed line) in different environments.*

transmitter height. Therefore, the prediction of PLE and standard deviation of shadow fading for LoS and NLoS was improved, bringing novelty to the work.

A probabilistic approach was followed, which was not addressed in the previous works. These are useful parameters for A2G channel which are modeled with Rician fading in different environments, created for simulation, as described in Sec. 2.2. Also, spatial correlation of shadowing in these three considered scenarios was investigated, which has not been addressed in previous works.

In this chapter, the focus is also on fading channel characteristics such as AoA and delay spread with their CDFs and spatial correlation properties at different ABS altitudes and environments from ray tracing simulations. AoA signifies the azimuth and elevation angles at which a ray in multipath signal is incident and delay spread is the time interval between first and

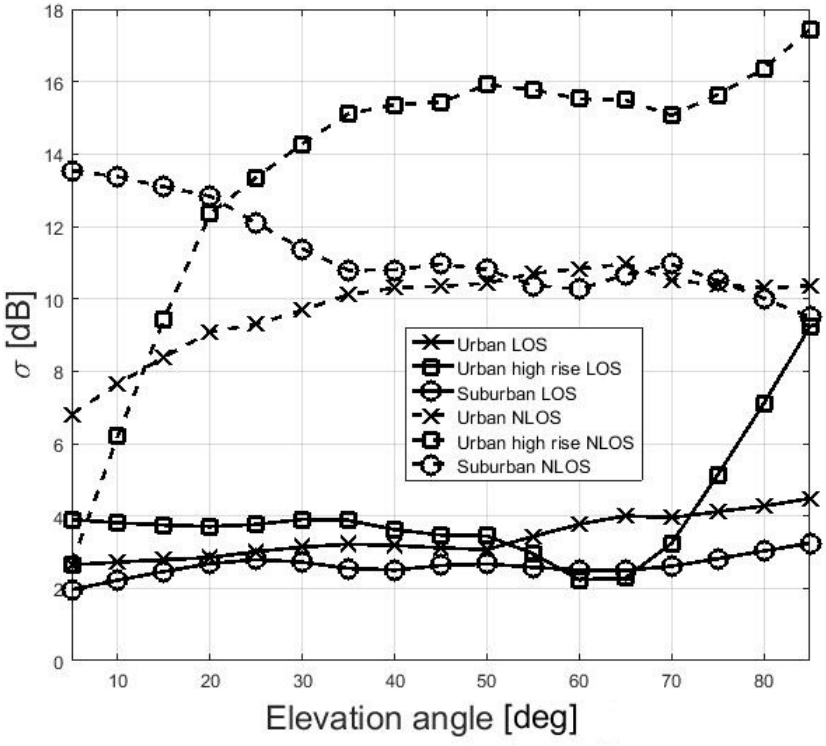

Figure 2.9: *Standard deviation of Shadowing as a function of elevation angle for LoS (continuous line) and NLoS (dashed line) links in different environments.*

last ray of that multipath signal. The elevation angle considered here, is the angle made by LoS ray at ground receiver to the perpendicular at ABS towards the ground. This is important in computing fading channel coefficient for further transceiver design. The ray tracing provide accurate and efficient predictions [Mededovic et al., 2012] of electromagnetic propagation and fading channel characteristics with broader simulation parameters and environment options, which may not be feasible with realistic channel measurements through channel sounding. Also, drone flight permission are not easily granted by aviation administration authorities in dense city scenarios or near airports, hospitals etc, for public safety. However, UAV flight standardization are being refurbished, due to outset of drone usage in civil applications. Therefore, ray tracing serves as the best option for channel parameterization of LAPs, presently.

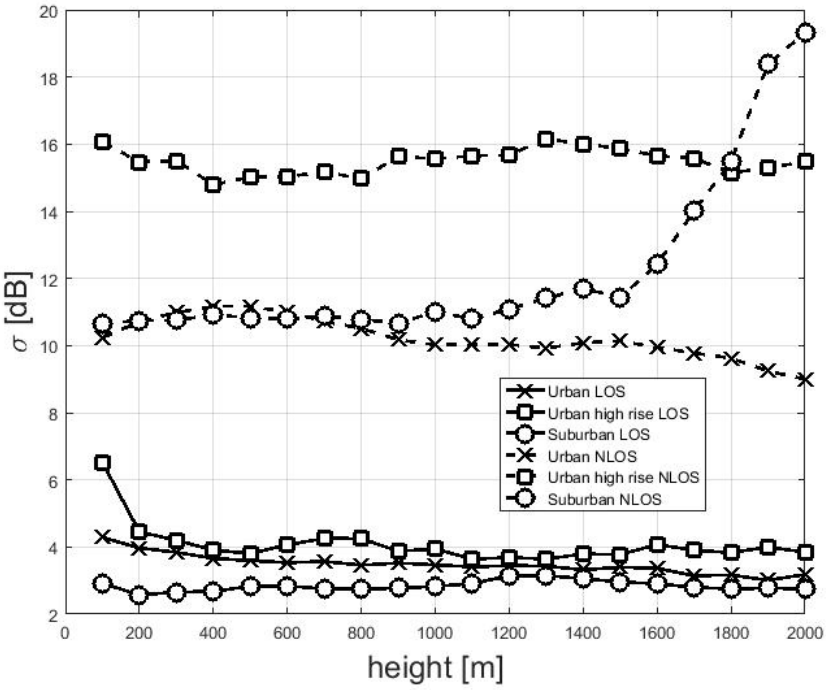

Figure 2.10: *Standard deviation of Shadowing as a function of transmitter height for LoS (continuous line) and NLoS (dashed line) links in different environments.*

2.1.3 Organization of the Chapter

The chapter is organized as follows. Section 2.2 describes generation of simulation environment, performed on a commercial Computer Aided Design (CAD) software, created for ray tracing simulation. Further, different channel modeling approaches developed during various channel modeling campaigns are addressed in Sec. 2.3. Later, three-dimensional channel model, considerably used for current scenarios is discussed in Sec. 2.4. Section 2.5 shows the PL model. Section 2.6 reports the simulation results. Finally, Sec. 2.7 draws the conclusions for this chapter. To the best of my knowledge, this is the first research work addressing channel fading characteristics for low altitude ABS for generalized environments.

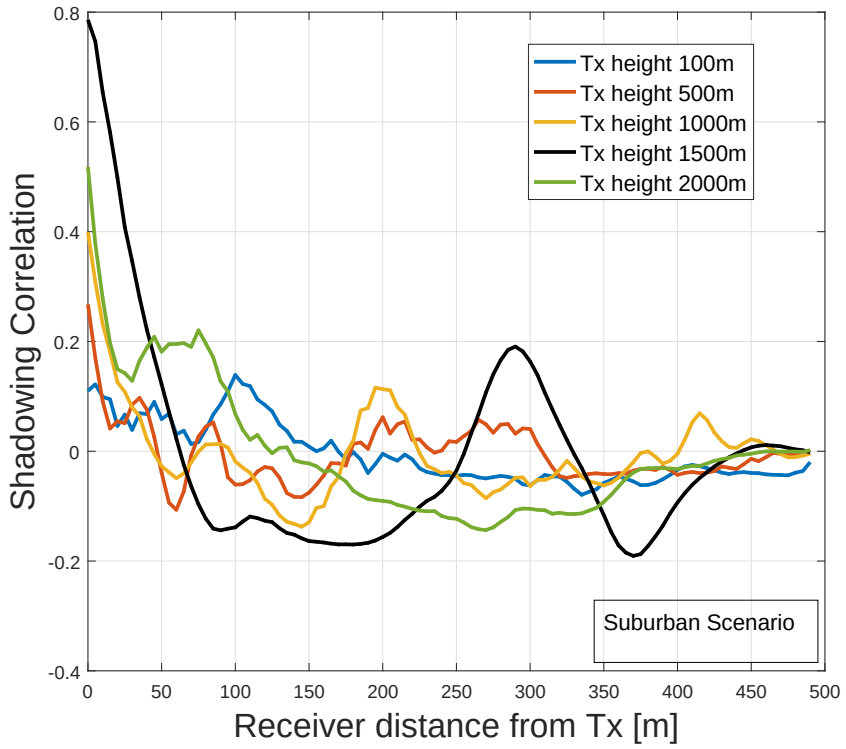

Figure 2.11: *Spatial Autocorrelation of Shadow fading over Suburban environment*

2.2 Ray Tracing and CAD Simulation Setup for channel parameter measurements

The customized simulation setup was developed to address wide range of scenarios with different ABS altitudes and transmitting power, to find channel characteristics of a generic A2G channel model for LAPs, using one-type-fits-all design philosophy. For developing the model, 3D ray tracing simulations were performed using Wireless InSite simulator 3.0.1 [Rem,], which is an accurate calculation tool for designing mobile wireless systems as addressed in [Medeović et al., 2012]. Three simulation environments were created in CAD Software, 3DS MAX [3ds,] for Suburban, Urban and Urban High Rise scenarios [Sharma et al., 2018a], as shown in Fig. 2.3, 2.4 and 2.5, with maximum building heights and density in Urban High Rise, lower in Urban and minimum in Suburban scenario. The three scenarios were created based on the parameters as given by ITU-R document [Al-

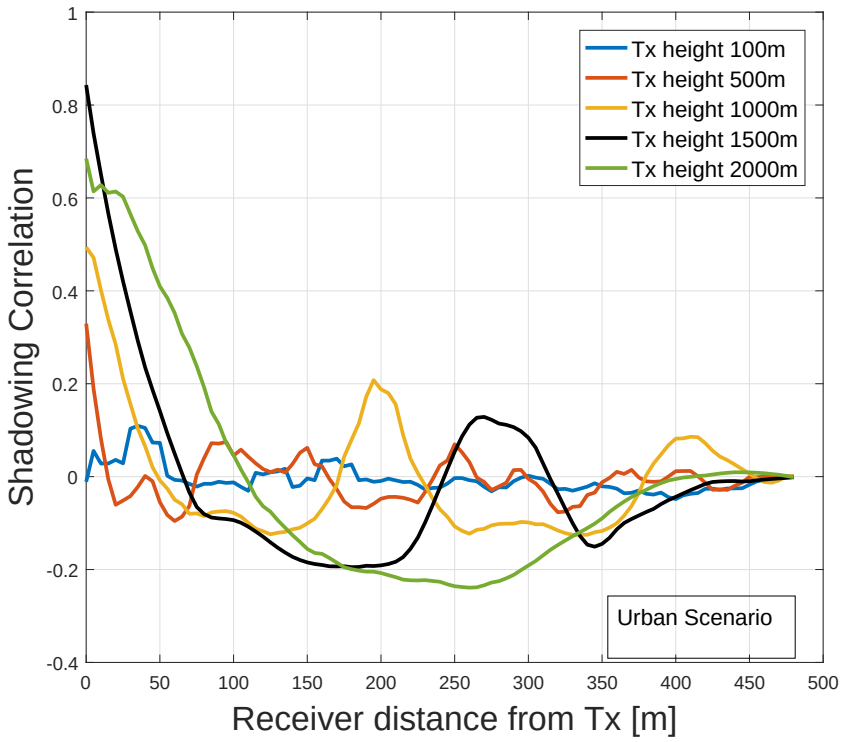

Figure 2.12: *Spatial Autocorrelation of Shadow fading over Urban environment*

Hourani et al., 2014a].

- α = Ratio of land area covered by the buildings out the total area $(dimensionless)$.
- β = Mean number of buildings per unit area $(building/km^2)$.
- γ = Variable determining the building height distribution. Usually Rayleigh distribution is used as per ITU-R guidelines.

The CAD simulation area was chosen equal to $2000 \times 2000\,\mathrm{m}^2$ out of which simulations were conducted over $1000 \times 1000\,\mathrm{m}^2$ to reduce the computation time while maintaining the accuracy of the snapshots. The CAD environments were further exported to the ray tracing software for conducting radio propagation. Two snapshots from each scenario were simulated to improve the accuracy of numerical results. Building width and street width were calculated following [Al-Hourani et al., 2014a] using the parameters shown in Table 2.1. The terrain is assumed to be flat. The properties of

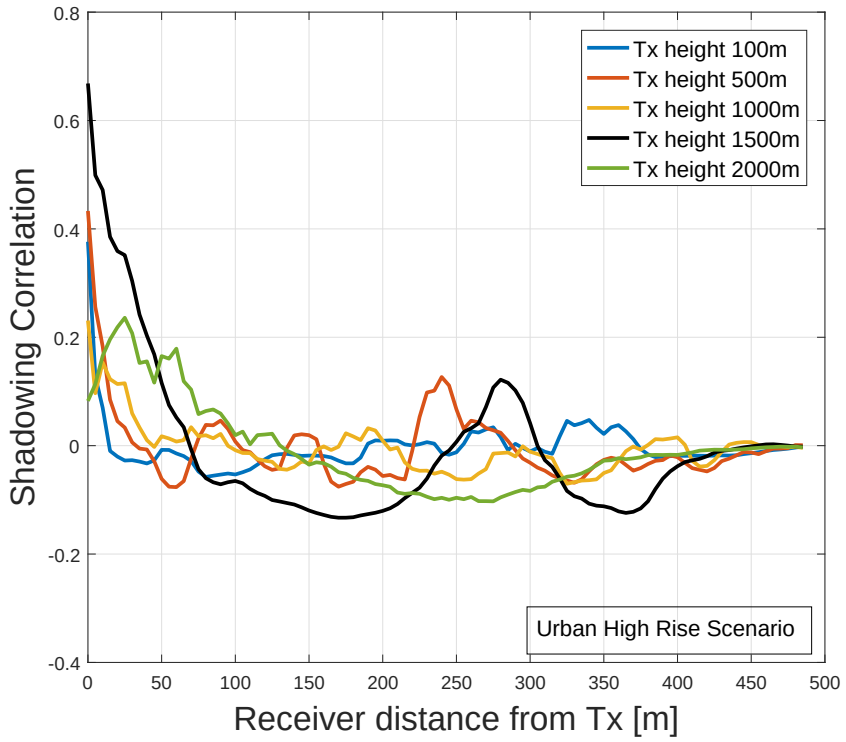

Figure 2.13: *Spatial Autocorrelation of Shadow fading over Urban High Rise environment*

the materials used for the terrain and the external walls and the rooftops of the buildings are described in Table 2.2. Materials such as concrete for the buildings and wet earth for the terrain were used. In Fig. 2.3, 2.4 and 2.5, the red dots patched on the streets are the receiving mobile users. The transmitter, *i.e.*, the ABS, was in the center of the area at a certain height. A number of approximately $32,500$ receivers, red dots in Fig. 2.3, 2.4 and 2.5, uniformly spaced 5 m apart in each direction from each other was used for simulation environment. There were no receivers inside the buildings, since outdoor propagation was studied to support flash crowd of mobile users. The building density and Rayleigh distributed heights in Suburban were the least and most in Urban High Rise. All receivers were 2 m above the ground and equipped with an isotropic antenna. The receiver threshold was kept -120 dBm and the noise figure was set to 3 dB, keeping in consideration the practical RSSI (Received Signal Strength Indicator) values for LTE supported cellphones. The simulations were repeated placing the

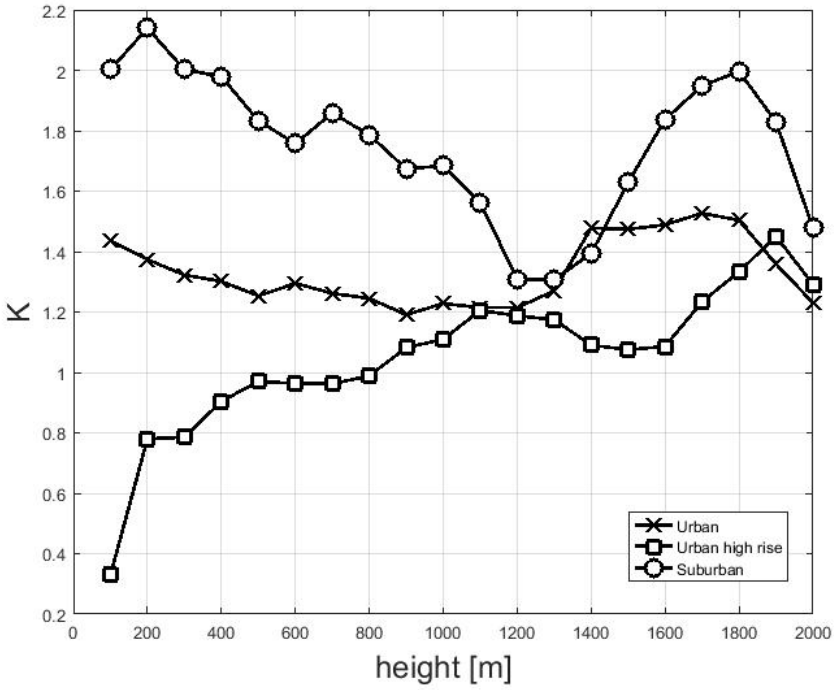

Figure 2.14: *Rice factor K as function of transmitter height in different environments.*

transmitter at increasing heights from 100 to 2000 m, with step of 100 m, in order to appreciate the sensitivity of the results to the height of the transmitter. The results from different snapshots were averaged at each ABS altitude. This improved accuracy of the results. Figure 2.6 shows a snapshot of the simulation in Urban High Rise environment. The antenna at the transmitter was assumed to be isotropic, to remove the effects of antenna directivity on the channel measurements, with a transmitting power of 18 dBm to 46 dBm, at every 2 dBm interval. The voltage standing wave ratio (VSWR), which defines the amount of power reflected from the antenna, was set to 1. Also, standard sea level atmospheric conditions were used to perform the simulations. A sinusoidal waveform was transmitted with carrier frequency of 2.442 GHz spanning a bandwidth of 20 MHz. The LTE unlicensed spectrum was preferred since there is not a standard allocated spectrum for such a system, till now.

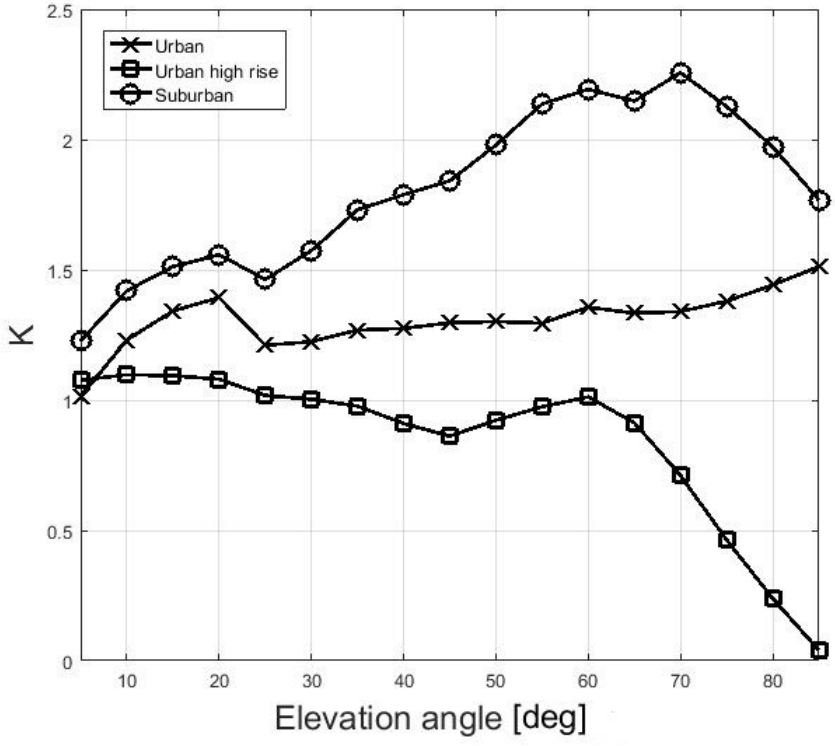

Figure 2.15: *Rice factor K as function of elevation angle in different environments.*

2.3 Channel Modeling Approach

There have been several channel modeling projects such as 3rd Generation Partnership Project (3GPP/3GPP2), International Telecommunications Union (ITU), Wireless World Initiative New Radio (WINNER I, WINNER II and WINNER+), Mobile and Wireless Communications Enablers for the Twenty-Twenty Information Society (METIS I and on-going METIS II in collaboration with 5G Infrastructure Public Private Partnership). Apart from these, there are several Millimeter-Wave channel modeling campaigns to support 5G users. METIS I addresses three different channel modeling approaches [METIS, 2015], which are currently followed by researchers and industries- Map-based, Stochastic and Hybrid. The map-based model is based on ray tracing simulation in a propagation environment which inherently accounts for propagation mechanisms such as specular reflection, scattering, diffraction etc and geometrical description of the environment

such as building and terrain material with roughness. This model provides realistic channel characteristics. The stochastic model is based on parameter distributions extracted from the measurements. The hybrid model provides scalable and flexible framework between map-based and stochastic approach. In hybrid model, large scale parameters (LSPs) such as PL and shadowing are obtained via map-based approach and SSPs via stochastic approach. Currently recognized channel models such as 3GPP/3GPP2 spatial channel model, WINNER geometry based a stochastic channel model, COST-259, 273, 2100 and ITU-R IMT-Advanced model, are based on stochastic approach and not sufficient to fulfill upcoming 5G requirements. Also, these focus on 2D channel modeling where only azimuth angular characteristics are considered, since the transmitters and receivers are at comparable altitudes. However, for an ABS, elevation angle becomes an important parameter due to high altitude difference between ABS and receivers. Therefore in this chapter, a map-based channel modeling approach was focused instead of stochastic and hybrid, since previous experimental measurements do not cover a wide range of environments and ABS altitudes.

2.4 3D Channel Model

For the development and evaluation for ABS downlink and uplink, a 3D Channel Model (3CM) was investigated in this chapter, developed by 3GPP, where significant importance was given to the elevation angle of the antenna and height of terrestrial base stations. The initial 2D Channel Models (2CM) from 3GPP spatial channel model, ITU and WINNER II, assumes a 2D plane for location of transmitters, receivers, reflectors and scatterers, which is not valid for ABSs. Being an extension of 2CM, 3CMs also extracts LSPs and SSPs using the stochastic approach. However, to further develop from 3GPP 3CM, LSPs such as PL, shadowing and LoS and SSPs such as AoA, AoD and delay spread, are based on ray-tracing or map-based approach, as done in METIS channel model [METIS, 2015]. The complex channel impulse response between receiver antenna u and transmitter antenna s in METIS time-variant 3CM is given as:

$$\begin{aligned}\mathbf{H}_{u,s}(t,\tau) = \sum_{k=1}^{K} \left[\begin{Bmatrix} \mathbf{F}_{Rx,u,\theta}(\theta_{EAoA,k,u}, \phi_{AAoA,k,u}) \\ \mathbf{F}_{Rx,u,\phi}(\theta_{EAoA,k,u}, \phi_{AAoA,k,u}) \end{Bmatrix}^{T} \times \right. \\ \left. \begin{bmatrix} \begin{Bmatrix} \mathbf{F}_{Tx,s,\theta}(\theta_{EAoD,k,s}, \phi_{AAoD,k,s}) \\ \mathbf{F}_{Tx,s,\phi}(\theta_{EAoD,k,s}, \phi_{AAoD,k,s}) \end{Bmatrix} \end{bmatrix} \times \right. \\ \left. \mathbf{h}_{k,u,s}(t) \times \mathbf{Z}_{k,u,s}(t) \times \delta(\tau - \tau_{k,u,s}(t)) \right.\end{aligned}$$

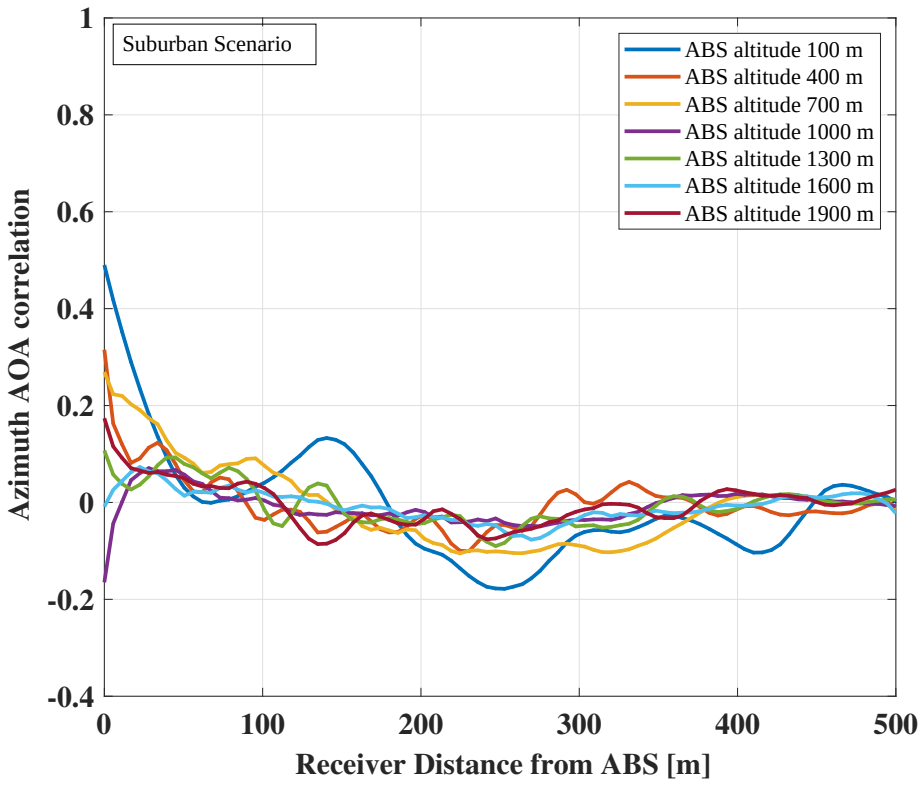

Figure 2.16: *Spatial Correlations of Azimuth AoA with receiver distance in Suburban Environment.*

where for path k, $\mathbf{F}_{Rx,u,\theta}$ and $\mathbf{F}_{Rx,u,\phi}$ are receiver antenna field pattern in the direction of Elevation-AoA $(\theta_{EAoA,k,u})$ and Azimuth-AoA $(\phi_{AAoA,k,u})$. Similarly, transmitter antenna field pattern for Elevation-AoD $(\theta_{EAoD,k,s})$ and Azimuth-AoD $(\phi_{AAoD,k,s})$, are $\mathbf{F}_{Tx,s,\theta}$ and $\mathbf{F}_{Tx,s,\phi}$, respectively. The function $\delta(\tau - \tau_{k,u,s}(t))$ represents an impulse function corresponding to delay τ and time, t in the multipath channel. $\mathbf{h}_{k,u,s}$ is a 2×2 polarization matrix and $\mathbf{Z}_{k,u,s}$ is the divergence factor, which signifies the geometrical effect arising from the divergence of rays, causing reduction in refection coefficient in process of specular reflection from spherical surface. A step-by-step procedure to obtain the 3D channel model is given in [METIS, 2015].

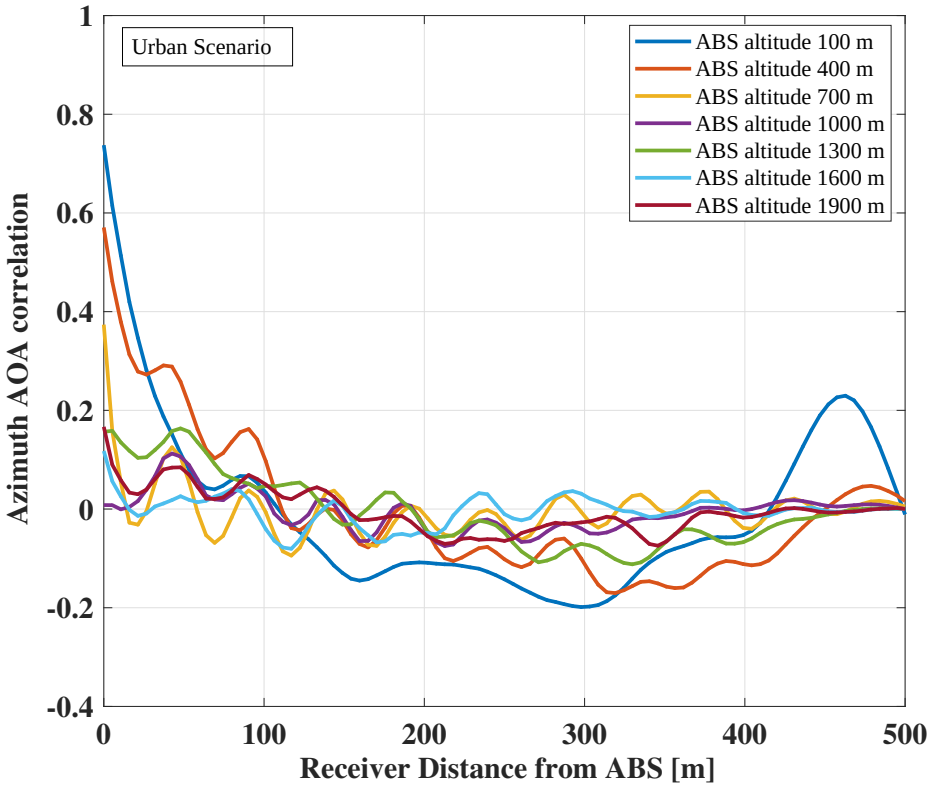

Figure 2.17: *Spatial Correlations of Azimuth AoA with receiver distance in Urban Environment.*

2.5 Air-to-Ground Channel Model

2.5.1 Overview

In this study CI free space reference distance PL model was considered as it is a standard approach for describing propagation at any frequency and it is more stable, simple, and reliable than other models such as, for example, Alpha-Beta-Gamma (ABG) model [Thomas et al., 2015, Sun et al., 2015]. The model is based on two fundamental parameters, the PLE and the standard deviation of fading σ, both dependent on the environment. Typical values of path loss exponent are $\mathrm{PLE} = 2$, for free space propagation, and $\mathrm{PLE} = 4$, for two ray propagation and asymptotically large link distance [Goldsmith, 2005].

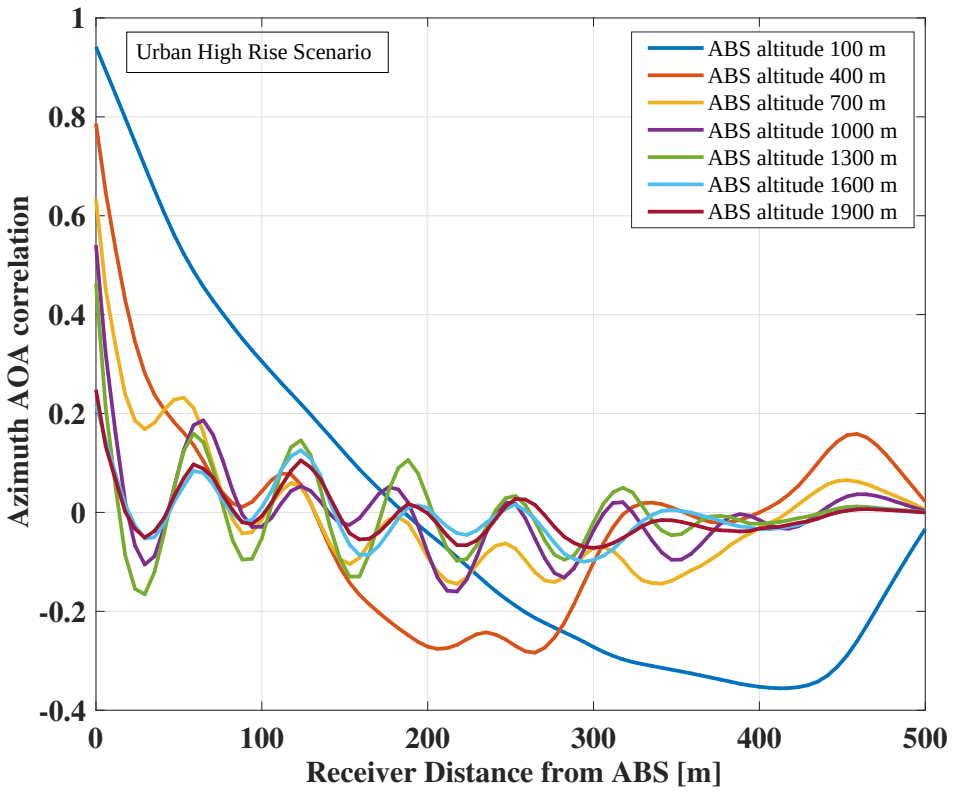

Figure 2.18: *Spatial Correlations of Azimuth AoA with receiver distance in Urban High Rise Environment.*

The large-scale shadowing PL equation is given by

$$PL(d)[\text{dB}] = 20\log_{10}\left(\frac{4\pi d_0}{\lambda}\right) + 10n\log_{10}(d) + X_\sigma, \qquad (2.1)$$

where λ is the wavelength, n is the PLE, d is the link distance, $d_0 = 1\,\text{m}$ is the reference distance, and X_σ, in dB, is the log-normal random variable (Gaussian in dB) with standard deviation σ that models the large scale shadowing effects. Considering that for A2G communication in Suburban, Urban and Urban High Rise environments, increasing the height of the transmit antenna and the link elevation, the propagation characteristics result are much more sensitive to LoS and NLoS conditions as seen in Sec. 2.6. To improve path loss prediction a LoS probabilistic approach was followed, proposed in [Al-Hourani et al., 2014b], which provides analytically and graphically, the relation between LoS probability and elevation angle for LAP, based on mathematical steps defined by ITU-R for modeling LoS

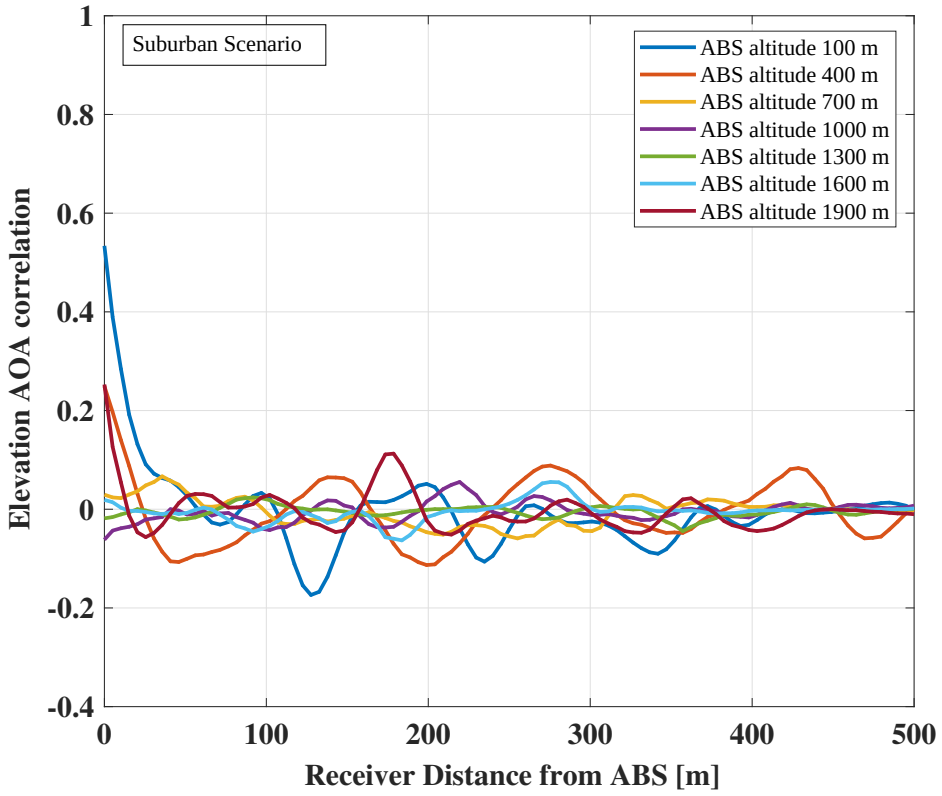

Figure 2.19: *Spatial Correlations of Elevation AoA with receiver distance in Suburban Environment.*

probability. Hence, the CI model and the probabilistic approach for LoS and NLoS path losses can be combined as

$$PL_{LoS}(d)[\text{dB}] = 20\log_{10}(\frac{4\pi d_0}{\lambda}) + 10n_{LoS}\log_{10}(d) + X_{\sigma,LoS}, \quad (2.2)$$

$$PL_{NLoS}(d)[\text{dB}] = 20\log_{10}(\frac{4\pi d_0}{\lambda}) + 10n_{NLoS}\log_{10}(d) + X_{\sigma,NLoS}, \quad (2.3)$$

The average PL is given by

$$PL(d)[\text{dB}] = P_{LoS} \cdot PL_{LoS}(d)[\text{dB}] + (1 - P_{LoS}) \cdot PL_{NLoS}(d)[\text{dB}], \quad (2.4)$$

where P_{LoS} is the probability of having a LoS link [Al-Hourani et al., 2014c], defined as a link where one of the paths is free space LoS, $PL_{LoS}(d)[\text{dB}]$ is the path loss when the link is in LoS condition, with parameters n_{LoS} and σ_{LoS}, and $PL_{NLoS}(d)[\text{dB}]$ is the path loss when the link

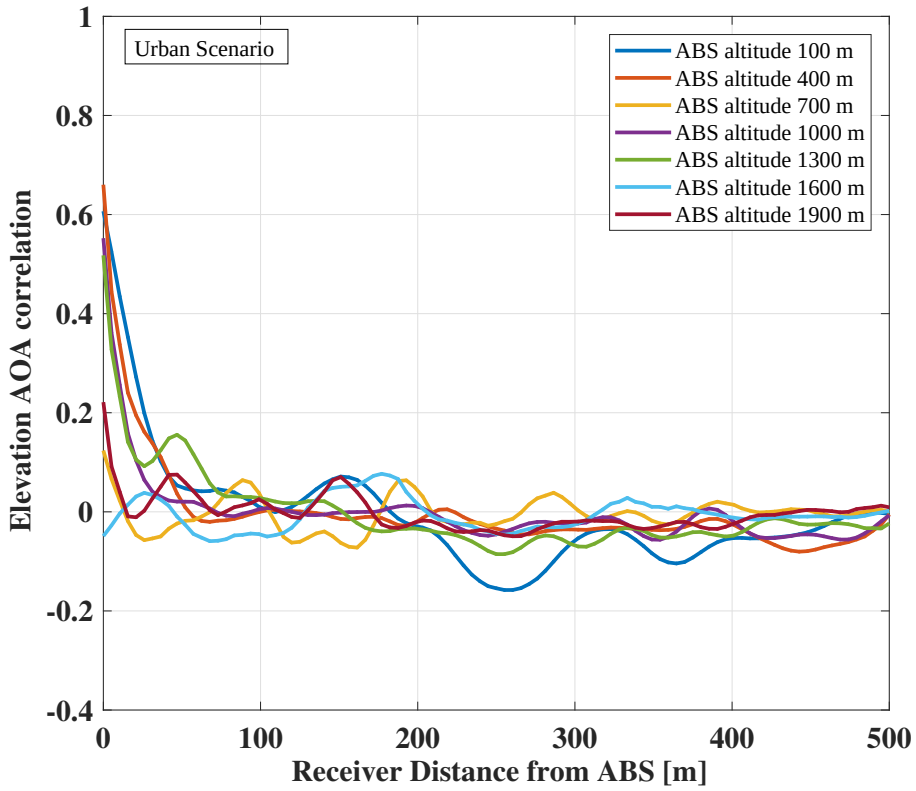

Figure 2.20: *Spatial Correlations of Elevation AoA with receiver distance in Urban Environment.*

is in NLoS condition, *i.e.*, there is no a free space LoS path, with parameters n_{NLoS} and σ_{NLoS}.

For defining the small scale fading characteristics for our simulations, the channel power gain is assumed to follow a Rician distribution since in the A2G channel there is a dominant LOS component. However, this also depends on the environment chosen.

The values of the model parameters, P_{LoS}, n_{LoS} and σ_{LoS}, n_{NLoS} and σ_{NLoS} are studied separately as function of the height of the transmit antenna and of the elevation angle of the link (by taking also into account the 3D link distance d between transmitter and receiver and the transmitter height h). From the simulation results of the PL, the mathematical closed form expressions was used to derive the best model parameters by minimizing the standard deviation of the shadowing term, as given in [Sun et al.,

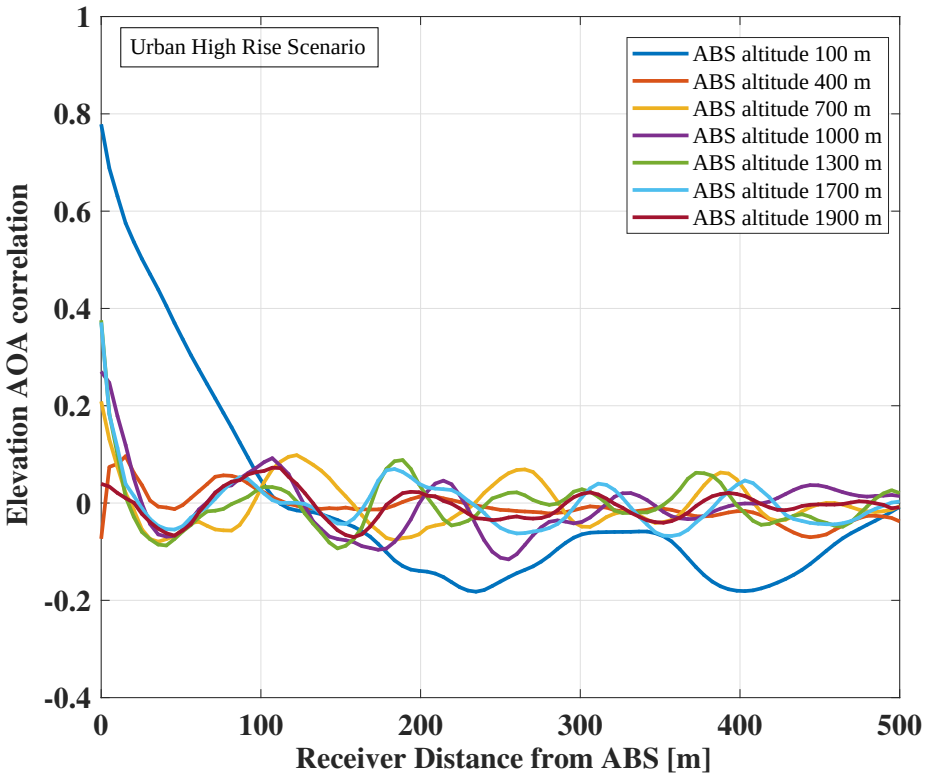

Figure 2.21: *Spatial Correlations of Elevation AoA with receiver distance in Urban High Rise Environment.*

2015]:

$$X_\sigma = PL(d)[\text{dB}] - 20\log_{10}(\frac{4\pi d_0}{\lambda}) - 10n\log_{10}(d) = A - nD, \quad (2.5)$$

where A represents $PL(d)[\text{dB}] - 20\log_{10}(\frac{4\pi d_0}{\lambda})$ and D represents $10\log_{10}(d)$. Then, the shadow fading standard deviation is given as

$$\sigma = \sqrt{\frac{\sum X_\sigma^2}{N}} = \sqrt{\frac{\sum (A - nD)^2}{N}}, \quad (2.6)$$

where N is the number of simulated PL points. Thus minimizing σ means minimizing $\frac{\sum (A-nD)^2}{N}$, *i.e.*, by setting to zero its derivative w.r.t. n in order to derive the PLE as

$$n = \frac{\sum DA}{\sum D^2}. \quad (2.7)$$

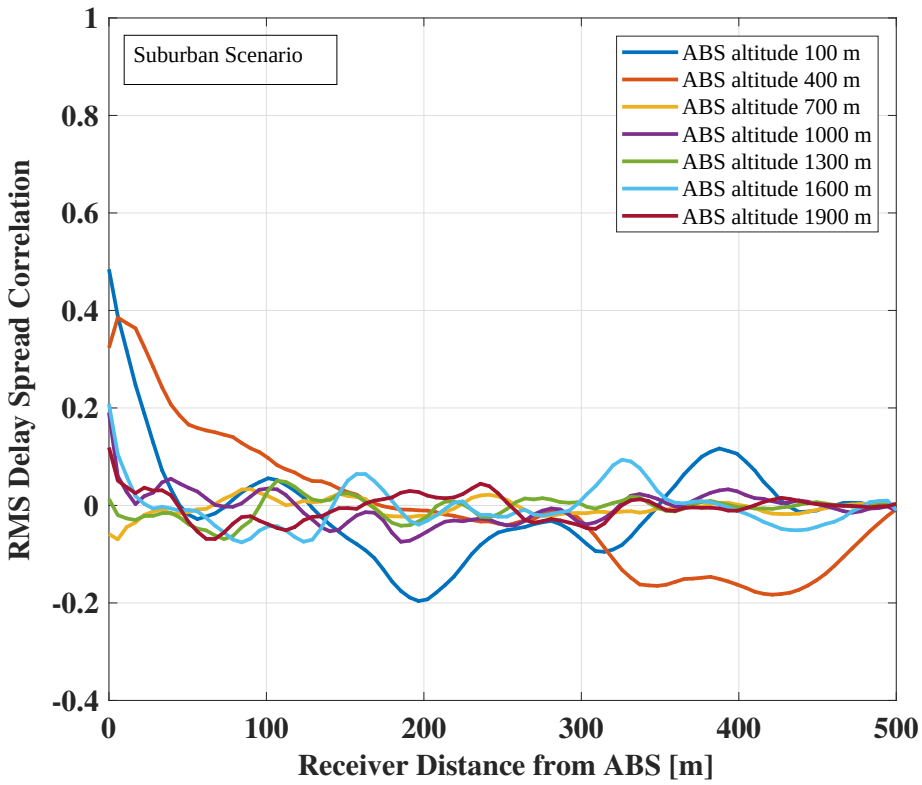

Figure 2.22: *Spatial Correlations of RMS delay spread with receiver distance in Suburban Environment.*

2.6 Channel Measurement Results and Analysis

The propagation links simulated by ray tracing software can be either LoS or NLoS, as shown in Fig. 2.2. Figs. 2.7 and 2.8 shows the PLE against the transmitter height h and the elevation angle θ, respectively, for the three scenarios considered in the cases of LoS and NLoS links. The interpretations of the results as a function of the elevation angle are not straightforward. In fact, being $\cos\theta = \frac{h}{d}$, where d is the 3D link distance between transmitter and receiver, as seen in Fig. 2.2, same elevation angles correspond to different couples (h, d). For LoS links both the figures show PLE values around 2, as expected from propagation theory, since LoS path contribution is dominant. In the NLoS case, PLE values shown in Fig. 2.7 range between about 2.5 and 3 in Suburban and Urban environment but in Urban High Rise environment, instead, for heights less than $400m$, PLE increases due to strong reflections from nearby tall buildings. PLE patterns versus

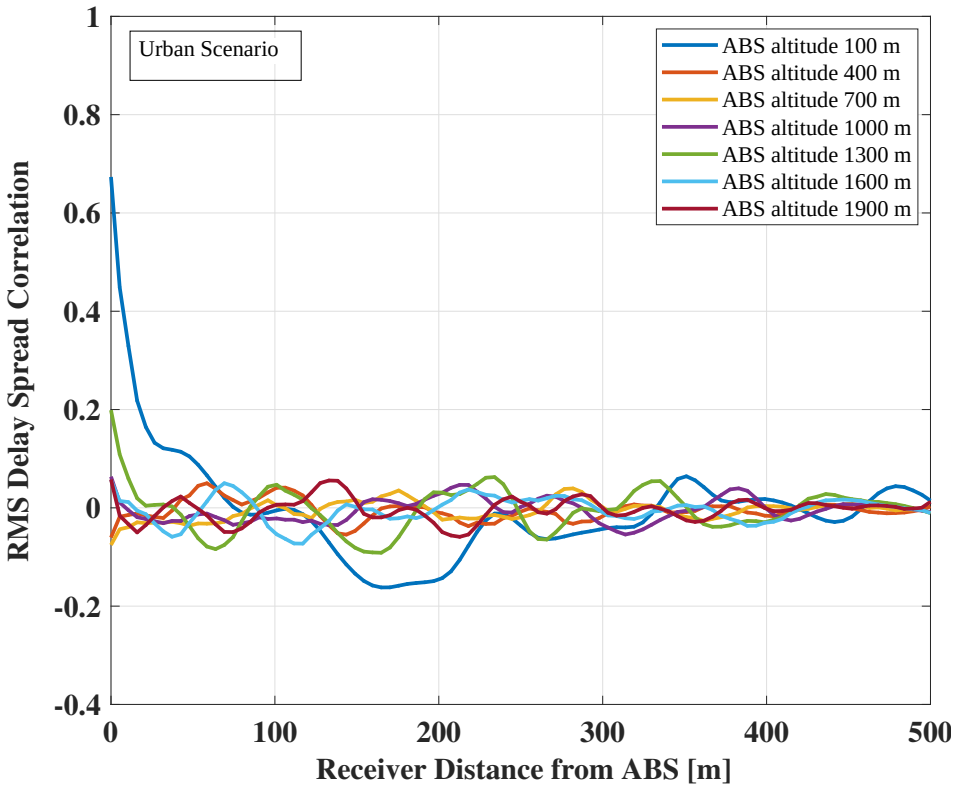

Figure 2.23: *Spatial Correlations of RMS delay spread with receiver distance in Urban Environment.*

elevation (Fig. 2.8) in NLoS links are similar as the ones versus height for all the scenarios. This is due to the geometrical considerations, where elevation angle is higher when transmitter height is low, considering d to be constant for all the receivers as seen from the cosine relationship between h and d, previously. Therefore, also in Urban High Rise case, PLE exhibits an increasing trend for elevation angle $\theta > 60°$.

Concerning the random large-scale shadow fading, it was derived from simulations, the theoretical amplitude as log-normal distributed of shadowing samples obtained from receivers radially moving away from the transmitter, for different transmitter heights in all simulated scenarios. Analogously to previous PLE curves, Figs. 2.9 and 2.10 show the standard deviation $\sigma[\mathrm{dB}]$ against the transmitter link elevation angle and the height, respectively, for the three scenarios considered in the cases of LoS and NLoS links. For LoS links, Fig. 2.10 highlights standard deviation values around 3 to 5 dB independently from the height. In the NLoS case, standard devi-

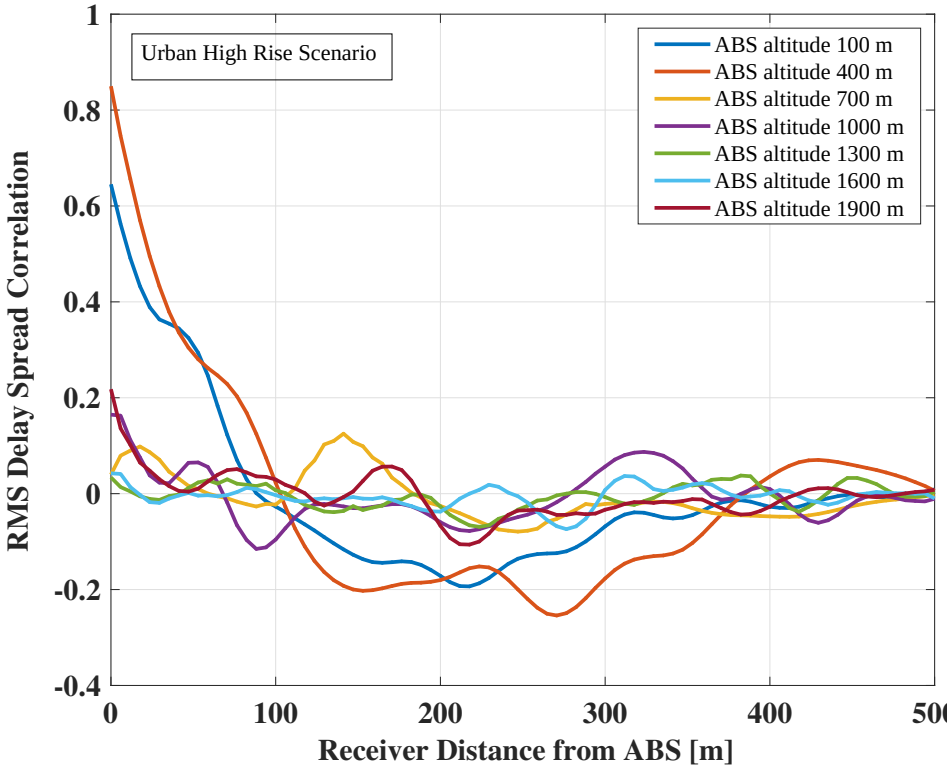

Figure 2.24: *Spatial Correlations of RMS delay spread with receiver distance in Urban High Rise Environment.*

ations vary between 10 to 17 dB and they increase with transmitter height, showing similar values in both LoS and NLoS links. Again, the standard deviation values in Fig. 2.9 exhibit a clear trend for all scenarios. Standard deviation is higher for Urban High Rise scenario than Urban one because of the dense environment and tall buildings. In the LoS case w.r.t. the elevation angle, σ still remains approximately constant and, again, is clearly lower than in NLoS cases.

Figs. 2.14 and 2.15 show the Rice factor K, defined for LoS links as the ratio between the power in LoS path and the sum of power in NLoS paths, again as function of the transmitter height and elevation angle. The Urban High Rise case shows a clear increasing trend with the height while the Urban case shows a constant behavior and Suburban case shows a decreasing trend till $1200m$. This is due to a higher probability of LoS paths blockage in Urban High Rise and Urban scenarios at low transmitter heights while the inverse is true for the Suburban one, due to low building density and

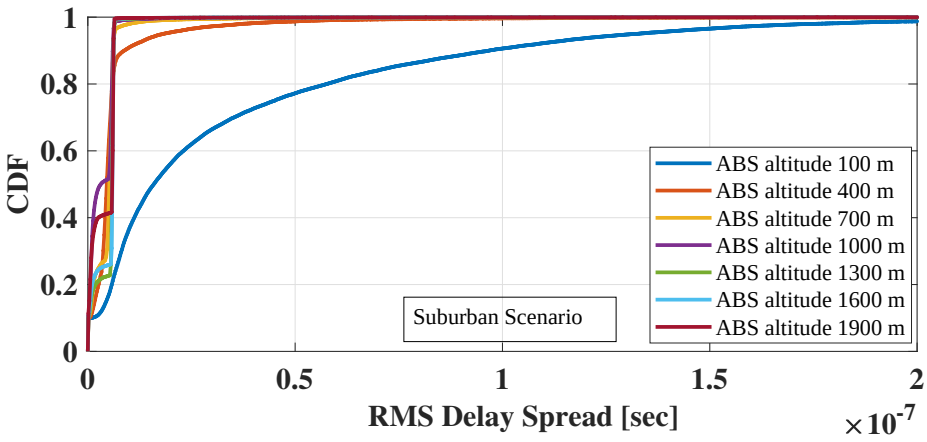

Figure 2.25: *Cumulative Distribution function of RMS delay spread in Suburban Environment.*

heights. Therefore, Rician fading for Suburban scenarios was obtained and almost Rayleigh fading for Urban High Rise at low transmitter heights and Ricean fading at high transmitter heights for all the scenarios, as observed also in [Zajić, 2012] for A2G channels. When the results were gathered and averaged with respect to the elevation angle, as in Fig. 2.15, it was seen that at very high elevation angles (greater than $60°$), K in Urban High Rise scenarios decreases remarkably (this case corresponds to the low transmitter heights) because of the dense multipath reflections from buildings. It appears reasonable to assume, for all elevation angles, K between 1.5 and 2 for Suburban case, 1.5 for Urban one and, for Urban High Rise, 1 up to $60°$ and then decreasing till to 0 at $85°$.

Finally, Fig. 2.11, 2.12 and 2.13 shows the spatial correlation of shadowing over the considered scenarios as in [Sun et al., 2015]. Spatial Correlation is the correlation among the values of a variable strictly characterizing to their relatively close locational positions in 2D plane, introducing a deviation from the independent value assumption of conventional statistics. It has been a significant parameter for channel characterization, generally for performance of MIMO systems in terms of directional receiver and transmitter antenna elements' spacing to achieve maximum space and time diversity of multipath channels. Here, spatial correlation is addressed with an analogous perspective for single isotropic antenna mounted ABS and closely spaced multiple mobile users on the ground. A lower correlation factor is likely to increase independent reflected and scattered rays,

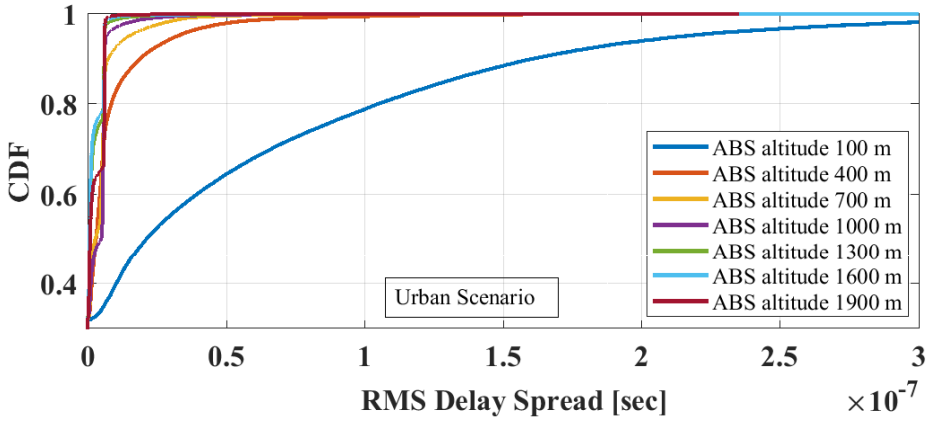

Figure 2.26: *Cumulative Distribution function of RMS delay spread in Urban Environmental.*

thereby reducing the interference at the receivers. Also, it governs the minimum spatial separation required at receivers to achieve Independent and Identically Distributed (IID) signals.

Here, the correlation of each receiver with its neighboring receiver is calculated and plotted with respect to the distance of each receiver from transmitter. Receivers are present 5m apart from each other. The correlation is plotted in one direction radially away from ABS to the end of snapshot, since correlation along different directions from ABS were found have nearly homogeneous behavior. The variation in spatial correlation at different ABS altitudes and environments is shown. From, Fig. 2.11, 2.12 and 2.13, it was observed for the three scenarios that correlation is higher for the receivers near to the transmitter and decreases as the distance from transmitter increases. Also, correlation was found to be very low for low transmitter heights except in the case of Urban High Rise scenario where the transmitter is below the buildings heights and high correlation can be observed. It was observed that correlation increases from low transmitter heights to higher ones but after a certain threshold again start decreasing as seen for 1500m and 2000m transmitter heights. Also, a smooth behavior of the curves can be seen at higher transmitter heights with a higher correlation and anti-correlation values.

Also, CDFs of SSPs have been presented in this chapter, which gives an interpretation about the likelihood of the SSPs lower than a given threshold. Figure 2.16, 2.17 and 2.18 represents the spatial correlation of Azimuth-AoA (A-AoA) and Fig. 2.19, 2.20 and 2.21 represents Elevation-AoA (E-

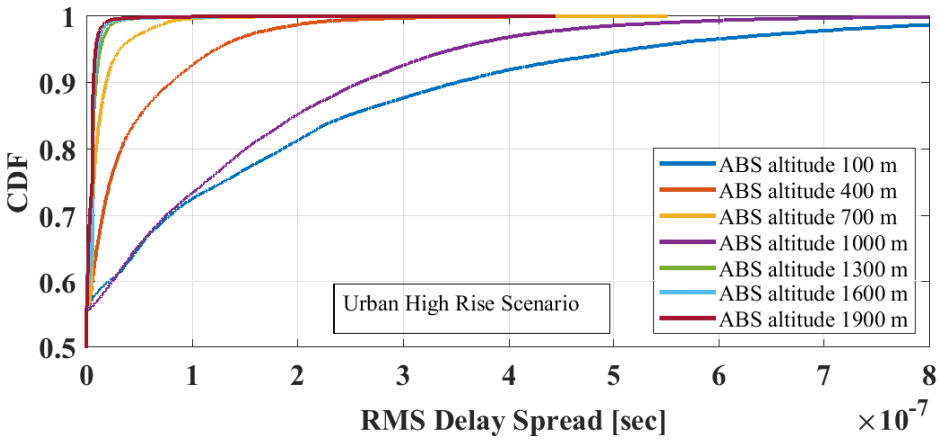

Figure 2.27: *Cumulative Distribution function of RMS delay spread in Urban High Rise Environment.*

AoA) with respect to receiver distance from ABS, respectively. As can be clearly observed from Fig. 2.16, 2.17 and 2.18, Suburban environment has a lower A-AoA correlation than Urban environment which in turn is again lower than Urban High Rise. However, such prominent pattern cannot be clearly distinguished for E-AOA in Fig. 2.19, 2.20 and 2.21. This is due to the fact that correlation are found along one radial direction in the snapshots. Therefore, likelihood of A-AoA arriving from one particular direction is high but E-AoA along that direction would be different as the receiver distance increases. Also, spatial correlation for both A-AoA and E-AoA are higher for the receivers near the ABS and decreases as the receiver distance increases. Also, AoA correlations were found to high for lower ABS heights and decreases as the altitude of ABS increases. This implies, Suburban environments exhibit higher probability of IID channel than Urban and Urban High Rise scenarios, which leads to better performance in Suburban zones. Similarly, the receivers far from ABSs with higher ABS altitudes should expect better performance. However, expectation of IID fading channel has to be optimized with the transmission power of ABS for best system performance, since for larger link distances between ABS and receivers, transmission power will be less. A counter result was observed in shadowing correlations with respect to ABS altitudes and environments in [Sharma et al., 2018a]. However, certain anomalies can be seen such as ABS altitude at 1000 m in Suburban scenario in Fig. 2.16, 2.17 and 2.18, ABS altitude at 400 m and 1700 m in Urban and Urban High Rise scenarios,

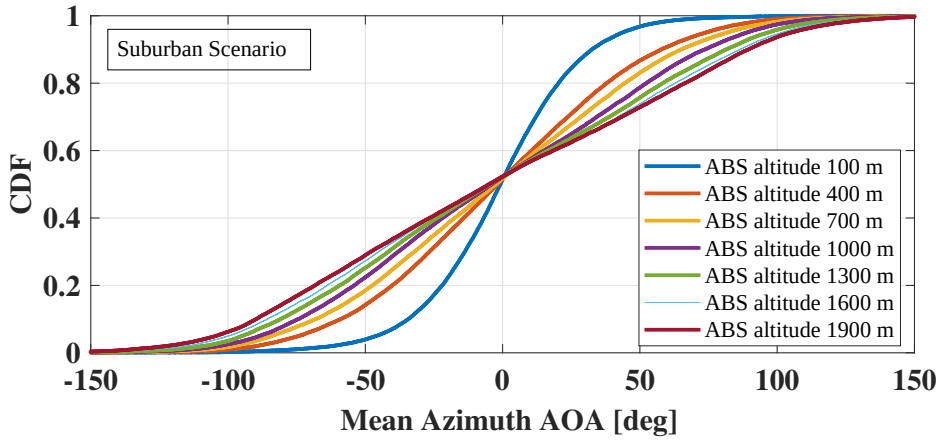

Figure 2.28: *Cumulative distribution function of mean Azimuth AoA in Suburban Environment.*

respectively in Fig. 2.19, 2.20 and 2.21. These are due to stochastic nature of channel modeling phenomenon, with certain constructive or destructive interference in multipath channels for a randomly generated city scenario, even following a map-based approach. Also, a smooth behavior can be scrutinized in Urban High Rise and Urban environments, as compared to Suburban, particularly for lower ABS altitudes with high correlation and anti-correlation values. This is probably due to different fading in A2G links as seen in [Sharma et al., 2018a]. The Suburban scenarios tend to follow Rayleigh fading due to higher scattering losses while Urban and Urban High Rise follows a Rician fading due to better LoS probability in A2G, which is different from terrestrial networks.

Similarly, Fig. 2.22, 2.23 and 2.24, shows the spatial correlation of RMS delay spread with receiver distance from ABS at different ABS altitudes and environments. The RMS delay spread is an important factor for transceiver design, as the it addresses the nature of the fading channel, i.e. flat or frequency-selective fading channel, causing inter-symbol interference. The value of correlation is much lower at higher altitudes of ABS, except for Urban High Rise scenario where delay spread correlation is lower for ABS altitude of 100 m. This is due to low ABS altitude than the building heights in the scenario, due to which ABS lies in the cluster of buildings, which leads to higher scattering and multipath effects, thereby creating bigger differences in mean delay spread values for far and near receivers to ABS.

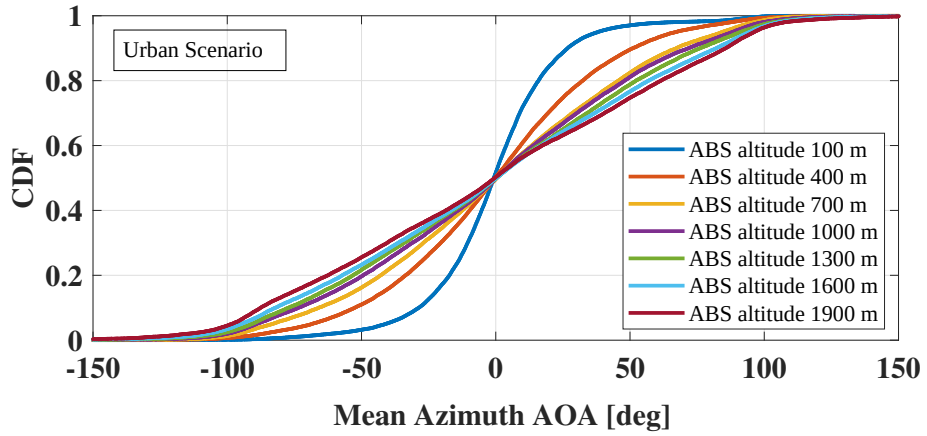

Figure 2.29: *Cumulative distribution function of mean Azimuth AoA in Urban Environment.*

Figures 2.25, 2.26 and 2.27, Figs. 2.28, 2.29 and 2.30 and Figs. 2.31, 2.32 and 2.33 displays the CDFs of delay spread and AoA, respectively for different ABS altitudes and scenarios. Here, unlike spatial correlation, the results obtained for CDF are not along one direction but for the receivers in complete snapshot. Also, the figures have been scaled for clear interpretation of the curves, with respect to height of ABS. However, statistical parameters such as mean (μ) and standard deviation (σ) have been provided in Table 2.3, to re-create the results for transceiver design and clear understanding. In Fig. 2.25, 2.26 and 2.27, a significant, difference for CDF values between lower and higher ABS altitudes were observed for Suburban and Urban scenarios. This implies that at lower ABS altitudes, the probability of delay spread lower than a specific value of delay spread is much less. Therefore, the delay spread is higher for lower altitudes of ABS due to heavy scattering and diffraction, leading to Rayleigh Fading A2G channel. As the height of ABS increases, with high probability of LoS, a Rician fading behavior is seen with lower delay spread values. However, at Urban High Rise scenario, along with low ABS altitudes, large delay spread values were seen and expected at high altitudes as well. This is probably due to higher building densities and heights, which further increase the multipath effects. Also, the CDFs are closely spaced in Suburban scenario rather than higher differences in Urban High Rise and intermediate difference in Urban scenarios. Figures 2.28, 2.29 and 2.30 displays the CDF for A-AoA and Figs. 2.31, 2.32 and 2.33 E-AoA, respectively. These CDFs

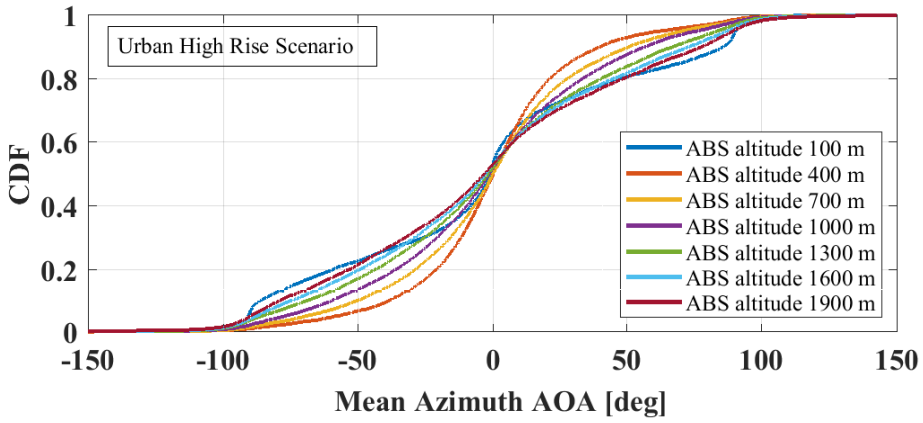

Figure 2.30: *Cumulative distribution function of mean Azimuth AoA in Urban High Rise Environment.*

were obtained in the same way as delay spread CDFs, by using ray tracing simulation results for the entire snapshot. Also, here the result for Suburban and Urban scenario at low ABS altitude is different from Urban High Rise. In Fig. 2.28, 2.29 and 2.30, the values of CDFs are monotonically increasing with ABS altitudes for negative A-AoA, and monotonically decreasing for positive A-AoA, for all environments. However, such pattern cannot be observed for E-AoA in Fig. 2.31, 2.32 and 2.33. From E-AoA CDFs, the variation in elevation angles with ABS altitude can be interpreted. For the low altitudes of ABS, E-AoA are higher, ranging from 80-95 degrees in Urban High Rise scenario and more than more than 85 degrees in Suburban and Urban scenarios. As the altitude of ABS increases, the elevation angle decreases. According to the simulation setup, the maximum elevation angle at the Rxs should be 90 degrees. However, due to several reflections and scattering effects in multipath fading environments, E-AoA higher than 90 degrees were observed.

The SSPs discussed addressed in this chapter, are considered to follow various probability distributions for different ABS altitudes and scenarios, which are not similar to the terrestrial communications. Figures 2.25, 2.26 and 2.27, shows that RMS delay spread follows an exponential distribution, while from Figs. 2.28, 2.29 and 2.30, mean A-AoA follows Normal distribution at lower ABS altitudes in all environments. However, with the increase in ABS altitude, the distribution tends to become Uniform. But since we are addressing LAPs in this chapter, we assume a Normal distribution

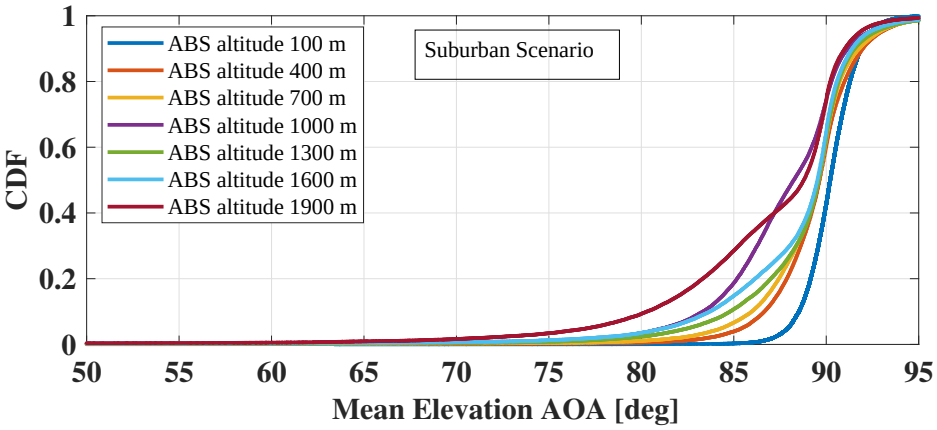

Figure 2.31: *Cumulative distribution function of mean Elevation AoA in Suburban Environment.*

till ABS altitude of 2000 m. Also, we consider mean E-AoA to be Normally distributed. The parameters, such as μ and σ for above distributions are given in Table 2.3, for all heights of ABS and environments, addressed in this chapter. Since ABSs have become a significant targeted application in 5G, these parameters can be used by researchers for waveform, frame structure and numerology design for LTE, LTE-Advanced or LTE-Pro technology based transceivers, where new waveforms such as GFDM, Universal Filtered Multi-Carrier (UFMC), Filter Bank Multi-Carrier (FBMC), Filtered Orthogonal Frequency Division Multiplexing (F-OFDM) with various channel coding techniques to develop a New Radio (NR) network. However, validation of these parameters with experimental measures is necessary before implementation for ABSs, to remove any errors pertaining to software calculations.

2.7 Conclusions and Future Work

In this chapter, we discuss about fading channel characterization for A2G channel for LAPs, such as UAVs, mounted with base stations. Such ABS provide cellular network to ground users and is one of targeted application in 5G. Here, the CI propagation model is applied to the simulated results obtained by a commercial 3D ray-tracing software on a generalized Suburban, Urban and Urban High Rise environments, developed in a CAD software according to ITU-R defined parameters, for LAP acting as a ABS for pro-

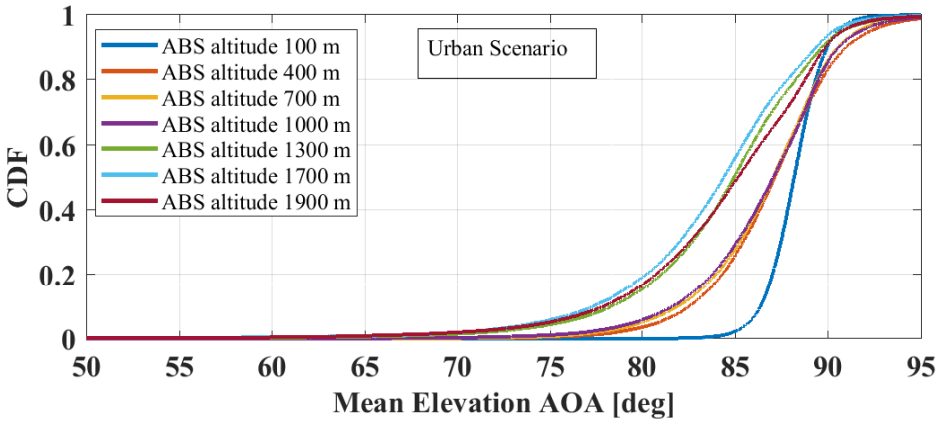

Figure 2.32: *Cumulative distribution function of mean Elevation AoA in Urban Environment.*

viding cellular coverage to ground users. This brings novelty to the work, since due to generalized environments, results given in this chapter can be implemented in realistic scenarios with certain margin of error, which would be addressed in future works. The simple CI propagation model assumes the well-known dependence of the PL (in dB) on the logarithm of the distance multiplied by the PLE.

In this study the PLE and the standard deviation of the shadowing is calculated as a function of the transmitter height and the elevation angle of the link, highlighting the effects of the transmitter height alone which is the fundamental design parameter. Moreover, LoS and NLoS cases are distinguished based on the presence or not of the free-space LoS path in the simulated link (whereas in [Al-Hourani et al., 2014a] they were estimated from the shape of the PL histogram across the test area), and the corresponding PLE, Shadow Fading Standard deviation and Rice factor, are calculated again as a function of elevation angle and transmitter height, to better understand the role of global geometrical parameters in the different environment. Further, different channel modeling approaches have been addressed here, from which map-based approach is followed in this chapter. The details of SSPs such as delay spread and AoA have been discussed, by providing spatial correlations at ground receivers and CDFs of simulation snapshots, at different ABS heights and environments. Also, a 3D METIS channel model, originally proposed by 3GPP for multipath fading is described, which is the preferred fading channel for ABSs. Also, prob-

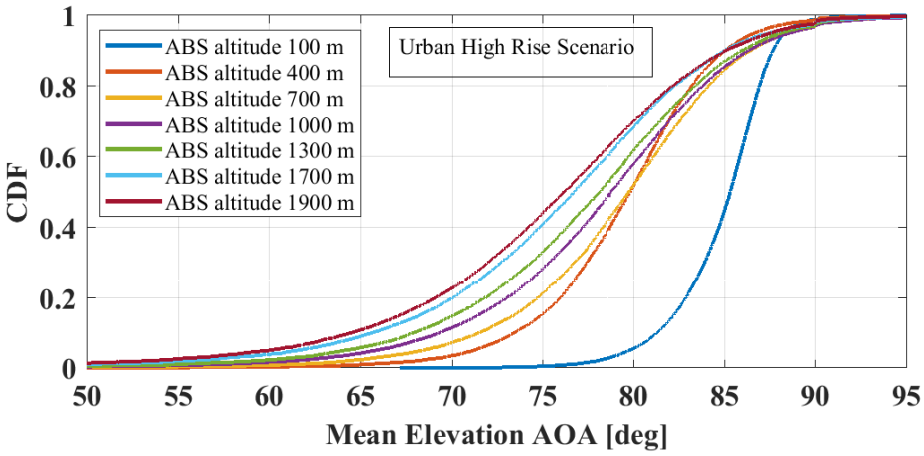

Figure 2.33: *Cumulative distribution function of mean Elevation AoA in Urban High Rise Environment.*

ability distribution parameters have been provided with mean and standard deviation for the considered SSPs, which can be utilized by researchers for transceiver design of ABSs. Also, spatial correlation for shadow fading was simulated for three considered environments and the behavior of the correlation with respect to the transmitter height and receiver distance from transmitter was shown. For fulfilling 5G requirements, multiple ABSs integrated with terrestrial network operating at millimeter-wave and sub-6 GHz frequency bands are needed, for which appropriate channel models need to be designed along with their validation in realistic environments. The results developed in this chapter were published in [Sharma et al., 2018a].

Table 2.3: *Probability Distribution Parameters*

ABS Altitude [m]	Small-Scale Parameter	Distribution	Suburban		Urban		Urban High Rise	
			μ	σ	μ	σ	μ	σ
100	RMS Delay Spread	Exponential	3.872×10^{-08}	-	8.193×10^{-08}	-	2.269×10^{-07}	-
200			1.524×10^{-08}	-	2.831×10^{-08}	-	5.462×10^{-09}	-
300			9.552×10^{-09}	-	1.663×10^{-08}	-	9.043×10^{-08}	-
400			7.253×10^{-09}	-	1.054×10^{-08}	-	5.107×10^{-08}	-
500			4.797×10^{-09}	-	8.653×10^{-09}	-	3.086×10^{-08}	-
600			4.788×10^{-09}	-	7.983×10^{-09}	-	2.094×10^{-08}	-
700			5.277×10^{-09}	-	6.391×10^{-09}	-	1.566×10^{-08}	-
800			5.359×10^{-09}	-	4.634×10^{-09}	-	1.166×10^{-08}	-
900			3.435×10^{-09}	-	4.906×10^{-09}	-	1.002×10^{-08}	-
1000			3.852×10^{-09}	-	5.486×10^{-09}	-	1.687×10^{-07}	-
1100			3.724×10^{-09}	-	5.195×10^{-09}	-	8.844×10^{-09}	-
1200			4.471×10^{-09}	-	5.725×10^{-09}	-	8.307×10^{-09}	-
1300			5.440×10^{-09}	-	3.186×10^{-09}	-	8.031×10^{-09}	-
1400			5.214×10^{-09}	-	4.503×10^{-09}	-	7.247×10^{-09}	-
1500			4.299×10^{-09}	-	5.174×10^{-09}	-	7.712×10^{-09}	-
1600			5.307×10^{-09}	-	2.8802×10^{-09}	-	7.3819×10^{-09}	-
1700			4.145×10^{-09}	-	5.335×10^{-09}	-	6.037×10^{-09}	-
1800			3.021×10^{-09}	-	3.431×10^{-09}	-	6.597×10^{-09}	-
1900			4.471×10^{-09}	-	3.710×10^{-09}	-	5.910×10^{-09}	-
2000			3.232×10^{-09}	-	4.289×10^{-09}	-	5.519×10^{-09}	-
100	mean Azimuth-AOA	Normal	-1.065	27.877	-0.539	26.001	-2.955	56.280
200			-0.880	38.028	-0.575	32.819	-0.484	41.008
300			-0.967	42.663	-1.045	37.559	-0.883	35.376
400			-1.185	45.162	-0.459	40.566	0.222	35.087
500			-2.073	49.018	-0.627	44.407	0.219	36.859
600			-2.095	50.314	-0.034	47.476	-0.152	38.872
700			-1.707	51.102	0.711	49.554	-0.220	40.064
800			-1.077	51.500	-0.390	51.616	-0.870	41.494
900			-1.248	54.155	-0.125	52.381	-1.374	42.974
1000			-1.651	56.276	-0.401	53.345	-1.482	44.373
1100			-1.430	58.383	-1.650	54.380	-1.809	46.324
1200			-1.313	60.369	-0.739	54.489	-1.961	47.763
1300			-1.371	61.278	-0.110	56.554	-1.995	49.351
1400			-1.579	62.210	0.710	57.707	-2.345	50.764
1500			-1.479	62.959	0.245	59.493	-2.828	51.844
1600			-1.331	65.023	-0.014	59.692	-2.620	52.610
1700			-1.559	65.376	-0.360	61.085	-3.254	53.933
1800			-1.344	67.451	0.243	62.183	-3.186	54.555
1900			-1.962	68.059	-0.719	63.316	-2.950	55.234
2000			-1.610	69.061	-0.734	62.936	-3.118	56.081
100	mean Elevation-AOA	Normal	90.196	1.469	88.152	1.615	84.851	2.779
200			89.879	2.302	87.818	3.379	81.438	2.937
300			89.325	3.057	87.884	3.152	80.190	4.280
400			89.372	2.904	86.846	4.283	79.409	5.430
500			88.198	4.821	87.196	3.818	79.223	6.145
600			88.545	4.290	87.368	3.480	79.191	6.604
700			89.015	3.973	86.551	4.055	79.198	6.677
800			88.992	4.149	85.495	4.885	78.163	7.864
900			87.232	5.690	85.883	4.945	78.268	7.700
1000			87.439	5.733	86.441	4.688	78.117	7.783
1100			87.064	6.132	86.223	4.761	78.219	7.790
1200			87.746	5.236	86.680	4.237	77.886	7.820
1300			88.660	4.728	84.168	6.151	77.224	8.335
1400			88.288	5.027	85.371	5.570	77.969	7.894
1500			86.995	6.719	86.071	4.885	77.608	8.354
1600			88.238	5.211	83.498	6.492	75.694	9.115
1700			86.504	6.487	86.207	4.817	76.666	8.957
1800			84.652	8.146	83.938	6.684	75.800	9.226
1900			86.5710	6.678	84.182	6.795	75.050	9.680
2000			84.059	9.151	84.851	6.531	75.225	9.656

CHAPTER 3

Cell Coverage, Capacity and Interference analysis for Low Altitude Aerial Base Station

WITH the advancing 5G technology of base stations mounted on aerial platforms, such as UAVS, the issue of coverage area, capacity, and inter-cell interference is assuming higher importance for the cellular networks. In this chapter, a deterministic approach was followed to analyze these problems using the data obtained at different ABS altitudes and and transmitting powers, using a commercial software for wireless electromagnetic wave propagation. The above mentioned parameters were analyzed by varying the threshold of the received power. Also, an optimal altitude and power consumption model was found for an ABS. Similar to Chap. 2, simulations were carried out in three generalized environments, Suburban, Urban and Urban High Rise, developed according to ITU-R parameters. To derive these results, the same A2G channel model was implemented as described in Chap. 2. Further, an analytical framework for cell coverage area by an ABS using a solid angle approach was provided. Also, change in Euler angles such as roll, pitch and yaw due

to perturbations by wind gusts or intentional maneuvers, were taken into account for analytical analysis.

3.1 Introduction

As described in Chap. 2, UAVs, commonly known as drones have been used as LAPs for many purposes. Initially, they were massively used for military purposes, like surveillance or reconnaissance activities [Ma'sum et al., 2013, Zafar and Khan, 2016]. Nowadays, they have received enormous interest in civil applications too [Hayat et al., 2016]. Recently, with the development of 5G technology, the idea of using base stations mounted UAVs has gained substantial interest in research literature [Mozaffari et al., 2016c, Yaliniz et al., 2016], with the aim of getting an increment in cellular networks capacity and coverage area. This is also what is addressed in this chapter by adopting of the idea to bring access nodes as near as possible to the ground users.

This realization can be made feasible by considering a base station mounted on-board UAV [Wu et al., 2018, Wu et al., 2017], that provides cellular network to a mobile Ground Station (GS) using an appropriate A2G channel model, which has been obtained using the deterministic solution of ray tracing [Nurmela et al., 2014] as in Chap. 2, practically advantageous for flash crowds. These can be deployed in real time based on the increase in the requirement of the data traffic. An ABS can be used both in the support of terrestrial networks and in remote locations in the absence of the terrestrial network. Such architecture has been previously proposed for rescue operations in case of disasters, where terrestrial cellular networks become non-functional [Absolute Project,].

Some previous work is available making similar analysis. In [Azari et al., 2016], [AL-Hourani et al., 2016] authors provide the analytical solutions for coverage and comparison of sum rate and power gains of ABS with terrestrial base station using a generic channel model. However, they do not take into account different generalized environments defining some fundamental characteristics such as, for example, PLE or shadowing. In these references numerical results have not been verified neither using real measurements nor by accurate channel models like those provided by ray tracing or any other deterministic tool. Similarly, in [Al-Hourani et al., 2014c] a formulation is provided for LoS probability and optimal altitude but without taking into account large and small scale fading effects. In [Mozaffari et al., 2016b], an optimal deployment of multiple ABSs has been proposed to cover the given geographical area using circle packing

theory, with the constraints on downlink coverage probability, maximum coverage, and minimum transmit power by each ABS. In this chapter we take into account all these limitations to provide more accurate results. Different types of generalized environments will be considered in order to get more realistic results. We also characterize A2G channel for these environments and take into account large and small scale fading effects in order to maintain high accuracy.

In this chapter, the results are based on the similar ray tracing simulation setup as described in Sec. 2.2. However, here the receiver threshold was varied in ray tracing simulations (-120 dBm, -100 dBm and -80 dBm) considering the LTE standards in order to analyze the coverage, capacity and interference results in generalized city environments. For obtaining the results, A2G channel was used as defined in Sec. 2.5. Also, optimal altitude was obtained at a constant transmitting power 18 dBm of the ABS and variation of cell coverage shown with increasing power levels up to 46 dBm. Further in this chapter, a solid angle based approach is defined to describe the cell coverage area from an ABS analytically, which isn't achievable via threshold received signal power approach [Cileo et al., 2017]. Also, the rotation angle of ABS was introduced due to unavoidable wind gusts or intentional maneuvers and perform an analytical analysis to define the cell coverage equation with the information of critical parameters- altitude, elevation angle, rotation angle of ABS, and propagation factors in A2G channel such as PL, shadowing and rician fading, which are not available in the literature, bringing novelty to this work. Also same A2G was used which significantly impacts the coverage performance at different ABS altitudes, as shown in numerical results. Also, the concept of increase of geometrical cell coverage due to rotation angle was introduced. Here, the transmission by only an ABS was assumed and no terrestrial network. To the best of my knowledge, this is the first work addressing the closed form expressions with proofs of cell coverage by ABS.

This chapter is organized as follows. In Sec. 3.2 we discuss about the cell coverage calculation and optimal ABS height. The power consumption model of the ABS and its dependency on transmitted power and power needed by the ABS to fly are reported in Sec. 3.3. Section 3.4 reports the formulation of signal to noise ratio (SNR) and capacity, whereas Sec. 3.5 reports about signal to interference ratio (SIR) and signal to interference plus noise ratio (SINR) analysis. Sec. 3.6 provides the results and discussion for above analysis. Further, Sec. 3.7 and 3.8, provides the analytical expressions for ABS, under different variable information available and expression for geometric increase in ABS coverage, respectively. Sec. 3.9,

evaluates the performance of the expressions described in Sec. 3.7 and 3.8, followed by conclusions and future work in Sec. 3.10. Lastly, Sec. 3.11, provides the proof of all analytical expressions.

3.2 Optimal height of Aerial Base Station for Maximum Coverage

LAPs are quasi-stationary aerial bodies, such as rotor-crafts, balloons, helikites, drones etc. In this thesis, LAP as a drone is considered because of its easy maneuverability, reliability and better stability in wind conditions. For the coverage analysis, with respect to wireless communications, we consider it to be defined as the portion of the cell in which the received power of GS is above the threshold, which is established by the mobile operator. Therefore, following [Richter et al., 2009], the cell coverage is defined by

$$C = \frac{1}{A_c} \int_{A_C} r \cdot P(P_{rx}(r) \geq P_{min})\, dr\, d\phi, \tag{3.1}$$

where A_C is the cell area of chosen radius 200 m, r is the distance between receiver and ABS, and P is the probability that the received power P_{rx} is greater than the threshold P_{min}. The value of the cell coverage lies in [0,1] and shown as a percentage in the later sections. For obtaining the coverage, a sectorization of the snapshot was done on the basis of 2° elevation angle between the ABS and GS as shown in Fig. 3.1. The purpose of sectorization was only to discretize the simulation area for improving accuracy of the results while implementing (3.1). For each sector, the probability P was calculated from the simulated data for the receivers within that sector at a given distance from the transmitter. The cell area was taken to be of radius 200 m by removing the building area as shown in Table 3.1. Finally, the optimal height was evaluated from the maximum cell coverage obtained using ray tracing simulation results.

3.3 Optimal Power Consumption of Aerial Base Station for Maximum Coverage

One of the most important aspect when using ABSs is the amount of power they are consuming while flying. For this reason, a power consumption model was used here, that takes into account both the power needed by the drone to hover P_{drone}, *i.e.*, the power needed for flying, assuming 100% efficiency [dro,], and the transmitted power P_{TX} from the ABS. The power

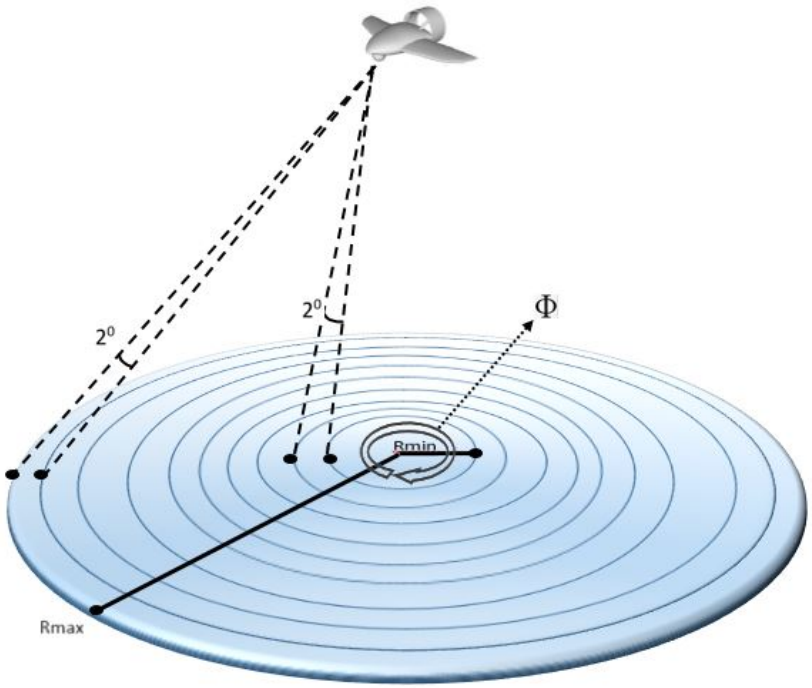

Figure 3.1: *Sectorization used for coverage analysis from ABS.*

Table 3.1: *Cell Area for the simulation*

Scenario	Cell Area (m^2)	No. of build-ings	Building Area (m^2)	Final Cell Area (m^2)
Suburban	$\simeq 104.000$	750	10.379	93.543
Urban	$\simeq 104.000$	500	31.189	72.733
Urban High Rise	$\simeq 104.000$	300	51.961	51.961

needed by the drone is given by

$$P_{drone} = \sqrt{\frac{(2Mg)^3}{16\rho A}}, \tag{3.2}$$

where ρ denotes the density of air at sea level, *i.e.*, $1.2\,\text{Kg/m}^3$, M is the mass of the drone plus payload, g is the gravitational force, *i.e.*, $9.8\,\text{N/Kg}$, and A is the rotor area. It was observed that P_{drone} can be assumed as a constant

value since it depends only on the physical dimensions and overall weight of the drone. The expression that regulates the total power consumed by an ABS is

$$P_{consumed} = P_{TX} + P_{drone}. \tag{3.3}$$

Therefore, from this model, it was understood that the power consumed by the ABS is entirely dependent on P_{TX}, whose behavior will be discussed in Sec. 3.6.2. Also, in the real flights, the power consumption by the ABS will also depend on several atmospheric factors such as wind, altitude, speed of the drone, time of flight, trajectory of the drone etc, as discussed in [Vasquez-Gomez et al., 2016]. The relationship was found between P_{TX} and cell coverage, shown from the simulation results.

3.4 Capacity Analysis

Channel capacity is the key parameter that defines the performance of a communication system. It is the upper bound limit on the rate at which information can be reliably transmitted over a wireless communication channel with arbitrarily low probability of error. A flat fading channel was assumed with stationary and ergodic time-varying gain $g(i)$, with $g(i) \geq 0$, and additive white gaussian noise (AWGN) $n(i)$ at each time i. Also, it was assumed that $g(i)$ is an IID random process distributed according to Rician probability density function in order to take into account small scale fading effects. However, the majority of propagation loss is due to large scale fading. Capacity is defined as [Goldsmith, 2005]

$$C = B \log_2(1 + \mathrm{SNR}) \tag{3.4}$$

where B is signal bandwidth and SNR is the instantaneous SNR defined by

$$\mathrm{SNR}(i) = \frac{\overline{P}_{TX}(i)}{P_N} = \frac{\overline{P}_{TX} g^2(i)}{N_0 B} \tag{3.5}$$

with $\overline{P}_{TX}$ denoting the average transmitted power, P_N being the average noise power. In the above equation N_0 is the power spectral density of AWGN $n(i)$. Since $\overline{P}_{TX}/P_N$ is a constant, the distribution of $\mathrm{SNR}(i)$ is the same as that of $g^2(i)$.

3.5 Interference Analysis

Another important aspect analyzed in this chapter is the impact of inter-cell interference coming from the adjacent cells. This affects the received

power of a GS and, therefore, it defines the areas of the cell covered by the ABS. To analyze this, the phenomenon of interference was described as a function of the distance and of the PLE obtained from analyzing the data provided by the Wireless InSite simulator. The SIR was described as follows. Considering the ABS positioned in the center of the interfering cells and limiting the analysis to the first tier of adjacent cells,

$$\mathrm{SIR} = \frac{P_{rx}}{P_I} = \frac{d^{-\eta}}{\sum_{i=1}^{l} r_i^{-\eta}} \tag{3.6}$$

where P_{rx} is the received power and P_I is the power of the interference. In the above equation d is the distance of each receiver from primary ABS, l is the number of interfering ABS, and r is the distance of each receiver from each interfering ABS.

Equation (3.6) is valid, assuming same P_{TX}, antenna gain and transmission frequency of interfering ABSs. Here six interfering ABSs are assumed, as happens for a terrestrial scenario to compare existing cellular architectures. However, more than six interfering ABSs can be assumed since the cells are moving and interference could be avoided using an appropriate trajectory planning for the ABS. The SINR can be calculated using (3.5) and (3.6) as

$$SINR = \frac{P_{rx}}{P_N + P_I} = \frac{\mathrm{SNR} \cdot \mathrm{SIR}}{\mathrm{SNR} + \mathrm{SIR}}. \tag{3.7}$$

The considered interference scenario is shown in Fig. 3.2. Here the coverage area for each ABS is clearly shown. Actually, to have interference coverage areas should overlap but for clear understanding of the scenario, in the Fig. 3.2, representing them separately was preferred in order to make them clearly distinguishable.

3.6 Results and Discussion

In this section, the coverage, capacity and interference results were plotted with respect to transmitter heights and power. The results plotted with respect to transmitter height were simulated at 18 dBm transmitter power and those plotted with respect to transmitter power were simulated at 320 m. Altitude of 320 m was chosen, because it was obtained as an optimal altitude for ABS as will be seen in Sec. 3.6.1. Also, 18 dBm was selected keeping in consideration the payload and dimensioning constraints of UAVs, for generating higher transmitter power.

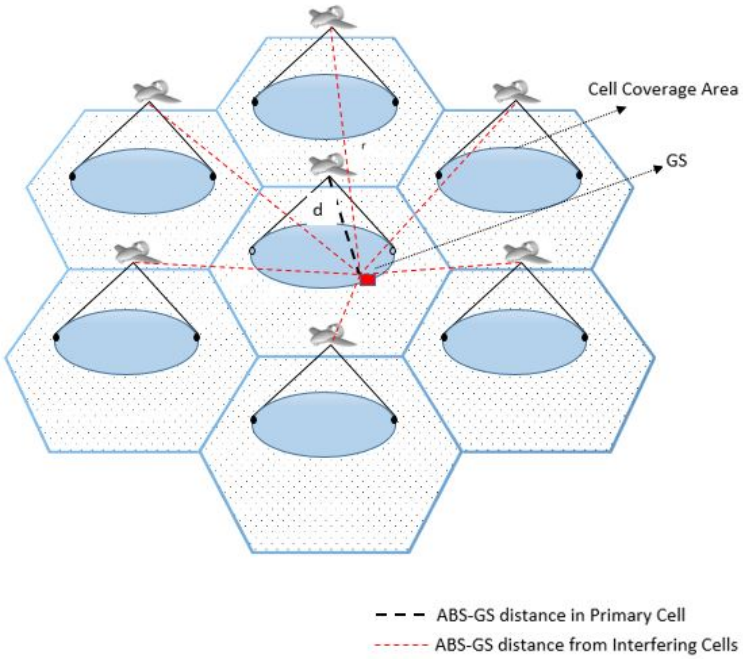

Figure 3.2: *Interefernce Scenario from interfering ABS*

3.6.1 Cell Coverage Analysis with variation in ABS height

From the ray tracing simulation data, the received power was obtained for each receiver in two snapshots for each environment and plotted as the percentage of cell coverage by an ABS as shown in Fig. 3.3. The cell coverage was obtained using (3.1). From Fig.3.3, it can be observed that maximum cell coverage increases with lesser received power threshold at the edge of the cell. In our simulation, the maximum coverage was obtained by setting the threshold to -120 dBm. Practical RSSI values were assumed for our simulations as obtained in practical scenario to maintain the accuracy of our results. As the RSSI was increased to -80 dBm, the cell coverage decreases because less number of receivers full fill the probability condition in (3.1). Also, it was found that the optimal altitude of ABS for maximum coverage at 18 dBm was between $300 - 350$ m for all environments. This was verified from [Mozaffari et al., 2016d], where an analytical framework was used to find ABS coverage probability for downlink user. Lower ABS transmission power of 18 dBm was considered, in comparison to 46 dBm of terrestrial base station, because UAVs' are power constrained devices. However, with increase in transmitter power, the coverage is expected to

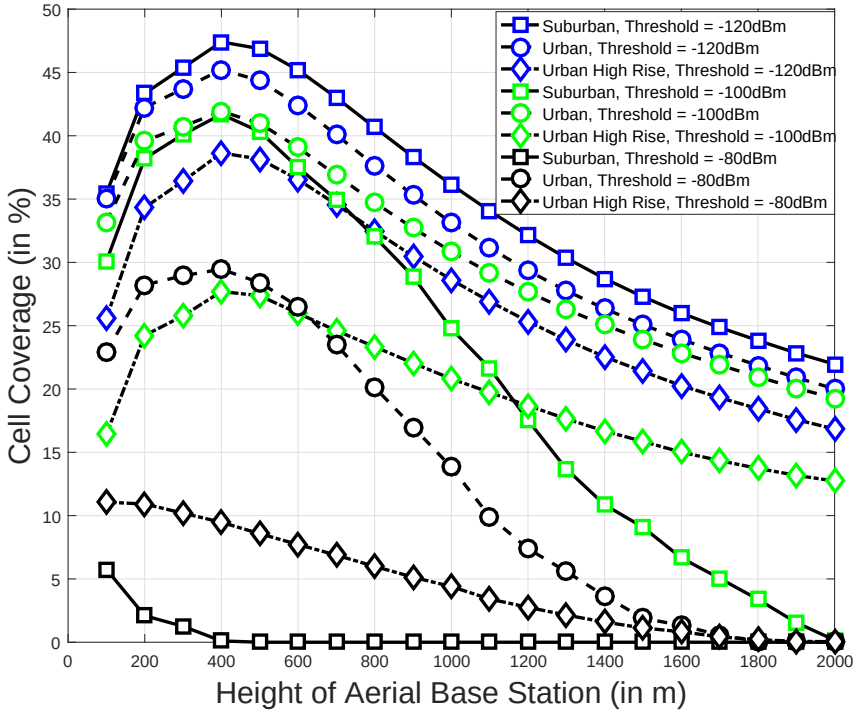

Figure 3.3: *Coverage Analysis from an ABS at 18dBm transmitter power for different receiver threshold*

increase as seen in Sec. 3.6.2. Finally, it was also analyze that cell coverage is higher for Suburban environment and lowest for Urban high rise for -120 dBm threshold. However, this trend was seen changing as the threshold increases, where Suburban has the least coverage than Urban and Urban high rise environments. This is because, in urban conditions, A2G channel experiences Rician fading due to the presence of LOS path. In suburban areas, a Rayleigh fading is experienced due to the presence of reflected signals that are stronger than LOS [Zajić, 2012]. This is opposite for terrestrial communication. Therefore, as received power threshold is increased, fading changes from Rayleigh to Rician in Suburban environments and vice versa in Urban. So, a generalized approach is to use a Rician distribution where both LoS and NLoS paths are considered.

3.6.2 Cell Coverage Analysis with variation in ABS Transmitted Power

As mentioned in Sec. 3.6.1, the cell coverage is expected to increase as the transmitted power of the ABS increases. This can be seen in Fig. 3.4. The

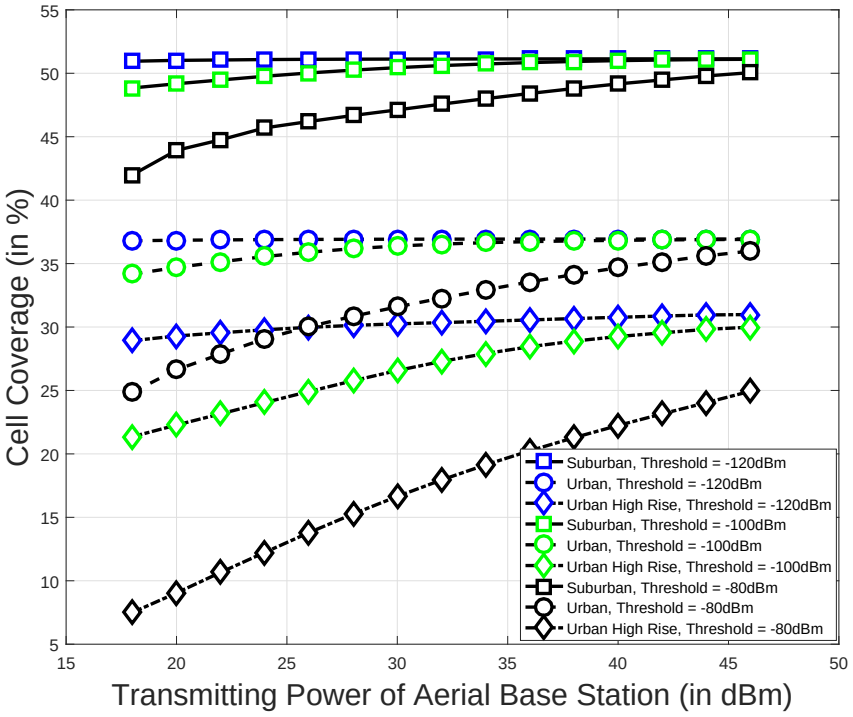

Figure 3.4: *Coverage Analysis from an ABS at* $320\,m$ *height with varying transmitter power for different receiver threshold*

simulations were carried for one snapshot in each environment at optimal ABS height of $320\,\text{m}$. As seen from the simulations, the cell coverage increases linearly with receiver sensitivity at $-80\,\text{dBm}$ but becomes almost constant at $-120\,\text{dBm}$. This is because the receivers receiving $-120\,\text{dBm}$ are already receiving the least value of received power to maintain the connectivity with the ABS. Therefore, the receivers receiving lesser than $-120\,\text{dBm}$ are not present in the coverage area of the cell. Also, as expected the cell coverage is higher for Suburban environment than Urban environments, due to Rayleigh fading where multi-path and scattering effects dominate leading to constructive and destructive addition of received power with their phase and delay and therefore leading to higher received power. Finally, we also analyze from (3.3) and (3.2), that dependency of cell coverage will follow a similar behavior with respect to $P_{consumed}$.

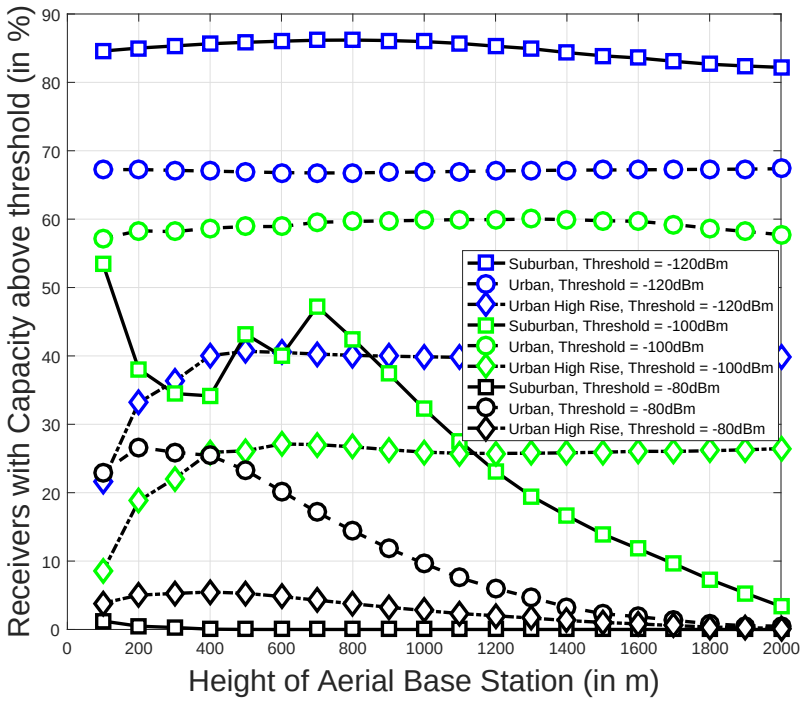

Figure 3.5: *Capacity Analysis from an ABS at* $18\,dBm$ *transmitter power for different receiver threshold*

3.6.3 Capacity Analysis above Threshold with variation in ABS height

For the capacity analysis, Eq. (3.4) and (3.5) were referred. A threshold was set for the received power for each environment and snapshot as -120 dBm. The value was chosen considering practical RSSI in cellphones. For this threshold of received power, we obtained, the SNR threshold from (3.5), considering only AWGN channel and thermal noise of the receiver. Therefore, after formulating the capacity, percentage of receivers getting capacity above the threshold, were investigated, for different ABS heights. This result is depicted in Fig. 3.5. It was observe that since at $-120\,$dBm threshold, the SNR threshold is also minimum, so capacity of receivers is highest. As the threshold increases, the capacity decreases. However, any change was observed in the behavior for percentage of receivers having capacity above the threshold, with respect to change in height of ABS. But a significant drop was seen, in Suburban scenario at $-100\,$dBm and $-80\,$dBm. This is probably due to different fading environment than the other cases, as mentioned previously.

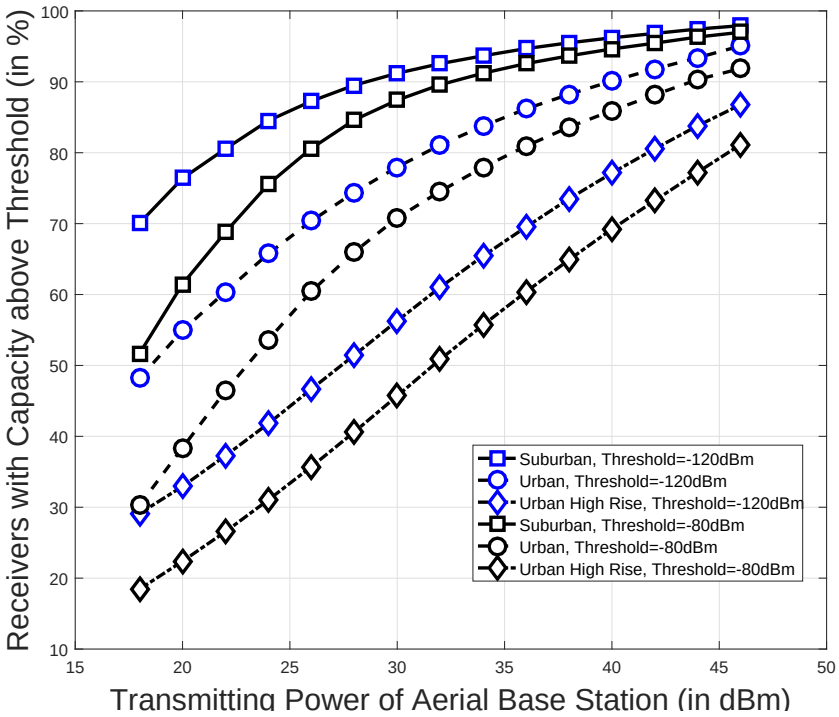

Figure 3.6: *Capacity Analysis from an ABS at 320m height with varying transmitter power for different receiver threshold*

3.6.4 Capacity Analysis above Threshold with variation in ABS Transmitted Power

In Fig. 3.6, the cases for minimum and maximum RSSI were considered for the simulations carried. It was seen that percentage of receivers with capacity above the threshold, increases with increase in transmitted power as expected, since as per (3.5) and (3.4), the SNR increase linearly with transmitter power and capacity increases logarithmically with SNR. Similarly, as was observed in Sec. 3.6.3, the percentage is higher for simulation with -120 dBm threshold than -80 dBm. Also, the behavior of percentage is similar at both thresholds unlike the variation due to transmitter height, with Suburban having the maximum percent than Urban and Urban High rise. The reason being again due to Rayleigh fading in Suburban and Rician for Urban environments.

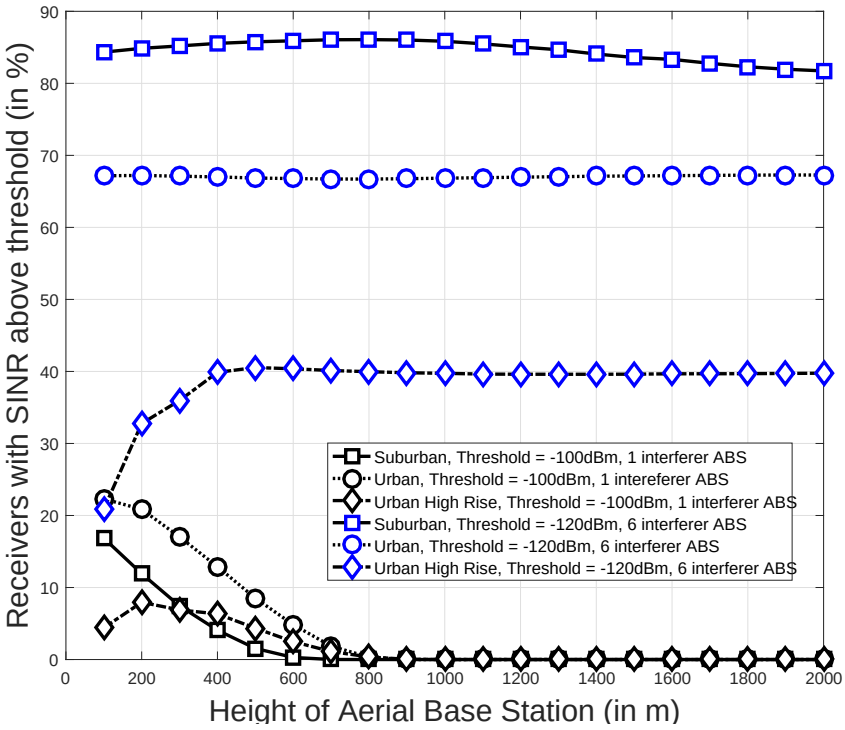

Figure 3.7: *SINR Analysis from an ABS at 320m height with varying transmitter power for different receiver threshold*

3.6.5 SINR Analysis above Threshold with variation in ABS Transmitted Power

Figure 3.7 discusses about the SINR calculated at different ABS heights. All interfering ABSs were assumed to be operating with the same parameters as the primary ABS. While considering one interfering ABS, it was observed that percentage of receivers with SINR above the threshold follow a constant behavior for received power threshold kept as -120 dBm. However, for higher thresholds like -100 and -80 dBm, the SINR tends to zero, *i.e.*, there is high interference from one ABS. For a new set of simulations with 6 interfering ABS, it was seen that percentage decreases rapidly for -120 dBm, and still remains zero for higher thresholds. Also, since the simulations were carried out at 18 dBm transmitter power, it was recognized that it was needed to increase the transmitter power in order to have a better SINR for each receiver in the scenario.

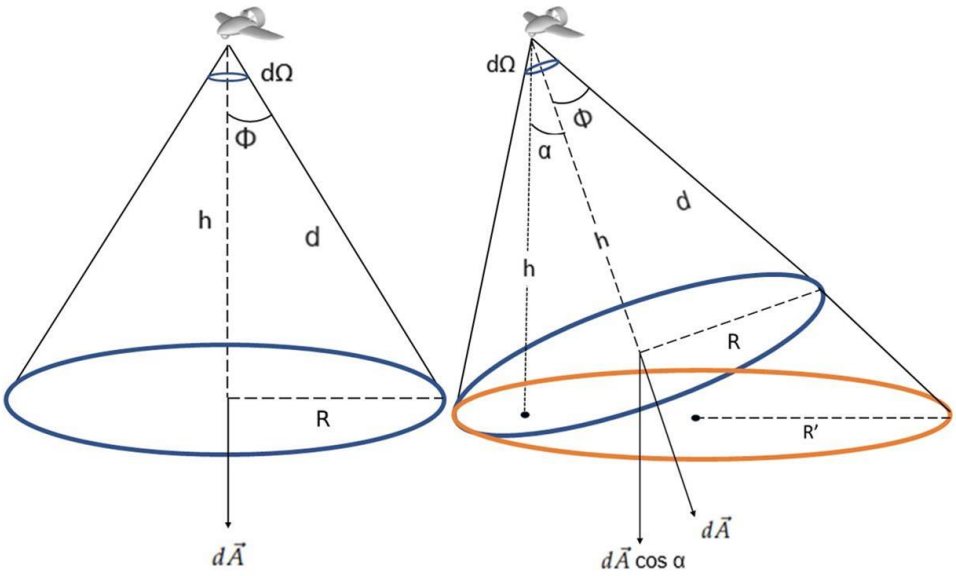

(a) Without rotation angle (b) With rotation angle

Figure 3.8: *Coverage Area by ABS.*

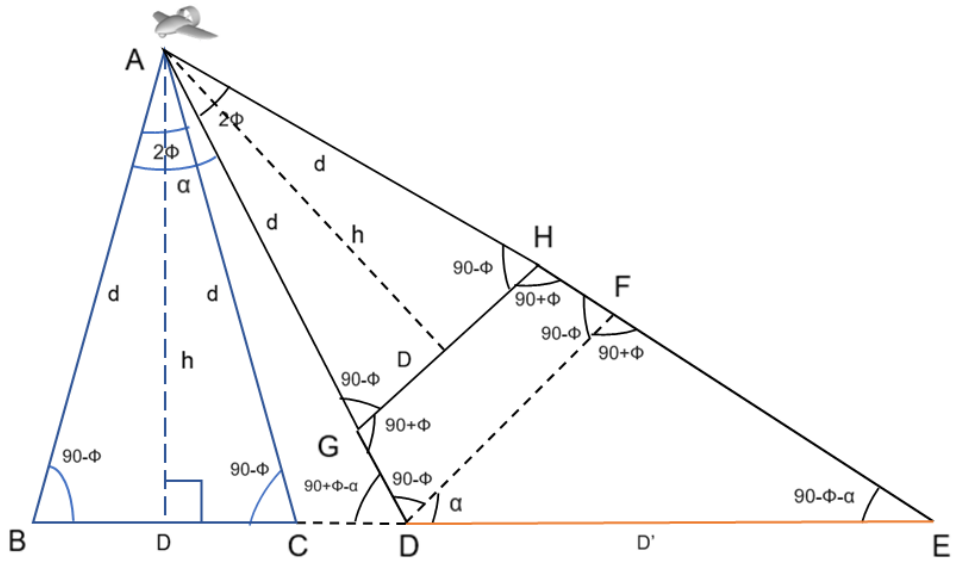

Figure 3.9: *Increase in Geometric Coverage Area.*

3.7 Analytical framework for Drone Cell Coverage

The coverage from an ABS is shown in Fig. 3.8a. For analytical simplifications, an arbitrary circular area of radius R is assumed with the cell coverage area by ABS defined using the solid angle. Solid angle is a 3D analogue of an angle, enclosed by a conical surface at the apex. Therefore, the solid angle Ω subtended by the circular cell area over the ABS is given by the expression

$$\Omega = \int_{\theta_1}^{\theta_2} \int_{\phi_1}^{\phi_2} \sin\phi \, d\theta \, d\phi \ , \tag{3.8}$$

where $d\phi$ is the elevation angle and $d\theta$ is the azimuth angle, with lower and upper limits as ϕ_1,ϕ_2 and θ_1,θ_2, respectively, subtended by the elemental area dA on the ground at the ABS. Therefore, the expression of the cell coverage area can be given as

$$A = \frac{2h^2}{R}(\sec\phi_{max} - 1) \left[\left(\frac{1-\mathrm{erf}(a)}{2}\right) - \frac{1}{2}\exp\left(\frac{1-4ab}{4b^2}\right)\left[\mathrm{erf}\left(\frac{1}{2b} - a\right) - 1\right]\right]. \tag{3.9}$$

where h is the height of ABS, ϕ_{max} is the maximum elevation angle, depending on the type of antenna used, erf is the error function, a and b are substitution parameters, given in the Appendix 3.11.1 along with the proof of (3.9). (3.9) does not consider the rotation angle of the ABS which can be introduced due to perturbations by wind gusts or maneuvers such as roll, pitch and yaw. The expression for coverage area by ABS including a certain rotation angle α is given as

$$A = \frac{h^2}{R'}\ln\left|\frac{1+\sin\alpha_{max}}{1-\sin\alpha_{max}}\right|(\sec\phi_{max} - \sec\alpha_{max}) \left[\left(\frac{1-\mathrm{erf}(a)}{2}\right) - \frac{1}{2}\exp\left(\frac{1-4ab}{4b^2}\right)\left[\mathrm{erf}\left(\frac{1}{2b} - a\right) - 1\right]\right], \tag{3.10}$$

where R' is the radius of geometrically increased coverage area as seen in Fig.3.8(b) and α_{max} is the maximum rotation angle. The derivation of R' can be found in Appendix 3.11.4 and the proof of (3.10) is given in Appendix 3.11.2. This equation is only valid when $\alpha \neq n\pi$ for $n \,\epsilon\, [0, 1, 2, 3, ..., \infty]$. Although for maintaining stable flight, α assumes a lower value and $\alpha \not> \frac{\pi}{2}$. From (3.10), coverage area is known when altitude and the rotation angle of the ABS is known. The coverage can also be

obtained by the following expression when ABS altitude is unknown. The proof is available in Appendix 3.11.3.

$$A = R' \ln\left|\frac{1+\sin\alpha_{max}}{1-\sin\alpha_{max}}\right| \ln\left|\frac{\tan\frac{\phi_{max}}{2}}{\tan\frac{\alpha_{max}}{2}}\right| \left[\frac{1}{6} - \frac{1}{2}\left[erf(a) - \frac{1}{3}\exp\left(\frac{9}{4b^2} - \frac{a}{b}\right)\left[erf\left(\frac{-3}{2b} + t\right) - 1\right]\right]\right]. \quad (3.11)$$

For all the proofs, we have assumed R, R' and h to be fixed. However, the cell coverage is sub-area of the total circular area of radius R and R'. It depends on variables ϕ, α and parameter $\mathbb{P}(P_{RX}(r) \geq P_{th})$, given in Appendix 3.11.1.

3.8 Increase in the Geometric Coverage area by ABS

Due to rotation angle, the coverage area by ABS is bound to increase geometrically, as shown in Fig. 3.8. However, it also results in increase in A2G link propagation losses, such as , shadowing and multipath effects with the same transmitting power and antenna gains. Therefore, the final coverage area may increase or decrease depending on the propagation environment and effects. But, this geometric increase in coverage area needs to be taken into account into (3.10) and (3.11) to obtain the final coverage area. Figure 3.9, shows a 2D layout of Fig. 3.8b for calculation of radius of coverage area due to rotation. Thus, the radius R' of coverage area due to rotation can be written is

$$R' = \frac{d\sin^2(90+\phi)\,\sin 2\phi}{2\sin(90+\phi-\alpha)\sin(90-\phi)\sin(90-\phi-\alpha)}. \quad (3.12)$$

3.9 Numerical Results

In this section, the results at different ABS altitudes are shown, for Suburban, Urban and Urban High Rise scenarios, with a constant transmission power of 18 dBm, from the previous analytical analysis. Fig. 3.10, corresponds to (3.9), while Fig. 3.11 to (3.10). Here, we use the ray tracing measurement results, which includes all propagation link factors, for practical RSSI values from poor to good LTE connectivity, i.e, -120, -100 and -80 dBm, respectively. From Fig. 3.10, the results are in correlation with [Cileo et al., 2017], with higher cellular coverage at lower RSSI. The decrease in coverage for Suburban environments is much higher as compared to Urban

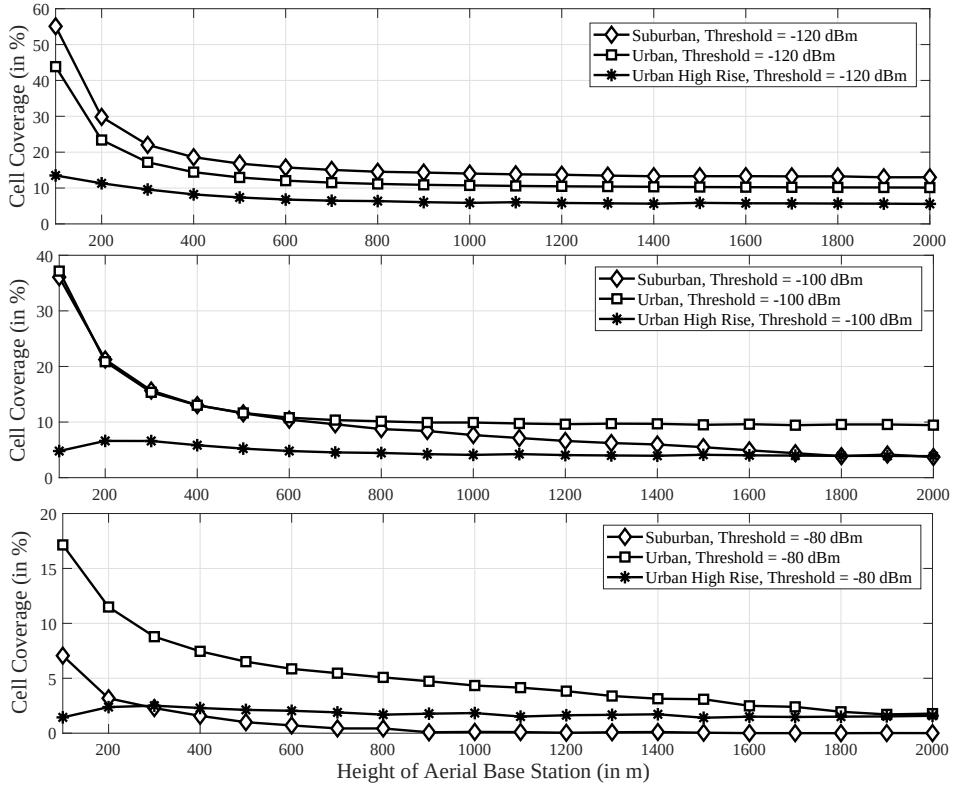

Figure 3.10: *Cell coverage with known ABS altitude without rotation.*

due to change in fading conditions experienced by the A2G channel, as detailed in [Cileo et al., 2017]. Also, by introducing the rotation angle in the range of $[-20°, 20°]$, a significant increase in geometrical coverage can be observed from Fig. 3.11. However, by using non-directional antenna at ABS, the effect of rotation angle will be limited as compared to directional antenna. Further, as the ABS altitude is increased the cell coverage tends to zero, which can be clearly observed for RSSI -80 dBm in Fig. 3.10. However, for lower receiver sensitivity of -120 dBm, the cell coverage doesn't completely reaches to zero at 2000 m but at higher altitudes. As expected, intermediate results are observed at RSSI of -100 dBm in Fig. 3.10.

3.10 Conclusions and Future Work

In this chapter, analysis for cell coverage, capacity and inter-cell interference from ray tracing simulation results for an ABS at 2.4 GHz in different generalized environments, created following ITU-R parameters was done.

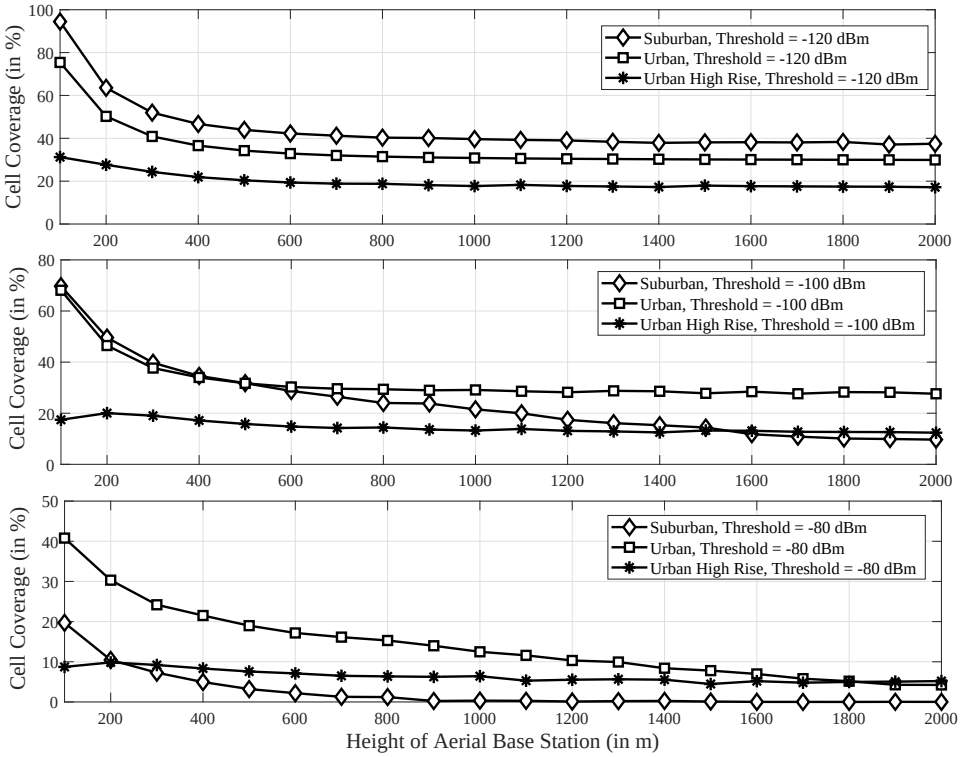

Figure 3.11: *Cell coverage with known ABS altitude with rotation.*

From coverage results the optimal altitude for ABS was reported and a coverage dependency for power transmitted by flying base station was shown. Also, capacity and signal to interference plus noise results were presented with the percentage of receivers getting them above the thresholds, which were set keeping -120 dBm, -100 dBm and -80 dBm of received power, taking into account practical RSSI values. The cell coverage and transmitting power results prove the feasibility of using UAVs with Picocells and Femtocells formation with transmission power in the range of 33 dBm and 20 dBm. The results from this chapter were published in [Cileo et al., 2017]. Further, the analytical expressions with proofs for obtaining cellular coverage by an ABS are provided, depending on the available variable information. Also, a geometric aspect of rotation angle due to wind perturbations or intentional maneuvers, is described. Finally, simulation results from realistic ray tracing measurements were used to verify the behavior of the graphs to define the feasibility of expressions. However, an error factor leading to a certain mismatch of the graphs from measurements, will be part

of future activity along with new measurements for link propagation losses with rotation angle and possible inclusion of multiple drone network.

3.11 Appendices

3.11.1 Proof for Coverage Area by ABS with known Altitude without Rotation Angle

As seen from Fig. 3.8a, the solid angle subtended by an element on the ground at ABS is given by

$$d\Omega = \frac{\vec{dA}}{d^2} \cdot \hat{n}, \tag{3.13}$$

where d is the $3D$ distance or the slant height of the cone formed from the geometry in Fig. 3.8 and $\hat{n}$ is the unit vector from the origin. The direction of $\hat{n}$ and $\vec{dA}$ is same when no rotation angle is present. From (3.13) we have $dA = d^2\, d\Omega$ and from (3.8), $dA = \sin\phi\, d^2\, d\theta\, d\phi$. This relationship is only based on the geometrical aspects of Fig. 3.8a. Therefore, the parameter $\mathbb{P}(P_{RX}(r) \geq P_{th})$ is added to the above expression. This produces the actual coverage by the ABS. This parameter denotes the probability that the received power by the ground user (P_{RX}) is greater than the received power threshold (P_{th}) and r is the $2D$ distance between the ABS and the user. Thus we have

$$dA = \sin\phi\, d^2\, \mathbb{P}(P_{RX}(r) \geq P_{th})\, d\theta\, d\phi\, dr. \tag{3.14}$$

Thereby integrating (3.14), we have

$$A = \frac{d^2}{A_C} \int_{\phi=0}^{\phi=\phi_{max}} \sin\,\phi\, d\phi \int_{\theta=0}^{\theta=2\pi} d\theta \int_0^R \mathbb{P}(P_{RX}(r) \geq P_{th}) dr, \tag{3.15}$$

where R is the cell radius and corresponds to ϕ_{max}. $A_C = \pi R^2$ is the cell area used to normalize the final cell coverage A. Thus, from Fig. 3.8 and (3.15) we have

$$A = \frac{2\pi h^2}{A_C} \int_{\phi=0}^{\phi=\phi_{max}} \frac{\sin\,\phi}{\cos^2\phi}\, d\phi \int_0^R \mathbb{P}(P_{RX}(r) \geq P_{th}) dr.$$

Now integration of each part is shown separately as

$$A = \frac{2\pi h^2}{A_C} I_1 I_2, \tag{3.16}$$

where

$$I_1 = \int_{\phi=0}^{\phi=\phi_{max}} \frac{\sin\,\phi}{\cos^2\phi}\,d\phi = \sec\phi_{max} - 1 \tag{3.17}$$

and

$$I_2 = \int_0^R \mathbb{P}(P_{RX}(r) \geq P_{th})dr. \tag{3.18}$$

The term I_2 can be calculated using Q-function as $\mathbb{P}(P_{RX}(r) \geq P_{th}) = Q\left(\frac{P_{th}-\overline{P}_{RX}(r)}{\sigma}\right)$, where σ is standard deviation of log-normal shadow fading. The Q-function is defined in as $Q(x) = \int_x^\infty \frac{1}{\sqrt{2\pi}}\exp\left(-\frac{y^2}{2}\right)dy = \frac{1}{2}\left[1-\mathrm{erf}\left(\frac{x}{\sqrt{2}}\right)\right]$, where $\mathrm{erf}(\cdot)$ is an error function. Therefore we have $\mathbb{P}(P_{RX}(r) \geq P_{th}) = \frac{1}{2}\left[1-\mathrm{erf}\left(\frac{P_{th}-\overline{P}_{RX}(r)}{\sigma\sqrt{2}}\right)\right]$. From the log-distance path loss model (in dB), $\overline{P}_{RX}(r) = P_{TX}+G_T+G_R-PL$, and by substituting for PL, we have, $\overline{P}_{RX}(r) = P_{TX}+G_T+G_R-\left(PL_0+10\eta\log_{10}\left(\frac{r}{r_0}\right)\right)$, where P_{TX} is the transmitted power, G_T and G_R are the transmitting and receiving antenna gain, respectively, PL is the path loss which is further written as a function of reference path loss PL_0, at distance r_0 from the transmitter, and PLE η, as per close-in reference distance PL model [Sun et al., 2016]. Therefore, we have

$$\mathbb{P}(P_{RX}(r) \geq P_{th}) = \frac{1}{2}[1-\mathrm{erf}(\frac{P_{th}-[P_{TX}+G_T+G_R-[PL_0+10\eta\log_{10}(\frac{r}{r_0})]]}{\sigma\sqrt{2}})],$$

$$= \frac{1}{2}-\frac{1}{2}\,\mathrm{erf}\left(\frac{P_{th}-P_{TX}-G_T-G_R+PL_0+10\eta\log_{10}(R/r_0)}{\sigma\sqrt{2}}+\frac{10\eta\log_{10}(r/R)}{\sigma\sqrt{2}}\right)$$

where we substitute the following for clarity

$$a = \left(\frac{P_{th}-P_{TX}-G_T-G_R+PL_0+10\eta\log_{10}(R/r_0)}{\sigma\sqrt{2}}\right) \tag{3.19}$$

and

$$b = \frac{10\eta\log_{10}(e)}{\sigma\sqrt{2}}. \tag{3.20}$$

Therefore, we represent

$$\mathbb{P}(P_{RX}(r) \geq P_{th}) = \frac{1}{2} - \frac{1}{2}\,\mathrm{erf}\left(a + b\ln\frac{r}{R}\right) \text{ and}$$

$$I_2 = \int_0^R \mathbb{P}(P_{RX}(r) \geq P_{th})dr = \int_0^R \frac{1}{2} - \frac{1}{2}\operatorname{erf}\left(a + b\ln\frac{r}{R}\right)dr. \quad (3.21)$$

Replacing $t = a + b\ln\frac{r}{R}$

$$I_2 = \frac{R}{2} - \frac{R}{2b}\int_{-\infty}^{a} \exp\left(\frac{t-a}{b}\right)\operatorname{erf}(t)dt.$$

Integrating by parts, we obtain $I_2 = R\left[\left(\frac{1-\operatorname{erf}(a)}{2}\right) - \frac{1}{2}\exp\left(\frac{1-4ab}{4b^2}\right)\left[\operatorname{erf}\left(\frac{1}{2b} - a\right) - 1\right]\right]$. Now substituting for I_1,I_2 and A_C in (3.16), we finally get (3.9).

3.11.2 Proof for Coverage area by ABS with known Altitude and Rotation Angle

As seen from Fig. 3.8b, the coverage area by ABS is tend to change due to the introduction of rotation angle α. Therefore, (3.13), (3.14), (3.15) and (3.16) will be modified as $d\Omega = \frac{dA\cos\alpha}{d^2}$

$$dA = \frac{1}{\cos\alpha}\sin\phi\, d^2\, \mathbb{P}(P_{RX}(r) \geq P_{th})\, d\theta\, d\phi\, dr d\alpha, \quad (3.22)$$

$$A = \frac{d^2}{A_C}\int_{\alpha=0}^{\alpha=\alpha_{max}} \frac{d\alpha}{\cos\alpha}\int_{\phi=\alpha_{max}}^{\phi=\phi_{max}} \sin\,\phi\, d\phi \int_{\theta=0}^{\theta=2\pi} d\theta \int_0^R \mathbb{P}(P_{RX}(r) \geq P_{th})dr, \quad (3.23)$$

$$A = \frac{2\pi h^2}{A_C} I_1 I_2 I_3, \quad (3.24)$$

where $I_3 = \int_{\alpha=0}^{\alpha=\alpha_{max}} \frac{d\alpha}{\cos\alpha}$. Thus far, $I_1 = \sec\phi_{max} - \sec\alpha_{max}$, I_2 remains unchanged and we obtain $I_3 = \frac{1}{2}\ln\left|\frac{1+\sin\alpha_{max}}{1-\sin\alpha_{max}}\right|$. Substituting I_1, I_2 and I_3 in (3.24), we obtain (3.10).

3.11.3 Proof for Coverage area by ABS with unknown Altitude and known Rotation Angle

From Fig. 3.8, d can be expressed as $d = \frac{r}{\sin\phi}$. Substituting in (3.22), $dA = \frac{1}{\cos\alpha}\frac{r^2}{\sin\phi}\mathbb{P}(P_{RX}(r) \geq P_{th})\, d\theta\, d\phi\, dr d\alpha$. By integrating, as done for

(3.23), we have

$$A = \frac{1}{A_C} \int_{\alpha=0}^{\alpha=\alpha_{max}} \frac{d\alpha}{\cos\alpha} \int_{\phi=\alpha_{max}}^{\phi=\phi_{max}} \frac{1}{\sin\ \phi}\, d\phi \int_{\theta=0}^{\theta=2\pi} d\theta \int_0^R r^2\, \mathbb{P}(P_{RX}(r) \geq P_{th}) dr. \quad (3.25)$$

Here I_1 and I_2 (from (3.21)) are updated as $\int_{\phi=\alpha_{max}}^{\phi=\phi_{max}} \frac{1}{\sin\ \phi}\, d\phi = \ln \left| \frac{\tan\frac{\phi_{max}}{2}}{\tan\frac{\alpha_{max}}{2}} \right|$, and $\int_0^{R'} r^2 \mathbb{P}(P_{RX}(r) \geq P_{th}) dr =$
$\int_0^R r^2 \left[\frac{1}{2} - \frac{1}{2}\,\mathrm{erf}\left(a + b\ln\frac{r}{R'}\right)\right] dr$. However I_3 remains the same. Following the same steps for solving I_2 by replacing $t = a + b\ln\frac{r}{R'}$, we get

$$\int_0^{R'} r^2 \mathbb{P}(P_{RX}(r) \geq P_{th}) dr = \frac{R'^3}{6} - \frac{R'^3}{2b} \int_{-\infty}^{a} \left[\exp\left(\frac{t-a}{b}\right)\right]^3 \mathrm{erf}(t) dt,$$

By integrating the above expression

$$\int_0^{R'} r^2 \mathbb{P}(P_{RX}(r) \geq P_{th}) dr = \frac{R'^3}{6} - \frac{R'^3}{2} \left[erf(a) - \frac{1}{3}\exp\left(\frac{9}{4b^2} - \frac{a}{b}\right)\left[erf\left(\frac{-3}{2b} + t\right) - 1\right]\right],$$

Substituting above expressions in (3.25), the final expression obtained is (3.11).

3.11.4 Proof for increase in Geometric Coverage Area by ABS due to rotation angle

From Fig. 3.9, $\triangle ABC$ is rotated by $\angle BAD = \alpha$ to form $\triangle AGH$. Therefore, sides and angles of both triangles are equal. The elevation angle is $\angle\phi$ corresponding to Fig. 3.8. Therefore, $\angle BAC$ and $\angle GAH$ are 2ϕ. Also, corresponding to Fig. 3.8, $AB = AC = AG = AH = d$ with height of both triangles equal to h. Without rotation, the diameter of covered area by the ABS is $BC = D$ and the diameter of covered area after rotation is $DE = D'$. Here, we find the analytical expression for D' assuming that D is known.
From $\triangle ABC$, $\angle ABC = \angle ACB$ due to property of an isosceles triangle

since $AB = AC$. As known from the property of a triangle, $\angle BAC + \angle ABC + \angle ACB = 180°$. This implies, $2\phi + 2\angle ABC = 180°$. Therefore, $\angle ABC = \angle ACB = 90 - \phi$. Similarly, from $\triangle ABD$, we have $\angle BAD + \angle ABD + \angle ADB = 180°$. This implies, $\alpha + 90 - \phi\angle ADB = 180°$. Thus we have, $\angle ADB = 90 + \phi - \alpha$.
Now, from the exterior angle property of the triangle, the measure of an exterior angle of a triangle is equal to the sum of the measures of its interior opposite angles. Thus, $\angle ADB = \angle DAE + \angle AED$. This implies, $90 + \phi - \alpha = 2\phi + \angle AED$ and $\angle AED = 90 - \phi - \alpha$. Dropping a segment DF on AE such that DF is parallel to GH. From Fig. 3.9, we observe $\angle AHG + \angle FHG = 180°$. Therefore, $\angle FHG = 90 + \phi$. Following the same concept, $\angle DGH = 90 + \phi$.
From the theory of corresponding angles, when two parallel lines are crossed by a transversal, its corresponding angles are equal. Therefore, $\angle AGH = \angle ADF = 90 - \phi$ and $\angle AHG = \angle AFD = 90 - \phi$. Also from geometry, $\angle ADB + \angle ADF + \angle FDE = 180°$. This implies, $90 + \phi - \alpha + 90 - \phi + \angle FDE = 180°$. Therefore, $\angle FDE = \alpha$.
Now, from the Sine rule of triangles, in $\triangle ACD$

$$\frac{AC}{\sin\angle ADC} = \frac{AD}{\sin\angle ACD} = \frac{d}{\sin(90+\phi-\alpha)} = \frac{AD}{\sin(90+\phi)},$$

$$AD = \frac{d\sin(90+\phi)}{\sin(90+\phi-\alpha)},$$

Again from Sine rule in $\triangle ADF$

$$\frac{AD}{\sin\angle AFD} = \frac{DF}{\sin\angle DAF},$$

$$\frac{d\sin(90+\phi)}{\sin(90+\phi-\alpha)\sin(90-\phi)} = \frac{DF}{\sin 2\phi},$$

$$DF = \frac{d\sin(90+\phi)\sin 2\phi}{\sin(90+\phi-\alpha)\sin(90-\phi)},$$

Now applying the Sine rule in $\triangle DEF$

$$\frac{DF}{\sin\angle DEF} = \frac{DE}{\sin\angle DFE} =$$
$$\frac{d\sin(90+\phi)\sin 2\phi}{\sin(90+\phi-\alpha)\sin(90-\phi)\sin(90-\phi-\alpha)} = \frac{D'}{\sin(90+\phi)},$$

Therefore, the radius of coverage area, i.e, half its diameter, is given in (3.12).

CHAPTER 4

On-Demand Ultra-Dense Cloud Drone Networks

THE paradigm of previous 4G cellular technology has led to increase in requirements for high data rate demands of the mobile users in 5G. In order to meet this demand, constant densification of communication network was required in this racetrack. UDNs have been proposed as a promising 5G technology to fulfill these requirements by the efficient and dynamic distribution of the radio resources. However, for implementation of UDN, the mobile operators have to face many challenges such as severe interference resulting in a limited capacity due to the dense deployment of small cells, site location and acquisition for the deployment of base stations, backhauling issues, energy consumption, etc. In this chapter, in order to alleviate these limitations, a novel idea of UDCDN is proposed. This scheme is featured with "on-demand" quality and substantial flexibility in terms of deployment. This anchors the challenges of traditional UDN settings and offers numerous benefits. Through simulation results of cell coverage, the genuineness of implementing the proposed scheme were verified and offer a new paradigm shift for UDN.

4.1 Introduction

The rapid growth in communication traffic has evolved the current macrocell network to become more tight and compact, eventually leading to small cell architecture or UDN. However, not only the growing traffic drives the future network demands, but also the request for higher data rates by the subscribers. According to a recent survey in [Nok, b], data rates are expected to increase up to 10 Mbps in 2020 and 100 Mbps in 2030, from 1 Mbps in 2010 with monthly consumption rising from 1 GB/month to 30 GB/month.

To meet these requirements, current macrocells are evolving towards multi-carrier aggregation, use of mmWave spectrum, and increased spectral efficiency, through advanced antenna solutions such as MIMO and Distributed Antenna Systems.

However, the high maintenance cost and renting of a macrocell base station lead mobile operators to prefer the deployment of a UDN due to low power transmission and increase of capacity by efficient spatial reuse of the spectrum. There are several challenges to be met for successful implementation of UDN. Major limitations of UDN are high signal to noise plus interference ratio, due to the compact cell architecture and high overlapping of the coverage areas, high mobility scenarios with a large number of handovers occurring simultaneously, management of mobile-Xhaul, operator and vendor management, conflict resolutions between the service providers, etc [Nok, b, Yang et al., 2017a].

In this chapter, a novel idea of UDCDN is proposed. Drones, earlier developed for military applications, are now being actively implemented for many civil applications and recently in 5G [Naqvi et al., 2018]. It coud be argued that this is a timely and an efficient replacement for UDN in terms of on-demand deployment, energy efficiency, cost reduction and simpler network architecture with cloud-based and edge-based processing. However, some issues need to be addressed in UDCDN, starting from system design and technical aspects of administrative and legal ground for implementation. A fog-cloud based Radio Access Network (FC-RAN) architecture, which combines centralized (C-RAN), heterogeneous (H-RAN) and fog (F-RAN) radio access networks [Peng et al., 2016], was preferred to meet the LTE architecture requirements of low latency, high traffic volumes, and data rate. The motivation of this idea is to reduce the mobile operator's cost and radio resource continuous utilization by the real-time deployment of UDN using the drone-assisted network, while still meeting the cellular traffic requirements of 5G. Also, due to multitude of use cases of 5G,

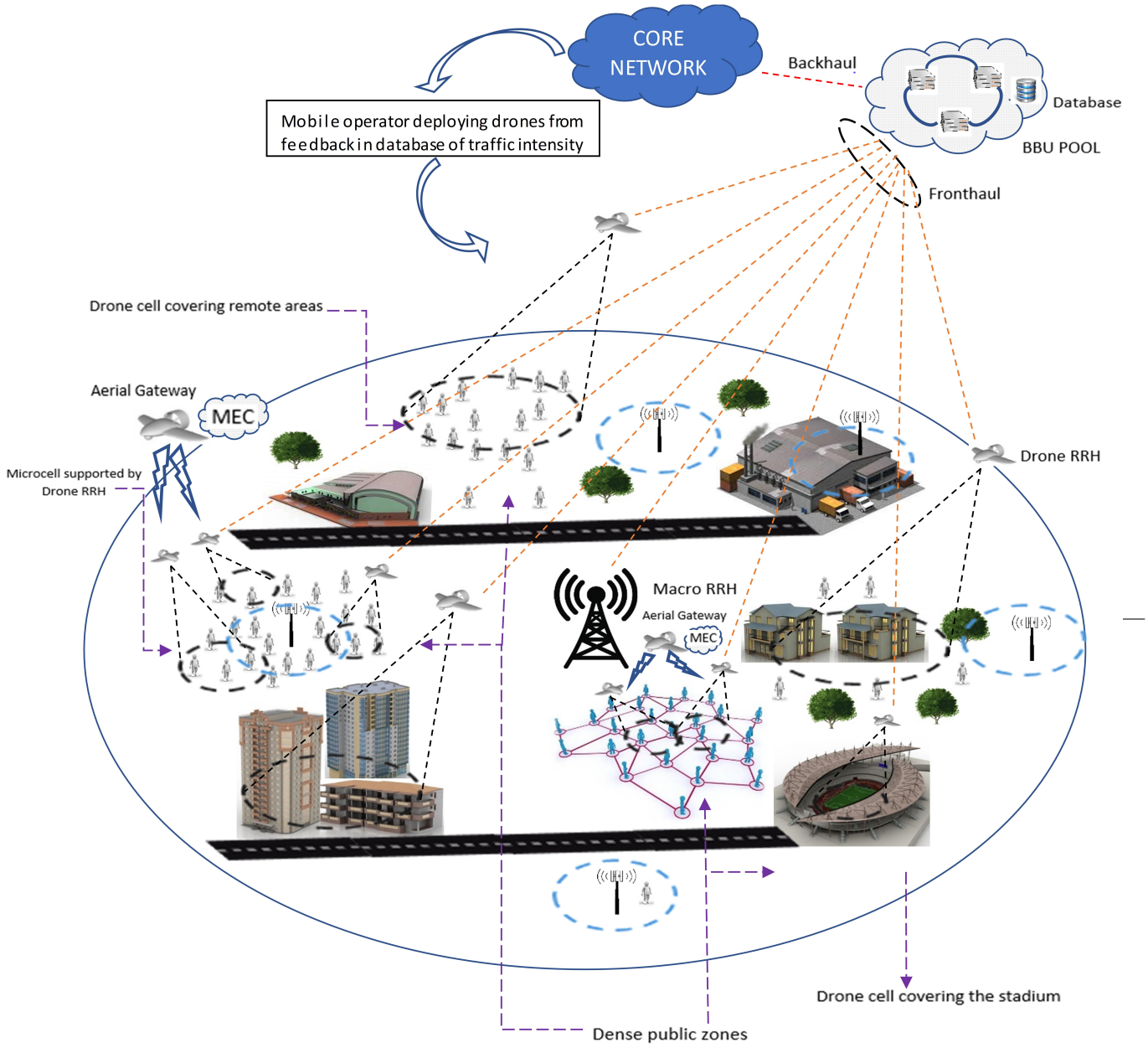

Figure 4.1: *UDCDN System Architecture*

network slicing is a fundamental key aspect to be inherited with UDCDN. With powerful Network Function Virtualization (NFV) technology, quick deployment of network slices is possible with better management and uti-

lization of resources to fulfill one-type-fits-all philosophy [Vassilaras et al., 2017]. For employing UDCDN on a certain slice, network operators should decide slice functionality and resources, for example, processing, storage, bandwidth resources, etc. Then, the slice request is notified through a specific interface and therefore, embedding a virtual network into the physical network in an efficient way. On this aspect, several algorithmic considerations are given in [Vassilaras et al., 2017].

To the extent of my knowledge, this is the first work proposing such a system architecture for UDN. However, in [Bor-Yaliniz and Yanikomeroglu, 2016], authors envision a multi-tier drone cell network with terrestrial HetNets, where they focus on proposing a drone-cell management framework benefiting from network function virtualization and cloud computing with potential advantages and challenges. This is different from the vision for UDN since a multi-tier network is not considered and also *on-demand* UDN formation was emphasized. Also, aspects such as health monitoring and autonomous control of UDCDN were addressed here.

The rest of the chapter is organized as follows: first, the major challenges and benefits for deploying UDCDN are presented, followed by a description of its system architecture. Then, a brief discussion on drone control by means of LTE and its WSN based health-monitoring is provided. Furthermore, a discussion on the appropriate fronthauling and backhauling technologies is given. Finally, simulation results are used to illustrate the coverage analysis for the drone-mounted base stations and then final concluding remarks are presented.

4.2 Proposed System Architecture

A HetNets based on drone cells is proposed, constituting the UDN, where microcells are formed by low power terrestrial base stations and macrocells are formed by high power terrestrial base station, for providing cellular coverage to the mobile users as shown in Fig. 4.1. The drone Radio Remote Head (RRH), or ABS, connects various parts of the city, where high traffic intensity is observed. The macro RRH covers a large part of the city with the macrocell overlap with the drone cell. The microcells are also integrated to support the density of user environment, as in the present cellular architecture. The size of the drone cell can be in the range from the femtocell to picocell as shown by simulation results. This distribution in a HetNet with overlap in microcell and macrocell leads to unequal distribution of radio resource among the users. However, this issue for a terrestrial UDN can be solved with the use of UDCDN, as explained in upcoming sections.

Each UDCDN cluster is supported by an aerial gateway for health monitoring of the drone network using Mobile Edge Computing (MEC). The vast traffic information pattern managed by a cluster of ABS, micro base station, and macro base station, are processed and stored partly in the local databases of their edge cloud servers and partly by virtualized Base Band Unit (BBU) pool hosted in the Central Offices (CO) in metro segments. The information from these databases is one of the driving conditions in the ABS trajectory planning and autonomous deployment of higher numbers towards the city area to manage high traffic overload. Moreover, two interfaces are needed to connect drones with operator orchestrators - X2 and S1 [Peng et al., 2016]. X2 will be present between drone RRH for handover and coordination schemes, while S1 are needed between BBU and the core network. Using the NFV technology, the BBU pool in CO can also host the virtual network functions (VNF), which can reconfigure the network depending on the users and network operators' requirements. VNF can also run as virtual machines (VM) deployed on Commercial-Of-The-Shelf servers in data centers, thus enabling better use of network resources and increasing network scalability and flexibility. The VMs can be scaled according to drones added or removed from the network based on the data traffic using different scaling methods, such as dynamic memory and core scaling, virtual memory streaming, cost-aware scaling, etc. This architecture is on-demand with the deployment of a dense network in real time only when it is needed, depending on the feedback obtained from the cloud-stored database. Therefore, it provides several benefits over the proposed terrestrial UDNs due to several challenges that need to be taken care off such as site location and acquisition, energy expenditure, backhauling, etc. [Nok, b, Yang et al., 2017a]. The trajectory planning of the drone depends on several factors such as information on the traffic intensity in different cells, primarily requiring UDCDN formation, collision avoidance with surrounding infrastructure and other drones, remaining power for flight and transmission and health of on-board integrated circuits and devices. This challenging problem will be addressed in a section below.

Due to limited availability of spectrum, it was proposed to use LTE-Unlicensed spectrum at 2.4 GHz and 5 GHz for ABS, as is used by WiFi and Bluetooth devices. Since the adaptive nature of the architecture, it is not always mandatory to form a dense network, but only when there is a huge traffic demand in certain areas of the city as happens, for example, in concert zones, sports stadiums, public rally etc. In such scenarios, a large mass of users' requests for a huge amount of data at high data rates. Due to this flexibility, the ABS should operate at lower frequency bands in order

to cover a vast cell area flying at an optimal height, as it will be shown in the simulation results. However, when there is the need to form a dense network, the altitude can be decreased to reduce the transmitter-receiver distance to increase the data rate.

4.3 Challenges and Benefits

The introduction of UDCDN to HetNets has certain limitations and advantages as discussed below. Hence, with appropriate trade-offs, UDCDN demonstrates to be an upgrade in technology as compared to UDN. In following subsections, list of the challenges and benefits associated with UDCDNs are provided.

4.3.1 Benefits of UDCDNs

Dynamic Cell Coverage Area

An ABS is capable of dynamically change the area of coverage depending on its altitude and transmission power as shown in [Cileo et al., 2017]. Due to this possibility, UDCDN cell coverage ranges from 10 m (femtocell) to 300 m (picocell), making UDCDN a suitable substitute for UDN. Therefore, the density of the network can be flexibly changed. In the simulations section, the dependence of ABS altitude to the cell coverage was analyzed.

Energy efficiency

The energy budget of a drone is contributed by the maintenance of the flight status, on-board processing, and the power required by the base station to transmit to users, for downlink, and also for fronthaul and backhaul. The power consumed by the drone for flight and on-board processing is assumed to be constant in this chapter. However, the power utilized by a drone to fly depends on standard lift, drag, and propulsion models when the assumption of a quasi-static equilibrium flight is done. For analysis, the dependence of power consumption was kept only on the power transmitted by the ABS. As it was shown in the simulation results in Chap. 3, the cell coverage depends on the power transmitted by the ABS. Due to the adaptable and flexible behavior of UDCDN, high power consumption is only needed when deploying a dense network. Meanwhile, a lower power is maintained in flying and transmission. In order to meet the demands of power, a continuous renewable source is required, therefore several solar-powered drone flight tests have been conducted by Facebook (Project Aquila), Google (Project Loon), and many others fulfill the requirements. But natural resources like

sunlight, may be inefficient due to its irregular and unforeseeable nature, therefore a fly-and-recharge strategy can also be implemented for meeting power requirements via RF energy harvesting or another far field energy source. In this domain, simultaneous wireless information and power transfer (SWIPT) is emerging as a promising energy harvesting technology, through which ABS can transfer power and information simultaneously [Jayakody et al., 2018], among neighboring ABS and ground users with significant gains in spectral efficiency, time delay and energy consumption. Since wireless power transfer was proposed for near-field regions due to health concerns of users by electromagnetic radiation (EM), drones have the leverage to fly near to the EM source.

Easy Deployment

On-demand deployment and flexibility of this system define the real-time formation of UDCDN based on the feedback requirement of data rate obtained from the cloud database, depending on the amount of traffic generated. This on-demand deployment leads to the formation of an adequate number of dense networks, as per the requirement to avoid the use of continuous radio resources and energy of the drone. This reduces the overall cost of the system as an on-demand use of radio resource is a form of dynamic spectrum management, using the wireless channels only upon the requirement.

Site Location

The deployment of a terrestrial base station has been a topic of discussion for UDNs. The macrocell base station deployment is based on maximizing the cell coverage area and obtaining a higher throughput [Nok, b]. For small cell networks, instead of higher site availability due to low antenna heights, still is a challenging task because of the geo-location of network traffic and types of devices used [Nok, b]. This can be overcome by UDCDN due to its on-demand deployment and flying potential.

Cost

The cost of on-demand UDCDN is much lower than terrestrial UDN. This is because of the lower cost of solar cells, UAV and sensors, which collectively reduce the cost of the ABS as compared to the terrestrial base stations. Also, due to the use of solar-powered drones, power costs will reduce drastically. This is beneficial for mobile operators because it reduces the TCO of the cells [Nok, b] and of other factors such as site location and

site acquisition, which therefore do not constitute a problem due to the vast availability of the airspace for this system.

Data Offloading

To manage a large amount of data traffic, data offloading to WiFi band [Bennis et al., 2013] or D2D radio links [Andreev et al., 2014] are required to improve the performance of the system. These data offloading techniques reduce the traffic load on the network without any additional cost on the infrastructure. Also, since drone cells operate in the low-frequency bands, as proposed here, they might interfere with the unlicensed WiFi band. Therefore, in order to avoid this interference, a mitigation technique was needed to be employed. Delay in data traffic takes place during offloading, which enforces the requirement of dynamic data offloading techniques with delay-tolerant data to offload over WiFi or D2D and delay-intolerant remaining on the cellular network.

Payload Considerations

Several sensors, circuit boards and batteries are required to operate the drone. Apart from these, base station and solar cells also add to the payload weight in this system. The requirement is to minimize the payload weight for efficient system design. The payload weight depends on the size of the drone as per the guidelines of respective aviation authority in each country.

Apart from these challenges, there are several challenges arising from the use of UDCDNs.

4.3.2 Challenges of UDCDNs

Interference Management

ABS has a small coverage area in the order of femtocell. Due to a limited coverage area, there is a probability of cell overlapping, which causes co-channel interference (CCI) for the A2G links, between the user and the ABS, and wireless backhaul/fronthaul. Also, a high Doppler shift is observed due to the mobility of ABS, which leads to inter-carrier interference (ICI) and therefore, decreases the capacity. The problem of CCI can be solved by optimizing the trajectory of the drone to minimize the overlap between cells. However, for ICI, several interference mitigation techniques like receiver windowing and ICI self-cancellation exist.

Drone Flight Standardization

For commercial use of drones, standard regulations have been developed by aviation regulatory authorities in each country, with the goal of minimizing the possible risk and damage to other aircrafts, people, and property on the ground. The International Civil Aviation Organization (ICAO), a United Nations agency, is responsible for deploying these standards in 191 member countries worldwide. However, each country sets up its own standard based on these guidelines. For example, Federal Aviation Administration (FAA) regularizes standards in the USA and European Aviation Safety Agency (EASA) in Europe. Standardization of rules is a stringent and long process, which ensures complete safety for the people and the public property.

Drone health monitoring and position monitoring

For the development of this system, ensuring the safety of the people is of primary importance. Therefore, continuous operation and position monitoring of the drone is needed. This can be accomplished by placing wireless sensors on the drone for its structural and operational component monitoring such as rotor torque, vibration, crosswind force or gust force etc, as discussed in later section. Position monitoring can be done by implying advanced global positioning and navigation systems.

Drone trajectory planning with group optimization

The trajectory of the drone depends on various factors with the primary one being the geographical region of the city, which generates the maximum data traffic. The drone detects this parameter in the real-time from the cloud database and establishes its waypoints, autonomously. However, there are certain other factors which would affect the drone trajectory, such as wind and gust force, infrastructure planning, minimizing energy constraint, optimal path with collision avoidance from buildings, and surrounding drones. This trajectory can be modeled using genetic algorithms and swarm optimization techniques. Solutions are also required for cooperative rendezvous and mutual coordination between multiple aerial vehicles.

Handover Management

Handover is one of the crucial concerns with the UDNs. Efficient strategies are required to regulate the handovers without excessive signaling overhead and latency because of more users near user-site Access Points (APs). Further, with the advent of UDCDN, a new handover scenario may arise between the users to drones and the infrastructure to drone. Since UAVs

provides better coverage, it is easier to consider existing LTE handover standards for managing handoffs that arise from the high mobility of users. Software Defined Networking (SDN) can be an efficient solution to handle handovers in UDCDN, allowing for efficient control, management, and cooperation between the UAVs and the users. Also, there is a major requirement for handling vertical handovers if one considers the differences in the technologies used by the underlying infrastructure. For handover management between the infrastructure and drone, successful techniques have been performed by Qualcomm in their practical tests using high and low power terrestrial base station by forming macrocell and microcells, respectively, as shown in Fig. 4.1.

Adaptive distribution of radio resource

As mentioned in the previous section, due to cell overlapping in HetNet, a radio resource is non-uniformly exploited by the users. The reason is when a uniform distribution of the users in the entire area of operation is assumed, only a few users will lie under the terrestrial UDN. They have access to maximum resources while most of the users don't. This problem is solved in the proposed architecture since the deployment of a number of ABS towards an area depends on traffic intensity obtained from a database in the cloud.

4.4 Aerial Base Station Control over LTE

For maintaining UDCDN, there is the requirement of controlling a swarm of ABS via LTE network. However, fast maneuvering of the drones is needed to work in highly populated urban environments for quick UDCDN deployment and collision avoidance. To execute this, ultra-low latency in the order of 1 ms or less and ultra-high reliability communications are needed, which can be achieved through recent advances in 5G PHY and NET layer design. New 5G waveforms such as GFDM, UFMC and FBMC along with numerologies and frame structure are designed in PHY [Lien et al., 2017]. In NET layer, the current progress thrives towards the development of FC-RAN [Peng et al., 2016] for low latency applications where C-RAN consists of global centralized communication and control cloud which facilitates resource pooling, layer inter-working, capacity and scalability by exploiting data-centric processing for both centralized and distributed RAN architectures, while F-RAN consists of distributed communication and storage cloud which comprises of devices at the network edge. Also, trajectory planning of ABS in the city has much

importance as explained in previous sections. Several field tests have been performed by Qualcomm and China mobile recently for coverage, signal strength, throughput, and latency. Successful handovers and strong signal strength were observed, making the entire system suitable for deployment in the market.

4.5 Aerial Base Station Health Monitoring Via Wireless Sensor Network

The ABS on-board equipment and structure monitoring are of extreme importance for any mobile operator to avoid ABS accidents and jeopardize human lives. However, to the best of my knowledge, there is no existing literature addressing these aspects. Here, a simple IoT based architecture to monitor the health of each ABS in the city, is proposed. Also, it was proposed to deploy a UAV as an aerial gateway, with a sole function of collecting the information from the various sensors present on the ABSs, performing the task of data aggregation and forwarding this data towards the cloud via LTE network established by other ABS, micro base station or the macro base station, as shown in Fig. 4.1. However, there is a possibility of processing the data in the cloud using MEC algorithms rather than local processing on-boards ABS to conserve power of the drone. It is required to identify the data rate from the sensors in order to prioritize the information to be computed using MEC. For high data rate sensors, MEC is recommended, while for low data rate sensors, on-board processing can be implemented. Here, a similar study present in the literature [Hall, 2016] was mentioned, where UAVs have been used as an IoT platform, creating the Internet of Drones (IoD).

4.6 Fronthauling and Backhauling

Fronthauling is one of the major design challenges for this system [Zhang et al., 2016, Siddique et al., 2015]. Many network functions, such as a cooperative management of CCI and smooth handover call for the need of efficient fronthauling between the BBU pool and drone RRH, are needed. However, few challenges that need to be addressed are as follows:

- Adaptive deployment of UDCDN makes fronthauling complex.
- Higher fronthauling capacity is needed when UDCDN is deployed.
- Wired fronthaul solutions based on the optical fiber cannot be used for such a system. Therefore, wireless options have to be explored.

There is an existing rich literature on the fronthaul and backhaul of 5G systems [Zhang et al., 2016, Siddique et al., 2015]. However, there is limited research available for C-RAN based UDN [Zhang et al., 2016]. For UDCDN, it was proposed to use millimeter-wave (mm-Wave) and free space optical (FSO) as potential fronthaul technologies. The factors influencing mm-Wave are as follows:

- There is a spectrum scarcity in cellular networks. A common range of frequencies used in the LTE goes from 699 MHz to 3800 MHz. They can be used in combination with other telecom generation technologies such as HSPA and GSM. The scarcity of spectrum resources led researchers to move towards mm-Wave spectrum ranging from 30 GHz to 300 GHz. Among these high-frequency bands, 60 GHz is an unlicensed band with 9 GHz bandwidth that has attracted researchers to use this band. Several channel modeling studies have been done by research groups such as 5G mm-Wave channel model alliance, NYU Wireless, MMmagic, Miweba, etc.
- Due to the extremely low wavelength of mm-Wave frequency bands, there is high attenuation due to atmospheric effects in the mm-Wave transmission. Therefore, mm-Wave communication is preferred over short distances and in LOS conditions. As low altitude ABS was adopted for UDN, both of these conditions are met for the proposed architecture while deploying an on-demand UDN.

Similarly, a few factors that influence the use of FSO are as follows:

- Wide bandwidth, which results in higher fronthauling capacity.
- Exploring the frequency band above 300 GHz and high directionality of the laser beam leading to better LOS conditions.

For backhauling, it is possible to use both wired and wireless solutions for this system, similar to the terrestrial UDN. To reduce the TCO, including capital expenditure (CAPEX) and operational expenditure (OPEX) of network operators, reconfigurable network functions using NFV for S1 and X2 interfaces are needed in the core segments, depending on high traffic periods, delay and capacity constraints, on-demand quick deployment, link failures and dynamic FC-RAN topology reconfiguration. Using UDCDN, such network functions can be avoided through low-complex management of the drone network. However, still to guarantee above restrictive constraints and service specific parameters in Service Level Agreements such as quality of service and minimum bitrate, Customer Virtual Network

reconfiguration [Asensio et al., 2016], can be supported in the core and metro segments of the network. The detailed comparison of fronthauling technologies can be found in [Zhang et al., 2016]. Backhauling, however, does not pose as trivial challenges as compared to fronthauling. Backhauling connections are required to send/receive data from the end user of the UDCDN to/from the core network, respectively, and exchange information among ABS over the X2 interface for smooth handovers, mobility and traffic load management. For backhauling, it is possible to use both wired and wireless solutions for this system, similar to the terrestrial UDN. Various backhauling challenges and solutions for small cells are described in [Siddique et al., 2015].

4.7 Discussion for Dynamic Cell Coverage Analysis by Aerial Base Station

Dynamically changing cell coverage area based on ABS height and transmitting power is one of the major benefits of UDCDN. This allows the mobile operator to control the density of UDCDN by deploying a low number of drones to provide the same throughput to the users and also avoid overlapping of the cells to avoid interference. Here, the simulation results obtained from a commercial software of ray tracing, Wireless InSite as in Chap. 2 are addressed. The simulation snapshot of ray tracing is shown in Fig. 2.6. As described in previous chapters, three generalized scenarios were simulated: Suburban, Urban, and Urban High Rise, developed on a CAD, 3DS Max, based on the ITU-R parameters for designing the layout of a city.

The cell coverage was obtained at different ABS altitudes for different received power thresholds and an optimal altitude was found for a specific transmission power of ABS. This argued to the fact that cell coverage by ABS depends primarily on the propagation environment, its altitude, elevation angle with respect to UEs and transmission power and furthermore, there are other factors such as interference from nearing base stations, ABS antenna orientation, ABS trajectory etc. However, a single drone scenario is being discussed here. Therefore, by modifying the above mentioned parameters, ABS cell coverage can be varied depending, whether the flash crowds demands for higher data. Thereby, according to this information obtained from the cloud, ABS cell coverage can be modified. Thus by varying the cell coverage of many ABS, ABS network can be managed by the mobile operator with higher performance and satisfying the needs of the ground users. Also, it is expected to have a high density of users in

an urban environment, in order to demonstrate the $on - demand$ quality of the system, but a suburban environment can also be considered where an impulsive demand for a higher data rate and volume is anticipated (via rural events, rallies, and public gatherings).

4.8 Conclusion

We have presented an on-demand and flexible UDCDN, deployed in a real-time based communication traffic feedback from various areas of a city. An architecture is proposed for this system by introducing the challenges and benefits for its implementation followed by a detailed discussion. We then highlighted the operational monitoring of the drone as one the key factors for this architecture. Also, the control of the drone using an LTE base station is discussed together with fronthauling and backhauling technologies for this system. Finally, we have discussed the simulation results for dynamic cell coverage area variation with height and transmitting power of the aerial base station. This is effective to avoid and manage cell overlapping and mitigate interference. In our future work, we plan to integrate UDCDN with terrestrial network operating at sub-6 GHz and millimeter-wave bands with main focus on inter-cell and multi-tier interference, spectral and energy efficiency with drone trajectory optimization and handover performance.

CHAPTER 5

Low Latency-Enabled "LTE-Compatible" Aerial Base Station: Performance and Trade-off

THE use of UAVs as ABSs has recently received high attention in academia and industry for fulfilling communication traffic growth in 5G NR. In this chapter, the focus is that of obtaining the optimal altitude of an ABS using two criteria - maximum cell coverage area and minimum SER, implemented on a probabilistic A2G channel model, described in Chap. 2 for LAPs via simulations on a commercial ray tracing software, for scenarios such as Suburban, Urban and Urban High Rise. A system model was presented based on GFDM used for SER analysis in a time-frequency grid compatible with LTE by implementing parameters for uRLLC of 5G physical layer towards low latency. Also, the received power probability distributions of the ground users and power delay profile at optimal ABS altitude, will be provided. Further, the variation of optimal altitude with cell area is demonstrated. As it is well known, flexible pulse shaping is the main feature of GFDM system that is achieved by properly choosing the pulse shaping filters. In this chapter, the impact

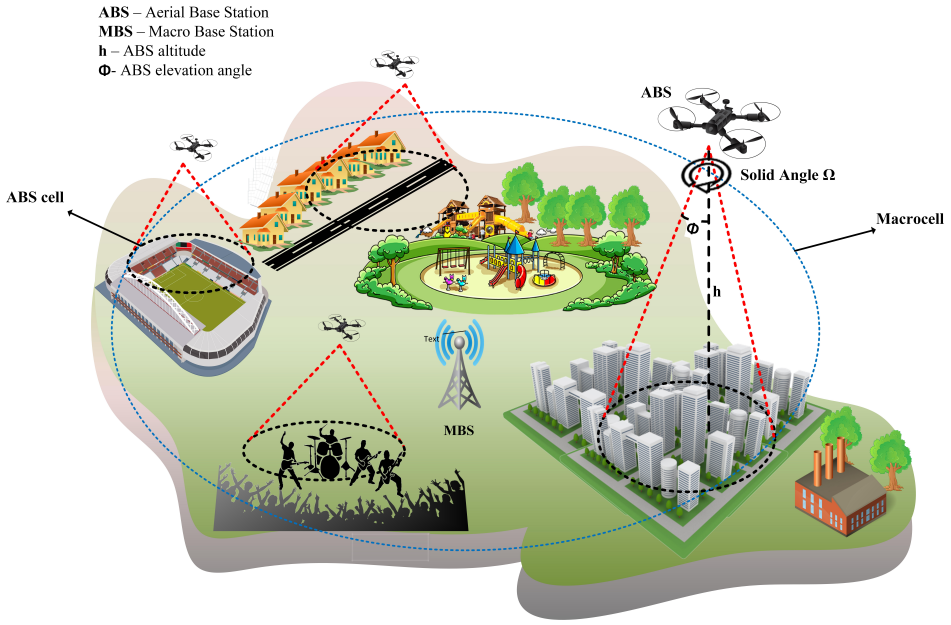

Figure 5.1: *Aerial Base Station network architecture.*

of "Better than Nyquist" pulses on the GFDM system is also analyzed and SER performance was evaluated. From the proposed results, significant improvement is clearly visible as compared to Nyquist pulse.

5.1 Introduction

Due to the recent advances in wireless communications, UAVs operating as low altitude ABSs, integrated with current cellular architecture to provide high speed data to ground users, as shown in Fig 5.1, has recently gained a lot of attention in telecommunication industry and research. The technology still being at its infancy, has a lot of research literature and experimental measurements available for channel modeling and characterization, cell coverage, optimal ABS placement etc. Some of the recent literature on these aspects were reviewed. An overview of UAV-aided wireless communications, with three use cases: UAV-aided coverage, UAV-aided relaying, and UAV-aided information dissemination is provided in [Zeng et al., 2016]. In [Chen et al., 2017], the problem of pro-active deployment of cache-enabled UAVs for optimizing the Quality of Experience (QoE) of wireless devices in a CRAN is studied. Apart from academic research, industrial experiments have also been performed by various companies to

Table 5.1: *Power Delay Profile of received power at optimal altitude*

Suburban		Urban		Urban High Rise	
Delay (in ns)	Power (in dB)	Delay (in ns)	Power (in dB)	Delay (in ns)	Power (in dB)
2100	-66.44	1450	-23.51	2023	151.09
2530	-51.51	1496	14.35	2131	111.76
2595	25.67	1645	6.98	2324	80.49
2826	-19.77	1703	-56.25	2429	76.64
2836	-57.51	1752	-38.87	2732	92.23
3085	-31.31	1784	-71.12	2745	135.52
3390	22.59	1935	-56.66	2916	115.11
3463	28.87	2055	-41.83	3027	112.40
3870	-48.47	2191	-39.72	3105	82.96
3951	-34.55	2346	-63.87	3138	79.16

provide cellular and internet connectivity through aerial platforms. Qualcomm was able to demonstrate smooth handovers with zero link failures while autonomous drone control over LTE network [Qua,]. Facebook Aquila project conducted successful flights with solar powered drones to provide internet connectivity in suburban areas [Fac,]. Also, Nokia has been working on the project of "Connected UAVs" working together in a cooperation which has multiple use cases in smart cities, transportation, search and rescue, etc [Nok, a]. Thus far, some studies has also been done for ABSs cell coverage, cell association and A2G channel modeling. In [Mozaffari et al., 2017], the authors propose a novel framework for optimal cell association for ABSs based cellular network using optimal transport theory. Similarly, [Lyu et al., 2017] proposes a polynomial-time algorithm to find minimum number of ABS to cover a given set of mobile users. Also, [Sharma et al., 2016] investigates on the user demand based ABS assignment over an area based on a neural cost function. However, research on information transmission with different modulation schemes and PHY numerology in UAV is limited. In [Wu et al., 2005] performance of IEEE 802.11a compatible Orthogonal Frequency Division Multiplexing (OFDM) for UAV downlink with large doppler shift and inter-carrier interference is analyzed. In [Blümm et al., 2012], the authors work upon the waveform design on OFDM with customizable modulation parameters. The implementation on a self-designed hybrid software defined radio (SDR) platform is discussed, which consists of an FPGA (Xilinx Virtex 5) and a GPP (Intel Atom), for a UAV acting as a relay between an unmanned ground vehicle and a ground control station. The main contributions of this chapter are given in Chap. 1.

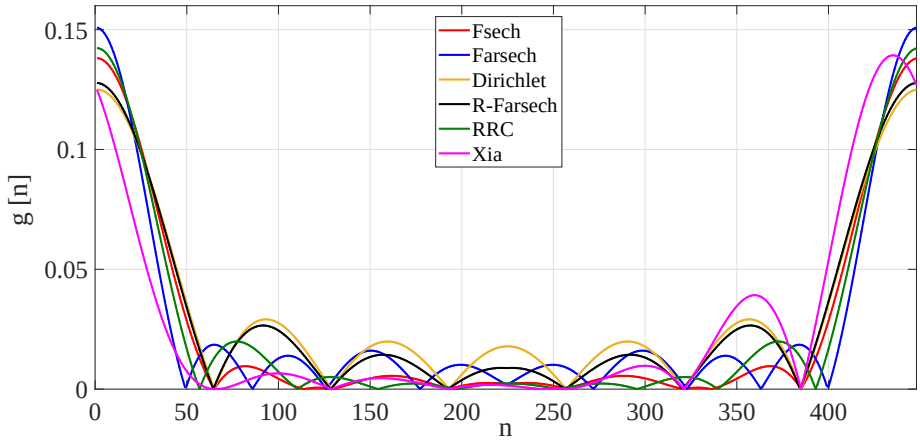

Figure 5.2: *Frequency response of the employed pulse shaping filters.*

The rest of the chapter is organized as follows. In Sec. 5.2, the GFDM system model for LAP A2G channel model was addressed. Sec. 5.3, shows the ray tracing simulations for moving ABS. In Sec. 5.4, a trade-off analysis is performed to obtain optimal ABS altitude for maximum cell coverage and minimum SER. Later, analytical expression of optimal altitude, power delay profile, received power distribution parameters of ground receivers and variation of optimal altitude with cell radius were also provided. Further, in Sec. 5.5 various pulse shaping filters were reported and results for obtaining minimum SER in different environments were presented. To the best of my knowledge, this chapter presents a unique study of performance analysis for ABS with different optimal altitude determination criterion, which has not been addressed in the existing literature.

5.2 System Model

As is well known, GFDM is one of the multi-carrier modulation scheme under consideration for the future cellular networks. Due to its low out-of-band (OOB) radiation obtained by circular pulse shaping filter, which allow to improve the spectral efficiency in short data burst transmission with ultra low latency scenario and its backward compatibility with OFDM and SC-FDMA, GFDM was implemented for the simulations. According to the GFDM transmission scheme given in [Michailow et al., 2014], the high data-rate stream in vector $\mathbf{d}$ contains N elements, which can be further decomposed into low symbol-rate streams of K sub-carriers with M sub-symbols, by inserting $\mathbf{d}$ in the GFDM modulator. As shown in Fig. 5.3, the

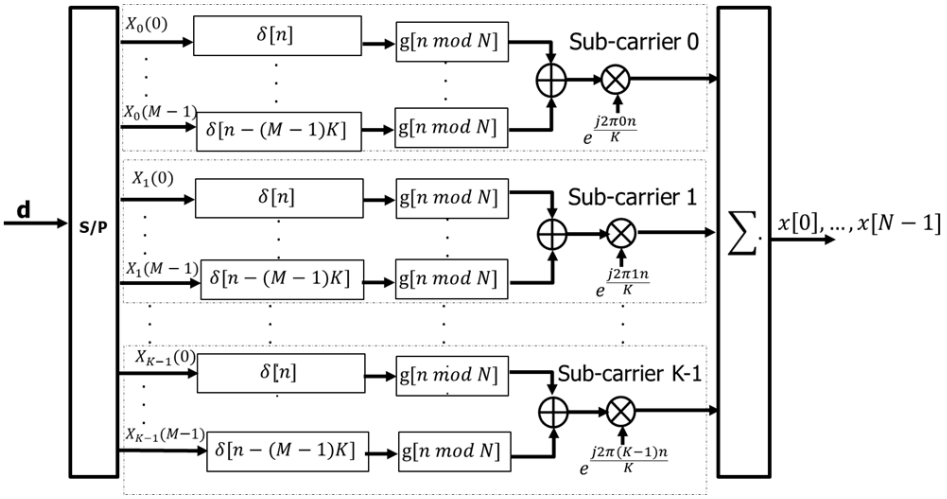

Figure 5.3: *GFDM modulator block diagram [Michailow et al., 2014].*

output of the GFDM modulator [Michailow et al., 2014] is given as

$$\mathbf{d}=\left[(\boldsymbol{d}_0)^T,(\mathbf{d}_1)^T,\ldots\ldots,(\mathbf{d}_{K-1})^T\right]^T,$$

where

$$\mathbf{d}_k=[d_{k,0},\, d_{k,1},\ldots\ldots,d_{k,M-1}]^T,$$

where $d_{k,m}$ is the *m*-th sub-symbol transmitted on k-th sub-carrier of the block and $(\cdot)^T$ is the transpose operator. The total number of symbols are $N = KM$. The time-duration of each data block $\mathbf{d}_k$ is MT_s and the sub-carrier spacing is equal to $1/T_s$, where T_s is sub-symbol duration.

With reference to Fig. 5.3, the transmitted signal can be expressed as

$$x\,[n]=\sum_{k=0}^{K-1}\sum_{m=0}^{M-1}d_{k,m}g_{k,m}\,[n],n=0,1,\ldots\ldots KM-1. \qquad (5.1)$$

being $d_{k,m}$ the mth complex data symbol transmitted on the kth sub-carrier and $g_{k,m}$ is the corresponding pulse shaping filter

$$g_{k,m}\,[n]=g\,[(n-mK)\bmod N]\,e^{\frac{-\mathrm{j}2\pi\mathrm{kn}}{K}},$$

being $g\,[n]$ the prototype filter, $\bmod$ denotes the modulo *N* operation which makes $g_{k,m}\,[n]$ a circularly shifted version of $g_{k,0}\,[n]$, the exponential function performs the frequency shifting operation and *n* is the sampling index.

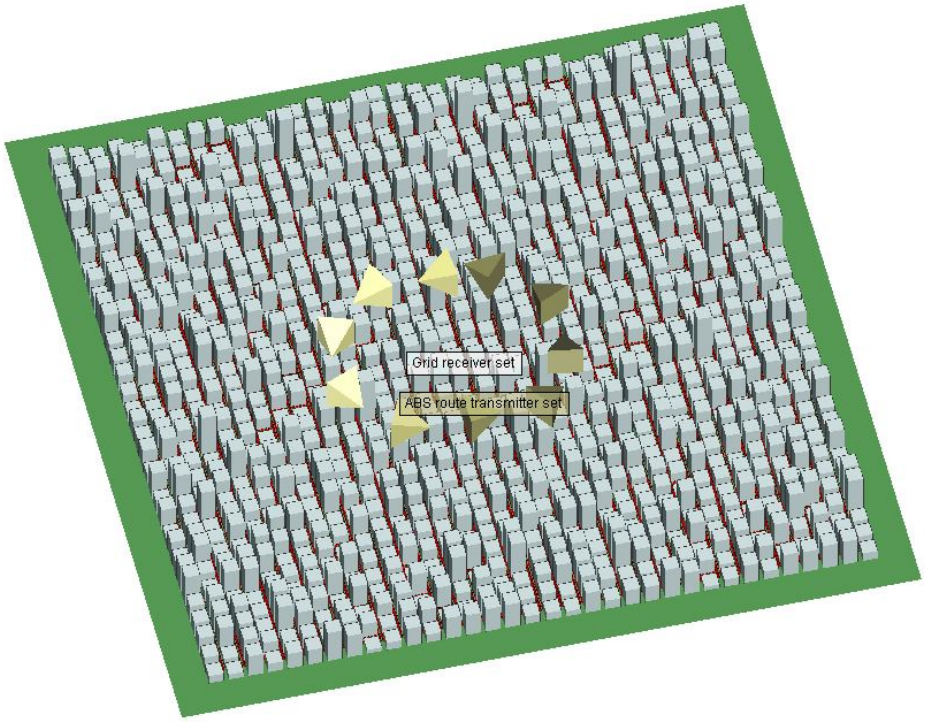

Figure 5.4: *Ray Tracing setup with moving ABS.*

The vector representation of (5.1) can be written by collecting the N samples of $g_{k,m}[n]$ in the matrix form as

$$\mathbf{x} = \mathbf{A}\,\mathbf{d}, \tag{5.2}$$

where

$$\mathbf{x} = [x[0], x[1], \cdots, x[N-1]]^T$$

and

$$\mathbf{A} = \left[\boldsymbol{g}_{0,0} \cdots \boldsymbol{g}_{K-1,0} \cdot \boldsymbol{g}_{0,1} \cdot \boldsymbol{g}_{K-1,1} \boldsymbol{g}_{0,M-1} \cdots \cdot \boldsymbol{g}_{K-1,M-1}\right].$$

Before transmitting over the A2G channel, a cyclic prefix (CP) of length N_{CP} is added to create the vector given as

$$\widehat{\boldsymbol{x}} = \left[\mathbf{x}\,(N - N_{CP} : N-1)^T, \mathbf{x}^T\right]^T. \tag{5.3}$$

The length of CP is taken to be the same as the number of channel taps in the simulations, *i.e*, 10 as shown in Table 5.1. Transmission over multipath A2G probabilistic channel with PL and large scale fading effects can be

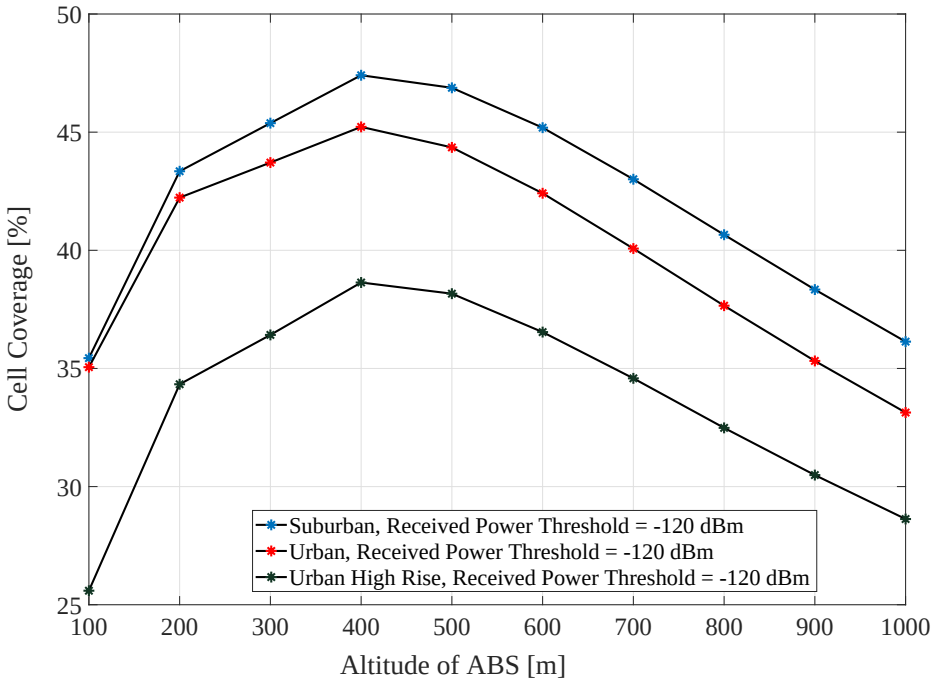

Figure 5.5: *Cell coverage variation with altitude of ABS for trade-off analysis.*

shown as

$$\mathrm{PL}_{\mathrm{LoS}}(\mathbf{d})[\mathrm{dB}]=20\log_{10}\left(\frac{4\pi\mathbf{d_0}}{\lambda}\right)+10\eta_{\mathrm{LoS}}\log_{10}(\mathbf{d})+X_{\sigma,\mathrm{LoS}}, \tag{5.4}$$

$$\mathrm{PL}_{\mathrm{NLoS}}(\mathbf{d})[\mathrm{dB}]=20\log_{10}\left(\frac{4\pi\mathbf{d_0}}{\lambda}\right)+10\eta_{\mathrm{NLoS}}\log_{10}(\mathbf{d})+X_{\sigma,\mathrm{NLoS}}, \tag{5.5}$$

where LoS and NLoS represent line of sight and non-LoS, respectively, with PL denoting the PL, η the PLE, $\mathbf{d}$ is the distance between ABS and ground receiver with $\mathbf{d_0}$ be the reference distance, here assumed as $\mathbf{d_0} = 1$. X_σ is the log-normal random variable with standard deviation σ which includes the large scale fading effects. The average PL model can be obtained as

$$\mathrm{PL}(d)[\mathrm{dB}] = \mathbb{P}_{\mathrm{LoS}} \cdot \mathrm{PL}_{\mathrm{LoS}}(d) + (1 - \mathbb{P}_{\mathrm{LoS}}) \cdot \mathrm{PL}_{\mathrm{NLoS}}(d), \tag{5.6}$$

where $\mathbb{P}_{\mathrm{LoS}}$ is the probability to have a LoS link [Al-Hourani et al., 2014b] which is modeled as

$$\mathbb{P}_{\mathrm{LoS}} = \frac{1}{1 + p\exp(-q[\phi - p])} \tag{5.7}$$

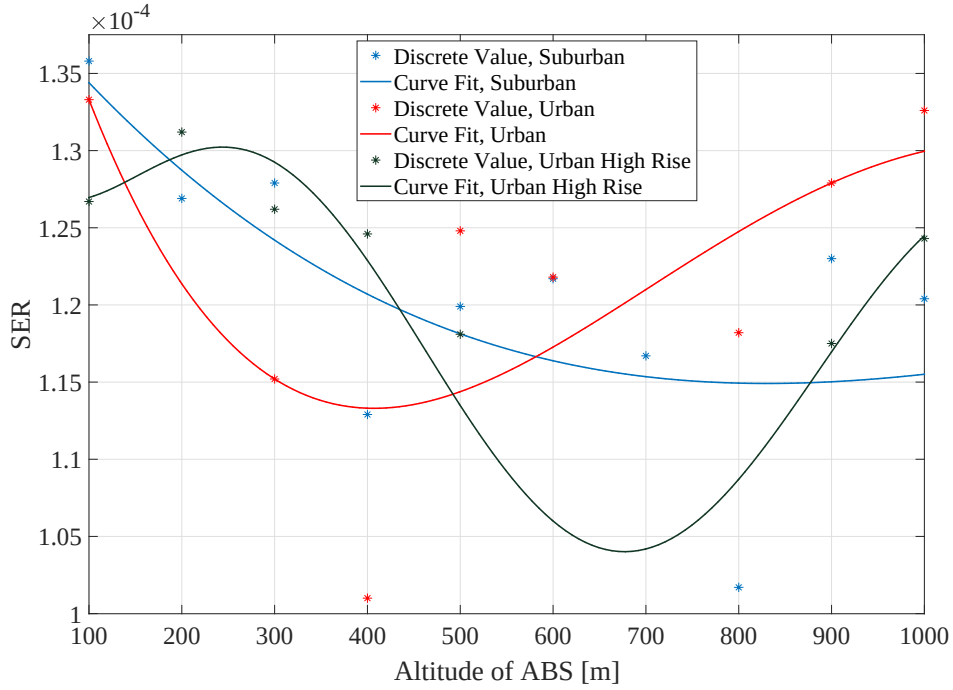

Figure 5.6: *SER variation with altitude of ABS for trade-off analysis.*

where p and q are parameters of the LoS curve, depending on the environment planning parameters, α, β and γ as given in Sec. 5.3. However, this model does not include the small scale fading effects $h\,[n]$, which are usually modeled as Rician for A2G channel [Khawaja et al., 2018]. $h\,[n]$ can be obtained from stochastic approach through empirical data, geometric analysis and simulations [Khawaja et al., 2018]. Here the map-based approach was used to obtain the data and model $h\,[n]$ as

$$h\,[n] = \sum_{k=0}^{L-1} h_k \delta\,[n-k]\,, \tag{5.8}$$

where h_k is the Rician faded k-th complex coefficient is obtained from ray tracing data as PG $= -(\mathrm{PL}_{\mathrm{tot}}(d)[\mathrm{dB}] - (\mathbb{P}_{\mathrm{LoS}} \cdot \mathrm{PL}_{\mathrm{LoS}}(d) + (1 - \mathbb{P}_{\mathrm{LoS}}) \cdot \mathrm{PL}_{\mathrm{NLoS}}(d)))$ and L denotes the number of channel taps. PG represents the path gain of each multipath component or channel tap and $\mathrm{PL}_{\mathrm{tot}}(d)[\mathrm{dB}]$ is the total PL including both large and small scale fading effects. At the receiver side of the GFDM, it was considered that the length of CP must be higher than the maximum delay spread of the multipath channel, i.e, $N_{CP} \geq L$. Under these assumptions, the received signal vector after re-

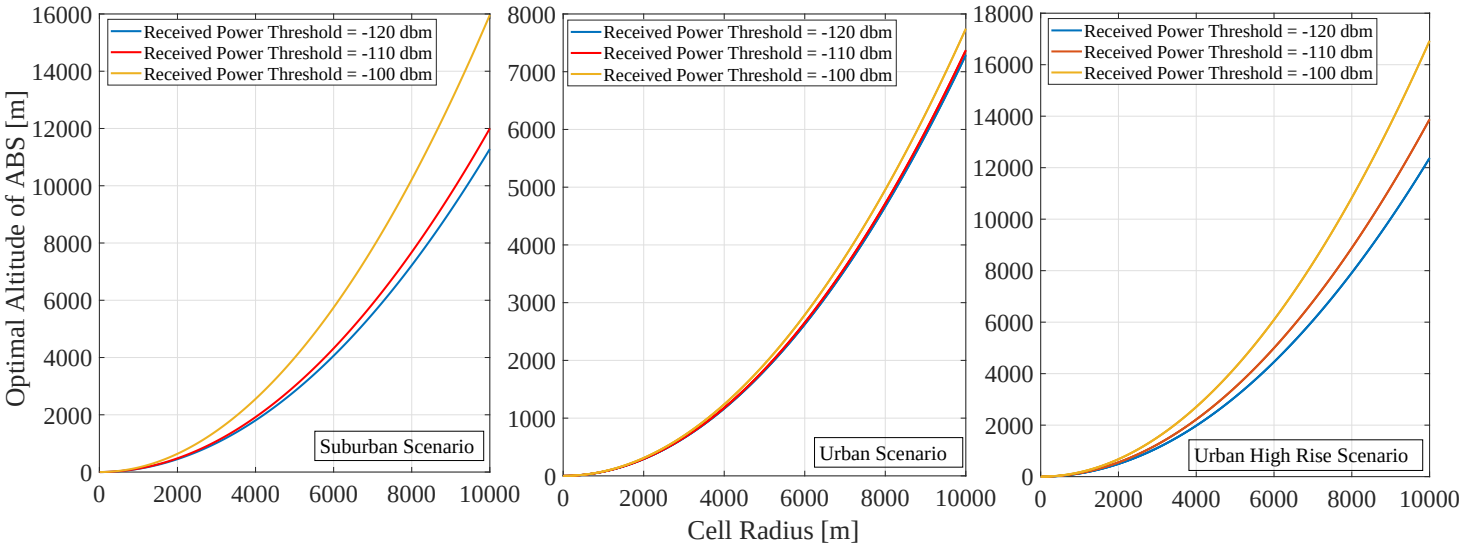

Figure 5.7: *Optimal ABS altitude variation with cell radius.*

moval of the CP is written as

$$\mathbf{y} = \mathbf{H}\mathbf{x} + \mathbf{w}, \tag{5.9}$$

where $\mathbf{H}$ is circulant matrix of size $N \times N$ based on the $\mathbf{h}$, where $\mathbf{h}$ is $(N \times 1)$ vector whose first L elements represent impulse response the channel and remaining $N-L$ elements are zero and $\mathbf{w}$ is noise vector of size $N \times 1$ in which each entry is an i.i.d. zero mean complex Gaussian random variable with variance σ_w^2. Here, Matched Filter (MF) receiver is considered. By following the equalized signal in time domain using the modulator matrix $\boldsymbol{B}_{MF} = (\boldsymbol{A}^H \boldsymbol{A})^{-1} \boldsymbol{A}^H$, the estimated data vector is

$$\hat{d} = \boldsymbol{B}_{MF} \boldsymbol{y}_{eq} = \boldsymbol{B}_{MF} \boldsymbol{A} \boldsymbol{d} + \boldsymbol{B}_{MF} \boldsymbol{H}^{-1} w \tag{5.10}$$

where $\boldsymbol{y}_{eq}$ is the equalized signal in time-domain and MF receiver maximizes the SNR per sub-carrier.

The pulse shaping filter $g[n]$ in the GFDM system affects the spectral efficiency and it performance. Here, "Better than Nyquist (BTN)" pulse shaping filters were used as shown in Fig. 5.2. A standard approach for choosing the pulse shaping filter is to sample a continuous-time impulse

Table 5.2: *Parameters for GFDM simulation with LTE grid [Gaspar et al., 2014]*

Parameter	Normal mode
Subframe duration	1 ms or 30.720 samples
GFDM symbol duration	66.67 μs or 2048 samples
Subsymbol duration	4.17 μs or 128 samples
Subcarrier spacing	240 KHz
Subcarrier bandwidth	240 KHz
Sampling freq. (clock)	30.72 MHz
Subcarrier spacing factor N	128
Subsymbol spacing K	128
active subcarriers N_{on}	75
Subsymbols per GFDM symbol M	15
GFDM symbols per subframe	15
CP length	4.17 μs or 128 samples

response $g(t)$ windowed as

$$g_w(t) = \begin{cases} g_{wdown}(t) & 1 \leq t \leq KT_s \\ g_{wup}(t) & (MK-K)Ts \leq t \leq (MK)T_s \\ 0 & otherwise \end{cases} \tag{5.11}$$

where $g_{wup}(t)$=$g_{pulse}(t)$, $g_{wdown}(t)$=1-$g_{pulse}(t)$ and T_s symbol interval, being $g_{pulse}(t)$ one of the different types of pulse shaping filters reported below. In the results, the impact on the SER performance using BTN pulse shaping filters will be considered.

5.3 Ray Tracing Simulation Setup

Two set of simulations were performed - moving ABS (to include the Doppler effect) and static ABS. For static ABS, it was presented at the center of the snapshot, with approximately 32,500 receivers uniformly spread over the entire environment surface with 5 m spacing from each other as shown in Fig. 2.6. There were no receivers inside buildings, since outdoor propagation was studied to support flash crowds. For moving ABS, a circular trajectory of ABS was given with set of receivers as shown in Fig. 5.4. The remaining configuration of the setup on Wireless InSite was similar as provided in Sec. 2.2.

Table 5.3: *Probability Distribution Parameters of received power at optimal altitude*

Environment	Optimal Altitude [m]	Distribution type	Distribution parameters			
			μ (location)	σ (scale)	ν (degrees of freedom)	k (shape)
Suburban	600	t location-scale	-94.9520	2.5348	1.7666	-
Urban	400	Extreme Value	-75.7450	6.0756	-	-
Urban High Rise	600	Generalized Extreme Value	-95.5724	15.5478	-	-0.5446

5.4 Trade-off analysis for Optimal Altitude of ABS

In this section, the optimum altitude of an ABS was obtained by focusing on two different parameters - minimum SER and maximum ABS cell coverage area. For obtaining the SER, a flexible multi-carrier modulation scheme, GFDM, was used where the sub-carriers are individually pulse-shaped in a block structure of K sub-carriers and M sub-symbols. Further description of this waveform, is provided in Sec. 5.2.

5.4.1 Optimal Altitude for Maximum Cell Coverage by ABS

As given in Chap. 3, the variation of cell coverage with height of ABS is given in Fig. 3.3 where 300-400 m was observed as an optimal altitude for the same ray tracing simulations, in different environments. Here, a generic received power threshold approach was used, where the cell coverage depends on the distance between the ABS and ground users receiving power, greater than the threshold required to maintain connectivity with the ABS. However, such approach is implementable for any power source to define its boundaries. Therefore, a novel equation using a solid angle approach was also reported in Chap. 3, taking into account A2G channel, antenna characteristics, ABS altitude, transmission power and elevation angle with respect to users.

Therefore, on the similar lines as given in Sec. 3.11.1, by replacing x with $\left(\frac{P_{th}-\overline{P}_{RX}(\mathbf{r})}{\sigma}\right)$,

$$Q\left(\frac{P_{th}-\overline{P}_{RX}(\mathbf{r})}{\sigma}\right)=\frac{1}{2}\left[1-\operatorname{erf}\left(\frac{P_{th}-\overline{P}_{RX}(\mathbf{r})}{\sqrt{2}\sigma}\right)\right].$$

By further substitution with log distance PL model given in Sec. 3.11.1, (3.9) is easily derived. From (3.16), the optimal height of ABS for maximum coverage can be obtained as $\frac{dA}{dh}=0$. Therefore,

$$h=\frac{R^2}{4\,I_1\,I_2} \tag{5.12}$$

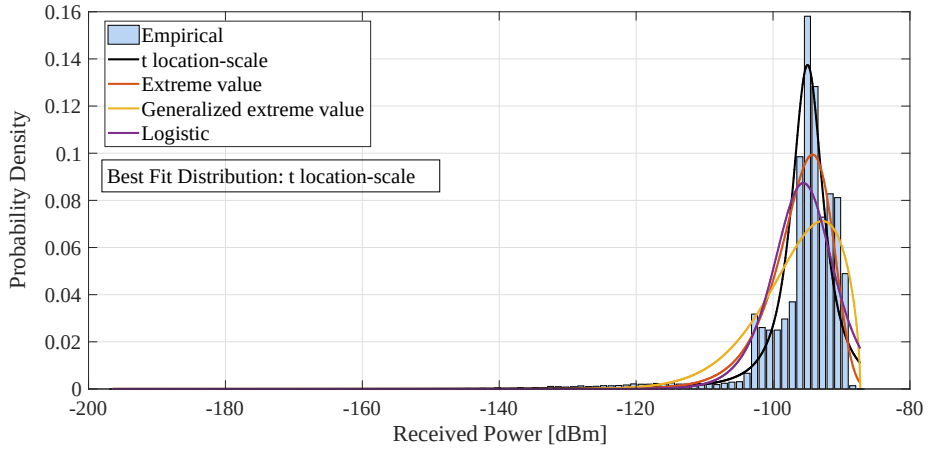

Figure 5.8: *Received power distribution of ground receivers in Suburban environment at ABS optimal altitude of 600 m.*

$$h = \frac{R}{4(\sec\phi_{max} - 1)\left[\left(\frac{1-\mathrm{erf}(a)}{2}\right) - \frac{1}{2}\exp\left(\frac{1-4ab}{4b^2}\right)\left[\mathrm{erf}\left(\frac{1}{2b} - a\right) - 1\right]\right]} \tag{5.13}$$

By implementing the parameters of ray tracing simulations for cell coverage as given in Chap. 3 in Eq. 5.13, the curves of cell coverage with respect to ABS altitude from (3.9) were found to be similar. Therefore, 300-400 m was acknowledged as the optimal altitude of ABS in different environments as shown in Fig 5.5.

Remark 1: From, (5.12), I_1 and I_2 cannot be equal to zero, for the equation to hold. Therefore, analytically from (3.17),

$\sec\phi_{max} - 1 \neq 0 \Rightarrow \phi_{max} \neq \frac{n\pi}{2}$, where $n \subset \mathbb{Z}$ (set of integer values) and since ϕ is the elevation angle, max(ϕ) = $\frac{\pi}{2}$. Also from (3.18),

$\mathbb{P}(P_{RX}(\mathbf{r}) \geq P_{th}) = Q\left(\frac{P_{th} - \overline{P}_{RX}(\mathbf{r})}{\sigma}\right) \neq 0.$

$\Rightarrow \left(\frac{P_{th} - \overline{P}_{RX}(\mathbf{r})}{\sigma}\right) \leq 3$ or $P_{th} \leq 3\sigma + P_{RX}$, since $\lim_{x \geq 3} Q(x) \rightarrow 0$.

Therefore, the threshold received power should not be greater than received power by three times the standard deviation of log-normal shadowing for (5.12) to be valid.

Remark 2: For mobile operators to use ABS network, they have to tune the parameters such as P_{th}, P_{TX}, G_T and G_R depending on the SER, height and ABS cell coverage required. From Fig. 5.5 and 5.6, it was inferred that, for the desired value of SER, SER_{th}, a corresponding ABS altitude h_{th} can

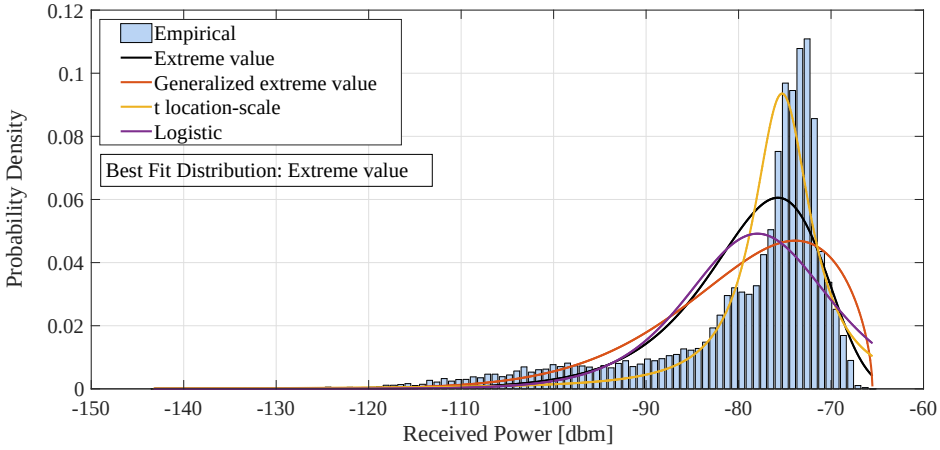

Figure 5.9: *Received power distribution of ground receivers in Urban environment at ABS optimal altitude of 400 m.*

be obtained, depending on the type of environment and waveform used for transceiver. Therefore from Fig. 5.1, a geometrical coverage area A' can be obtained excluding channel propagation effects as

$$A' = \pi R'^2 = \pi (h_{th} \tan\phi_{max})^2$$

where R' is the radius of ABS cell coverage. From (3.9), A can be replaced by A' and reorganized as follows

$$\frac{A'R}{2h^2(\sec\phi_{max} - 1)} = \left[\left(\frac{1-\text{erf}(a)}{2}\right) - \frac{1}{2}\exp\left(\frac{1-4ab}{4b^2}\right)\left[\text{erf}\left(\frac{1}{2b} - a\right) - 1\right]\right] \quad (5.14)$$

It is important to mention from (3.19) and (3.20), if $c = \frac{1}{\sqrt{2}}\left(10\eta\log_{10}(e) - 10\eta\log_{10}\left(\frac{R}{r_0}\right)\right)$, it will imply that $a = b$, where $c = \frac{P_{th} - P_{TX} - G_T - G_R + \text{PL}_0}{\sqrt{2}}$. Also, for special case $R = e \times r_0$, b from (3.20) can be rewritten in the form of a defined in (3.19) as

$$b = a - \frac{c}{\sigma}. \quad (5.15)$$

Therefore, (5.14) can be rewritten as

$$F(a) - Y = 0, \quad (5.16)$$

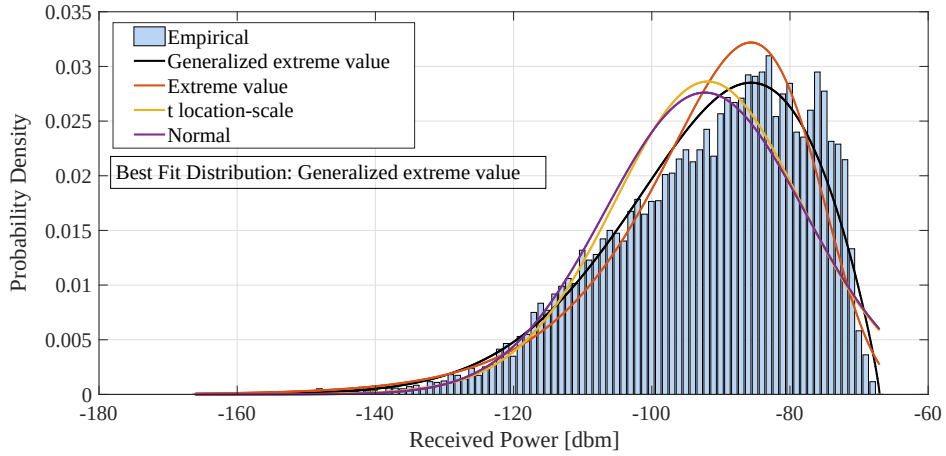

Figure 5.10: *Received power distribution of ground receivers in Urban High Rise environment at ABS optimal altitude of 600 m.*

where F(a) can be obtained by substituting b from (5.15) into Right Hand Side (RHS) of (5.14) and $Y = \frac{A'R}{2h^2(\sec\phi_{max}-1)}$. The root of (5.16) can be easily found, which will give the value of a. The channel parameters such as η and σ can be obtained at different altitudes from [Sharma et al., 2018a].

5.4.2 Optimal Altitude for minimum SER by ABS

For obtaining the optimal altitude for minimum SER, a GFDM transceiver system on an LTE grid was implemented considering a low latency scenario. The parameters of the simulation have been taken from [Gaspar et al., 2014], and are provided in Table 5.2. Reference [Gaspar et al., 2014] also describes the implementation of GFDM for a low latency scenario, where the main approach is to reduce the GFDM symbol duration and add a single cyclic prefix for the M sub-symbols. Here, GFDM symbol duration was kept to 1 ms subframe duration. Based on these parameters, SER simulations were carried for Suburban, Urban and Urban High Rise environments to obtain optimal ABS altitude, with different power delay profiles at different altitudes. These profiles were obtained from ray tracing simulations for probabilistic A2G LoS channel model. A Rician fading model was considered since LoS probability increases with increase in ABS altitude [Al-Hourani et al., 2014b]. In Fig. 5.6, SER vs ABS altitude was plotted for considered environments as discrete values and obtain a curve fit to show the variation. Less variation of SER was observed with altitude for Suburban scenario as compared to Urban and Urban High rise scenar-

ios. This is probably due to higher LoS probability in Suburban than Urban and Urban High Rise [Al-Hourani et al., 2014b]. This implies that the ground users would receive to a LoS ray component of Rician channel with higher probability which also increases with ABS altitude, thereby producing lower variation in SER with ABS height. Conversely, in Urban and Urban High Rise scenarios, SER variation is high due to low LoS probability, which tend to increase the effect of scattered components of multipath. Also the range in y-axis is limited in Fig.5.6 due to the frequency-flat fading scenario observed for ABS. As seen from Fig. 5.6, the optimal altitude for minimum SER is as follows: Suburban - 800m, Urban - 400m and Urban high Rise - 800m.

5.4.3 Optimal Altitude with varying Cell Radius for different Received Power Thresholds

As observed in Sec. 5.4.1 and 5.4.2, the optimal altitude of ABS has to be a trade-off for maximum coverage and minimum SER as reported in Table 5.3. In this section we address the probability distributions of the received power of ground users at optimal altitude of ABS, which are given in Figs. 5.8 5.9 and 5.10. The received power has been obtained from ray tracing simulations as described in Sec. 5.3. The received power was fitted with several probability distributions such as Normal, Nakagami, Rayleigh, Rician, Exponential, Beta, Birnbaum-Saunders, Extreme value, Generalized extreme value, Gamma, t location-scale, Weibull, Logistic, Gaussian etc. From all these distributions the closest and best fit distribution is shown in Figs. 5.8 5.9 and 5.10. The parameters of the distributions are provided in Table 5.3. With such parameters, the received power can be extracted as random values without performing ray tracing simulations or practical measurements. These values were used to obtain the variation of optimal ABS altitude h with respect to cell radius R for all considered environments as shown in Fig. 5.7. The behavior of the curves expects to follow (5.13), where h depends on R and substitution parameter a, which also depends on R. However, [Al-Hourani et al., 2014b] shows a linear variation of optimal LAP altitude with radius of the cell when constrained on maximum allowed PL, which is the threshold value for maintaining the link connectivity. This is different from the approach used here since minimum SER and maximum cell coverage constraints were considered for obtaining optimal altitude. Here, also the variation with received power threshold of ground users was shown. It was observed, for higher thresholds, that a higher optimal altitude is required to cover the same cell radius with minimum SER.

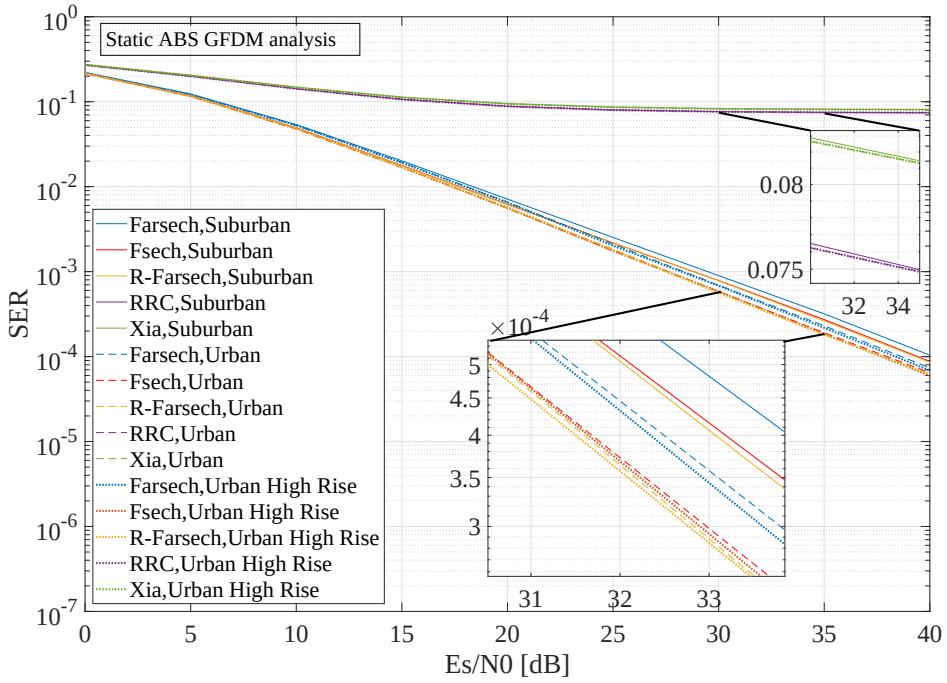

Figure 5.11: *GFDM SER analysis for static ABS.*

Also, the optimal altitudes for Suburban and Urban High Rise are higher than Urban, as shown in Fig. 5.7 and Table 5.3.

5.5 Performance evaluation with "Better than Nyquist" Pulse shaping filters

Flipped-hyperbolic secant (Fsech), Flipped-inverse hyperbolic secant (Farcsech) and Reverse-Farcsech (R-Farcsech) pulse shaping filters, were implemented. These filters were proposed in [Tan and Beaulieu, 1999] to improve sensitivity to timing jitter in the context of single-carrier modulation. The results of these filters were compared with Root-raised cosine and Xia pulses. In Fig. 5.11, the SER analysis was shown using the BTN filters for the three considered environments at optimal altitude of static ABS. The power delay profile given in Table 5.1 was used and Rician factors given in [Sharma et al., 2018a], as A2G channel parameters for this simulation. It was observed that the ABS downlink at 2.4 GHz frequency band, follows a frequency-flat fading channel. Also, SER was found to be lower for all SNR values, for ABS downlink communication as compared to terrestrial

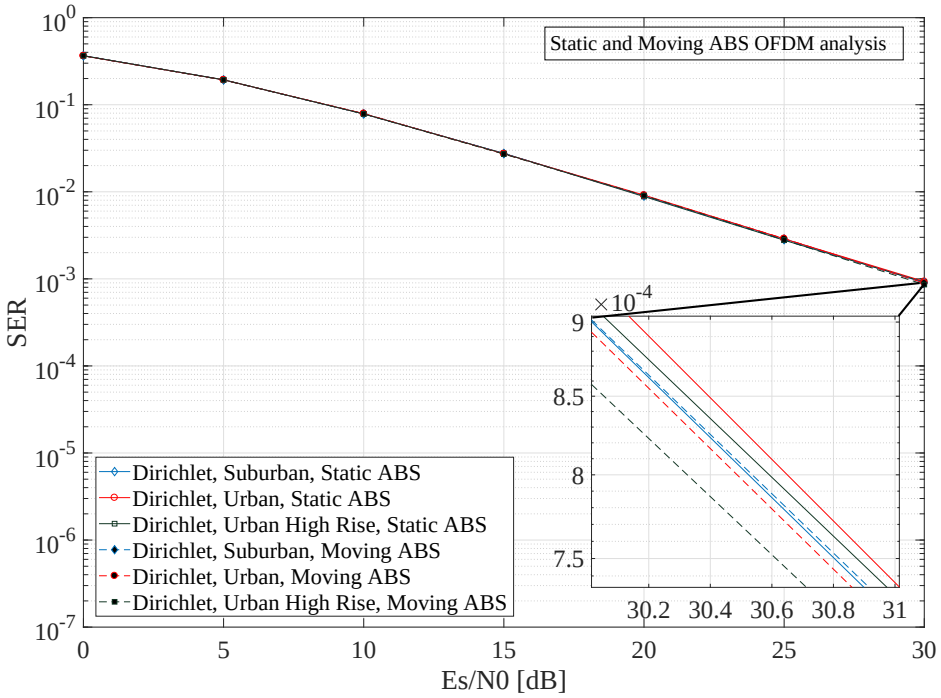

Figure 5.12: *OFDM SER analysis for static and moving ABS.*

one. From Fig. 5.11, it was observed that SER is higher for Suburban environment, lower for Urban and least for Urban High Rise environment, for optimal altitude. This can also be addressed from Fig. 5.6. This is probably due to higher optimal altitude in Suburban scenario than Urban environments, chosen according to two different criterion as mentioned in previous sections. Therefore, this addresses for an effective use of ABS in Urban environments. The results were also addressed with moving ABS with maximum Doppler shift of 3704 Hz, as shown in Fig. 5.13. Any large variations were not observed in moving ABS as compared to static ABS due to frequency-flat fading scenario, although SER values were found to be higher.

Since GFDM is a the base waveform as mentioned in Sec. 5.1, OFDM waveform was derived by changing the number of sub-carriers, $K = 64$ and number of sub-symbols to $M = 1$ with Dirichlet pulse shaping filter. Simulations have been performed with static and moving ABS with the same maximum Doppler shift considered in GFDM system, as shown in Fig. 5.12. The simulation parameters were taken from [Wu et al., 2005], considering the maximum relative movement between the ABS and user. It

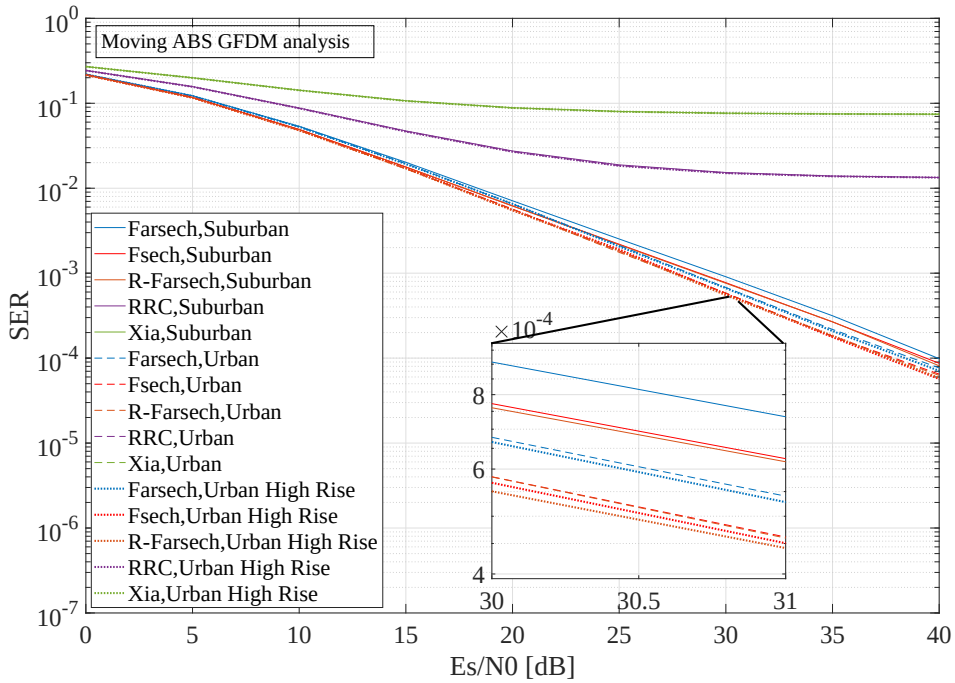

Figure 5.13: *GFDM SER analysis for moving ABS.*

was observed that a similar result behavior was obtained as reported in [Wu et al., 2005] with certain deviation since realistic A2G channel parameters obtained from ray tracing were used. This also provides insight to the validation of the OFDM and GFDM simulations.

5.6 Conclusion

In this chapter, the SER analysis of LTE-Compatible GFDM was shown, under ultra low-latency scenario with GFDM symbol duration of 66.67 μs and BTN pulse shaping filters for a static and moving ABS providing cellular connectivity to ground users. Also the SER results for OFDM, were addressed. These simulations ave been performed in different generalized environments- Suburban, Urban and Urban High Rise, developed according to ITU-R parameters, at optimal altitude of ABS. The optimal altitude was defined based on two criterions'- maximum cell coverage are and minimum SER. Also, A2G channel parameters were used to obtain SER simulation results, obtained from ray tracing results on a commercial radio propagation software. The power delay profile and probability distribution parameters of received power were also provided at the optimal altitude to reproduce

the entire set of results without redoing the whole stack of operations. This also supplemented to show the variation of optimal altitude with cell area.

CHAPTER 6

Impact of Carrier Frequency Offset on Low Latency-Enabled UAV using "Better than Nyquist" Pulse Shaping in GFDM

For an ABS network supporting flash crowds, the effect of carrier frequency offset on the SER in the downlink is evaluated in this chapter, where a LTE compatible time-frequency grid based on GFDM for low latency is considered. The choice of GFDM as multi-carrier modulation is motivated by its widely proposed application in the PHY of 5G cellular systems and its backward compatibility with LTE. Simulation results are shown for BTN pulse shaping filters in the different environments. The use of BTN allows for higher robustness to carrier frequency offset compared to root-raised cosine filters. Simulation results are shown considering realistic A2G channels parameters, reported in Chap. 2.

6.1 Introduction

With the advancement in cellular technology, IMT-2020, commonly known as 5G offers numerous features with high data rate, uRLLC in 5G NR

[Dahlman et al., 2014]. For fulfilling high data rate demands by mobile users, ABS network as shown in Fig. 5.1, has achieved much attention for flash crowds and on-demand deployment.

In this chapter the PHY transmission by ABS was addressed as there is limited research conducted on this aspect and, in particular, about the effect of synchronization errors and of impairments on the performance. Some related works regarding this are addressed in [Wu et al., 2005], [Blümm et al., 2012]. The UAV mobility to provide performance gain for delay-constrained applications, such as online gaming and video conferencing is addressed in [Wu and Zhang, 2017]. The authors study a UAV-enabled downlink orthogonal frequency division multiple access (OFDMA) network by taking into account the delay-specified minimum-rate-ratio constraints of the users, to maximize the minimum user throughput by jointly optimizing the UAV trajectory and the communication resource allocation. Article [Kakar and Marojevic, 2017] discusses OFDM waveform and spectrum management, projecting the growth of ABS beyond 2025. To efficiently operate multiple UAVs by different operators, [Nishiyama et al., 2017] proposed a centralized radio resource management assuming OFDM and time-frequency grid of LTE system. The work in [Vahidi and Saberinia, 2017] focuses on channel matrix estimation and ICI mitigation for moderate-to-high Doppler OFDM systems.

However, to the best of my knowledge, there is no existing literature on implementing generalized 5G waveforms in ABS downlink to support high data rate requirements by the users of 5G NR. Therefore, this chapter studies GFDM with low latency parameters in LTE time-frequency grid to address low latency scenario [Simsek et al., 2016]. For this, GFDM was considered with 1ms of frame structure as given in Table 5.2 compared to 10 ms in OFDM for transmitting equivalent data.

The SER was estimated by Monte Carlo simulations at different altitudes of the ABS, as done in [Gaspar et al., 2014]. In the simulations, A2G channel model was implemented for LAPs as addressed in Chap. 2. BTN pulse shaping filters are considered in the simulations, as proposed in [Kumar and Magarini, 2016], due to the improved error rate performance and less OOB emission as compared to Nyquist pulses and less sensitivity to CFO.

LAPs were implemented for improved SER with better LoS probability, lower PL and higher SNR. Also, it was not considered the case of moving ABSs since the users were addressed to be in flash crowds. Such a scenario would be well served by a static UAV, with the possibility of hovering close to the users while maintaining a safe distance. Simulations were performed

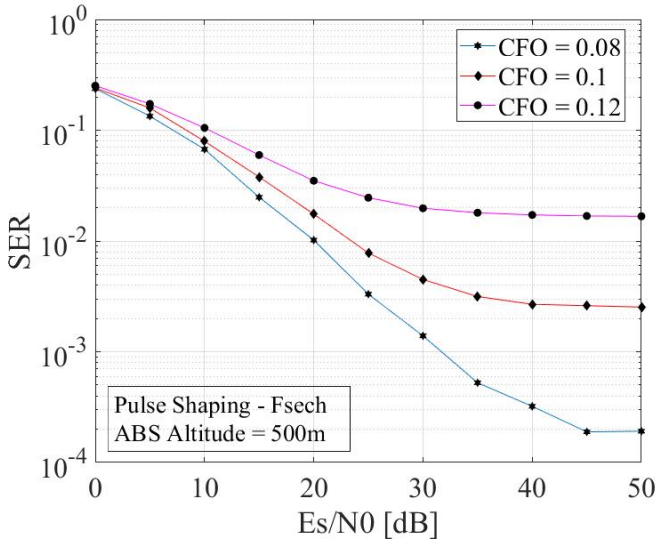

Figure 6.1: *[Group A] SER analysis for CFO variation in Suburban Environment.*

for three considered scenarios, by using A2G channel parameters obtained from ray-tracing, in the GFDM system model.

The rest of the chapter is as follows. In Sec. 6.2, the GFDM system model was shown with factor introducing CFO. Sec. 6.3 provides the SER simulation results with CFO and BTN pulse shaping at different ABS altitudes. Finally, the chapter was concluded in Sec. 6.4.

6.2 System Model

The system model used here is similar to that referred in Sec. 5.2. However, to introduce CFO, the received signal vector after removal of the CP is written as

$$\mathbf{y} = \exp\left(\frac{j2\pi\epsilon n}{K}\right)\mathbf{Hx}+\mathbf{w}, \tag{6.1}$$

where $\epsilon = \Delta f M T_S$ is the residual CFO Δf normalized to the sub-carrier spacing $\frac{1}{MT_S}$, T_S being the symbol interval.

6.3 Simulation results

The SER analysis was carried out using three BTN pulse shaping filters - Fsech, Farcsech and R-Farcsech in the GFDM system with variation in

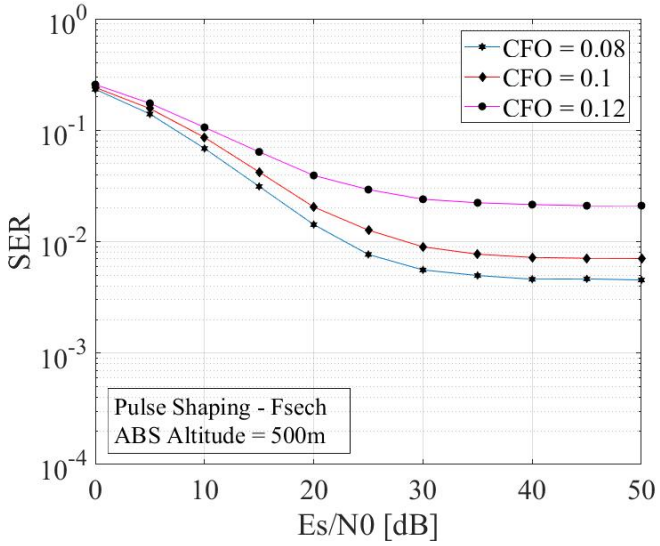

Figure 6.2: *[Group A] SER analysis for CFO variation in Urban Environment.*

CFO and ABS altitude in different environments. Simulation parameters of low latency 5G PHY were used as shown in Table 5.2. In this section, the results were presented in three categories to obtain an optimal ABS altitude and pulse shaping filter.

- *Group A*: SER analysis with CFO variation for fixed pulse shaping filter and ABS altitude.
- *Group B*: SER analysis with ABS altitude variation for fixed CFO and pulse shaping filter.
- *Group C*: SER analysis with pulse shaping variation for fixed CFO and ABS altitude.

6.3.1 Group A Results

Here "Fsech" was implemented as the pulse shaping filter and ABS altitude as "500 m", since these values were found to be optimal according to the simulation results of Group B and C. In GFDM synchronization is a well-known problem which happens due to timing offset and CFO. Here CFO was introduced in the system model to calculate the SER variation. It was observe from Figs. 6.1, 6.2, and 6.3 that SER increases with the increase in the value of CFO. This happens due to the introduction of ICI between adjacent sub-carrier in all environments.

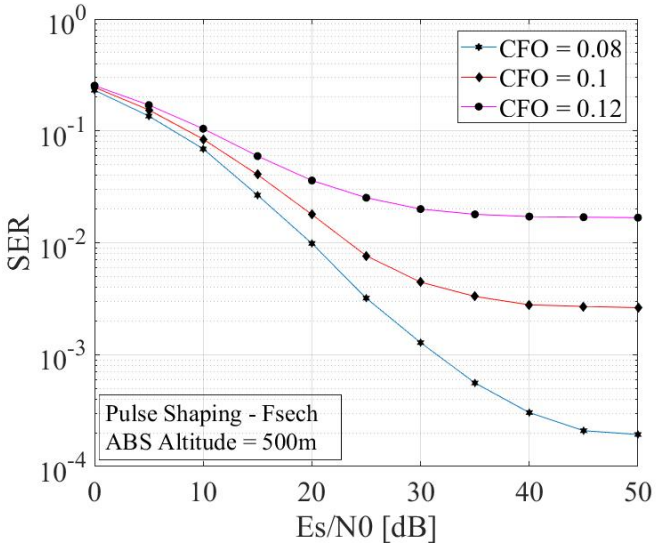

Figure 6.3: *[Group A] SER analysis for CFO variation in Urban High Rise Environment.*

6.3.2 Group B Results

In this section, SER with "CFO = 0.1" and "Fsech" pulse shaping filter was analyzed. ABS altitudes ranging from 100 to 2000 m were simulated. However, certain number of values were shown here. It was observed that for lower altitudes of ABS, SER values tend to be higher. This is due to presence of large multipath effects leading to large and small scale fading effects and finally attenuation of the received signal strength at the ground user. Also at much higher altitudes, the SER was found to be higher, due to large distance between ABS and ground user leading to large PL values. Therefore, there exists a trade-off for an optimal altitude where minimum SER is obtained. From the simulations, minimum SER was obtained at 500 m ABS altitude, as seen from Figs. 6.4, 6.5 and 6.6 for Suburban, Urban and Urban High Rise scenario, respectively. It can also be noted that similar range of optimal altitude has been proposed in the literature for maximum cell coverage by the ABS [Al-Hourani et al., 2014b, Cileo et al., 2017]. It was also observed from the simulations, that SER variation is not high at different altitudes. This is due to the frequency flat fading scenario observed for UAV communication. A similar work done on OFDM systems, addresses this in [Wu et al., 2005].

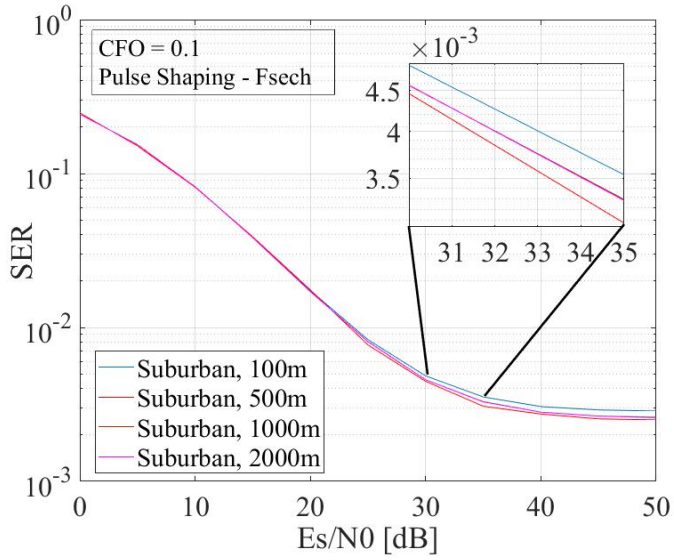

Figure 6.4: *[Group B] SER analysis for ABS altitude variation in Suburban Environment.*

6.3.3 Group C Results

In this section, the variation of SER with different BTN pulse shapig filters for "CFO = 0.1" and "ABS altitude = 500 m" was addressed. BTN pulse shaping was implemented for this work, since it proves to provide a lower OOB emission and better SER performance as compared to Nyquist ones. This has been reported in [Kumar and Magarini, 2016], for Rayleigh fading channel, which is usually used for terrestrial communication. However, this is the first work implementing these filters in Rician A2G channel model. It was observed from Figs. 6.7, 6.8 and 6.9 for Suburban, Urban and Urban High Rise environments, respectively, that "Fsech" is an optimal BTN pulse shaping filter from the three considered ones with minimum SER. However, this is different from the case of Rayleigh fading, where minimum SER was obtained with "Farsech" pulse shaping.

6.4 Conclusion

In this chapter ABS network serving ground mobile users in different environments was addressed. SER calculations were performed at different ABS altitudes ranging from 100-2000 m in a GFDM system model with low latency consisting of CFO with BTN Pulse shaping filters. The variation of SER was addressed for different CFO values and obtain optimal

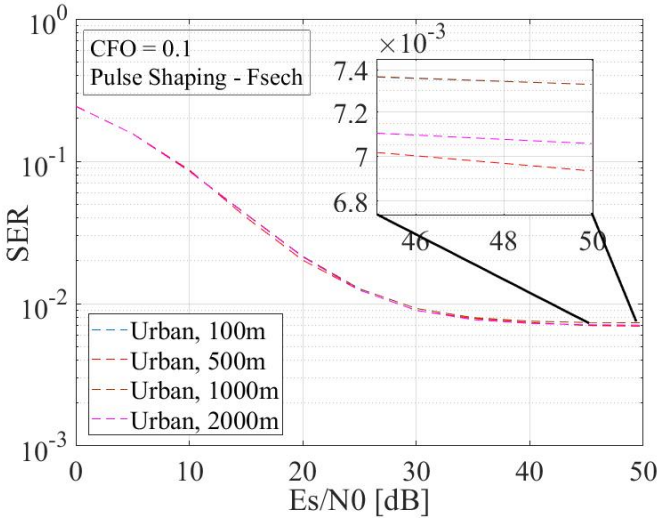

Figure 6.5: *[Group B] SER analysis for ABS altitude variation in Urban Environment.*

altitude of ABS and optimal pulse shaping filter for minimum SER. It was observed that range of optimal ABS altitude matches that of optimal altitude for maximum cell coverage. Also, A2G channel parameters obtained from commercial ray tracing software were used in the system model.

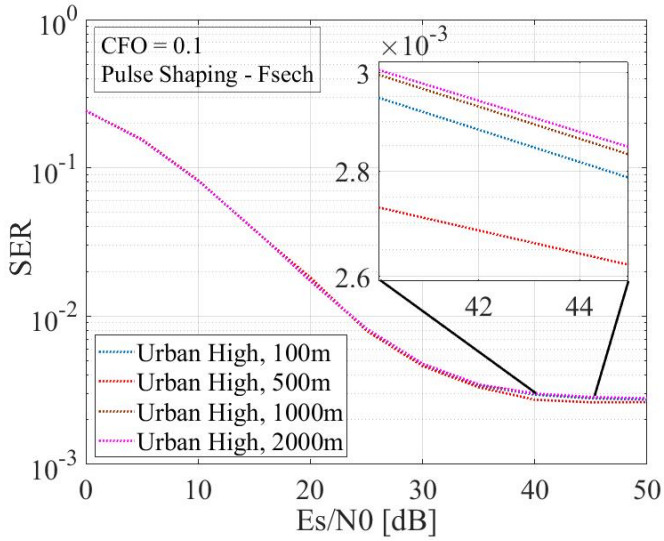

Figure 6.6: *[Group B] SER analysis for ABS altitude variation in Urban High Rise Environment.*

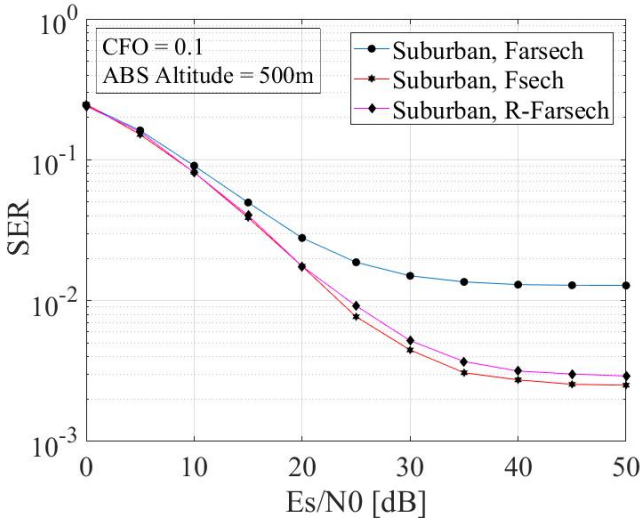

Figure 6.7: *[Group C] SER analysis for pulse shaping variation in Suburban Environment.*

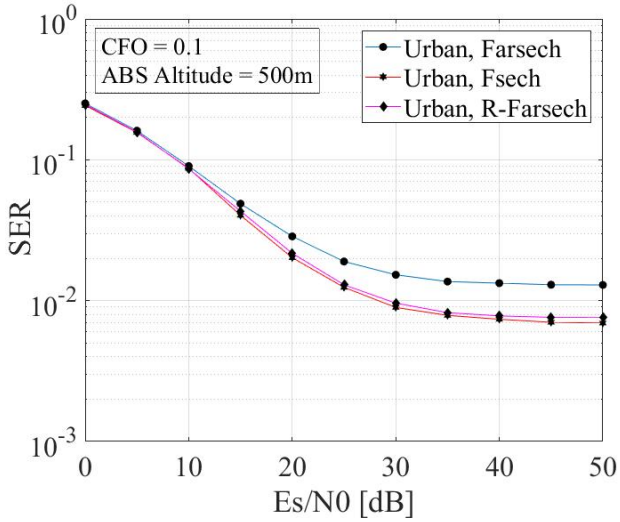

Figure 6.8: *[Group C] SER analysis for pulse shaping variation in Urban Environment.*

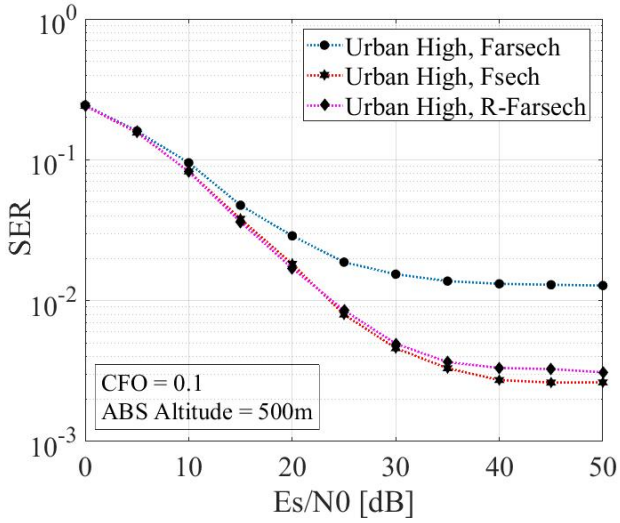

Figure 6.9: *[Group C] SER analysis for pulse shaping variation in Urban High Rise Environment.*

Part II

Secondary Contributions of the Thesis

CHAPTER 7

Control over Skies: Survivability, Coverage and Mobility Laws for Hierarchical Aerial Base Stations

To achieve an efficient ABS network, many factors pertaining to ABS flight, governing laws and information transmissions have to be studied. In this chapter, multi-drones communications are studied in three major aspects, survivability, coverage and mobility laws, which optimize the multi-tier ABS network to avoid issues related to inter-cell interference, deficient energy, frequent handovers, lifetime, etc. Moreover, this chapter discusses several optimization constraints along with the proposed solution for the management of hierarchical ABS network. In addition, the chapter includes simulation results of hierarchical ABS allocations for handling a set of users over a defined geographical area. Further, several open issues and challenges are presented to provide deep insights into ABS network management and its utility framework.

7.1 ABS: Utilities and Extensions

Due to recent advancement of vehicular technology in 5G, UAVs, have gained a significant consideration to be used as ABSs for facilitating cellular connectivity to ground mobile users [Kaleem and Rehmani, 2018] [Naqvi et al., 2018] in flash crowds. On-demand ABS deployments ensure offloading of traffic in Terrestrial Cellular Network (TCN). Multi-tier drone architecture complements TCN to serve the users under high shadowing and interference effects and is well-studied in [Sekander et al., 2018]. ABS network offers certain benefits over TCN, such as dynamic and adaptive cell coverage, being deployed as a flying relay with drone cells integrated with macro and micro cells [Sharma et al., 2017], where drone cell coverage can be changed by varying the drone power and altitude depending on the data traffic. However, severe interference from macro, micro, and other drone cells have to be minimized using interference mitigation techniques and drone trajectory planning to avoid cell overlap. Moreover, TCO of mobile operators is reduced by integrating ABS network with TCN, since energy requirements of ABSs are lower compared to terrestrial base stations and site availability for cell planning is not required. However, ABS is not the only use case for UAVs in 5G. UAVs play important role in public safety networks used by military, police, fire, and emergency medical services in case of natural disasters, search and rescue operations, surveillance and reconnaissance. Reference [Gomez et al., 2016] provide details of European project ABSOLUTE that deals with designing and prototyping of high capacity IP data network for public safety scenarios using drones. Also in [Motlagh et al., 2017], UAVs equipped with IoT devices provide services with crowd surveillance through facial recognition tools and cloud-based processing.

There are several research domains that are currently being studied in wireless communication while integrating with UAV networks that improve the services for 5G. Artificial Intelligence (AI) can be used as a powerful tool to reap the benefits of ABS network by addressing several challenges such as efficient Xhaul and trajectory planning with cooperative and secured multi-UAVs data transmission with machine learning algorithms for predicting on-demand deployment of drone network. Another domain of research facilitated by the use of UAVs is MEC enabled F-RAN, where functions such as signal processing and computing, resource management and allocation, distributed storing and caching abilities are performed at UAVs which act as a moving cloudlet. The details about this aspect are described further in [Jeong et al., 2018].

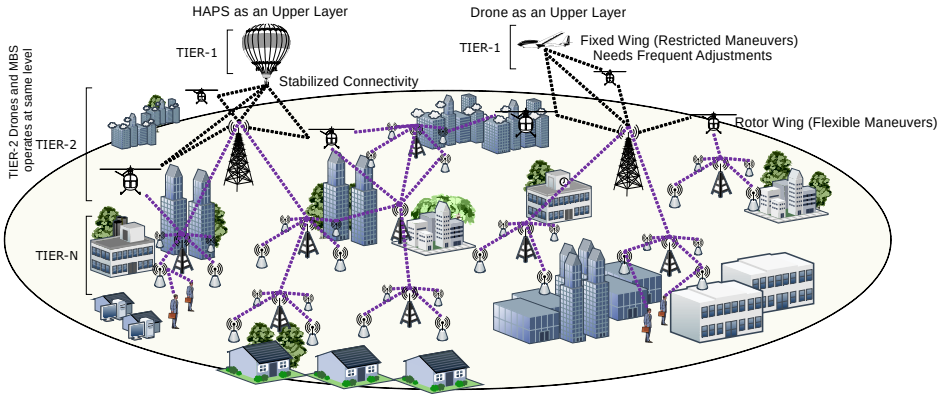

Figure 7.1: *An exemplary illustration of hierarchical ABS setup for maximum coverage and agile reconfigurability. Multi-tier of drones facilitates easier network management and allows better service facilities to its users. Tier-2 drones and MBS are operated as same network level with a similar set of instructions and capacities.*

However, to accomplish aspects of ABS network, well-defined coverage and mobility controls are of essential importance. There is very limited research for UAVs on these issues. In [Sharifi et al., 2015], the authors propose a distributed control algorithm for unmanned aerial and ground vehicles to perform desired tasks with minimum cost functions. The cost function for each agent or vehicle is different and results are validated with experimental tests. In [Marier et al., 2013], the authors address a similar problem with different cost function which is based on the health state of UAVs. Many authors have addressed the problem of coverage and mobility control in wireless sensor networks based on different objective and cost functions. However, to the best of my knowledge, this is the first chapter to address such prospects, particularly in a multi-tier ABS network.

7.2 Multi-ABSs and Hierarchy

Multi-ABSs allow the use of drones as Macro Base Station (MBS) to facilitate the connectivity to the users with the similar capacity to that of a traditional MBS. There exist a plethora of approaches which fixates on a single layer of drones to enhance the Quality of Service/Quality of Experience (QoS/QoE) for end users while using drones as APs. Such solutions have gained quite an attention because of their theoretical idealizations. Amalgamation of drones and traditional setup is not that convenient as assumed by the existing solutions. To counterfeit such challenge, it is suggested by different researchers and organizations to use drones as a network compo-

nent and manage traffic by using drones similar to a normal network node. However, there are no concurrent studies which involve the evaluation of drones' behavior as well as its properties and maneuverability while deploying them in the network[1]. Such assumptions are unable to identify the exact role of drones and their inclusion in TCN. In order to reduce the considerable impact on TCO, this chapter recommends using drones in multiple layers similar to TCN and then fixating technologies and mechanisms of sharing the load between both distinctly operating networks. As illustrated in Fig. 7.1, N-layers can be formed for incorporating drones in TCN with Tier-2 drones acting similar to MBS; and HAPS and Tier-1 drones facilitate the movement and control over the underlying network with Tier-2 drones and entities of TCN. It is to be noted that the type and the make of drone pose a considerable effect on the performance of the network as it is easier to regulate the network with rotor-wing drones, whereas fixed-wing drones require specialized algorithms for generating the waypoints.

7.3 Problem Statement and Scope

Single tier ABSs are easier to manage, control and operate irrespective of the scalability in terms of the number of drones functional at the same time over a specified area. In contrast to this, multi-tier ABSs help to define a new set of network architecture with a wide range of capacity, coverage, and operations, but with a complex formation. Such layered architecture, if optimized successfully, offers a large number of applications through elongated connectivity. Multi-tier ABSs suffer from the critical issues of survivability, coverage enhancement, and mobility management. The problem with survivability is dependent on the resource depletion of drones, which leads to its failure and non-functioning after a particular period. The problem with coverage is related to positioning of drones and network planning, which causes issues related to fading, interference and signal distortion. The problem with mobility is related to shifting of services between the drones and allocation of resources, failure of which leads to an isolated network with increased overheads. Thus, it is desired to design a multi-tier ABSs because of their capabilities but with a resolution of issues related to survivability, coverage and mobility management.

This chapter considers the scenario of multi-tier ABSs while fixating a solution for optimized positioning and maneuvering of drones for maximizing the probability of connectivity and likelihood of mapping between the UAVs and the demand areas through a novel N-block recursive learning

[1]Most of the existing studies assumes the flying capabilities and mobility management of drones

(NBRL) framework. In addition, this chapter discusses the optimization issues and constraints related to the laid requirements of multi-tier ABSs. Moreover, a simulation case study is presented, which shows significant gains observed for the different set of metrics while supporting communications between the ABS, designated TCN-MBS and a set of users in a defined geographical area.

7.4 Optimization Issues and Constraints

To fulfill the functional requirements of multi-tier ABSs and TCN, several optimization issues have to be taken care off. There are several variables that need to be optimized to balance the trade-offs in the system model. These optimized variables are described as follows:

7.4.1 Dynamic Cell Coverage Area and Trajectory Planning

One of the interesting features of ABS network over TCN is its dynamically changing cellular coverage which depends mainly on ABS's altitude, power and propagation environment. Also, the probability of LoS is an important factor for an ABS which depends on the type of propagation environment and elevation angle between the ABS and the ground user. To obtain appropriate coverage control, the major design constraints that need to be optimized are ABS altitude and power. However, in multi-tier architecture, ABS cell coverage would be affected by the inter-cell interference from other ABS cells, microcells and macrocell. Therefore, appropriate trajectory planning of ABS is needed to avoid cell overlaps taking into account the UAVs' flying speed, direction, and acceleration with certain perturbation that may arise due to wind gusts, which also brings another constraint for mobility control.

7.4.2 Energy Consumption

Energy utilization is one of the most important factors on which all the functions of ABS network depends and it plays a vital role for survivability, coverage and mobility control. UAVs are energy critical machines, therefore alternative sources of power such as mounted solar panels, stop and recharge techniques, radio frequency power sources are currently being researched and tested by deployment. Reference [Zeng and Zhang, 2017] describes this aspect in further details. Also, energy consumption by drones is divided into two functions- drone flight with on-board processing and information transmission by mounted LTE base station. The power required

for on-drone flight is higher than the transmission power. However, the power needed for fixed-wing aircrafts is lower than the rotary ones of the same size and payload carrying capacity but rotary wing UAVs can provide better coverage with lower hand-offs and Doppler effects due to their hovering capability at different altitudes whereas fixed-wing UAVs need to fly at velocity above a certain threshold to maintain stable fight, which causes higher Doppler and hand-offs.

7.4.3 ABS Placement

ABS placement depends mainly on the user density requesting for services and its power. However, some other factors affecting the placement includes the probability of LoS with the ground mobile user, type of propagation environment and implied collision avoidance techniques with other ABS or surrounding infrastructure. With a priori placement decision, ABSs discover the optimal trajectory and altitude towards the required set of ground users. Therefore, optimal ABS placement is needed to achieve coverage and mobility control. In [Alzenad et al., 2017], the authors address ABS placement for minimum energy and maximum cell coverage in Sub-urban, Urban, Dense Urban and High Rise Urban environments.

7.4.4 Fast Handovers

Handover is another crucial optimization concerns with ABSs. As described in the previous section, fixed-wing UAVs tend to have higher handovers than rotary wing UAVs. Since UAVs provides better coverage, it is easier to consider existing LTE handover standards for managing handoffs that arise from the high mobility of users. SDN can be an efficient solution to handle handovers, allowing for efficient control, management, and cooperation between the UAVs and the users [Sharma et al., 2017]. Also, there is a major requirement for handling vertical handovers if one considers the differences in the technologies used by the underlying infrastructure. For handover management between the infrastructure and the drone, successful techniques have been performed by Qualcomm in their practical tests using high and low power terrestrial BS by forming macrocell and microcells, respectively.

7.4.5 Resource Allocation and Management

Appropriate allocation and management of the radio resources ensure the survivability of the drone. The resources addressed herein are for both Physical (PHY) and Network layers (NET) such as available spectrum,

Physical Resource Blocks (PRBs) of LTE grid, channel state information and capacity. Apart from resources required to accomplish the ABS transmission and reception, resources are also needed to achieve successful flight and maneuvers which depends on the energy efficiency and waypoint prediction for optimal trajectory. Also, coordination of ABS network is needed to prevent the use of same PHY and NET resources for interference mitigation.

7.4.6 Quality-of-Service (QoS)

QoS defines the overall performance of the network which includes the ability of the network to achieve maximum bandwidth, end-to-end latency, cloud computing service, etc, and deals with network performance elements such as error rate, and jitter (variance in latency). To achieve the appropriate QoS, apart from data packet and bandwidth management mechanisms, data traffic from the mobile users must be differentiated based on the priority of service requested. Based on the geographical zones demanding for prioritized data, ABS altitude and trajectory should be optimized to provide best possible service to the users. Therefore, QoS serves as one of the most important metrics for survivability, coverage and mobility control laws that need to be optimized.

7.4.7 Drone Security

In addition to above discussions, ABSs need to be secured in their operations. ABS security is defined in terms of protection against privacy, trust and other types of cyber attacks. Eliminating drones from being cyberbullies and preventing them from exposing the network are the major issues for ABS-enabled cellular setup. An insecure network formation with drones may expose the ABS and their functions that result in over-utilization of resources, which in turn affect the survivability, coverage control, and mobility laws for using hierarchical ABSs. Confidentiality, integrity, authenticity, and availability of ABS at all times are the major aspects of drone security. Moreover, provisioning of component abstraction and limited accessibility to operational configurations help in avoiding the exploitation of different vulnerabilities, which might have been left during the designing or the deployment phase.

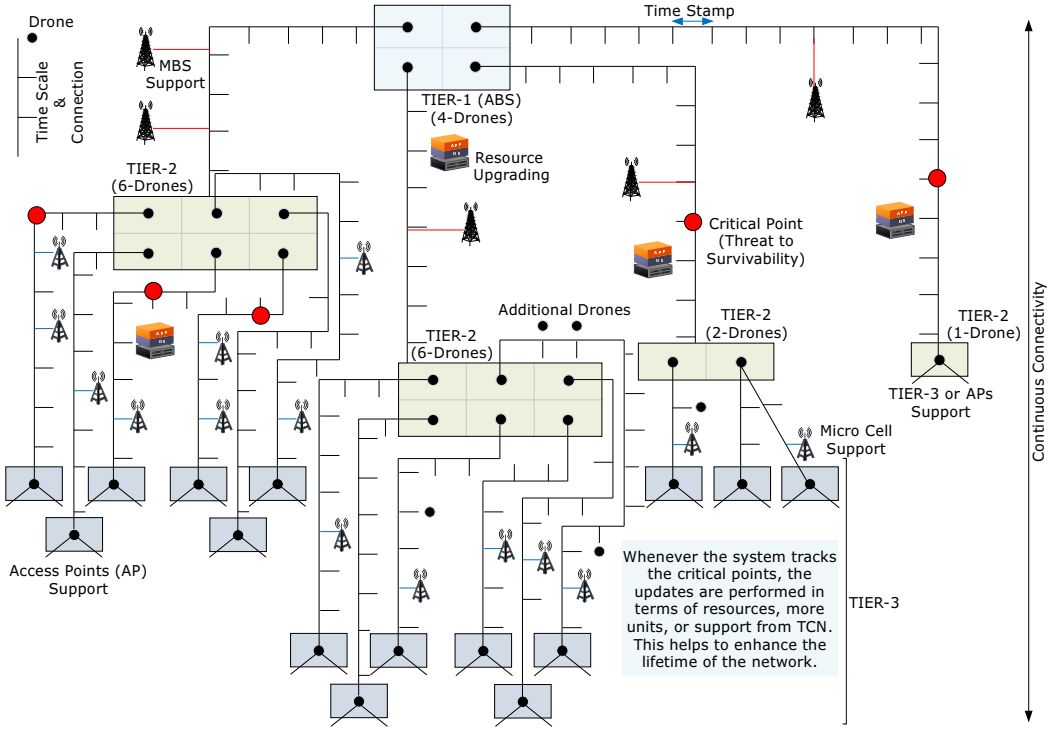

Figure 7.2: *An illustration of the matrix-timing diagram for tracking the survivability of the system and deciding the requirements for additional resources, entities or support in terms of load balancing.*

7.5 Proposed Solution

Despite the advantages of UAVs in the next generation of wireless networks, there are certain limitations on their full-fledged use, which include, control over the movement of the UAVs by identification of waypoints, identification of appropriate location to increase the view over geographical area, number of users to be shifted over UAVs, and identification of the number of UAVs to perform a particular task [Wei et al., 2017]. All these are optimization issues and can be controlled by forming laws for each of the problems.

To resolve the above-described issues, this section introduces the concepts of survivability, coverage and mobility laws for efficient localization of multi-ABSs and non-failure based network formation for supporting QoS to the end users. In addition, NBRL framework is proposed, which takes into account the derived policies on survivability, coverage, and mo-

bility for fixating the final decisions on the operations of hierarchical ABSs.

7.5.1 Survivability

The survivability is defined through resource-based policing, which depends on the prediction and estimation of the lifetime of each drone based on its maneuverability as well as consumption of available resources. At first, the network is assumed to operate with a set S of MBS whose coverage is to be improved by deploying a set D of drones in N tiers. Now, the survivability of the system is obtained by modifying the Lusser's formula[2], according to which, the survivability of hierarchical ABSs can be obtained as $\mathcal{S}_{\mathcal{T}}^{(t)} = \prod_{i=1}^{N} \left(\mathcal{S}_{\mathcal{L}}.\frac{\mathcal{D}_A}{|D|}\right)_i$, where $\mathcal{D}_A$ is the active drones in a given layer, and $\mathcal{S}_{\mathcal{L}} = \prod_{j=1}^{|D_i|} \left(\mathcal{S}_{\mathcal{D}}.\frac{\mathcal{C}_A}{\mathcal{C}_T}\right)_j$, $\mathcal{T}$ is the total operational time. Here, $\mathcal{C}_T$ is the total connections and $\mathcal{C}_A$ is active connections between the nodes, which can be expressed as a function of different metrics, such that $\mathcal{C}_A = f_t\left(\beta, \mathcal{E}, \mathcal{R}, \tau, \lambda\right)$.

β and $\mathcal{E}$ denote the memory and energy associated with each drone, respectively, $\mathcal{R}$ is the radio range, τ is the transmission time, and λ is the mean user distribution. $\mathcal{S}_{\mathcal{D}}(t)$ can be calculated over same function as $\frac{-1}{t}\log\left(\frac{f_t}{f_0}\right)$, where $t \leq \mathcal{T}$. The details on the survivability can be obtained by following the illustration presented in Fig. 7.2. The diagram shows the $n \times m$ $(n,\ m \geq 1)$ matrix-timing tree for each aerial node and their corresponding interacting node in the network. This diagram helps to understand the impact of a particular node on the functionality of the entire network as well as it can be used for enhancing the maximum lifetime of the network by controlling the survivability inputs at any instance.

7.5.2 Coverage Control

For coverage laws, a Voronoi-based strategy, inspired by Córtes et al. [Cortes et al., 2004], is considered, which aims at the formation of control laws for UAVs. The proposed approach utilizes the centroid, mass, and polar moment of inertia to allow efficient placement and coordination of multiple UAVs as expressed in [Cortes et al., 2004], however w.r.t. the movement of multi-ABSs.

The 3D placements, as well as controller selection, is performed to keep a check on the mobility of ABS through a layered module. Note that ABSs

[2]http://www.ausairpower.net/PDF-A/Reliability-PHA.pdf [Accessed June, 2018]

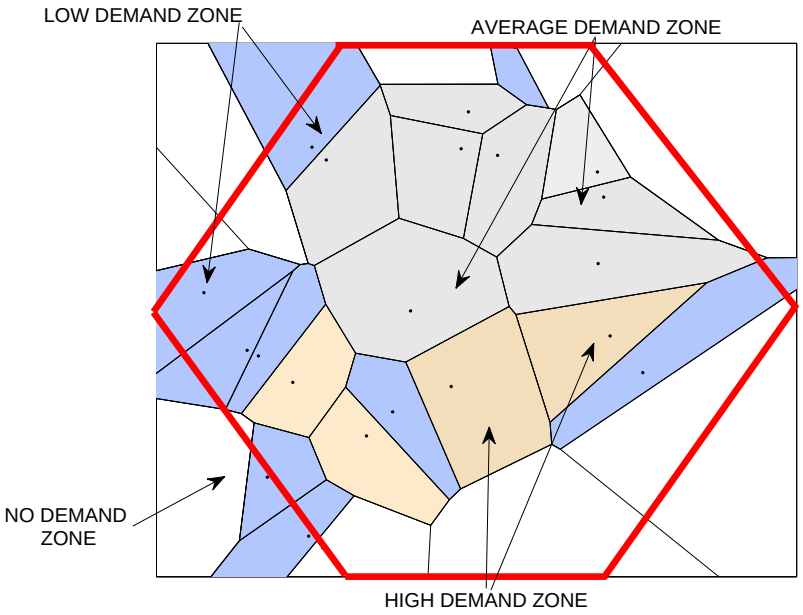

Figure 7.3: *An exemplary illustration of Voronoi-based area division as observed by an aerial node. The four types of areas considered in the zone under communication are marked by a variation in color.*

in Tier-1 are responsible for the majority of calculations and sharing the details with the underlying ABSs (Tier-2, Tier-3, ..., Tier-N). The individual evaluations are dominated only in the case of isolations.

The coverage model is developed with respect to a single ABS, which is then extended to the entire network. For the geographical division of the area, the region under ABS is marked by Voronoi constellations denoted by a convex polytope[3], $\mathbb{P}$. Coverage control is obtained by location and placement optimization of the ABS, which can be attained by managing the polytope divisions and allocating UAVs according to their physical properties. The polytope operates over 2D coordinates of geographical areas (x, y), which are obtained by marking 3D location of a drone to its corresponding 2D point on the ground. The polytope constellations for entire area $\mathbb{P}$ is obtained as the union ($\cup$) of sub-polytopes i.e. $\mathbb{P}$=$\{a_1 \cup a_2 \cup \ldots a_k\}$, where k is the number of divisions of the area A. The placement of $|D|$ UAVs in the entire polytope $\mathbb{P}$ is controlled by the location polytope $\mathbb{L}$, such that $\mathbb{L}$=$\{L_1 \cup L_2 \cup \ldots L_D\}$. For controlled mapping, $\mathbb{L}$ is also a con-

[3]A polytope is a finite set of points which are always bounded by flat sides. A convex polytope is the one such as a line segment joining any two points in a geometry.

vex polytope. The mapping between the two polytopes $\mathbb{L}$ and $\mathbb{P}$ is obtained by matching points Q in $\mathbb{L}$ to the points G in $\mathbb{P}$, such that after mapping, Q is a subset of G.

In a network, it is difficult to perfectly match each drone to the desired location. Thus, there may exist an error in the location of drone, which is marked by some error correction ϵ such that the actual location of a drone for L_1 is changed to $L_1 \pm \epsilon_1$. All the sub-polytopes resulting from drone to area mappings are reunited to form the final Voronoi set V. Considering this mapping, the number of users around the MBS region is marked as high demand area, medium demand area, low demand area, and no demand areas as shown in Fig. 7.3, and set V can be written as $V = \{v_1, v_2, \ldots, v_k\}$, where v_k denotes the submapping between the drones and the kth demand area. The location marking from these sets can be determined by similar strategy used by Córtes et al. [Cortes et al., 2004], however, by replanning their Gaussian function with the area under displacement generated by the movement of each UAV.

7.5.3 Mobility Laws

The mobility laws are operated over control laws by taking into account the survivability of multiple drones as well as their operational hierarchy. As performed earlier, the mobility laws are also defined for a single Tier-1 ABS and then extended to its corresponding ABS in the same tier. For mobility laws, the movement of drones is managed through optimal placement based on Voronoi constellations. The mobility laws remain similar in all the tiers of drones irrespective of their functionality. However, the primary aim of connectivity is maintained throughout the movement. This helps to avoid issues related to network partitioning as well as isolations.

At first, the UAVs are entitled to move according to their survivability factors and the request from the area, which is marked by demand zones of Voronoi. The demand zones of Voronoi[4] provide a non-overlapping placement of UAVs along with the generation of estimated waypoints to control their movement.

The calculation of area covered by each of the deployed UAV allows removal of possible overlaps with an aim of maximum coverage with the minimum number of UAVs. The Tier-1 ABS is coordinated by its serving TCN-MBS, whereas the next Tier UAVs are coordinated by their previous Tier ABSs, and in the case of NLoS or absence of coordinating node, the available ground infrastructure supports the coordination.

[4]A single Voronoi division can have multiple UAVs depending on the area to be covered and the maneuverability of UAVs.

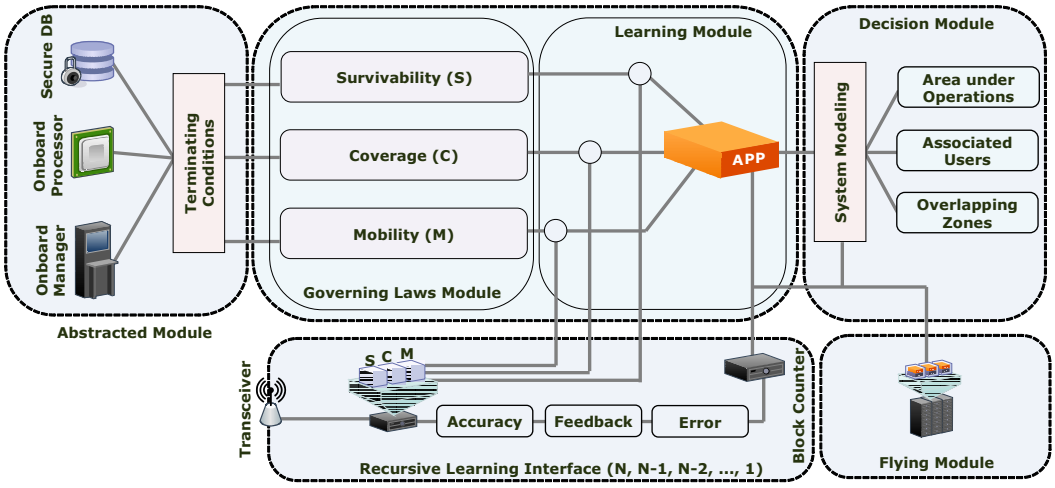

Figure 7.4: *An illustration of the N-Block Recursive Learning Framework (NBRL) used for updating the policies and generating governing laws for survivability, coverage, and mobility using recursive patterns.*

For better understanding, the mobility laws are derived considering two UAVs, which can be easily extended to $|\mathcal{D}|$ number of UAVs. Let D_i and D_j be the two UAVs deployed with three different possibilities of no overlapping, completely overlapping with difference in altitude, and the partial overlapping. Since, the waypoints of UAVs are decided by their corresponding ABSs, TCN-MBS or any available infrastructure, complete overlap of two or more UAVs is not observed throughout this deployment. However, there can be a case of partial overlap which also affects the coverage area and causes interference, and also increases the number of UAVs required to cover the entire MBS zone. Thus, overlapping of UAVs (O_A) irrespective of their tiers can be represented as $0\% \leq O_A \leq 100\%$. Now, to set mobility laws, the limits are defined for the total area covered by each of the two UAVs such that, $D_i = \{D_i.x_{\min}, D_i.x_{\max}, D_i.y_{\min}, D_i.y_{\max}\}$, and $D_j = \{D_j.x_{\min}, D_j.x_{\max}, D_j.y_{\min}, D_j.y_{\max}\}$. The overlap for the x and the y coordinates is calculated as $X_o = \max(0, \min(D_i.x_{\max}, D_j.x_{\max}) - \max(D_i.x_{\min}, D_j.x_{\min}))$, and $Y_o = \max(0, \min(D_i.y_{\max}, D_j.y_{\max}) - \max(D_i.y_{\min}, D_j.y_{\min}))$. Using these, O_A can expressed as a Boolean, i.e. 1 for $X_o > 0$ and $Y_o > 0$, which refers to overlapped movements, and 0 otherwise, which refers to non-overlapped movements of UAVs of single tier. Similar formulations can be extended for expanding mobility laws to inter-tier UAVs.

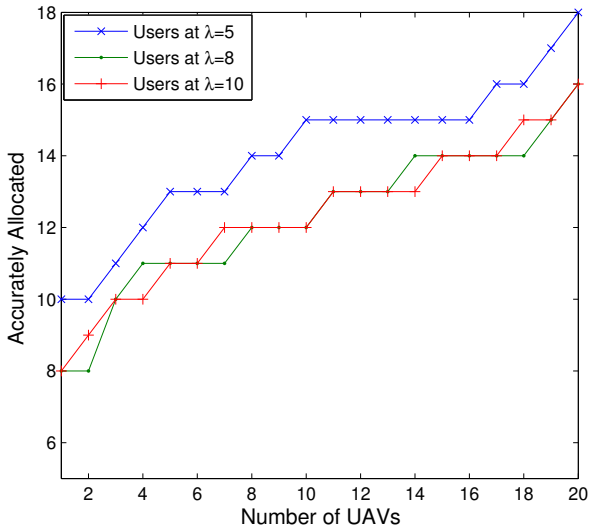

Figure 7.5: *Simulation study of accurately allocated UAVs vs. total number of tier-2 ABSs.*

7.5.4 N-Block Recursive Learning (NBRL) Framework

This chapter introduces NBRL framework, which helps to provide update policies for survivability, coverage and mobility laws, as shown in Fig. 7.4. The framework helps to get periodic information from the N-Tiers in a recursive manner until the required criteria of operations are not satisfied. Here, required criteria refer to the governing conditions for different laws associated with the successful operations of multi-tier ABSs.

NBRL is a block-based framework which can be extended for any number of laws and metrics; however, the system requires parsing for evaluating the new set of policies from other nodes in the same or different tiers. Moreover, NBRL framework accounts for the initial positioning of UAVs on the basis of demand area to Voronoi mapping and checks for the covered area along with mobility management of ABS in the range specified for their tier. This framework takes into account the area covered by the entire fleet of UAVs in a single zone, and then, checks for coverage control, survivability options, and mobility laws. In the case of maximum coverage and maximum survivability, the setup continues, whereas, in the case of non-mapping of the demand areas, the UAVs reshuffling and Voronoi remapping are performed to optimize the UAV placement and to maximize services without impacting the mobility laws. The framework is recursive

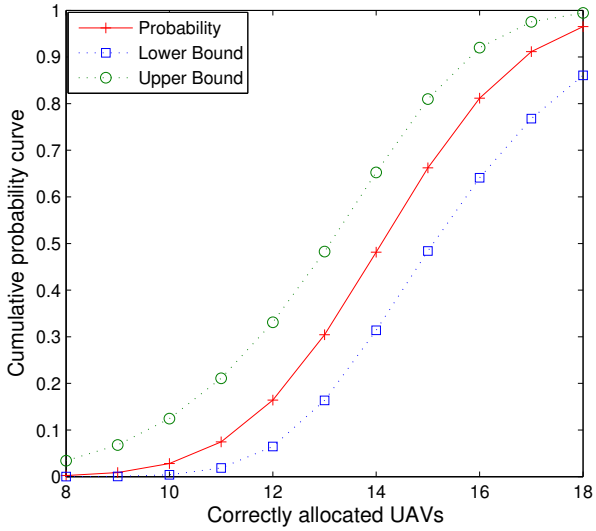

Figure 7.6: *Simulation study of cumulative probability for handling maximum users vs. total number of tier-2 ABSs.*

and obtains its update in $N, N-1, N-2, \ldots, 1$ pattern, which is iterated[5] until the conditions selected for operations of ABSs are not close enough to the maximum likelihood for the associated laws.

7.6 Performance Evaluation

The proposed approach is evaluated numerically using a sample network setting in $Matlab^{TM}$. The analyses are carried in an area of 2500x2500 m^2 with each MBS having one active Tier-1 ABS with a communication range of 1000 m. The total number of tiers is set at 2, with Tier-2 ABSs serving similar to the APs. The maximum number of Tier-2 UAVs used by the proposed approach is set to 20. The initial area assigned to each UAV is 1000 m^2. The number of users varied between 1000 to 2000 per MBS region and each user made a service request using Poisson distribution with λ varying between 5 and 10. The flying range of Tier-2 UAVs is set between 200 m and 500 m.

Initially, the proposed approach[6] is tested for accuracy in allocating Tier-2 ABSs to their respective zones using location optimization of Voronoi as

[5]The iterations also account for individual in each layer, which refers to the available TCN or companion drones.

[6]The proposed approach is not tested for communication errors, rather survivability, coverage control, and mobility laws are tested.

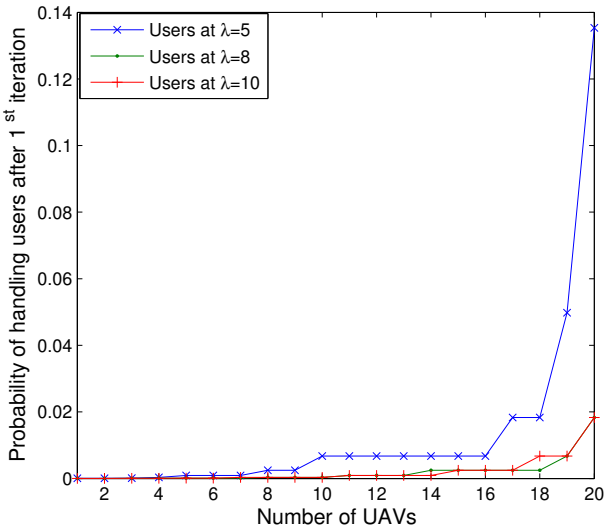

Figure 7.7: *Simulation study of probability of handling users after* 1^{st} *iteration vs. total number of tier-2 ABSs.*

shown in Fig. 7.5. The results show that the proposed approach is able to allocate Tier-2 ABSs accurately with accuracy varying between 90% and 40% depending on the arrival rate of service requests and iterations. After maximum iterations and with more users ($\lambda = 10$), the upper limit for accuracy is 80%, which is 10% lower than the case of lesser users ($\lambda = 5$). Fig. 7.6 shows the cumulative probability curve with upper and lower bounds for a maximum number of users handled by accurately allocated Tier-2 ABSs.

With more UAVs assigned to accurate locations, the probability of handling the users also increases. To showcase the performance, the results are evaluated for handling the users after the first iteration. Fig. 7.7 shows that the scenarios with maximum Tier-2 ABSs allocated accurately in the first iteration provide better coverage. Network with $\lambda = 5$ provides 83.9% and 84.9% better coverage than the networks with $\lambda = 8$ and $\lambda = 10$, respectively. Finally, the results are recorded for the likelihood of accurately moving and placing UAVs in respective zones. The results in Fig. 7.8 show that the proposed approach is capable of maximizing the likelihood of maximum coverage after fewer iterations. This suggests the high convergence of the proposed approach towards an optimal solution. Moreover, these results are evidence that it is desirable to consider survivability, coverage and mobility laws, irrespective of their mechanisms while using UAVs in

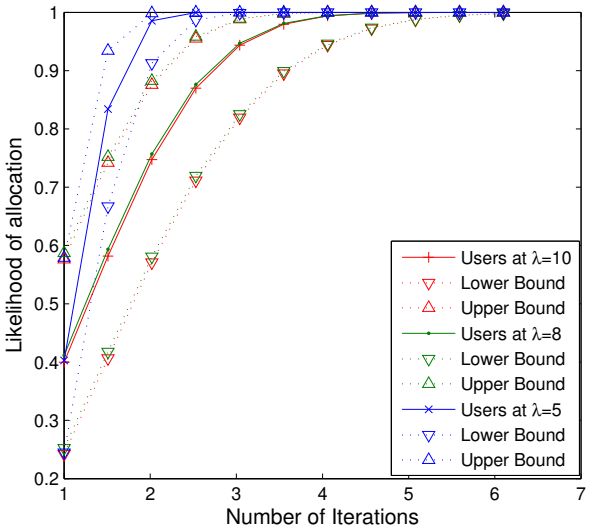

Figure 7.8: *Simulation study of likelihood of UAVs allocation vs. total number of tier-2 ABSs.*

multiple tiers in association with general TCN.

7.7 Discussions, Lessons Learned and Open Issues

ABS networks enhance the potential of TCN while resolving their performance issues and assisting them with additional services. Over the past few years, many research organizations have identified the tremendous amount of applications for using single tier ABS networks with multiple drones. Some of them have also emphasized the use of HAPS to facilitate the workflow of the network. However, the majority of them neglected the governing laws of using multi-ABSs in a hierarchy. This chapter emphasizes the need for operational laws, which include survivability, coverage, and mobility as core components.

The network formulations, result evaluations, and technological discussions provide an evidence of enhancement in the functioning of the network by the inclusion of multi-tier ABSs. Such an inclusion allows better lifetime, better coverage and also helps to control the variations due to the high mobility of aerial nodes. Finally, in order to summarize the understandings of the proposed work and research to follow, an illustration is presented in Fig. 7.9, which shows the direction of research and issues to be resolved for a fully-functional utilization of hierarchical multi-ABSs network.

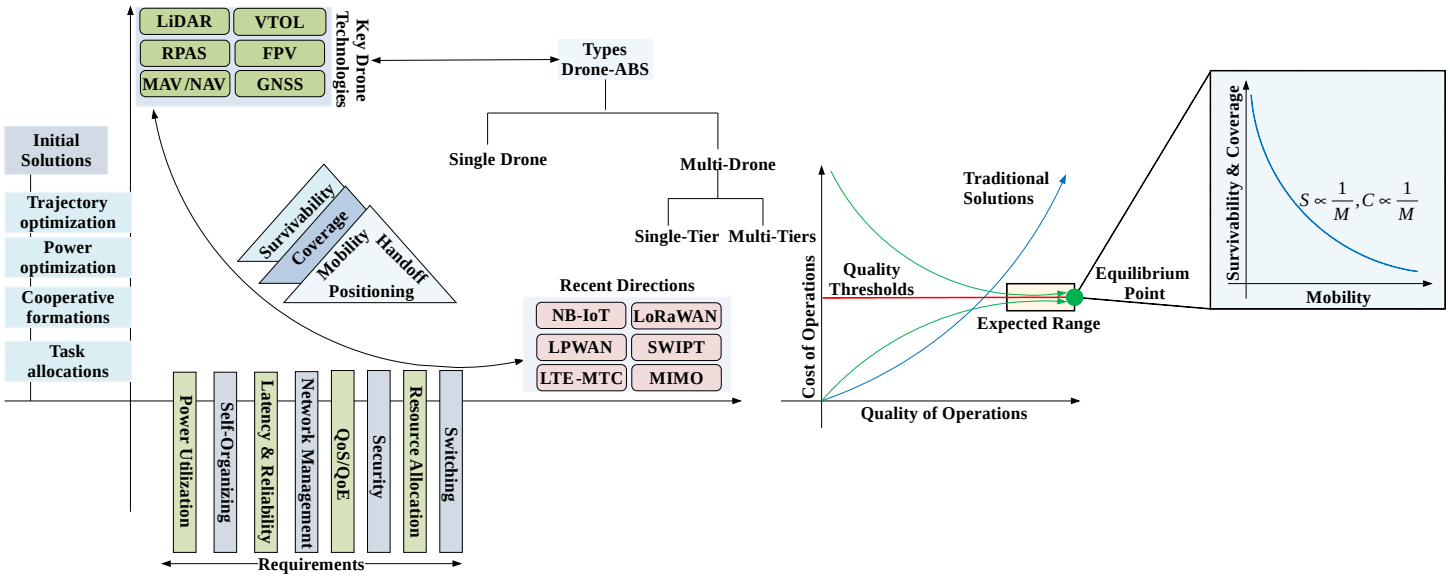

Figure 7.9: *An overview of existing solutions, technologies and research to follow for using ABSs with TCN.*

There are several challenges to resolve in this direction of research such as power utilization, self-organization of drones in tiers, ultra-high reliability and ultra-low latency, mobility management and enhancement of QoS/QoE for the users. Solutions like Narrow-Band IoT (NB-IoT), Long Range Wide Area Network (LoRaWAN), Low Power Wide Area Network (LPWAN), LTE-Machine Type Communications (LTE-MTC), SWIPT, MIMO or Massive-MIMO, Massive-IoT can be used in the formation of highly survivable ABS networks. The research issues related to the effective utilization of these technologies and their suitable incorporation for drone communications are still open and have a long way to follow.

7.8 Conclusions

This chapter focuses on the crucial aspects of survivability, coverage and mobility laws for the multi-ABSs network. The proposed approach provides an optimal solution for these three factors while maximizing the probability of connectivity and likelihood of mapping multi-tier ABSs and underlying users. Use of dynamic nodes, such as drones, not only provides flexibility of operations but also has a considerable impact on the TCO. With hierarchical formations, multi-ABSs can be operated in tiers, which

allow significant control over the network and enhance the overall performance. Results presented in this chapter show that the proposed approach accounts for maximizing the accuracy in using multi-tier ABSs according to the geographical area with lesser iterations. In addition, the chapter also presented details on the several optimization issues, overview of existing solutions, available technologies, and research to follow for using ABS with TCN.

CHAPTER 8

Effect of Imperfect CSI on Interference Alignment in Multiple-High Altitude Platforms based Communication with a Generalized Long Distance Line of Sight Channel Model

INTERFERENCE alignment has proven to achieve maximum sum-rate in an X Channel. Though IA is proposed for maximizing sum-rate, its application for exploiting high data rate communication in A2G communication has not been explored much. In this chapter, IA is considered in a HAP to GS communication link. As it is well known, IA achieves maximum sum-rate for multiple transmitter-receiver system. However, independent channels are inevitable to achieve IA conditions. In this scenario, application of IA is proposed in a more generalized channel for HAP to GS communication taking into account the AoA and AoD. In this chapter, the minimum distance criteria has been verified to achieve independent channels. The BER performance is reported for both non IA based communication and IA based communication, to identify optimal distance between

receivers to achieve better error performance. Furthermore, in view of an actual scenario, the effect of imperfect CSI was investigated, resulting from changes in imperfection in HAP's stabilization, in the performance of the model. The performance, in terms of BER is presented for IA and non-IA based communication. For this purpose, an analytical expression is developed for the probability of error. A perfect match is shown between the error rate measured with Monte Carlo simulations and the error probability found using the derived analytical expressions.

8.1 Introduction

Among multiple transmitter multiple receiver communication systems, the K-user interference channel and the K-user X network have found considerable attention [Jafar, 2011]. While K-user interference channel considers K transmitter-receiver pairs, an X channel has data in K transmitters, intended for each of K receivers.

A K-user X network is referred to as an X channel when $K = 2$. Capacity of an X channel, has been defined for high signal-to-noise ratio (SNR) region in [Maddah-Ali et al., 2008]. In a generalized form, at larger SNR, the capacity of a network versus SNR can be approximated as

$$C(\mathrm{SNR}) = d \cdot \log(\mathrm{SNR}) + \mathcal{O}(\log(\mathrm{SNR})), \tag{8.1}$$

where d defines the number of degrees of freedom (DoF) and SNR is the signal-to-noise ratio of the network. DoF is also referred to as multiplexing gain or capacity prelog. The DoF has been found to be $4/3$ for a X channel in [Jafar and Shamai, 2008], which further depicts the capacity of the channel in high SNR regime.

Though many schemes are applicable in an X channel, IA achieves the desired DoF of $4/3$ in an X channel [Cadambe and Jafar, 2008b]. This means that IA for a X channel attains upper bound in capacity than any other known scheme. In [Prasad et al., 2015], the authors propose sharing a huge amount of data (for eg. multimedia file) by two base stations and to communicate to mobile user which is in the vicinity of both the BSs. Hence X channel finds interesting applications and achieves maximum capacity. In this scenario, the possibility of using IA for HAP to GS based communication was investigated.

The main advantage of HAPs is to provide high spectral efficiency to larger geographical area over terrestrial and satellite communication due to its unique position. HAPs are located at heights between 17 Km and 22 Km above earth surface and ITU-T has allotted two bands, 31 GHz and 48 GHz

for its communication [Grace and Mohorcic, 2011]. Such heights provide a LoS path between HAP and GS [Grace et al., 2005, Mohammed et al., 2011]. In this work, the possibility of IA in the HAP communication system was explored. The system consists of two HAPs serving two GSs with overlapping service areas. This essentially forms a X channel for which IA allows maximization of capacity.

An important assumption made in [Cadambe and Jafar, 2008a] is that CSI is globally available at each transmitting and receiving node. Knowledge in global CSI enables us to write closed form expressions for the precoding and zero-forcing (ZF) matrices. This means that, performance of IA is heavily dependent on precise CSI. HAPs and GSs rely on locally available CSI for the computation of CSI, and hence for designing ZF and precoding matrices. To this end, the effect of imperfect CSI was investigated, which may occur due to the absence of station keeping of HAPs.

MIMO channel matrix plays a crucial role in dictating the nature of the communication channel. It is indeed a requirement of the communication system to have full rank channel matrix to exploit the property of eigenmode transmission. This is very important to achieve higher capacity in MIMO communication. In this regard, having independent channels is a must to exploit this capacity. However, since HAPs are located at a higher position, having independent channel is a bottleneck for the design of the communication system. In [Torkildson et al., 2011], suggest separating receiver nodes to provide independent channels. This separation is a function of center frequency, distance between transmitter and receiver, and antenna separation at transmitter and receiver [Torkildson et al., 2011, Irish et al., 2013b, Irish et al., 2013a].

The channel model suggested in [Torkildson et al., 2011] is applied for large distance LoS wireless communication. Hence, to achieve zero correlation between channels or to achieve independent channels for HAP communication, receivers are to be separated. However, since it is impossible to achieve IA in single rank MIMO communication, in this chapter, it was suggested a more generalized channel model for HAP to GS communication, considering the AoA at the receiver and AoD at the Transmitter.

The chapter is organized as follows. A review of system model and channel modeling is provided in Sec. 8.2. In Sec. 8.3 a detailed explanation of the IA scheme for 2×2 user X network A2G channel is given. Sec. 8.3, provides explanation for role of IA in HAP based transmissions. Sec. 8.4 is devoted to numerical results while conclusions are drawn in Sec. 8.5.

8.2 Interference Alignment for existing long distance LoS channel

In this section, the existing long distance LoS channel model proposed in [Torkildson et al., 2011] was discussed, and the possibility of applying IA in X channel was investigated. Multiple antennas are used at both HAP and GSs. The minimum receiver separation was also found to achieve independent channels. This is an important factor in capacity maximization.

8.2.1 Background

Under terrestrial communication, the channel is modeled as Rayleigh in urban areas and Rician in suburban areas. This is not the same for A2G channel [Zajić, 2012]. Under urban conditions, A2G channel experiences Rician fading due to the presence of LoS path. In suburban areas a Rayleigh fading is experienced due to the presence of stronger reflected signals which are stronger than LoS [Zajić, 2012]. A generalized approach consists in following a Rician distribution where both LoS and NLoS paths are considered. Therefore, the channel model can be represented as

$$\mathbf{H} = \sqrt{\frac{\kappa}{(1+\kappa)}}\mathbf{H}_{LoS} + \sqrt{\frac{1}{(1+\kappa)}}\mathbf{H}_{NLoS} \tag{8.2}$$

where $\mathbf{H}_{LoS}$ represents shadowed free space propagation loss and $\mathbf{H}_{NLoS}$ represents only the NLoS path. Hence $\mathbf{H}$ is the $N_R \times N_T$ matrix having complex fading coefficients, where N_R and N_T are the number of receiving and transmitting antennas. By denoting as σ^2_{LoS} and σ^2_{NLoS} the power of LoS path and NLoS path, respectively, the Rician factor κ is given by [Cho et al., 2010]

$$\kappa = \frac{\sigma^2_{LoS}}{\sigma^2_{NLoS}} \tag{8.3}$$

The MIMO channel is considered to be static and hence the LoS MIMO channel is defined, neglecting the distance between transmitter and receiver, as in [Cho et al., 2010]

$$\mathbf{H}_{LoS} = \begin{bmatrix} 1 \\ e^{j2\pi\frac{d_R}{\lambda}\sin(\mathrm{AoA}_R)} \\ \vdots \\ e^{j2\pi\frac{d_R}{\lambda}(M-1)\sin(\mathrm{AoA}_R)} \end{bmatrix} \begin{bmatrix} 1 \\ e^{j2\pi\frac{d_T}{\lambda}\sin(\mathrm{AoD}_T)} \\ \vdots \\ e^{j2\pi\frac{d_T}{\lambda}(N-1)\sin(\mathrm{AoD}_T)} \end{bmatrix}^T,$$

where d_R and d_T represents the antenna spacing in the receiver and transmitter, respectively, AoA_R represents the AoA at the receiver and AoD_T the AoD at the transmitter. Since $\mathbf{H}_{NLoS}$ represents only the NLoS path, the resulting NLoS MIMO channel follows a Rayleigh distribution.

A 3D MIMO based channel model for planar array of antennas in a single HAP, communicating to several randomly placed GSs are considered in [Hu et al., 2016]. Similar work in [Irish et al., 2013b] consider channel model for long distance wireless fiber application. The effective long distance channel from n^{th} transmitter to m^{th} receiver is modeled as

$$h_{m,n} = \frac{\lambda}{4\pi R} \exp(-j\frac{2\pi}{\lambda}(R + \frac{(md_T - nd_R)^2}{2R})), \tag{8.4}$$

where R is the distance between transmitter and receiver. However, the directional beam from a transmitter is attained using sub arrays with beamsteering. Hence, from the above mentioned setting, transmitter provides array gain rather than spatial multiplexing gain.

8.2.2 Imperfect CSI

With the transmitter-receiver separation of 17-22 kms, and absence of precise station keeping, it is difficult to obtain precise CSI, which is necessary to perform IA. In addition, ZF and precoding matrices are designed from locally estimated CSI. Hence, it is obvious to assume imperfection in the obtained CSI. In this chapter, imperfect CSI $(\hat{\mathbf{H}})$ was related to actual CSI $(\mathbf{H})$ using a correlation coefficient (ρ), as in [Ustok et al., 2013].

$$\hat{\mathbf{H}} = \rho\mathbf{H} + \bar{\rho}\Phi, \tag{8.5}$$

where the correlation coefficient, $\rho \in (0, 1)$ and $\bar{\rho} = \sqrt{1-\rho^2}$ and Φ is Normally distributed with $\mathcal{N}(0, 1)$. To analyze the effect of imperfect CSI on the model, precoding and ZF matrices are designed from locally available CSI ie. $\hat{\mathbf{H}}$.

8.2.3 Long distance LoS channel and Receiver separation

Firstly, transmission power and attenuation in HAP communication which influence the transmitter design were addressed. For an HAP communication, the minimum path loss experienced is due to the free space path loss. This is overcome in unmanned aircrafts like Helios [Karapantazis and Pavlidou, 2005] by employing solar cells, with wings spanning $35 - 70$ m. The mission is designed to last for about 6 months, and hence no extra human interference is needed throughout the mission. Hence, in the chapter, power allocation as a design consideration was not considered.

It was started with LoS MIMO as a basic structure to model LoS communication in HAP based communication. Though [Torkildson et al., 2011] used multiple antennas at the transmitter and receiver, it was intended to attain array gain and not spatial multiplexing gain. It is the required to have higher capacity in the system to meet the present and future demands. To this end, [Irish et al., 2013b, Irish et al., 2013a] suggested that spatial multiplexing can still be used at the long distance LoS channel, provided the separation between antennas in the sub arrays are large enough to provide zero correlation between subsequent channels. However, inter antenna separation distance varies with center frequency and separation between transmitter and receiver. The inter antenna distance should be chosen such a way that it complies with equation.

$$d_T d_R = n\frac{R\lambda}{DoF} \tag{8.6}$$

where n can be any integer except the DoF.

Here, the required inter antenna spacing for HAP to GS communication, was found. The operating band was considered as 48 GHz and height at which HAP is located as 18 Km. Hence from (8.6), with antenna separation at transmitter $d_T = 1$ m and $DoF = 2$, the inter antenna separation at the receiver was found as $d_R^{opt} = 56.2$ m. This means that it is possible to exploit spatial multiplexing in HAP communication, if the receiver antenna separation is 56.2 m, which further means maximum capacity transmission.

8.3 Role of Interference Alignment for HAP based transmission

In this chapter two HAPs serving a common area were considered, where two receivers are situated. This essentially forms a 2×2 X channel. Hence, the performance was investigated by considering the system as two-user MIMO X channel as shown in Fig. 8.1.

8.3.1 Background of Interference Alignment

The block diagram of the two-user MIMO X channel is shown in Fig. 1. Each transmitting and receiving node is equipped with three antennas. The received signal vectors for user 1 and user 2 are

$$\mathbf{y}_1 = \mathbf{H}_{11}\mathbf{x}_1 + \mathbf{H}_{12}\mathbf{x}_2 + \mathbf{n}_1 \tag{8.7}$$

and

$$\mathbf{y}_2 = \mathbf{H}_{21}\mathbf{x}_1 + \mathbf{H}_{22}\mathbf{x}_2 + \mathbf{n}_2, \tag{8.8}$$

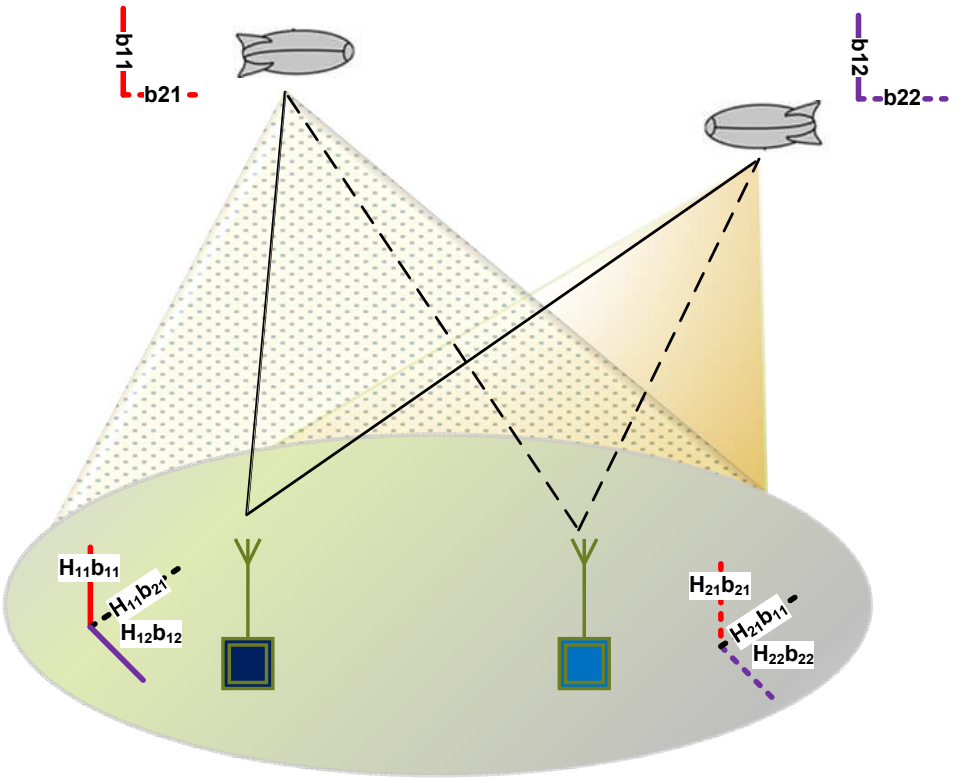

Figure 8.1: *HAP communication architecture with overlapped coverage area*

respectively, where $\mathbf{x}_i$ is the 3×1 signal vector transmitted by the i-th user, $\mathbf{H}_{ji}$ is a 3×3 channel matrix between transmitter i and receiver j, with $i, j \in \{1, 2\}$, whose elements are assumed to be IID complex Gaussian random variables with zero mean and unit variance, and $\mathbf{n}_j$ is a 3×1 vector of i.i.d. complex Gaussian random variables with zero mean and variance σ_n^2. Each transmitter is intended to transmit independent messages to each of the receivers separately. The two transmitted vectors are given by

$$\mathbf{x}_1 = \mathbf{b}_{11}x_{11} + \mathbf{b}_{21}x_{21}, \tag{8.9}$$

$$\mathbf{x}_2 = \mathbf{b}_{12}x_{12} + \mathbf{b}_{22}x_{22}, \tag{8.10}$$

where x_{ji} is the message to be transmitted from transmitter i to receiver j and $\mathbf{b}_{ji}$ is the beamforming vector associated with x_{ji}. By replacing (8.9) and (8.10) in (8.7) and (8.8), respectively,

$$\begin{aligned} \mathbf{y}_1 \;=\; & \mathbf{H}_{11}\mathbf{b}_{11}x_{11} + \mathbf{H}_{11}\mathbf{b}_{21}x_{21} + \\ & + \mathbf{H}_{12}\mathbf{b}_{12}x_{12} + \mathbf{H}_{12}\mathbf{b}_{22}x_{22} + \mathbf{n}_1 \end{aligned} \tag{8.11}$$

and

$$\begin{aligned}\mathbf{y}_2 &= \mathbf{H}_{21}\mathbf{b}_{11}x_{11} + \mathbf{H}_{21}\mathbf{b}_{21}x_{21} + \\ &+ \mathbf{H}_{22}\mathbf{b}_{12}x_{12} + \mathbf{H}_{22}\mathbf{b}_{22}x_{22} + \mathbf{n}_2. \end{aligned} \tag{8.12}$$

In order to satisfy the IA condition the interfering signals must span the same subspace [**?**]

$$SPAN\left\{\mathbf{H}_{12}\mathbf{b}_{22}\right\} = SPAN\left\{\mathbf{H}_{11}\mathbf{b}_{21}\right\}, \tag{8.13}$$

$$SPAN\left\{\mathbf{H}_{22}\mathbf{b}_{12}\right\} = SPAN\left\{\mathbf{H}_{21}\mathbf{b}_{11}\right\}. \tag{8.14}$$

A possible choice of beamforming vectors is

$$\mathbf{b}_{22} = \mathbf{H}_{12}^{-1}\mathbf{H}_{11}\mathbf{b}_{21} \tag{8.15}$$

and

$$\mathbf{b}_{12} = \mathbf{H}_{22}^{-1}\mathbf{H}_{21}\mathbf{b}_{11}. \tag{8.16}$$

Eqs. (8.15) and (8.16) define the original IA solution, here termed as "conventional IA". A ZF receiver is used to separate out undesired signals from the desired signals.

8.3.2 Achieving IA in rank 1 MIMO channel

It is required to choose $\mathbf{b}_{21}$ and $\mathbf{b}_{11}$ as two independent vectors and $\mathbf{b}_{22}$ and $\mathbf{b}_{12}$ are obtained from Eqs. (8.15) and (8.16).

For illustrating the communication along rank 1 channel, first the case of receiver 1 was considered. With $\mathbf{b}_{11}$ defined, with rank 1 channel matrix, $\mathbf{b}_{11}$ is nothing but an amplified/ attenuated version of $\mathbf{b}_{11}$. This essentially means that equation (8.16) results in non independent vectors. As a result, $\mathbf{H}_{22}\mathbf{b}_{12}$ and $\mathbf{H}_{21}\mathbf{b}_{11}$ are aligned along same direction in receiver 1, which further means that independent vectors intended for ZF data from two transmitters become dependent.

This is the same for receiver 2. Choosing $\mathbf{b}_{22}$ as attenuated/ amplified version of $\mathbf{b}_{21}$ leads to aligned vectors at receiver 2. In effect, due to the presence of rank 1 channel, the IA decoding is compromised. In this scenario a more generalized LoS channel for long distance wireless communication was proposed.

8.3.3 Achieving IA through Generalized channel model

Consider a MIMO link with N_t transmitter antennas and N_r receiver antennas. The beam leaves transmitter at an angle called AoD and is received in

the receiver at an angle called AoA. Now, it can be easily inferred that each antenna to antenna link is indeed dependent on AoA, AoD and R. Under these circumstances , the complex channel gain $h_{m,n}$ is modeled as

$$\begin{aligned} h_{m,n} &= \frac{\lambda}{4\pi R}\exp\Big(-j\frac{2\pi}{\lambda}\big(m\frac{\lambda}{2}\sin(AoA) \\ &\quad +n\frac{\lambda}{2}\sin(AoD) \\ &\quad +R+\frac{(m\frac{\lambda}{2}-n\frac{\lambda}{2})^2}{2R}\big)\Big) \end{aligned} \tag{8.17}$$

where n $= 1, \ldots, N_t$ and m $= 1, \ldots, N_r$. It can be easily inferred that the channel coefficients differ due to the AoA and AoD, as a result the beamforming vectors for performing IA will be independent and this in turn forms independent vectors at the receiver. At the receiver, data from both the transmitter are now aligned over independent vectors and information can be recovered. Hence with this generalized channel model, IA can be carried out.

8.4 Numerical Results

In this section the error performance of the long distance LoS MIMO X channel is analyzed for non IA based and IA based transmission. The symbols x_{11}, x_{21}, x_{12} and x_{22} are chosen from a quadrature phase-shift keying (QPSK) constellation. Assuming an average transmitted power from each antenna equal to P_{ave}, the signal-to-noise ratio is defined as $\mathrm{SNR} = P_{ave}/\sigma_n^2$. As in [Mahmoud et al., 2012], the coefficients of MIMO channels are assumed to remain constant for the entire duration of payload data transmission. Monte Carlo simulations are presented to evaluate the BER of the proposed IA scheme. The BER is computed as the ratio between the number of wrongly detected bits and total number of transmitted bits.

Figure 8.2 reports the BER performance of the non IA based system for different antenna separation distances. By non IA based system, singular-value decomposition (SVD) based transmission for single transmitter single receiver MIMO system, was implied. It was started by setting the inter antenna separation at receiver d_R as 10 m, while keeping inter antenna separation at transmitter d_T as 1 m. It can be seen that as d_R is varied from 10 m to 20 m, the performance is improved and this is again scene when d_R is 50 m. Hence the result coincide with the intuition in [Torkildson et al., 2011, Bohagen et al., 2005] that, antenna separation at receiver or transmitter provides independent channel further exploiting spatial multiplexing

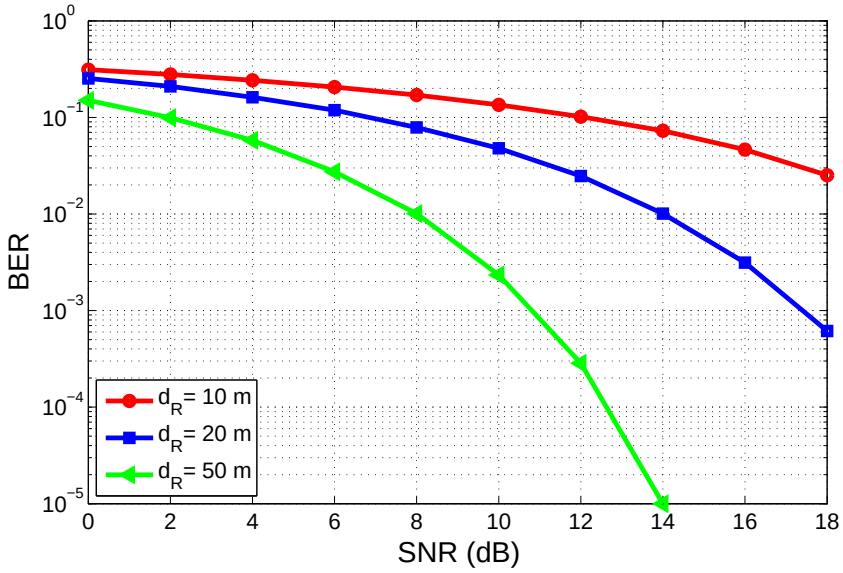

Figure 8.2: *BER versus SNR of non IA scheme for receiver antenna separation* $d_R = 10, 20, 50\,m$.

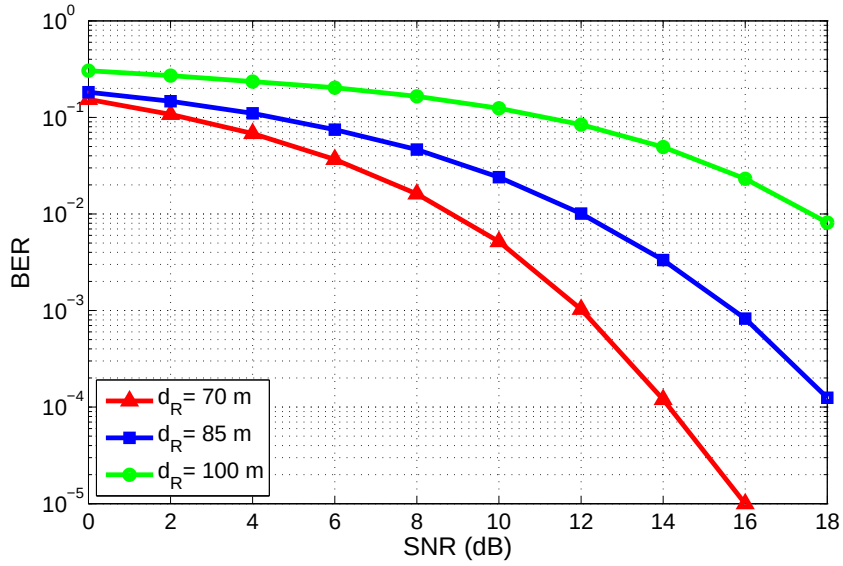

Figure 8.3: *BER versus SNR of non IA scheme for receiver antenna separation* $d_R = 70, 85, 100\,m$.

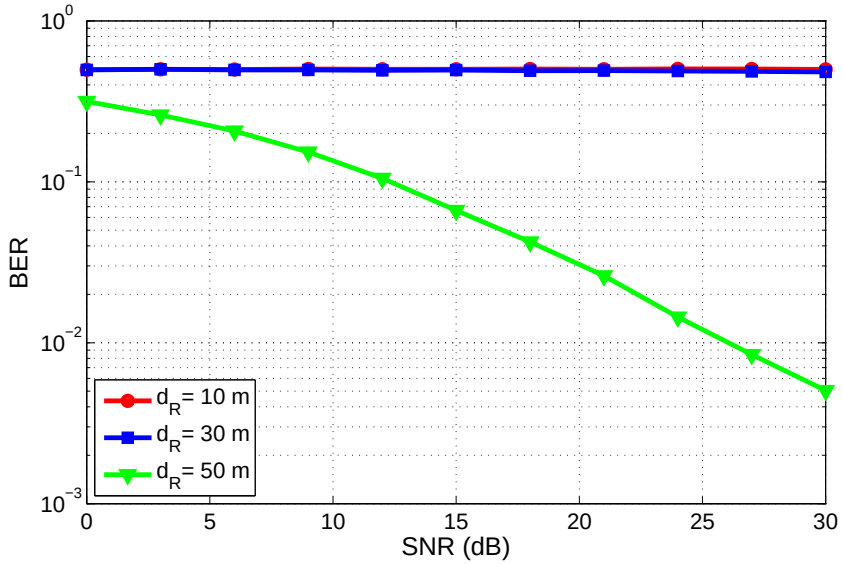

Figure 8.4: *BER versus SNR of IA scheme for receiver antenna separation* $d_R = 10, 30, 55\,m$.

and diversity.

Figure 8.3 shows results similar to those of Fig. 8.2, except that the inter antenna distances chosen are above the minimum inter antenna spacing found from 8.6. As d_R varies from $70\,\text{m}$ to $85\,\text{m}$ a significant reduction in BER performance can be noticed. This is in agreement with [Irish et al., 2013a], which states the performance decreases above $\frac{\lambda R}{N d_T}$. This was further investigated to observe behavior at higher SNR values. By further simulation, it is possible to observe that $\frac{n\lambda R}{N d_T}$ shows the best result when n is an odd number and worst performance when n is even. On increasing d_R to $100\,\text{m}$, performance is highly deteriorated. This effect is due to the correlation factor between successive channels. Analyzing Figs. 8.2 and 8.3, it can be concluded that inter-antenna spacing as calculated in (8.6) has the best BER performance and hence using (8.6), the optimal antenna separation at receiver can be found.

Now the impact of IA based communication was considered for a scheme with two HAPs and two GSs in overlapped coverage area. Eq. (8.17) is used for modeling MIMO channel from HAP to GS. With AoA and AoD set as 60 degree [Grace and Mohorcic, 2011], and d_T is set as 1 m for fair comparison. In Fig 8.4, it is interesting to note that the results are similar to non IA based transmission, as given in Fig 8.2. But there is a significant

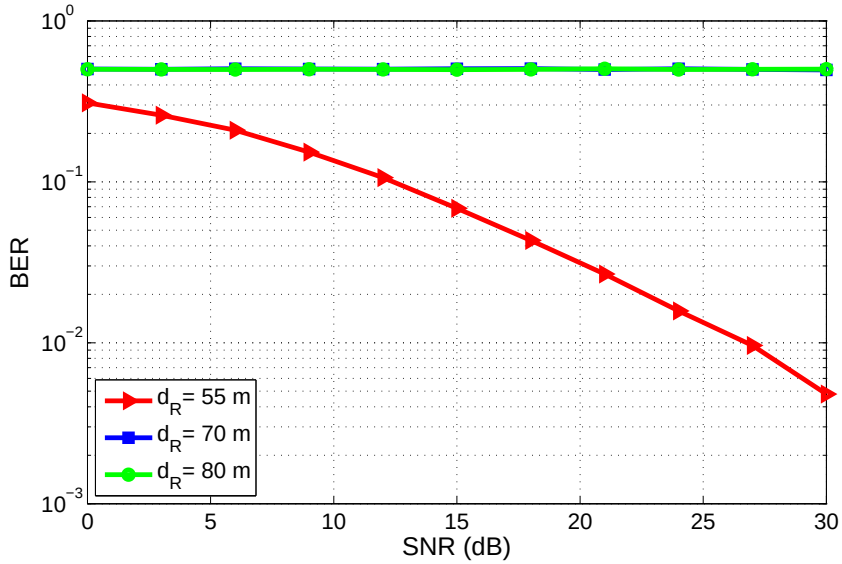

Figure 8.5: *BER versus SNR of IA scheme for receiver antenna separation* $d_R = 55, 70, 80\,m$.

difference in performance for $d_R \neq d_R^{opt}$. The reason behind such a heavy depredation in performance is that independent channels are available only at d_R^{opt}, where beam forming vectors in IA remain independent. This can again be seen in Fig 8.5 that performance is highly compromised as d_R is varied from 55 m to 70 m and 80 m. It is worth noting that the optimal inter antenna spacing d_R^{opt} remains valid in IA based transmission and with the proposed channel model.

In Fig. 8.6, the CDF of the sum-rate for imperfect channel was investigated. Channel imperfection is represented by ρ. $\rho = 1$ implies perfect CSI and lowering ρ represents larger channel imperfection. From the figure, it is clear that sum-rate degrades with ρ. This is due to the fact that, IA performs perfectly with precoding and ZF matrices, designed from perfect CSI. Beamforming vectors designed from imperfect CSI, shows deviation from desired vectors, and forms non correlated vectors. Results shows that, variation in locally available CSI, which is used to design ZF and precoding matrices, leads to drastic reduction in sum-rate. Furthermore, absence of station keeping will also lead to similar performance degradation. Note that, since IA was considered for multiple HAP-GSs communications, SINR is same as SNR.

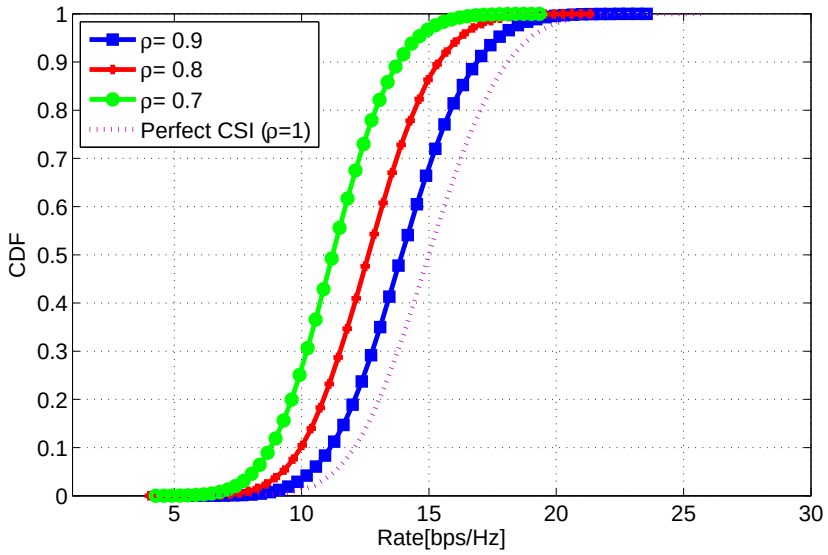

Figure 8.6: *CDF vs SNR for system with imperfect CSI*

8.5 Conclusion

Interference Alignment achieves upper bound in DoF in an X channel. Though IA in X channel provides higher capacity, performing IA in rank 1 MIMO channel is a challenge. In this scenario a new generalized MIMO channel model considering AoA and AoD and transmitter receiver separation has been proposed. This effectively overcomes the limitation to perform IA due to rank 1 MIMO channel.

Furthermore, the optimal receiver separation for HAP communication in an X channel has been found. The optimal separation found is the same for IA and non IA based communication. With IA being the key player in providing higher capacity in an X channel, IA based HAP to GS communication was proposed. The advantage of the proposed channel model is that, IA can be successfully carried out, due to variation in attenuation of independent channels. Effect of imperfect CSI for multiple HAPs-GS communications is also investigated. Higher channel imperfection leads to loss in data rate.

Part III

Minor Project

CHAPTER 9

Fault Recovery in Time-Synchronized Mission Critical ZigBee-based Wireless Sensor Networks

RELIABILITY and precise timestamping of events that occur are two of the most important requirements for mission critical wireless sensor networks. Accurate timestamping is obtained by synchronizing the nodes to each other while reliability can be obtained by eliminating SPF. In this chapter, the SPF problem of a ZigBee-based wireless sensor network is addressed by means of using multiple coordinators with different PAN IDs. A solution is proposed where members of a network switch from one coordinator to another in case of failure by changing their respective PAN ID. It is experimentally verified that the proposed solution provides gains in terms of recovery speed and, therefore, synchronization accuracy with respect to a solution proposed in the literature.

9.1 Introduction

In the recent years, use of WSNs has increased hugely due to the rapid development of information and communication technologies [ITU, a]. WSNs are characterized by the use of tiny, low cost and low energy devices, termed *nodes*, that are designed to provide connectivity in an environment without any preexisting infrastructure. Their main purpose is to collect and aggregate data acquired from sensors, installed on-board end nodes, that measure various physical quantities [ITU, b].

For instance, if wireless sensors are deployed in a battlefield to know the enemy tank movement, i.e. velocity of the tank, different sensor nodes observe this phenomenon and send the information to a sink. To get the correct information it is mandatory to keep all these nodes on a common notion of time [Chand Gautam and Chand Kaushal, 2014]. The protocols which provide this common notion of time are known as time synchronization protocols [Chand Gautam and Chand Kaushal, 2014].

When developing and designing a WSN platform, that is thought for a specific application, developers have to satisfy a rather wide range of requirements. The search for a balance between cost of sensor nodes and requirements represents a challenging task in each specific application. Therefore, one of the main goal in ongoing research activities is the improvement of WSNs technical characteristics to expand their field of application. This can be made possible, without significantly increased costs, by developing new technologies and protocols [ITU, b]. Concerning these two latter aspects, recently, increasing interest in the use of WSN for mission critical applications was witnessed, where the requirement of reliable data transmission from source to destination is one of the most important challenges together with the possibility of providing precise timestamping of events [Mahmood et al., 2015].

The flexibility of WSNs allows their use in a variety of innovative applications: from small body area networks, used to monitor health parameters [Lo et al., 2005], to large arrays of sensor nodes, used to monitor structural integrity [Xu et al., 2004] or dangerous physical phenomenons such as volcanic eruptions [Werner-Allen et al., 2006].

Besides providing sustainability against elements' failures, in order to correctly interpret data collected from multiple sensor nodes in different locations and time instants, it is necessary to maintain a common notion of time across all the nodes. This requirement is usually achieved by means of time synchronization protocols [Chand Gautam and Chand Kaushal, 2014]. A popular technology for providing connectivity in WSNs is the IEEE

802.15.4 standard for *"Low-Rate Wireless Personal Area Network"*, which has been specifically developed for low-power devices such as the nodes of a WSN [ITU, b]. Many standards are available that rely on IEEE 802.15.4 for the lower layers: ZigBee [ZBe,], WirelessHART [HCF,], and 6loWPAN [6Lo,]. Each of them has its own advantages and disadvantages when used for implementing a WSN. Among these protocols the focus here is on ZigBee, being it the most widely adopted standard in industrial applications mainly because its low cost hardware [Han and Lim, 2010].

Special attention is given to ZigBee, which is the most widely used standard for energy constrained applications including WSNs. ZigBee is a suite of high level communication protocols used to create PANs. Low energy consumption in ZigBee networks is achieved thanks to the distinction of nodes in two categories: Full Function Devices (FFDs) and Reduced Function Devices (RFDs). The FFD nodes are always on and are tasked with providing the infrastructure of the network, thus allowing extended sleep cycles for other devices. On the other hand, RFD nodes are sleepy end devices that establish a single link to one FFD, referred to as its parent [ZBe,]. The FFDs in a ZigBee network are divided in Coordinator and Routers. Each ZigBee network has a unique Coordinator, which is tasked with network formation and maintenance. Only one coordinator is allowed per network and once a network is formed no other coordinators may join it even if the original coordinator shuts down or has a failure. Different ZigBee coordinators operating in the same physical channel will be part of different networks, each one with its own unique PAN ID. ZigBee does not present a solution to deal with the loss of the coordinator, leading to a SPF problem [Willig and Karl, 2005]. The node which starts the network is called PAN coordinator and for every PAN only one coordinator is allowed. Since the coordinators tasked with starting the network it is not possible for a coordinator to join an existing network. This results in a conflict if the coordinator fails and a new coordinator needs to replace it. ZigBee supports different network topologies such as star, tree, and mesh [Willig and Karl, 2005], which all suffer from the mentioned SPF issue. The star topology, for example, will completely fail if the central coordinator fails. In a tree topology the coordinator needs to be the root node, therefore, in the event of a coordinator failure the network will experience a partial failure. A mesh topology is the most robust against coordinator failures as some parts of the networks can remain functioning if enough routers are left. Even in this topology, however, a coordinator failure can still cause the failure of the entire network in some cases.

Since this is a well known problem, a solution has been presented in

[Kölln and Zimmermann, 2009] to address this issue. The proposed approach solves the issue by storing back-ups of the coordinator on a router node which, in case of failure, is reprogrammed to become a clone of the missing coordinator. However, by using this approach a long time is required to recover and, consequently, the downtime of the network and synchronization error increase.

In this chapter, it was proposed and assessed a simpler alternative based on the changing of the PAN ID in place of reprogramming a router to become the new coordinator of the network. The new solution gives advantages in terms of lower downtime, because it takes advantage from ZigBee's low network joining time of end node devices, which is in the order of a few milliseconds [Baker, 2005], and in terms of ease of implementation, since it uses only features provided by the standard. Moreover the timing synchronization protocol is very important in mission critical applications where an accurate timestamping of the data collected by sensor nodes is required [Bae, 2014]. A simple technique was presented for achieving time synchronization at the sensor level and experimentally evaluate its performance, with special focus on the impact that the WSN recovery after a failure has on the synchronization of the sensor nodes within the network. Our experiments were performed using commercial off the shelf (COTS) devices, which are often ill suited to meet the requirements of mission critical applications. The purpose of this work is enabling devices that would otherwise be unsuitable for mission critical applications to at least meet requirements of link robustness. The specific requirements of mission critical applications can be very different and may include requirements that cannot be satisfied by ZigBee such as very low latency, in those cases different communication protocols may be able to overcome this issue. Link robustness, however, remains a common requirement to all critical applications where loss of connection will lead to loss of profit or worse. Therefore, this important aspect was focused. The three main issues focused in this chapter are:

- SPF problem in the ZigBee network.
- Timing synchronization problem in WSNs.
- Impact of SPF problem on the timing synchronization protocol.

The rest of the chapter is organized as follows. In Sec. 9.2, single point of failure problem is described. In Sec. 9.3, synchronization problems in WSNs' have been addressed. Section 9.4 gives a survey of the synchronization methods available for WSNs and of the solutions present in the

literature to solve the ZigBee's SPF problem. The proposed solution to the SPF problem is described in Sec. 9.5. Section 9.6 illustrates the specific synchronization protocol implemented in the prototype. Experimental results are given in Sec. 9.7 and, finally, Sec. 9.8 concludes the chapter.

9.2 Single Point Failure Problem

ZigBee is a standard designed specifically for low power and easy to deploy wireless devices. It is especially used for WSNs to build automation and low data rate measurement applications. There is a significant impact of failure of the device on the safety critical application [Dobslaw et al., 2013]. The interest was developed in the case where the failure of a node can compromise the entire network like that of the failure of a coordinator node in a ZigBee network. A solution was proposed where other coordinators in hot-standby can take over the network and a mechanism which allows orphaned nodes to detect coordinator failure and attempt to connect to a new coordinator. Data continuity can be achieved during the recovery process by introducing redundant elements as shown in Fig. 9.1. For the applications where data continuity is a safety critical requirement this setup allows the system to function with up to N-1 sensor failures and up to M-1 coordinator failures where N and M are the number of sensors and coordinators, respectively.

In each sensor node, a program monitors the connection, detects coordinator failures, and begins the recovery procedure from the SPF problem. The main difference from the solution proposed in [Kölln and Zimmermann, 2009] is that the proposed method is based on changing the PAN ID of the nodes rather than reprogramming a node to become the new coordinator. The procedure for PAN ID change is described by the flow chart shown in Fig. 9.2. As can be observed in the figure, the program is divided into two Sections: *Normal operation* and *Failure recovery*. Failure of the coordinator is detected through the lack of ACK packets from the coordinator with a timeout or alternatively through an ACK sent by the transmitter module after several retries. Once a failure is detected a subroutine which sends the command to change PAN ID is called. At this point the switch is considered successful if a network join notification is received, otherwise it is possible to switch to another PAN ID and try again. This procedure is applied to all nodes affected by the coordinator failure. While the experiments performed considered only one device, the procedure can recover multiple devices at the same time and any conflict during the re-association phase are resolved by the ZigBee MAC layer contention resolution algo-

rithm. The advantage of this method is to provide a shorter coordinator downtime. The downside of this approach compared to the alternative described in [Kölln and Zimmermann, 2009] is the increased hardware costs from having inactive nodes as backup coordinators. For the experimental verification this program was deployed on Arduino boards connected to XBee S2 ZigBee devices. The description of the experimental setup will be given in Sec. 9.7.

9.3 Synchronization problem in WSNs

All synchronization protocols rely on some sort of signal exchange between nodes. The time involved in sending a message is the result of the following four factors, which can vary in a non-deterministic way:

- send time, which is the sum of packetization and transmission times;
- access time, corresponding to the time spent for medium access;
- propagation time;
- receive time, which is the time required by processing at the receiver.

In this chapter, synchronization through TPSN [Djenouri and Bagaa, 2014] was performed. In this method timing offset is periodically estimated by exchange of relative timestamps T1, T2, T3 and T4 as shown in Fig. 9.4. The client sends his own timestamps in a packet to the server, which in turn sends back its own timestamps marking the time the packet is received and the reply is sent. The client then notes down its own timestamp when the reply is received and estimates the offset periodically as

$$Offset = \frac{(T_2 - T_1) - (T_4 - T_3)}{2} \tag{9.1}$$

While the periodic offset estimation is simple and easy to implement, the accuracy that can be achieved is strongly limited by the interval of time between synchronization exchanges. The frequency offset between the devices quickly builds up to a non-negligible error. Synchronization data is limited in size and the impact can be further reduced by attaching it to standard data frames in order to save on the protocol overhead. However, there are more efficient synchronization mechanisms that estimate the difference in frequency, called *Skew*, and compensate for it. As shown in Fig. 9.5, the skew is estimated as

$$Offset = \frac{Offset' - Offset}{TimingInterval} \tag{9.2}$$

Where Offset is calculated from the timestamps T1 to T4 and Offset' is calculated from the timestamps T1' to T4'. The downside of this approach is the increased complexity and memory footprint. Special measures, like avoiding the direct multiplying of the clock counter need to be taken to preclude machine precision errors. To measure the Skew and compensate for it an experiment was performed using general-purpose hardware and CoTS devices. While the Server/Client architecture used in TPSN reduces the number of packets needed for synchronization, the critical time interval increases introducing a greater variance on the estimated offset. On the other hand, this technique provides a substantial gain in precision for long-term synchronization after the initial setup. It must be preferred when network resources are the most important constraint, as in the case of ZigBee networks. The gain of this procedure was quantified in the experiment that is described in Sec. 9.7.

9.4 State of the Art in Synchronization and Solutions for Failure Recovery in Zigbee WSNs

9.4.1 Methods for WSN synchronization

Three basic methodologies for WSN synchronization are available in the literature [Bae, 2014]:

- *Relative timing:* each node monitors and compensates for offset and clock drifts with respect to other nodes. Synchronization is achieved by exchanging local timestamps between different nodes.
- *Relative ordering:* a relative order of events and communications is achieved by comparing local clocks. With this method it is not necessary to compensate clock offset.
- *Global synchronization:* if a global timescale such as GPS is available, all the nodes will synchronize.

Global synchronization is the best solution with respect to network overhead as each device can independently synchronize itself without using network resources. The main issue of *global synchronization* is the requirement of a GPS receiver in each node which is in direct contrast with requirements of low cost and low energy for WSNs. *Relative ordering*, on the other hand, is an attractive solution for its reduced burden on the nodes with respect to *global synchronization*. However, it is not a general solution as this method only establishes an order of events without offering actual clock synchronization. The most widespread synchronization

method for WSNs is *relative timing* as it gives a good compromise between the other two alternatives. Several timing protocols use this methodology: Timing-sync Protocol for Sensor Networks (TPSN), Flooding Time Synchronization Protocol (FTSP), and Reference Broadcast Synchronization (RBS) [Bae, 2014]. These protocols differ in the way they estimate the offset and clock drift for the independent nodes [Nayyer et al., 2011]. A brief overview of these protocols is given below:

- TPSN is based on a server client paradigm where the client sends a request for synchronization information to a timing server. It is divided in two phases: level discovery and synchronization. The level discovery phase has the goal of creating a hierarchy that establishes which nodes are servers and which nodes are clients for each synchronization phase. Multihop networks will have multiple levels where clients of one level will act as servers for the level above them. In this architecture the root node will always be at the bottom level. The estimation of the offset is achieved by the one-to-one exchange of timestamps between servers and clients.

- FTSP is a variation of TPSN which was developed to deal with frequent topology changes. There are two main differences with respect to TPSN: the root node is not fixed but it is instead constantly reelected and the synchronization information is flooded throughout the network.

- RBS differs from the other protocols as it is based on a receiver-to-receiver paradigm [Elson et al., 2002]. A reference beacon is broadcast by a third party and all receiving nodes exchange the relative time of reception for the beacon. The sent beacon does not contain any timing information and the synchronization is achieved by comparing the times of reception that the receivers exchange between one another.

As ZigBee provides a low transmission rate a TPSN protocol was implemented [Djenouri and Bagaa, 2014] that will be discussed in Sec. 9.6. In order to minimize protocol overhead, a static topology was focused on, where the levels have been manually assigned and where the discovery phase was not implemented. TPSN was chosen specifically over the other two methods that require broadcasts because they are poorly supported by the hardware used to build the prototype. The general advantages and disadvantages of a broadcast approach versus a uni-cast approach are covered in Sec. 9.6.

9.4.2 Solutions for failure recovery in Zigbee WSN

In WSNs for mission critical applications the goal is to avoid that the failure of a device impacts on the functionalities of the rest of the network [Dobslaw et al., 2013]. ZigBee has been designed for low power, low cost and easy to deploy wireless devices. It is mostly used in WSNs and other applications requiring low data rate transmissions and only provides limited solutions to manage failures. In the present work, interest was developed to the case where the failure of a node can jeopardize the operation of the whole network, as it might happen for the failure of the ZigBee PAN coordinator.

A ZigBee network can be set up as a tree, star or mesh network. However, all these topologies suffer from the SPF problem. In a star topology the coordinator is always the central node and, therefore, if the coordinator fails the whole network fails. For tree topology, the coordinator must be the root node and, in the event of a coordinator failure, the network will experience a partial failure. On the other hand, mesh topology is the most robust and, depending on its configuration, the whole network may remain intact after a coordinator failure. However, even in this last case, a failure of the entire network is possible if, for example, indirect binding of devices is used because binding tables are getting lost after a failure of the coordinator. New releases of the standard, such as ZigBee PRO, aim at reducing this problem and introduce a distributed storing of the binding tables across the routers [ZBA,]. Even in ZigBee PRO, however, it is required to have a trust center that is unique and, often, coincides with the coordinator of the network. Should this trust center fail, the network can continue working for some time, but functionalities such as authentication for joining/rejoining devices will be lost. Furthermore the network will progressively fail as the security keys expire [ZBA,].

Since the solution adopted in ZigBee PRO solves only partially the problem, a solution based on ZigBee is proposed in [Kölln and Zimmermann, 2009] where backups of the coordinator are stored in the routers. In the case of a coordinator failure the routers can be reprogrammed to become a clone of the coordinator. This solution is transparent to the application layer and requires minimal hardware overhead. The downside is the long time required to reprogram and reset a device, which leaves a gap in the data if the coordinator is used as the network sink. Moreover, many commercial devices do not allow resetting device parameters, including the 64-bit device *unique identifier*, thus making the solution difficult to implement using COTS hardware.

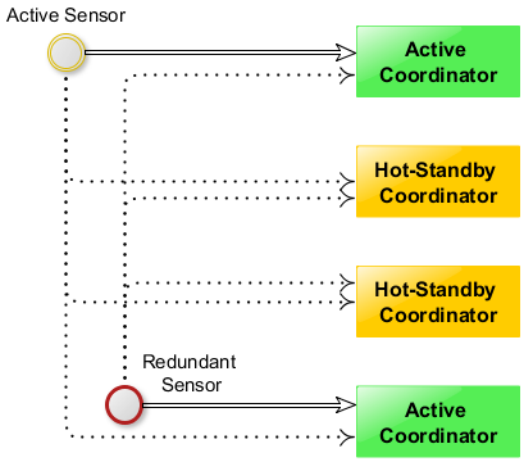

Figure 9.1: *Proposed scheme for maintaining data continuity through redundant sensor nodes during transition from active to backup coordinator. Dotted lines represent links formed only in case of failure. The scheme illustrates the case with N=4 coordinators and M=2 sensor nodes for a particular measure. The sensor nodes can have independent active and backup connections.*

9.5 Proposed Fast Recovery Procedure

The proposed fast recovery procedure relies on the use of redundant PAN coordinators in hot standby, ready to provide connectivity to other devices. Also, a procedure was introduced, implemented by the nodes belonging to the compromised network, to detect the failure and re-connect to a new coordinator. As is well known, ZigBee protocol is designed to have a low joining time. Our solution exploits this feature to minimize network downtime with respect to [Kölln and Zimmermann, 2009]. For real-time applications, where data continuity is a critical requirement, this can be achieved by introducing a redundant management of hardware components as illustrated in Fig. 9.1. The figure reports the case with 4 coordinators and 2 sensors that allows to recover up to 3 coordinator failures and 1 sensor failure. It is worth observing that, with such a setup, the system can recover up to $N-1$ coordinator failures and $M-1$ sensor failures, where N and M are the number of employed coordinators and sensors, respectively. Also, this allows us to separate the redundancy of the coordinator from that of the sensor which, as shown in Fig. 9.1, can have very different requirements. Gateways or data sinks are more critical than individual sensors thus they often have more stringent redundancy requirements which translate in a higher number of redundant components like the example shown in

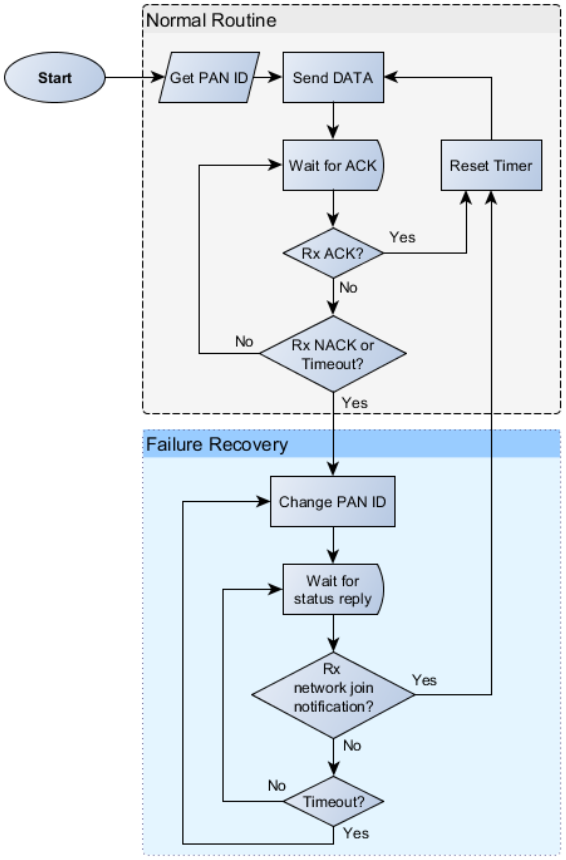

Figure 9.2: *Algorithm to automate PAN ID change on all nodes of the network. The PAN IDs of the available coordinator are assumed known.*

Fig. 9.1.

Each sensor node implements an algorithm to monitor the connection status and discover coordinator failures by timeouts. After detection of a failure it begins the recovery procedures. A block diagram of the monitoring algorithm which automates this procedure is reported in Fig. 9.2. The algorithm distinguishes between *Normal operation* and *Failure recovery*. A coordinator failure is detected by the lack of ACK replies to the data messages that are sent during normal operation. After a failure has been identified the recovery procedure begins switching trough PAN IDs to search for another coordinator. If no network joining notification is received, the algorithm will try again using a different PAN ID. The list of available PAN IDs for switching can be dynamically distributed by the coordinators when a new device joins the network. This procedure is executed

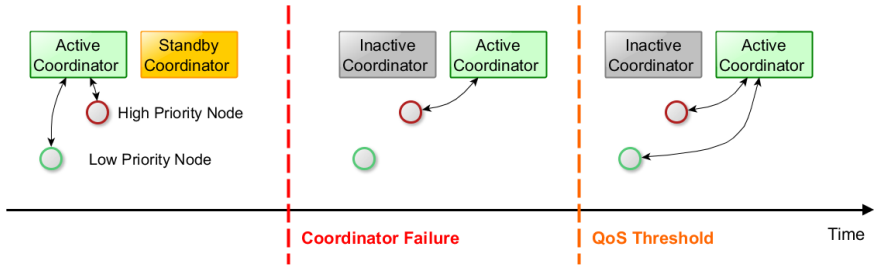

Figure 9.3: *Example of a QoS implementation for network switching based on time windows.*

on all network nodes that are affected by the failure of the coordinator. The proposed algorithm has been experimentally tested using commercial XBee S2 ZigBee devices mounted on Arduino boards. A full description of the experimental set-up will be given in Sec. 9.7.

The main difference with respect to the solution proposed in [Kölln and Zimmermann, 2009] is that the proposed method is based on switching to another network by changing the PAN ID rather than having a router reprogrammed to become the new coordinator. Both the cases of single and multiple device recovery were tested at the same time. The measured performance is the downtime with respect to the solution proposed in [Kölln and Zimmermann, 2009] as well as the impact of network formation overhead when multiple routers join a coordinator at the same time. In case the event of multiple devices switching exactly at the same time conflicts will be resolved at the MAC layer. The downside of this approach is the increased hardware cost required to improve the downtime performance. If only end-devices need to re-associate then the downtime will be very low as expected by the ZigBee standard. However, a much higher downtime is observed if routers also need to switch network as will be seen in Sec. 9.7. However, the performance of this solution can be improved by adding QoS classes, where highest class will be the first to be allowed to reconnect while other ones will have to wait a certain time before attempting reconnection. It is easy, for example, to implement QoS in the form of a time that lower classes have to wait before initiating the failure recovery procedure, as illustrated in Fig. 9.3.

9.6 Synchronization Management in WSNs

As explained in Sec. 9.4.1, synchronization protocols rely on the exchange of timing information between nodes. Because of this they are susceptible to random delays in the delivery of the information which can impact on the synchronization accuracy. The following non-deterministic factors are responsible for the degradation in the accuracy of synchronization protocols:

- **Sender uncertainty:** covers all the variable delays attributed to the sender. It can be subdivided in
  - **Send Time:** the time taken by the node to construct a packet and pass it to the MAC layer after its transmission has been decided.
  - **Access Time:** indicates how much the packet must wait at the MAC layer before being transmitted. It is highly variable and it depends heavily on network traffic.
  - **Transmission Time:** this is the delay introduced by the transmission at the physical layer. It is mainly deterministic, provided the connection speed does not change. There is still some variations given by possible interruptions during transmission.
- **Propagation Delay:** this delay is introduced by the transmission medium. However, since the distance between nodes in a WSN is often very small, in the order of a few hundred meters at most, this contribution is negligible.
- **Receiver uncertainty:** covers the variable delays attributed to the receiver. It can be further subdivided in:
  - **Reception Time:** analogous to the transmission time, it is the time taken to receive the bits and pass them to the MAC layer.
  - **Receive Time:** the time taken to construct a packet from the received bits and pass it to the upper layers. The uncertainty is introduced by the variable delays introduced by the operating system.

It will now be explained in detail how offset and skew are estimated within the synchronization protocol that was used. Offset is estimated by exchanging the four timestamps from T_1 to T_4 between server and client, as illustrated in Fig. 9.4. The timestamps indicate the following specific events:

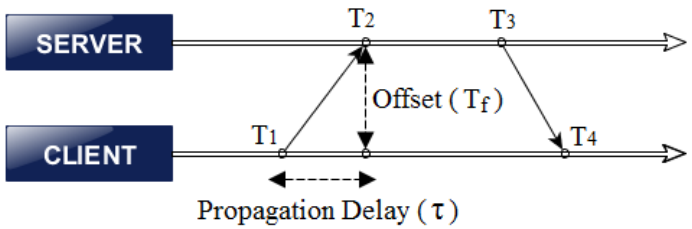

Figure 9.4: *Space-time diagram showing the four different time instants used in the protocol.*

- T_1 indicates the local time for the client when a synchronization request is sent.
- T_2 indicates the local time for the server when it receives the synchronization request.
- T_3 indicates the local time for the server when a synchronization reply is sent.
- T_4 indicates the local time for the client when it receives the reply to its request.

With reference to Fig. 9.4,

$$T_2 = T_1 + T_f + \tau, \tag{9.3}$$
$$T_4 = T_3 - T_f + \tau, \tag{9.4}$$

where T_f is the offset between the local clocks and τ is the transmission delay. Assuming the delay τ is symmetric, from (9.3) and (9.4), it can be written

$$T_f = \frac{(T_2 - T_1) - (T_4 - T_3)}{2}, \tag{9.5}$$
$$\tau = \frac{(T_2 - T_1) + (T_4 - T_3)}{2}. \tag{9.6}$$

A periodic compensation of the offset is simple to implement on most devices. However, the accuracy of the synchronization depends on the interval within which synchronization packets are exchanged. Using this approach the frequency offset between the various nodes quickly builds up and increases the synchronization error. The size of data used for synchronization is limited and its impact can be further reduced by attaching them

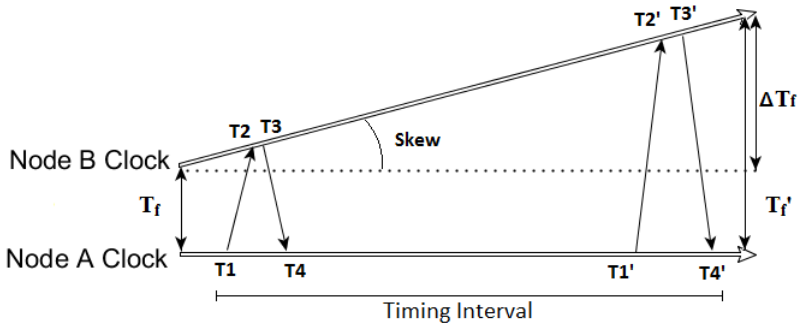

Figure 9.5: *Algorithm to calculate the timing skew and offset.*

to data frames. However, its burden remains proportional to the number of nodes to synchronize for TPSN and to the squared number of nodes to synchronize for RBS. In ZigBee networks, where the number of nodes can be in the order of thousands, this means that TPSN offers better scalability. It is therefore beneficial to implement not only clock offset correction but also frequency offset, or *skew*, estimation. With reference to Fig. 9.5, the skew can be calculated as

$$\text{skew} = \frac{T'_f - T_f}{\text{timing interval}}, \tag{9.7}$$

where T_f is obtained from the timestamps T_1 to T_4 and T'_f from the timestamps T'_1 to T'_4. The advantages on protocol overhead given by this approach come at the cost of increased complexity and memory footprint. Particular issues arise when skew estimation is implemented on hardware constrained devices, such as the end-sensor nodes, where sizeable precision errors can arise from floating point multiplications. Hence, it is necessary to avoid directly multiplying the clock but instead track offset from a recent point in time.

While the sender-receiver approach of TPSN reduces protocol overhead with respect to RBS, estimation of the offset suffers from all the variable delays described at the beginning of this section. It was therefore implemented a moving average filter in order to limit the impact of these errors on skew estimation. If from one side the implementation of skew estimation is resource consuming, on the other side the advantages in terms of reduced protocol overhead and precision are substantial. The gain was quantified by taking measures from experimental results as described in the next sec-

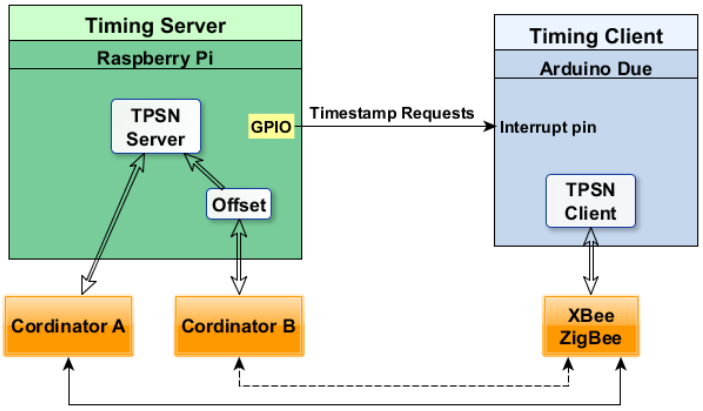

Figure 9.6: *A single client experimental set-up, multiple clients can be connected at the same time with the same configuration.*

tion. More details about the aspect of synchronization in WSNs can be found in [Ganeriwal et al., 2003] where the trade-offs of sender-receiver architectures like TPSN with respect to receiver-receiver ones like RBS are examined, together with the impacts of the different types of variable delays which affect these algorithms.

9.7 Experimental Results and Measures

For the SPF problem of ZigBee networks several tests have been performed using COTS devices to measure the downtime of the proposed method with respect to resetting a node, as proposed in [Kölln and Zimmermann, 2009]. Our experimental set-up consists of a Raspberry Pi board that controls two coordinators and several Arduino boards equipped with ZigBee S2 XBee transceivers [DIG,]. These boards are also wired to the Raspberry Pi via their interrupt pins which are used for forcing simultaneous events such as timestamping in order to measure synchronization errors. The experimental set-up is displayed in Fig. 9.6. A downtime defined as the interval between the failure of the coordinator and the successful joining to the new coordinator, was measured. The delay introduced by the fault discovery algorithm was not considered as it is a common factor. The data was logged by using the utility called XCTU which is freely provided by the module manufacturer [XCT,].

Fig. 9.7 shows results of the measures for a single router device for the two considered approaches. Data have been obtained by 100 runs for

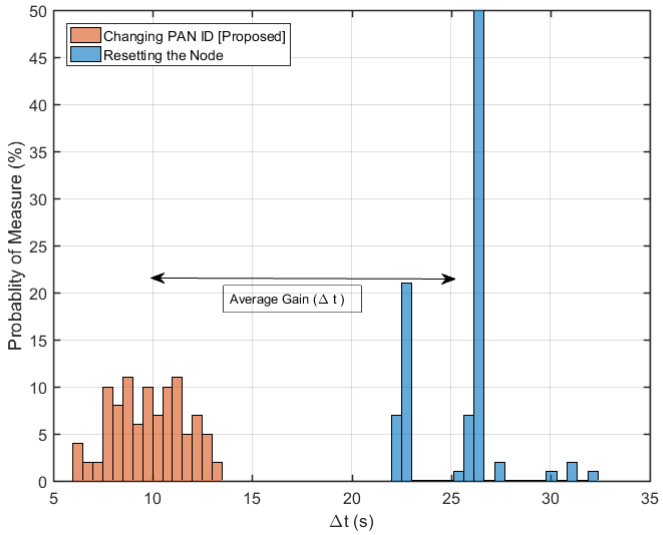

Figure 9.7: *Histogram of the observed downtime with the proposed scheme versus resetting the node for a single router.*

each method. Numerical results show that the proposed approach allows for a significant reduction in downtime with respect to the node resetting one. From a comparison of the results, the average downtime reduction is around 15 seconds. However, it is worth observing that the downtime of the proposed method depends on the number of routers that have to perform the switch. Since for end devices the switch happens very quickly, within a few milliseconds, the limiting factor is represented by the number of routers in the network because they must implement network formation. It is worth noting that while the proposed method presents a rather uniform distribution, resetting the node presents clear spikes at definite time instants. In order to establish a network after a reset, the module first selects possible channels and then, after an energy scan, probes them looking for other PAN to avoid possible conflicts. This causes it to wait a timeout on its probe. Forcing the module to use only one channel does not reduce the time taken to establish a network.

For the study of the synchronization, the experimental setup is shown in Fig. 9.8. It consists of three Arduino boards: one configured as the timing server and two as clients. All data are exchanged wirelessly through the XBee modules connected by UART interface to the Arduinos. For instantaneous timestamp capture an interrupt routine triggered by a wired

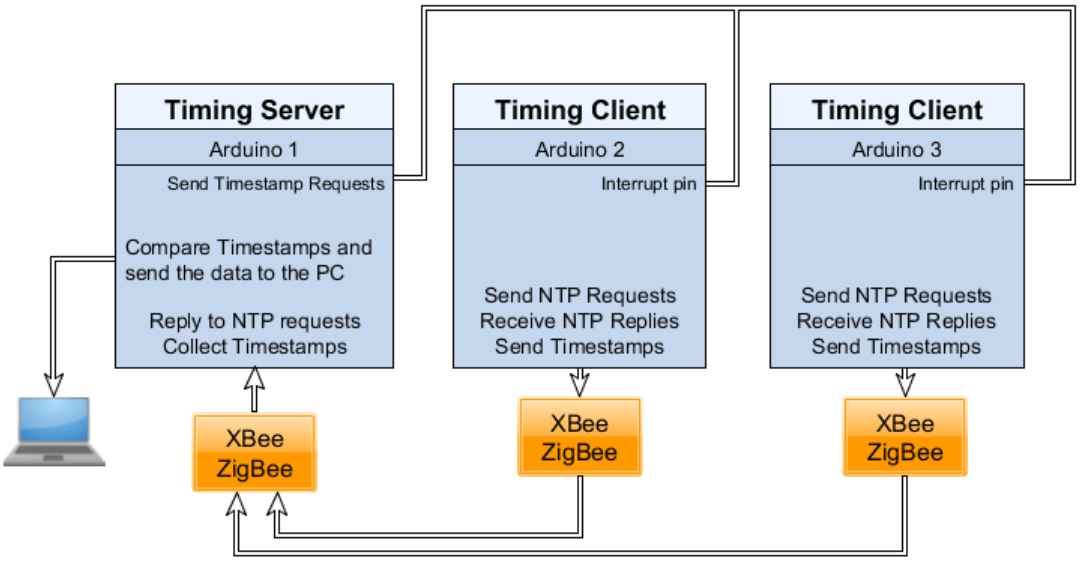

Figure 9.8: *Experimental setup for studying the synchronization error.*

connection was used. The Arduino boards programmed as clients send synchronization requests through ZigBee to the server at constant intervals. The server immediately replies to the requests in the same way. It also takes care of formatting and sending data to the PC via serial port when it is received. In the experiment the transmission of synchronization packets was stopped at T = 0 set as a reference time and have started measuring the error relative to the server both for the case with skew compensation and that without skew compensation. Results are reported in Fig. 9.10, where it is shown that without skew compensation the frequency offset between the two Arduino boards introduce a constant error every second that builds up over time. On the other hand, with skew estimation this error is reduced below the precision of the timing function used. This limitation also causes the small ripple visible in the skew estimation curve: for timestamping, the function "micros()" which returns only multiples of 4μs was used. The accuracy of the offset estimation was also limited by the usage of this application layer timestamping as the MAC layer timestamping was unavailable on the hardware used. From these results, the gain of changing PAN ID versus resetting a node can be quantified in terms of timing synchronization accuracy. By comparing Fig. 9.7 and 9.10, it is clearly visible that the proposed solution for the SPF problem has a significant gain in terms of downtime network reduction and because of this, synchronization error

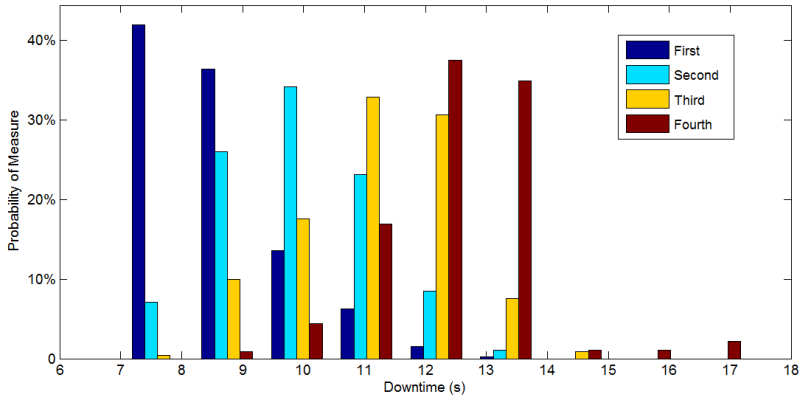

Figure 9.9: *Histogram of the observed downtime with multiple routers switching at the same time.*

is less. From Fig. 9.7 it was observed that without Skew compensation the proposed method has a downtime of the network comprised between 5 and 15 seconds for which, from Fig. 8, there was a synchronization error between 2 ms and 5ms. On the other side, if the method given in [Kölln and Zimmermann, 2009] was considered, the downtime of network varies from 20 to 30 sec and the corresponding timing synchronization error in Fig. 9.10 increases to values between 7 ms and 10 ms. When Skew compensation is present, the synchronization error is between 42 μs and 60 μs for the proposed method and between 70 μs and 85 μs using the approach of [Kölln and Zimmermann, 2009].

Further, results have been therefore expanded by performing a similar experiment where routers have been forced to reconnect at exactly the same time, using a wired interrupt. The measured downtime for each of them is shown in Fig. 9.9. From the numerical results it can be seen that each router, on average, adds between one and two seconds of downtime, that is caused by the overhead in establishing new network connections and bindings. This result means that the performance of the proposed solution is dependent on the number of routers that must perform this switch and it can quickly worsen with respect to [Kölln and Zimmermann, 2009] for large numbers of routers. On the other hand it was experimentally verified that end devices are capable of joining a new network within a few milliseconds, as expected by the ZigBee standard, provided an active router or coordinator is in the range. The experimental set-up in Fig. 9.6 has been used to study also the synchronization problem. A TPSN server was running on a Raspberry Pi and the TPSN clients running on Arduino boards connected

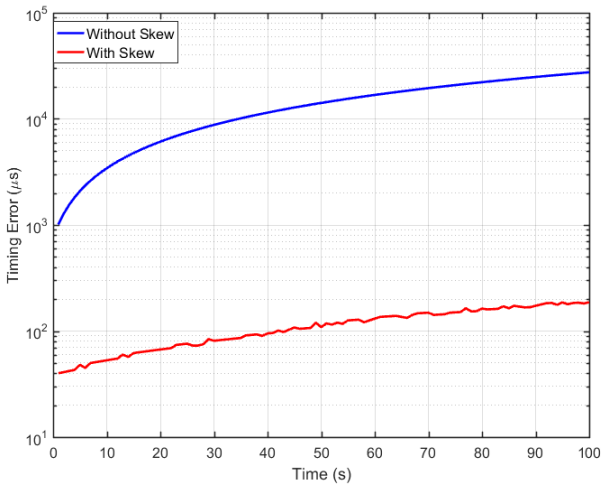

Figure 9.10: *Evolution over time of the synchronization error with and without skew compensation.*

to the server via the ZigBee XBee modules. In order to accurately measure the synchronization error, interrupts on the Arduinos triggered by the Raspberry Pi's GPIO, were used. Both the two devices were connected to a PC for data logging: the Arduino via UART and the Raspberry Pi via Ethernet. Our first experiment consisted in measuring the effects on the synchronization of the network outage in both the case of simple offset compensation and skew estimation. The clients synchronize to the server for some time in order to give enough samples for skew estimation. A number of 10 samples was used. After this, a network failure was simulated by unplugging the transceivers from the server and measuring the evolution of the synchronization error. The results for this experiment are shown in Fig. 9.10. At time $T = 0$ the connection is stopped and the evolution of the error is measured trough timed interrupts triggered by the wired connection. It was verified that skew estimation significantly reduces the error of synchronization, particularly over extended periods of time. The accuracy of the synchronization itself was limited by the use of application layer timestamping as MAC layer one was not available on the used COTS devices. The curves do not start exactly at zero because there was some error in the offset estimation itself caused by the variable delays explained in Sec. 9.6. Furthermore, a small ripple is visible in the skew corrected line. This is caused by the limited accuracy of the timestamps available on the Arduino, which, have a coarse graduation of 4 μs. This error, however, is at least

two orders of magnitude lower than that introduced in the offset estimation, which, as can be seen from the starting points in Fig. 9.10, is in the order of a few milliseconds. As the set-up consists of commercially available hardware and no further assumption was made on link reliability, the shown results can be expected in most deployment scenarios. It is worth noting that by comparing the different downtimes of the two methods reported in Fig. 9.7 with the evolution of the synchronization error reported in Fig. 9.10 it can be seen that there is an advantage in terms of synchronization accuracy. In particular, values can be measured ranging from 3 ms to 7 ms of reduction in synchronization error for the case of simple offset estimation and 20 μs to 40 μs for the case with skew estimation. Finally, the evolution of the synchronization error during a recovery process was studied using the set-up described in Fig. 9.6. For skew estimation a moving average filter was used with 10 samples in order to average the errors in offset estimation. A test was performed without any offset between the two networks and one with a 10 ms offset and studied its effects on the offset and skew estimation. Synchronization messages are exchanged every 4s. Hence, some time was allowed for filling up the skew estimation filters and, then, proceeded to crash the network coordinator at T=30s. After a timeout the end devices start synchronizing with the new network where, in set-up, the synchronization is provided by the same device to eliminate any uncertainty in the offset. The results that have been obtained are reported in Fig. 9.11, where it can be seen that in the case without offset the synchronization error follows the expected linear curve due to the clock drift and no impact is observed on the skew estimation. In contrast, for the case with offset its impact on the skew estimation as the slope of the skew line is highly skewed. This is corrected after 10 synchronization events as the error from the offset introduced by the network switch is discarded by the moving average filter.

9.8 Conclusion

This chapter focuses on the issue of time synchronization in WSNs, the problem of the Single Point of Failure for ZigBee coordinators, and how the latter impacts on the former. A new method was proposed for dealing with ZigBee coordinator failures based on using several coordinators with different identifiers where, if the primary coordinator fails the connections are switched to the other coordinator that is in hot stand-by. Our proposal consists in switching to a different network by changing the network identifier to achieve a lower downtime and it was experimentally verified a re-

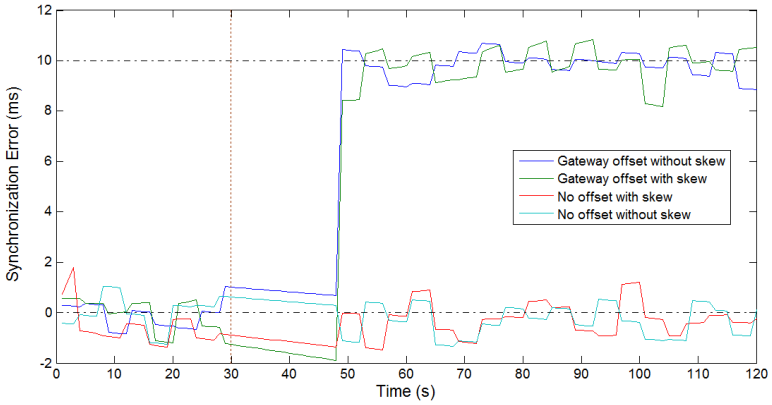

Figure 9.11: *Evolution over time of the synchronization error after a network switch in* $T = 30s$*. Results show both the case of no offset and a 10 ms offset between networks.*

covery which is up to 15 seconds faster than another solution present in the literature. The lower downtime further reduces the impact of a coordinator failure on the synchronization error. We tested the efficiency of the proposed solution with an experimental set-up using commercial hardware such as the XBee ZigBee modules and Arduino boards. Further developments of this work involve improvements of the synchronization algorithm to more energy efficient solutions. The SPF solution can be extended to a more general case of creation of an ad-hoc WSN with mobile gateways such as, for example, those obtained using drones.

CHAPTER 10

Conclusion and Future Works

THIS chapter concludes this thesis and presents some future research directions. The work presented here was divided into three major sections: primary contributions, secondary contributions and minor project. Primary and secondary contributions, includes the major work addressing to the thesis topic **"Increasing Capacity of Wireless Networks through Aerial Base Stations"**. The minor project deals with another project done apart from the main topic of this thesis.

10.1 Conclusion

The work presented in this thesis started with increasing demands of high speed data from mobile users, upto 10 Gbps data rate which is 10 to 100x more than 4 and 4.5 G networks. Further, $<$1 ms latency, $>$99.99% reliability, higher bandwidth and 100% coverage requirements led to the requirement of paradigm shift of cellular standard from Long Term Evolution (LTE) to LTE-Advanced and now to LTE-Pro. In IMT-2020 or 5G, new technologies were addressed to provide wider connectivity and high speed data, such as new radio interface, which defines the frequency, chan-

nel bandwidth, and modulation scheme. 5G networks will operate on a range of radio spectrum bands. In addition to the traditional sub-3 GHz bands, where additional spectrum will be allocated in the 700 MHz band to mobile communications, 5G will exploit higher frequencies of radio spectrum in the millimeter wave range roughly from 20 to 300 GHz, which can provide greater bandwidth, although over shorter distances. To support a high density of connections and large bandwidth, 5G wireless networks will be heterogeneous, being made up of both large and small cells using different technologies. Other technologies such as massive multiple-input-multiple-output (MIMO), adaptive beamforming, full duplex technology, cognitive radio etc support a wide variety of emerging applications such as device-to-device (D2D), machine-to-machine (M2M), internet-of-things (IoT), vehicle-to-vehicle (V2V), vehicle-to-infrastructure (V2X) etc. Under V2X, base stations being mounted on automobiles and trains got the attention of researchers, to develop a portable base stations. However, base station mounted on unmanned aerial vehicles (UAVs) or drones started gaining much consideration recently due to easy deployment, cost effectiveness, and approachability to the ground users. This thesis is based on this motivation. Further, in this thesis, various technical aspects and research related to an aerial base station (ABS) was studied.

Firstly, during the investigation phase of an ABS, an appropriate channel model was missing. Therefore, firstly the work done was to model a suitable channel based on line-of-sight (LoS) and non-LoS (NLoS) probabilities, because obtaining a LoS for an ABS was much higher due to its flying and hovering potential. Later, a close-in (CI) reference path loss (PL) model was preferred as a suitable option for both LoS and NLoS channel of ABS. This was because most of the signal attenuation happens in free space for ABS. Therefore, an average PL model was defined and parameters such as path loss exponent (PLE) and standard deviation of shadow fading was obtained. This modeling was done using a deterministic approach rather than a stochastic one due to higher accuracy. The air-to-ground (A2G) modeling was done using a commercial radio propagation software, in which the environments: Suburban, Urban and Urban High Rise were imported and simulation was performed with receivers on the ground at different ABS altitudes. ABS altitude and elevation angle with receivers was chosen as a fundamental design parameters. Also, the environments were created on a computer-aided-design (CAD) software based on ITU-R parameters. Therefore, the environments developed were generalized, so that the results can be implied in any real city scenario with few degrees of inaccuracy. Also other parameters, such as cumulative distribu-

tion function (CDF) and spatial correlation were shown for other propagation factors such as angle-of-arrival (AoA) (both azimuth and elevation), RMS delay spread and received power by UEs.

After obtaining the channel parameters, we used them for A2G channel for the remaining part of the thesis. Further, research was conducted on cellular coverage, capacity and interference analysis of an ABS with provision of closed-form expressions of cell coverage under a set of variables using solid angle approach. For the analytical expressions, proofs were provided in the appendices. The results of optimal altitude were obtained here. Also, geometric increase in cell coverage introduced due to rotation angle was shown. The graphs plotted from the ray tracing simulations were verified against the graphs plotted from the analytical expressions with same parameters. The results obtained were plotted with respect to the ABS height up to 2000 m and transmission power up to 46 dBm. The analytical expressions include all major design parameters required, such as, ABS altitude, transmission power, propagation factors, antenna gain, elevation angle and rotation angle.

Later, a novel system of Ultra-Dense Cloud Drone Networks (*UDCDNs*) was proposed in this thesis to serve as a suitable replacement for *UDNs*. The major challenges and benefits associated with this system were provided against Ultra-Dense Networks (*UDNs*). This system would reduce the total cost of operation (TCO) of mobile operators due to its *on-demand* deployment and lower operation cost. Further, discussions on ABS health monitoring is given utmost importance for the protection of users and infrastructure. Also, fronthauling and backhauling were discussed which are very important aspects for successful implementation of the system.

Next research was driven in the direction of Ultra-Reliable Low Latency Communication (uRLLC) or tactile internet, where sysmbol error rate (SER) calculations for ABS with A2G channel was shown. The time frequency grid of LTE was used with uRLLC parameters to support high signal-to-noise ratio (SNR) and lower latencies. Also generalized frequency division multiplexing (GFDM), waveform was implemented due to its backward compatibility with orthogonal frequency division multiplexing (OFDM) system which would help the mobile operators to adapt to this new waveform. Further, "Better than Nyquist" (BTN) pulse shaping filters were used and better results than Nyquist filters were observed. Also carrier frequency offset (CFO) was introduced in the system model later to make the system more realistic and its impact was observed in the simulation results. Simulations were performed with variation in altitude, CFO value and pulse shaping in this work. Also other results such as optimal altitude based on

minimum SER and maximum coverage was shown and received power distribution at optimal ABS altitude was shown. The probabilistic parameters associated with the distributions were given.

Later on work was done on a multi-tier drone network. To avoid issues such as inter-carrier-interference (ICI), energy consumption, fast handovers, etc, some laws on coverage, survivability and mobility were investigated. Moreover, several optimization constraints on ABS network were provided along with the proposed solution. Also simulations for hierarchical ABS allocations were provided. For updating the policies coverage and mobility control and survivability laws, N-Block Recursive Learning (NBRL) framework is also provided.

Also research on interference alignment (IA) is being done for HAPs based on a generalized long distance LoS channel model, to maximize the sum rate. For IA independent channels are required which is not feasible at low altitude aerial platforms (LAPs). the channel model here takes into account AoA and angle-of-departure (AoD). Also the optimal distance between the receivers was calculated to obtain the independent channel. The bit error rate (BER) is reported for both IA and non IA based communication. Also the effect of imperfect channel state information (CSI) was observed on the system to make it more realistic.

Finally, in the end, the work done on minor project has been shown. The project was to develop an IoT platform for health monitoring of helicopter components and its fleet management. Various sensors associated with monitoring different parts of the helicopter, were deployed. The information from these sensors was sent to a common gateway, known as a transmission data concentrator (TDC). The data from the TDC was delivered to the cloud using satellite and cellular network, which could be accessed by the air traffic controller (ATC) or mobile operators for real time evaluation and fleet management. A redundant TDC was kept which would take over the functions of the primary gateway in case of a failure. The system addressed here was performed using Zigbee technology doe energy consumption, apart from many proposed in wireless sensor network (WSN). Here, personal area network identifier (PAN ID) the Zigbee coordinator was changed, *i.e.* changing the network identifier in case of a failure. It was experimentally verified that a lower downtime was achieved. Also, SPF was discussed here with timing synchronization problem in WSNs and impact of single point of failure (SPF) problem on timing synchronization was shown.

10.2 Future Works

There are many future directions of this research, since it is a recently researched domain. Here are presented few aspects which can be explored further:

- Energy Deficiency: As it has been studied in some research articles, ABS battery is insufficient for long operations. ABS consumes higher amount of energy for flight rather than for transmission. Therefore, solar powered drones have been a significant are of research. Facebook's project *Aquila* have developed a prototype which provide internet access to suburban areas, being on-flight for months. Similarly, apart from solar drones, techniques such as stop and recharge and simultaneous wireless information and power transfer (SWIPT) can be further investigated. The benefit of using wireless power transfer is that ABS can hover near to the RF power source thereby increasing efficiency of the system since WPT and SWIPT are successful for near field power transfer.

- Fronthauling and Backhauling: For information transmission, from base band unit (BBU) towards ABS and from BBU to core network, techniques such as free space optics (FSO) and millimeter-wave can be investigated. However, some researchers also focused on tethered drones to address this area.

- ABS Simulator: Performing experimental analysis and measurements for an ABS network is not a feasible option currently, since laws for performing UAV flights in the city areas are very strict due to safety concern of people. Only flights in suburban zones are possible at lower altitudes. The development of these laws are in process. Therefore, researchers have to use simulators to get measurement results, as done in this thesis. Thus, developing simulators for analysis of such system in different city environments is of much requirement. Therefore, it would be useful to develop open source simulators for UAVs which take into account all the propagation factors, UAV maneuver, wind models etc to make it realistic city scenario.

- Physical Layer (PHY) numerology: Although, in this thesis, work has been done on implementing GFDM waveform for A2G channel with BTN pulse shaping filter with uRLLC parameters, but this work can be further extended with applying other waveforms such as Universal Filtered Multi-Carrier (UFMC), Filter Bank Multi-Carrier (FBMC), Fil-

tered OFDM (F-OFDM) etc in for other scenarios such as IoD. Also, introduction of timing offset and phase noise in this system model is another aspect of research. Further investigation on other pulse shaping filters can be done to obtain lower out-of-band (OOB) emission.

Apart from these, other 5G technologies such as millimeter wave communication, HetNet interference management, Non-Orthogonal Multiple Access, Machine and Deep Learning approaches, Antenna Beam forming and user equipment (UE) tracking can also be implemented for ABSs and better results can be expected.

Bibliography

[Rem,] http://www.remcom.com/wireless-insite.

[3ds,] https://www.autodesk.com/products/3ds-max/overview.

[dro,] https://www.wired.com/2013/12/physics-of-the-amazon-prime-air-drone/.

[6Lo,] 6LoWPAN working group. http://www.ietf.org/dyn/wg/charter/6lowpan-charter.html.

[ZBA,] Alliance, ZigBee."ZigBee-2007 Layer PICS and Stack Profiles 6, "ZigBee Document 08006r03, Rev 3 (2008).

[ITU, a] "Applications of Wireless Sensor Networks in Next Generation Networks" SERIES Y.2000.

[Qua,] Cellular Drone Communication. https://www.qualcomm.com/invention/technologies/lte/advanced-pro/cellular-drone-communication.

[Nok, a] Connected UAVs. https://networks.nokia.com/products/ConnectedUAVs.

[DIG,] Digi International Inc. http://www.digi.com.

[Fac,] Facebook, "The technology behind Aquila". URL:https://www.facebook.com/notes/mark-zuckerberg/the-technology-behind-aquila/10153916136506634/.

[HCF,] HART Communication Foundation (HCF). WirelessHART Communication Standard. HART 7.0 Specifications, 2007.

[Nok, b] Nokia, "Ultra Dense Network", white paper. URL:https://tools.ext.nokia.com/asset/200295[Accessedon:01/02/2018].

[ITU, b] V. Butenko, A. Nazarenko, V. Sarian, N. Sushchenko, and A. Lutokhin, Applications of wireless sensor networks in next generation networks,Telecommunication Standardization Sector of ITU, (2014). https://www.itu.int/dms_pub/itu-t/opb/tut/T-TUT-NGN-2014-PDF-E.pdf.

[XCT,] XCTU: Next generation configuration platform for XBee, Digi International Inc. http://www.digi.com/products/wireless-wired-embedded-solutions/zigbee-rf-modules/xctu.

[ZBe,] ZigBee RF4CE specification version 1.00. http://www.zigbee.org.

[Absolute Project,] Absolute Project, E. Fp7 absolute project.

[Afonso et al., 2016] Afonso, L., Souto, N., Sebastiao, P., Ribeiro, M., Tavares, T., and Marinheiro, R. (2016). Cellular for the skies: Exploiting mobile network infrastructure for low altitude air-to-ground communications. *IEEE Aerospace and Electronic Systems Magazine*, 31(8):4–11.

[AL-Hourani et al., 2016] AL-Hourani, A., Chandrasekharan, S., Kaandorp, G., Glenn, W., Jamalipour, A., and Kandeepan, S. (2016). Coverage and rate analysis of aerial base stations [letter]. *IEEE Transactions on Aerospace and Electronic Systems*, 52(6):3077–3081.

[Al-Hourani et al., 2014a] Al-Hourani, A., Kandeepan, S., and Jamalipour, A. (2014a). Modeling air-to-ground path loss for low altitude platforms in urban environments. In *2014 IEEE Global Communications Conference*, pages 2898–2904. IEEE.

[Al-Hourani et al., 2014b] Al-Hourani, A., Kandeepan, S., and Lardner, S. (2014b). Optimal lap altitude for maximum coverage. *IEEE Wireless Communications Letters*, 3(6):569–572.

[Al-Hourani et al., 2014c] Al-Hourani, A., Kandeepan, S., and Lardner, S. (2014c). Optimal lap altitude for maximum coverage. *IEEE Wireless Communications Letters*, 3(6):569–572.

[Altaf Khuwaja et al., 2018] Altaf Khuwaja, A., Chen, Y., Zhao, N., Alouini, M.-S., and Dobbins, P. (2018). A Survey of Channel Modeling for UAV Communications. *ArXiv e-prints*.

[Alzenad et al., 2017] Alzenad, M., El-Keyi, A., Lagum, F., and Yanikomeroglu, H. (2017). 3-d placement of an unmanned aerial vehicle base station (uav-bs) for energy-efficient maximal coverage. *IEEE Wireless Communications Letters*, 6(4):434–437.

[Amorim et al., 2017] Amorim, R., Nguyen, H., Mogensen, P., KovÃ¡cs, I. Z., Wigard, J., and SÃ¸rensen, T. B. (2017). Radio channel modeling for uav communication over cellular networks. *IEEE Wireless Communications Letters*, 6(4):514–517.

[Andreev et al., 2014] Andreev, S., Pyattaev, A., Johnsson, K., Galinina, O., and Koucheryavy, Y. (2014). Cellular traffic offloading onto network-assisted device-to-device connections. *IEEE Communications Magazine*, 52(4):20–31.

[Andrews et al., 2014] Andrews, J. G., Buzzi, S., Choi, W., Hanly, S. V., Lozano, A., Soong, A. C., and Zhang, J. C. (2014). What will 5g be? *IEEE Journal on Selected Areas in Communications*, 32(6):1065–1082.

[Asensio et al., 2016] Asensio, A., Ruiz, M., Contreras, L. M., and Velasco, L. (2016). Dynamic virtual network connectivity services to support c-ran backhauling. *IEEE/OSA Journal of Optical Communications and Networking*, 8(12):B93–B103.

[Azari et al., 2016] Azari, M. M., Rosas, F., Chen, K. C., and Pollin, S. (2016). Joint sum-rate and power gain analysis of an aerial base station. In *2016 IEEE Globecom Workshops (GC Wkshps)*, pages 1–6.

[Bae, 2014] Bae, S.-K. (2014). A survey on time synchronization protocols for wireless sensor networks. *Journal of The Korea Society of Computer and Information*, 19(6):61–69.

[Baker, 2005] Baker, N. (2005). Zigbee and bluetooth: Strengths and weaknesses for industrial applications. *Computing and Control Engineering*, 16(2):20–25.

[Bennis et al., 2013] Bennis, M., Simsek, M., Czylwik, A., Saad, W., Valentin, S., and Debbah, M. (2013). When cellular meets wifi in wireless small cell networks. *IEEE Communications Magazine*, 51(6):44–50.

[Blümm et al., 2012] Blümm, C., Heller, C., and Weigel, R. (2012). Sdr ofdm waveform design for a ugv/uav communication scenario. *Journal of Signal Processing Systems*, 69(1):11–21.

[Bohagen et al., 2005] Bohagen, F., Orten, P., and Oien, G. E. (2005). Modeling and analysis of a 40 ghz mimo system for fixed wireless access. In *2005 IEEE 61st Vehicular Technology Conference*, volume 3, pages 1691–1695 Vol. 3.

[Bor-Yaliniz and Yanikomeroglu, 2016] Bor-Yaliniz, I. and Yanikomeroglu, H. (2016). The new frontier in ran heterogeneity: Multi-tier drone-cells. *IEEE Communications Magazine*, 54(11):48–55.

[Bor-Yaliniz et al., 2016] Bor-Yaliniz, R. I., El-Keyi, A., and Yanikomeroglu, H. (2016). Efficient 3-d placement of an aerial base station in next generation cellular networks. In *Communications (ICC), 2016 IEEE International Conference on*, pages 1–5. IEEE.

[Cadambe and Jafar, 2008a] Cadambe, V. R. and Jafar, S. A. (2008a). Interference alignment and degrees of freedom of the k-user interference channel. *IEEE Transactions on Information Theory*, 54(8):3425–3441.

[Cadambe and Jafar, 2008b] Cadambe, V. R. and Jafar, S. A. (2008b). Interference alignment and degrees of freedom of the$k$-user interference channel. *IEEE Transactions on Information Theory*, 54(8):3425–3441.

[Chand Gautam and Chand Kaushal, 2014] Chand Gautam, G. and Chand Kaushal, N. (2014). Quantitative and qualitative analysis of time synchronization protocols for wireless sensor networks. *International Journal of Sensors Wireless Communications and Control*, 4(1):2–19.

[Chen et al., 2017] Chen, M., Mozaffari, M., Saad, W., Yin, C., Debbah, M., and Hong, C. S. (2017). Caching in the sky: Proactive deployment of cache-enabled unmanned aerial vehicles for optimized quality-of-experience. *IEEE Journal on Selected Areas in Communications*, 35(5):1046–1061.

[Cho et al., 2010] Cho, Y. S., Kim, J., Yang, W. Y., and Kang, C. G. (2010). *MIMO-OFDM wireless communications with MATLAB*. John Wiley & Sons.

[Cileo et al., 2017] Cileo, D. G., Sharma, N., and Magarini, M. (2017). Coverage, capacity and interference analysis for an aerial base station in different environments. In *2017 International Symposium on Wireless Communication Systems (ISWCS)*, pages 281–286.

[Cortes et al., 2004] Cortes, J., Martinez, S., Karatas, T., and Bullo, F. (2004). Coverage control for mobile sensing networks. *IEEE Transactions on robotics and Automation*, 20(2):243–255.

[Dahlman et al., 2014] Dahlman, E., Mildh, G., Parkvall, S., Peisa, J., Sachs, J., SelÃ©n, Y., and SkÃ¶ld, J. (2014). 5g wireless access: requirements and realization. *IEEE Communications Magazine*, 52(12):42–47.

[Djenouri and Bagaa, 2014] Djenouri, D. and Bagaa, M. (2014). Implementation of high precision synchronization protocols in wireless sensor networks. In *Wireless and Optical Communication Conference (WOCC), 2014 23rd*, pages 1–6. IEEE.

[Dobslaw et al., 2013] Dobslaw, F., Zhang, T., and Gidlund, M. (2013). Qos assessment for mission-critical wireless sensor network applications. In *2013 IEEE 38th Conference on Local Computer Networks (LCN 2013)*, pages 663–666. IEEE.

[Elson et al., 2002] Elson, J., Girod, L., and Estrin, D. (2002). Fine-grained network time synchronization using reference broadcasts. *ACM SIGOPS Operating Systems Review*, 36(SI):147–163.

[Ferreira et al., 2017] Ferreira, J. S., Rodrigues, H. D., Gonzalez, A. A., Nimr, A., Matthe, M., Zhang, D., Mendes, L. L., and Fettweis, G. (2017). Gfdm frame design for 5g application scenarios. *Journal of Communication and Information Systems*, 32(1).

[Ganeriwal et al., 2003] Ganeriwal, S., Kumar, R., and Srivastava, M. B. (2003). Timing-sync protocol for sensor networks. In *Proceedings of the 1st international conference on Embedded networked sensor systems*, pages 138–149. ACM.

[Gaspar et al., 2014] Gaspar, I., Mendes, L., MatthÃ©, M., Michailow, N., Festag, A., and Fettweis, G. (2014). Lte-compatible 5g phy based on generalized frequency division multiplexing. In *2014 11th International Symposium on Wireless Communications Systems (ISWCS)*, pages 209–213.

[Goldsmith, 2005] Goldsmith, A. (2005). *Wireless communications*. Cambridge university press.

[Gomez et al., 2016] Gomez, K., Kandeepan, S., Vidal, M. M., Boussemart, V., Ramos, R., Hermenier, R., Rasheed, T., Goratti, L., Reynaud, L., Grace, D., Zhao, Q., Han, Y., Rehan, S., Morozs, N., Jiang, T., Bucaille, I., Wirth, T., Campo, R., and Javornik, T. (2016). Aerial base stations with opportunistic links for next generation emergency communications. *IEEE Communications Magazine*, 54(4):31–39.

[Grace et al., 2005] Grace, D., Chen, G., White, G., Tozer, T., and Thornton, J. (2005). Improving the system capacity of broadband services using multiple high-altitude platforms. *IEEE Transactions on Wireless Communications*, pages 700–709.

[Grace and Mohorcic, 2011] Grace, D. and Mohorcic, M. (2011). *Broadband communications via high altitude platforms*. John Wiley & Sons.

[Hall, 2016] Hall, R. J. (2016). An internet of drones. *IEEE Internet Computing*, 20(3):68–73.

[Han and Lim, 2010] Han, D. and Lim, J. (2010). Smart home energy management system using ieee 802.15.4 and zigbee. *IEEE Transactions on Consumer Electronics*, 56(3):1403–1410.

[Hayat et al., 2016] Hayat, S., Yanmaz, E., and Muzaffar, R. (2016). Survey on unmanned aerial vehicle networks for civil applications: A communications viewpoint. *IEEE Communications Surveys Tutorials*, 18(4):2624–2661.

[Holis and Pechac, 2008] Holis, J. and Pechac, P. (2008). Elevation dependent shadowing model for mobile communications via high altitude platforms in built-up areas. *IEEE Transactions on Antennas and Propagation*, 56(4):1078–1084.

[Hu et al., 2016] Hu, Y., Hong, Y., and Evans, J. (2016). Modelling interference in high altitude platforms with 3d los massive mimo. In *Communications (ICC), 2016 IEEE International Conference on*, pages 1–6. IEEE.

[Irish et al., 2013a] Irish, A., Quitin, F., Madhow, U., and Rodwell, M. (2013a). Achieving multiple degrees of freedom in long-range mm-wave mimo channels using randomly distributed relays. In *Signals, Systems and Computers, 2013 Asilomar Conference on*, pages 722–727. IEEE.

[Irish et al., 2013b] Irish, A., Quitin, F., Madhow, U., and Rodwell, M. (2013b). Sidestepping the rayleigh limit for los spatial multiplexing: A distributed architecture for long-range wireless fiber. In *Information Theory and Applications Workshop (ITA), 2013*, pages 1–6. IEEE.

[Jafar, 2011] Jafar, S. A. (2011). *Interference Alignment: A New Look at Signal Dimensions in a Communication Network*. now.

[Jafar and Shamai, 2008] Jafar, S. A. and Shamai, S. (2008). Degrees of freedom region of the mimo$x$channel. *IEEE Transactions on Information Theory*, 54(1):151–170.

[Jayakody et al., 2018] Jayakody, D. N. K., Sharma, S. K., and Chatzinotas, S. (2018). *Introduction, Recent Results, and Challenges in Wireless Information and Power Transfer*, pages 3–28. Springer International Publishing, Cham.

[Jeong et al., 2018] Jeong, S., Simeone, O., and Kang, J. (2018). Mobile edge computing via a uav-mounted cloudlet: Optimization of bit allocation and path planning. *IEEE Transactions on Vehicular Technology*, 67(3):2049–2063.

[Kakar and Marojevic, 2017] Kakar, J. and Marojevic, V. (2017). Waveform and spectrum management for unmanned aerial systems beyond 2025. In *2017 IEEE 28th Annual International Symposium on Personal, Indoor, and Mobile Radio Communications (PIMRC)*, pages 1–5.

[Kaleem and Rehmani, 2018] Kaleem, Z. and Rehmani, M. H. (2018). Amateur drone monitoring: State-of-the-art architectures, key enabling technologies, and future research directions. *IEEE Wireless Communications*, 25(2):150–159.

[Kamel et al., 2016] Kamel, M., Hamouda, W., and Youssef, A. (2016). Ultra-dense networks: A survey. *IEEE Communications Surveys Tutorials*, 18(4):2522–2545.

[Karapantazis and Pavlidou, 2005] Karapantazis, S. and Pavlidou, F. (2005). Broadband communications via high-altitude platforms: A survey. *IEEE Communications Surveys Tutorials*, 7(1):2–31.

[Khawaja et al., 2016] Khawaja, W., Guvenc, I., and Matolak, D. (2016). Uwb channel sounding and modeling for uav air-to-ground propagation channels. In *2016 IEEE Global Communications Conference (GLOBECOM)*, pages 1–7.

[Khawaja et al., 2018] Khawaja, W., Guvenc, I., Matolak, D., Fiebig, U.-C., and Schneckenberger, N. (2018). A Survey of Air-to-Ground Propagation Channel Modeling for Unmanned Aerial Vehicles. *ArXiv e-prints*.

[Kölln and Zimmermann, 2009] Kölln, R. and Zimmermann, A. (2009). Transparent coordinator failure recovery for zigbee networks. In *Emerging Technologies & Factory Automation, 2009. ETFA 2009. IEEE Conference on*, pages 1–8. IEEE.

[Kong et al., 2011] Kong, M., Yorkinov, O., Tran, T. H. V., and Shimamoto, S. (2011). Elevation angle-based diversity access employing high altitude platform station and unmanned aerial vehicle (uav) for urban area communications.

[Kumar and Magarini, 2016] Kumar, A. and Magarini, M. (2016). Improved nyquist pulse shaping filters for generalized frequency division multiplexing. In *2016 8th IEEE Latin-American Conference on Communications (LATINCOM)*, pages 1–7.

[Lien et al., 2017] Lien, S. Y., Shieh, S. L., Huang, Y., Su, B., Hsu, Y. L., and Wei, H. Y. (2017). 5g new radio: Waveform, frame structure, multiple access, and initial access. *IEEE Communications Magazine*, 55(6):64–71.

[Lo et al., 2005] Lo, B. P., Thiemjarus, S., King, R., and Yang, G.-Z. (2005). Body sensor network–a wireless sensor platform for pervasive healthcare monitoring.

[Lyon, 2004] Lyon, D. H. (2004). A military perspective on small unmanned aerial vehicles. *IEEE Instrumentation Measurement Magazine*, 7(3):27–31.

[Lyu et al., 2017] Lyu, J., Zeng, Y., Zhang, R., and Lim, T. J. (2017). Placement optimization of uav-mounted mobile base stations. *IEEE Communications Letters*, 21(3):604–607.

[Maddah-Ali et al., 2008] Maddah-Ali, M. A., Motahari, A. S., and Khandani, A. K. (2008). Communication over mimo x channels: Interference alignment, decomposition, and performance analysis. *IEEE Transactions on Information Theory*, 54(8):3457–3470.

[Mahmood et al., 2015] Mahmood, M. A., Seah, W. K., and Welch, I. (2015). Reliability in wireless sensor networks: A survey and challenges ahead. *Computer Networks*, 79:166–187.

[Mahmoud et al., 2012] Mahmoud, A. R., El-Khamy, M., and Elsayed, K. (2012). Interference alignment performanceon mimo x channels with imperfect channel knowledge. In *2012 IEEE 13th International Workshop on Signal Processing Advances in Wireless Communications (SPAWC)*, pages 239–243.

[Marier et al., 2013] Marier, J. S., Rabbath, C. A., and LÃ©chevin, N. (2013). Health-aware coverage control with application to a team of small uavs. *IEEE Transactions on Control Systems Technology*, 21(5):1719–1730.

[Ma'sum et al., 2013] Ma'sum, M. A., Arrofi, M. K., Jati, G., Arifin, F., Kurniawan, M. N., Mursanto, P., and Jatmiko, W. (2013). Simulation of intelligent unmanned aerial vehicle (uav) for military surveillance. In *2013 International Conference on Advanced Computer Science and Information Systems (ICACSIS)*, pages 161–166.

[Mededovic et al., 2012] Mededovic, P., Veletic, M., and Blagojevic, Z. (2012). Wireless insite software verification via analysis and comparison of simulation and measurement results. In *2012 Proceedings of the 35th International Convention MIPRO*, pages 776–781.

[Medeović et al., 2012] Medeović, P., Veletić, M., and Blagojević, Ž. (2012). Wireless insite software verification via analysis and comparison of simulation and measurement results. In *MIPRO, 2012 Proceedings of the 35th International Convention*, pages 776–781. IEEE.

[METIS, 2015] METIS, D. (2015). D1. 4. *METIS Channel Models*.

[Michailow et al., 2014] Michailow, N., MatthÃ©, M., Gaspar, I. S., Caldevilla, A. N., Mendes, L. L., Festag, A., and Fettweis, G. (2014). Generalized frequency division multiplexing for 5th generation cellular networks. *IEEE Transactions on Communications*, 62(9):3045–3061.

[Mohammed et al., 2011] Mohammed, A., Mehmood, A., Pavlidou, F.-N., and Mohorcic, M. (2011). The role of high-altitude platforms (haps) in the global wireless connectivity. *Proceedings of the IEEE*, 99(11):1939–1953.

[Motlagh et al., 2017] Motlagh, N. H., Bagaa, M., and Taleb, T. (2017). Uav-based iot platform: A crowd surveillance use case. *IEEE Communications Magazine*, 55(2):128–134.

[Mozaffari et al., 2016a] Mozaffari, M., Saad, W., Bennis, M., and Debbah, M. (2016a). Efficient deployment of multiple unmanned aerial vehicles for optimal wireless coverage. *arXiv preprint arXiv:1606.01962*.

[Mozaffari et al., 2016b] Mozaffari, M., Saad, W., Bennis, M., and Debbah, M. (2016b). Efficient deployment of multiple unmanned aerial vehicles for optimal wireless coverage. *IEEE Communications Letters*, 20(8):1647–1650.

[Mozaffari et al., 2016c] Mozaffari, M., Saad, W., Bennis, M., and Debbah, M. (2016c). Optimal transport theory for power-efficient deployment of unmanned aerial vehicles. In *Communications (ICC), 2016 IEEE International Conference on*, pages 1–6. IEEE.

[Mozaffari et al., 2016d] Mozaffari, M., Saad, W., Bennis, M., and Debbah, M. (2016d). Unmanned aerial vehicle with underlaid device-to-device communications: Performance and tradeoffs. *IEEE Transactions on Wireless Communications*, 15(6):3949–3963.

[Mozaffari et al., 2017] Mozaffari, M., Saad, W., Bennis, M., and Debbah, M. (2017). Optimal transport theory for cell association in uav-enabled cellular networks. *IEEE Communications Letters*, 21(9):2053–2056.

[Naqvi et al., 2018] Naqvi, S. A. R., Hassan, S. A., Pervaiz, H., and Ni, Q. (2018). Drone-aided communication as a key enabler for 5g and resilient public safety networks. *IEEE Communications Magazine*, 56(1):36–42.

[Nayyer et al., 2011] Nayyer, A., Nayyer, M., and Awasthi, L. K. (2011). A comparative study of time synchronization protocols in wireless sensor network. *International Journal of Computer Applications*, 36(11):13–19.

[Nishiyama et al., 2017] Nishiyama, H., Kawamoto, Y., and Takaishi, D. (2017). On ofdm-based resource allocation in lte radio management system for unmanned aerial vehicles (uavs). In *2017 IEEE 86th Vehicular Technology Conference (VTC-Fall)*, pages 1–5.

[Nurmela et al., 2014] Nurmela, V., Karttunen, A., Roivainen, A., Raschkowski, L., Hovinen, V., EB, J. Y., Omaki, N., Kusume, K., Hekkala, A., Weiler, R., et al. (2014). Deliverable d1. 4 metis channel models. *Mobile Wireless Commun. Enablers Twenty-Twenty Inf. Soc.(METIS)*.

[Nurmela et al., 2015] Nurmela, V., Karttunen, A., Roivainen, A., Raschkowski, L., Imai, T., Jarvelainen, J., Medbo, J., Vihriala, J., Meinila, J., Haneda, K., et al. (2015). Metis channel models. *FP7 METIS, Deliverable D*, 1.

[Osseiran et al., 2014] Osseiran, A., Boccardi, F., Braun, V., Kusume, K., Marsch, P., Maternia, M., Queseth, O., Schellmann, M., Schotten, H., Taoka, H., et al. (2014). Scenarios for 5g mobile and wireless communications: the vision of the metis project. *IEEE Communications Magazine*, 52(5):26–35.

[Peng et al., 2016] Peng, M., Yan, S., Zhang, K., and Wang, C. (2016). Fog-computing-based radio access networks: issues and challenges. *IEEE Network*, 30(4):46–53.

[Prasad et al., 2015] Prasad, R., Bhashyam, S., and Chockalingam, A. (2015). On the sum-rate of the gaussian mimo z channel and the gaussian mimo x channel. *IEEE Transactions on Communications*, 63(2):487–497.

[Richter et al., 2009] Richter, F., Fehske, A. J., and Fettweis, G. P. (2009). Energy efficiency aspects of base station deployment strategies for cellular networks. In *2009 IEEE 70th Vehicular Technology Conference Fall*, pages 1–5.

[Sekander et al., 2018] Sekander, S., Tabassum, H., and Hossain, E. (2018). Multi-tier drone architecture for 5g/b5g cellular networks: Challenges, trends, and prospects. *IEEE Communications Magazine*, 56(3):96–103.

[Sharifi et al., 2015] Sharifi, F., Chamseddine, A., Mahboubi, H., Zhang, Y., and Aghdam, A. G. (2015). A distributed deployment strategy for a network of cooperative autonomous vehicles. *IEEE Transactions on Control Systems Technology*, 23(2):737–745.

[Sharma et al., 2018a] Sharma, N., Magarini, M., Dossi, L., Reggiani, L., and Nebuloni, R. (2018a). A study of channel model parameters for aerial base stations at 2.4 ghz in different environments. In *2018 15th IEEE Annual Consumer Communications Networking Conference (CCNC)*, pages 1–6.

[Sharma et al., 2018b] Sharma, N., Magarini, M., Jayakody, D. N. K., Sharma, V., and Li, J. (2018b). On-demand ultra-dense cloud drone networks: Opportunities, challenges and benefits. *IEEE Communications Magazine*, 56(8):85–91.

[Sharma et al., 2016] Sharma, V., Bennis, M., and Kumar, R. (2016). Uav-assisted heterogeneous networks for capacity enhancement. *IEEE Communications Letters*, 20(6):1207–1210.

[Sharma et al., 2017] Sharma, V., Song, F., You, I., and Chao, H.-C. (2017). Efficient management and fast handovers in software defined wireless networks using uavs. *IEEE Network*, 31(6):78–85.

[Siddique et al., 2015] Siddique, U., Tabassum, H., Hossain, E., and Kim, D. I. (2015). Wireless backhauling of 5g small cells: challenges and solution approaches. *IEEE Wireless Communications*, 22(5):22–31.

[Simsek et al., 2016] Simsek, M., Aijaz, A., Dohler, M., Sachs, J., and Fettweis, G. (2016). 5g-enabled tactile internet. *IEEE Journal on Selected Areas in Communications*, 34(3):460–473.

[Simunek et al., 2013] Simunek, M., FontÃ¡n, F. P., and Pechac, P. (2013). The uav low elevation propagation channel in urban areas: Statistical analysis and time-series generator. *IEEE Transactions on Antennas and Propagation*, 61(7):3850–3858.

[Sun et al., 2015] Sun, S., Rappaport, T. S., Rangan, S., Thomas, T. A., Ghosh, A., Kovacs, I. Z., Rodriguez, I., Koymen, O., Partyka, A., and Jarvelainen, J. (2015). Propagation path loss models for 5g urban micro-and macro-cellular scenarios. *arXiv preprint arXiv:1511.07311*.

[Sun et al., 2016] Sun, S., Rappaport, T. S., Rangan, S., Thomas, T. A., Ghosh, A., Kovacs, I. Z., Rodriguez, I., Koymen, O., Partyka, A., and Jarvelainen, J. (2016). Propagation path loss models for 5g urban micro- and macro-cellular scenarios. In *2016 IEEE 83rd Vehicular Technology Conference (VTC Spring)*, pages 1–6.

[Tan and Beaulieu, 1999] Tan, C. C. and Beaulieu, N. C. (1999). An investigation of transmission properties of xia pulses. In *1999 IEEE International Conference on Communications (Cat. No. 99CH36311)*, volume 2, pages 1197–1201 vol.2.

[Thomas et al., 2015] Thomas, T. A., Rybakowski, M., Sun, S., Rappaport, T. S., Nguyen, H., Kovacs, I. Z., and Rodriguez, I. (2015). A prediction study of path loss models from 2-73.5 ghz in an urban-macro environment. *arXiv preprint arXiv:1512.01585*.

[Torkildson et al., 2011] Torkildson, E., Madhow, U., and Rodwell, M. (2011). Indoor millimeter wave mimo: Feasibility and performance. *IEEE Transactions on Wireless Communications*, 10(12):4150–4160.

[Ustok et al., 2013] Ustok, R. F., Dmochowski, P. A., Smith, P. J., and Shafi, M. (2013). Aligned interference neutralisation for $2\times$ $2\times$ 2 interference channel with imperfect channel state information. In *Communications (ICC), 2013 IEEE International Conference on*, pages 5230–5235. IEEE.

[Vahidi and Saberinia, 2017] Vahidi, V. and Saberinia, E. (2017). Ofdm for payload communications of uas: channel estimation and ici mitigation. *IET Communications*, 11(15):2350–2356.

[Vasquez-Gomez et al., 2016] Vasquez-Gomez, J. I., Gomez-Castañeda, C., De Cote, E. M., and Herrera-Lozada, J. C. (2016). Multirotor uav coverage planning under wind conditions. In *Mechatronics, Electronics and Automotive Engineering (ICMEAE), 2016 International Conference on*, pages 32–37. IEEE.

[Vassilaras et al., 2017] Vassilaras, S., Gkatzikis, L., Liakopoulos, N., Stiakogiannakis, I. N., Qi, M., Shi, L., Liu, L., Debbah, M., and Paschos, G. S. (2017). The algorithmic aspects of network slicing. *IEEE Communications Magazine*, 55(8):112–119.

[Wei et al., 2017] Wei, Z., Wu, H., Huang, S., and Feng, Z. (2017). Scaling laws of unmanned aerial vehicle network with mobility pattern information. *IEEE Communications Letters*, 21(6):1389–1392.

[Werner-Allen et al., 2006] Werner-Allen, G., Lorincz, K., Ruiz, M., Marcillo, O., Johnson, J., Lees, J., and Welsh, M. (2006). Deploying a wireless sensor network on an active volcano. *IEEE Internet Computing*, 10(2):18–25.

[Willig and Karl, 2005] Willig, A. and Karl, H. (2005). Data transport reliability in wireless sensor networks. a survey of issues and solutions. *Praxis der Informationsverarbeitung und Kommunikation*, 28(2):86–92.

[Willink et al., 2016] Willink, T. J., Squires, C. C., Colman, G. W. K., and Muccio, M. T. (2016). Measurement and characterization of low-altitude air-to-ground mimo channels. *IEEE Transactions on Vehicular Technology*, 65(4):2637–2648.

[Wu et al., 2017] Wu, Q., Zeng, Y., and Zhang, R. (2017). Joint trajectory and communication design for uav-enabled multiple access. In *GLOBECOM 2017 - 2017 IEEE Global Communications Conference*, pages 1–6.

[Wu et al., 2018] Wu, Q., Zeng, Y., and Zhang, R. (2018). Joint trajectory and communication design for multi-uav enabled wireless networks. *IEEE Transactions on Wireless Communications*, 17(3):2109–2121.

[Wu and Zhang, 2017] Wu, Q. and Zhang, R. (2017). Delay-constrained throughput maximization in uav-enabled ofdm systems. In *2017 23rd Asia-Pacific Conference on Communications (APCC)*, pages 1–6.

[Wu et al., 2005] Wu, Z., Kumar, H., and Davari, A. (2005). Performance evaluation of ofdm transmission in uav wireless communication. In *Proceedings of the Thirty-Seventh Southeastern Symposium on System Theory, 2005. SSST '05.*, pages 6–10.

[Xu et al., 2004] Xu, N., Rangwala, S., Chintalapudi, K. K., Ganesan, D., Broad, A., Govindan, R., and Estrin, D. (2004). A wireless sensor network for structural monitoring. In *Proceedings of the 2nd international conference on Embedded networked sensor systems*, pages 13–24. Acm.

[Yaliniz et al., 2016] Yaliniz, R., El-Keyi, A., and Yanikomeroglu, H. (2016). Efficient 3-d placement of an aerial base station in next generation cellular networks. *arXiv preprint arXiv:1603.00300*.

[Yang et al., 2017a] Yang, C., Li, J., Ni, Q., Anpalagan, A., and Guizani, M. (2017a). Interference-aware energy efficiency maximization in 5g ultra-dense networks. *IEEE Transactions on Communications*, 65(2):728–739.

[Yang et al., 2017b] Yang, P., Cao, X., Yin, C., Xiao, Z., Xi, X., and Wu, D. (2017b). Proactive drone-cell deployment: Overload relief for a cellular network under flash crowd traffic. *IEEE Transactions on Intelligent Transportation Systems*, 18(10):2877–2892.

[Yanmaz et al., 2011] Yanmaz, E., Kuschnig, R., and Bettstetter, C. (2011). Channel measurements over 802.11a-based uav-to-ground links. In *2011 IEEE GLOBECOM Workshops (GC Wkshps)*, pages 1280–1284.

[Zafar and Khan, 2016] Zafar, W. and Khan, B. M. (2016). Flying ad-hoc networks: Technological and social implications. *IEEE Technology and Society Magazine*, 35(2):67–74.

[Zajić, 2012] Zajić, A. (2012). *Mobile-to-mobile wireless channels*. Artech House.

[Zeng and Zhang, 2017] Zeng, Y. and Zhang, R. (2017). Energy-efficient uav communication with trajectory optimization. *IEEE Transactions on Wireless Communications*, 16(6):3747–3760.

[Zeng et al., 2016] Zeng, Y., Zhang, R., and Lim, T. J. (2016). Wireless communications with unmanned aerial vehicles: opportunities and challenges. *IEEE Communications Magazine*, 54(5):36–42.

[Zhang et al., 2016] Zhang, H., Dong, Y., Cheng, J., Hossain, M. J., and Leung, V. C. M. (2016). Fronthauling for 5g lte-u ultra dense cloud small cell networks. *IEEE Wireless Communications*, 23(6):48–53.